EXPERIMENTAL AND COMPUTATIONAL INVESTIGATION OF THE THERMAL EFFECTS ON CVD DIAMOND FILMS BY OXY-ACETYLENE COMBUSTION METHOD

By

KIYOUNG BANG

Bachelor of Science
Sung Kyun Kwan University
Seoul, Korea
1986

Master of Science
Oklahoma State University
Stillwater, Oklahoma
1989

Submitted to the Faculty of the Graduate College
of the Oklahoma State University
in partial fulfillment of the requirements
for the Degree of
DOCTOR OF PHILOSOPHY
May, 1994

EXPERIMENTAL AND COMPUTATIONAL INVESTIGATION

OF THE THERMAL EFFECTS ON CVD DIAMOND

FILMS BY OXY-ACETYLENE

COMBUSTION METHOD

Thesis Approved:

A. J. Ghajar

Thesis Adviser

K. A. M. Gasem

David C. Riley

Ronald L. Dougherty

Thomas C. Collins

Dean of the Graduate College

ACKNOWLEDGMENTS

I wish to express my sincere gratitude to my advisor, Professor Afshin J. Ghajar, whose inspiration, guidance, and constant encouragement kept me motivated during this study. I am also grateful to my other committee members, Dr. D. G. Lilley, Dr. R.L. Dougherty, and Dr. K. A. M. Gasem for their valuable advisement and discussion during the course of this study.

I am greatly indebted to Dr. R. Komanduri for helping me in building the experimental setup and in the assessment of the diamond film analysis. Without his help, this study would not have been possible.

This study was supported by the University Center for Energy Research (UCER) at Oklahoma State University and the Oklahoma Center for Integrated Design and Manufacturing (OCIDM). I would like to thank Mr. D. Warnecker and Mr. S. Hudgens for their helpfulness in the experimental phase of this project.

I am most grateful to my parents, Mr. Suk Hong Bang and Mrs. Eui Yul Bang for their patiently providing financial support and encouragement through my graduate study at Oklahoma State University, and to my loving daughter, Estelle, and my wife, Jung Mi, for their love and prayer. This work is dedicated to them.

TABLE OF CONTENTS

Chapter Page

LIST OF TABLES

Table Page

LIST OF FIGURES

Figure Page

Figure Page

Figure Page

NOMENCLATURE

English Letters

A	surface area
a	coefficient in discretization equation, see Equation (22)
c_p	specific heat of coolant (water) evaluated at the average temperature of inlet and outlet (at heat sink) water temperature
D	diameter
D_f	diameter of synthetic diamond film
D_n	diameter of nozzle (see Figure 2.4)
f_c	constant part of the linearized boundary heat flux, see Equation (24)
F_{ij}	configuration factor, the fraction of the radiative energy leaving i-surface that arrives at j-surface
f_p	coefficient of T_p in the linearized boundary heat flux, see Equation (24)
G	irradiation absorbed at a control surface
g	acceleration of gravity
h	convective heat transfer coefficient
H_s	substrate height (see Figure 2.4)
h_t	total heat transfer coefficient
k	thermal conductivity
L	length
L_b	length of a side of square base in octahedral or cubo-octahedral crystal
L_c	characteristic length

L_i	length of the inner cone (see Figure 2.4)
L_n	distance between the substrate surface and tip of the nozzle (see Figure 2.4)
L_s	distance from the substrate surface to the inner cone (see Figure 2.4)
Nu	Nusselt number
P	pressure
Pr	Prandtl number
Q	volume flow rate
q	heat transfer rate
q"	heat flux
q_c	rate of heat transfer to the coolant, see Equation (16)
R	ratio of volume flow rates of oxygen to acetylene
r	radial direction
Ra	Rayleigh number
Re	Reynolds number
S	source term
S_c	constant part of the linearized source term, see Equation (21)
S_p	coefficient of T_p in linearized source term, see Equation (21)
T	temperature
t_d	diamond film deposition time
T_{in}	coolant inlet temperature
T_{out}	coolant outlet temperature
T_s	substrate temperature
T_∞	ambient fluid temperature
V	velocity
x	axial direction

Greek Letters

α	thermal diffusivity
β	volume expansion coefficient
Δ	difference
ΔV	volume of the control volume
δ	half thickness of control volume
ε	emissivity
μ	absolute viscosity
ν	kinematic viscosity
ρ	density
σ	Stefan-Boltzmann constant (5.67×10^{-8} W/m^2-K^4)

Subscripts

a	air
B	boundary
c	coolant
cu	copper
f	flame
i	control surfaces in i-direction
j	control surfaces in j-direction
nb	neighboring
p	central grid point under consideration
s	substrate
w	boundary wall exposed to fluid

Superscripts

$\bar{}$	average value
$''$	flux term (per unit surface area)

CHAPTER I

INTRODUCTION

Diamond is one of the most fascinating materials on earth. It has many unique properties and consequently its synthesis has been for many centuries, a great scientific challenge. It has the highest hardness (Knoop hardness ~10000 kg/mm^2), high wear resistance, low coefficient of friction (0.1 in air), high thermal conductivity (2000 W/m-K, five times that of copper), chemical inertness, high electrical resistivity (2.42×10^{13} Ω cm), optical transparency (at wavelength > 320 nm), and high sonic speed (7200 m/s). See Appendix A for details on the properties of diamond. Comparison of the properties of diamond and other competing materials are also included in Appendix A. The word 'Diamond' comes from the Greek word 'adamas', meaning invincible. Indeed, it is invincible in conducting and dissipating heat, in being hard, and in resisting electric flow as seen in Appendix A.

The unique properties of diamond have enabled its use in a variety of applications in industry. The bulk of world production of natural rough diamonds have been increased. Over half (55%) the world's production of natural rough diamond consists of industrial quality diamonds (some 40 tons of consumption in 1990, as shown in Table 1.1), with 45% being of gemstone quality. However, more industrial quality diamonds is required. The growing demand for diamond has fueled efforts to produce diamond synthetically. The reliable synthesis of diamond started in the 1950's. Before the 1980's, synthesized diamond had been used mainly for abrasive purposes (cutting, milling, drilling, grinding). The form of synthesized diamond during this time was grit, which was produced by high

pressure-high temperature techniques. Currently, 30 to 40 tons of diamond grit is produced each year using the same techniques. The applications of diamond had been limited to abrasive purposes before the 1980's. Starting in the 1980's, diamond films and coatings have been produced in laboratories all over the world by new techniques (mainly chemical vapor deposition, CVD, diamond synthesis) as well as by high pressure techniques. CVD techniques differ from high pressure techniques in employing low pressure during the synthetic process. The synthesized diamond film and coatings have significantly expanded the applications of diamonds in many industrial fields. Synthetic diamond films and coatings are rapidly taking on new roles that have the potential to coat aircraft turbine blades, surgical instruments, semiconductors, light-emitting diodes, and transistors.

Table 1.1 Industrial Diamond Usage since the 1940's (Buckley and Collins, 1992)

Year	Consumption (tons)
1950	3
1960	10
1970	12
1980	30
1990	40
2000	80

New uses for diamond films range from supercomputer heat sinks and heat seeking missile windows to such mundane things as gourmet knives and scratchproof sunglasses. Diamond film could insulate fuel cells to make them more efficient and heat exchangers to make them more resistant to corrosion and erosion. It can draw off the heat generated by closely packed electronic circuitry of desktop supercomputers and high-density semiconductors. Supercomputers using diamond printed circuits are on the drawing

boards that will run four times faster and be as much as 60 times smaller than conventional supercomputers. Diamond can be used as laser mirrors, which can suffer optical degradation and dielectric breakdown from high-powered laser light. Diamond coating on a laser mirror could increase the mirror's reflectivity while reducing weight and adding survivability. Recently, measurements on the synthesized diamond by General Electric showed 1000% more laser-resistant than natural stones (Brown, 1991). Table 1.2 shows a number of current or potential applications of diamond films and coatings.

From the filed patents over the last 10 years in the specific areas of diamond film, Japan was the first to file for patents beginning in 1981 onwards as shown in Figure 1.1. The specific areas of diamond film patent activity include electronics, semiconductors, electrical application, grit, heat sinks, cutting, tools, wear, and optics/optical. This figure shows the levels of interest and technology in diamond film in Japan, U.S.A., and Europe. Japan has exceeded U.S.A. and Europe in the investigation and application of diamond thin films according to the number of diamond film patents as shown in Figure 1.1. However, the number of diamond film patents in U.S.A. has increased significantly since 1988 while that in Japan has decreased since 1990: the center of gravity of diamond films is moving to U.S.A. from Japan. The breakdown of patents by industrial application over the period 1980-1991 is presented in Figure 1.2. As to the applications of diamond films, abrasive purpose(cutting, tools, wear) dominates others as seen in this figure. Actually, the products of diamond films for cutting, tools, and wear have an important market in the world. However, electrical/electronics related applications of diamond films are of great interest, and they have a heavy market potential.

There are two production types in manufacturing diamond films by all methods of CVD and high pressure techniques. These are: 1) coating 2) free standing film. Both types are available in CVD techniques. However, high pressure techniques can produce only free standing diamond films. Free standing film is a flat or curved free standing diamond sheet whose thickness is usually greater than 50 μm where as the thickness of

Table 1.2 Applications of CVD Diamond (Buckely and Collins, 1992)

CONSUMER	ELECTRICAL & ELECTRONIC	INDUSTRIAL & BIOMEDICAL	AEROSPACE	AUTOMOTIVE
• Hi-Fi coatings on speakers • free standing speaker membrances • thin films on lenses • thin films on memory disks • optical disk storage	• heat sinks • PC board • superlattices • insulation • high power electronics • diffusion barriers • high density IC's • high temp. sensors • high temp. semiconductors • microwave transmission • solar cell protection	• wear/corrosion resistance coating • cutting, polishing, grinding • scalpals • prosthesis • high pressure cells • wire drawing dies • temp. sensors • metrology instruments • microstructures • hardness indentors	• UV lasers/detectors • wear/corrosion resistant coatings • radiation resistant electronics • radiation detectors • UV/IR windows • heat/radiation resistant enclosures	• under-bonnet sensors • under-bonnet electronics

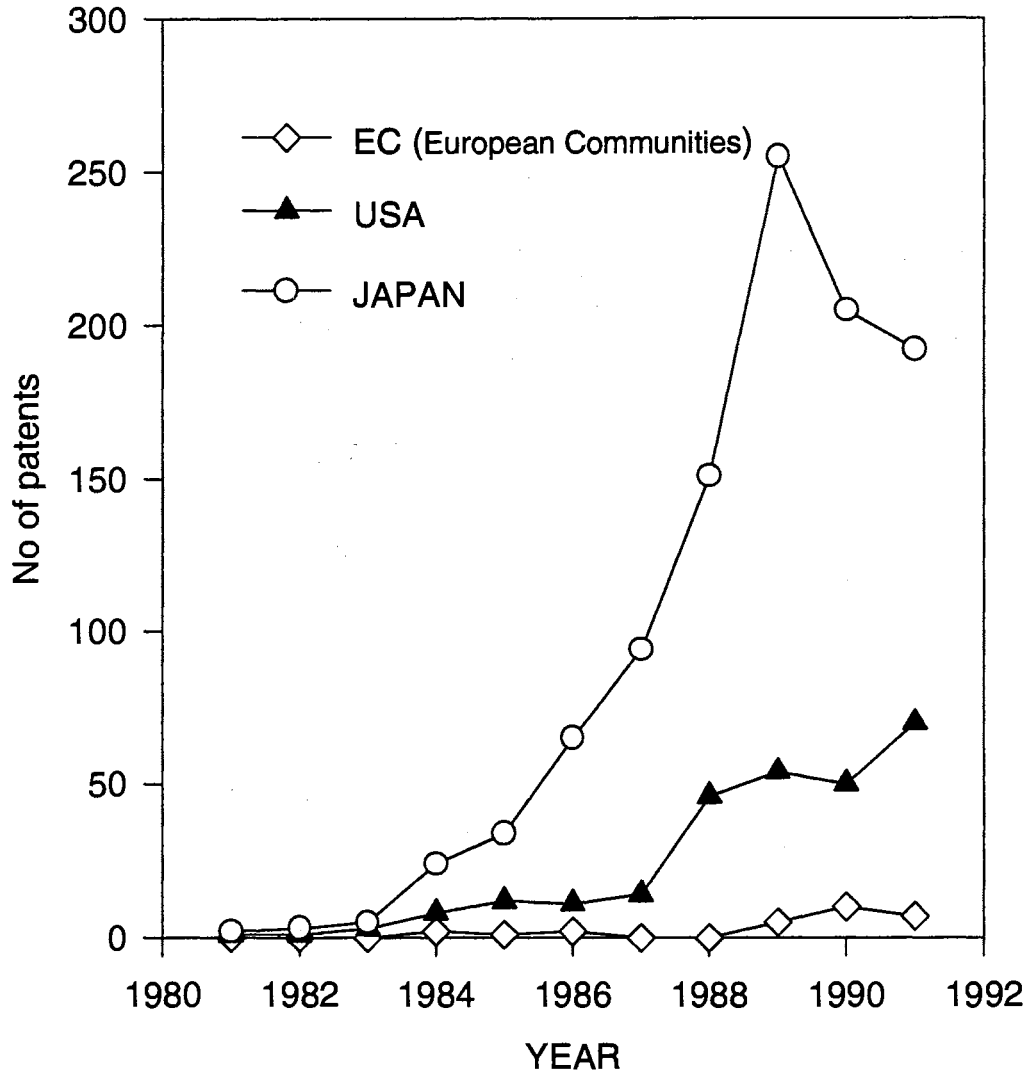

Figure 1.1 Diamond Thin Film Patent Activity Over the Period 1981-1991 Broken Down by Three Economic Territories: EC, United States, Japan (Buckley and Collins, 1992)

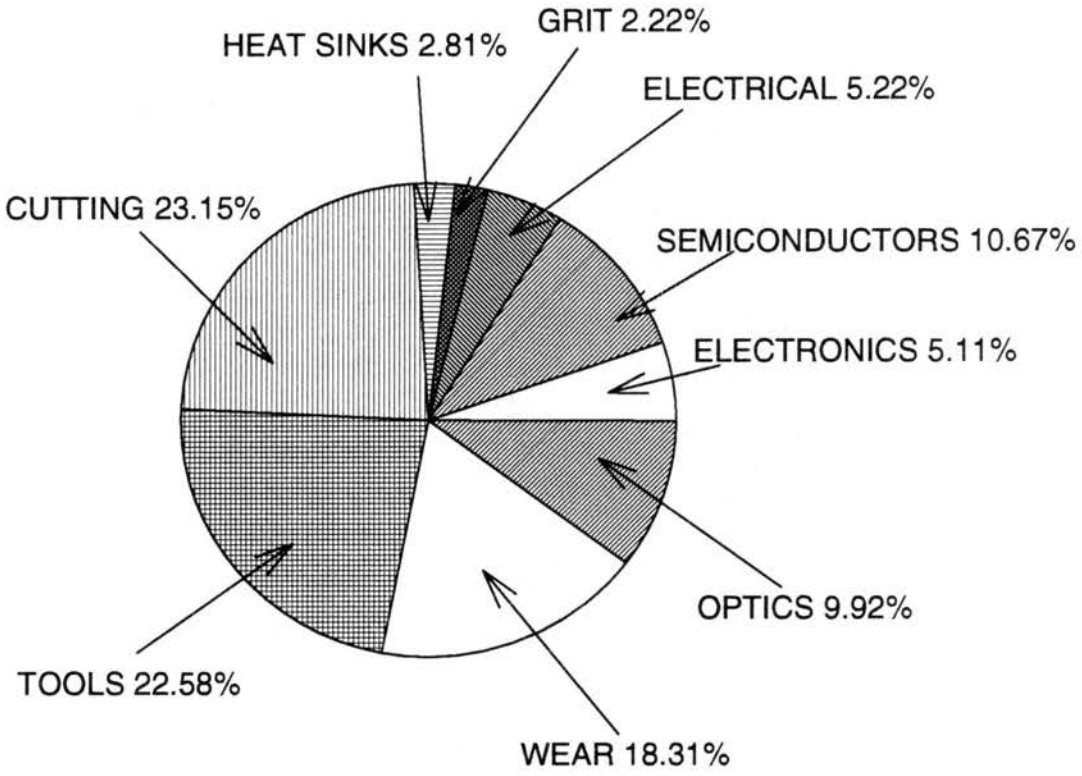

Figure 1.2 Division of Application of Diamond by Numbers of Patents Over the Period 1981-1991 (Buckley and Collins, 1992)

coating is less than 50 μm. Nondiamond and diamond are used as substrates in the coating process by CVD techniques. One of the advantages in CVD techniques compared to high pressure techniques, is that a complicated shape of substrate (three dimensional shape) can be coated by diamond film. Therefore, CVD diamond techniques have broaden the industrial applications of diamond films.

Commercial diamond films produced by CVD technologies are emerging in the market of tools. Tools with diamond films by CVD technologies have shown a good performance, long life time, and reasonable manufacturing cost. Even if costs are high compared to classical tools, the resulting increase in performance of the components for their applications are justified by highly competitive improvements. Industrial endmills

and metal-cutting tool inserts using bonded free standing CVD diamond have been commercially available for a few years. An example of production process of free standing CVD diamond sheets for cutting tools is described in Figure 1.3.

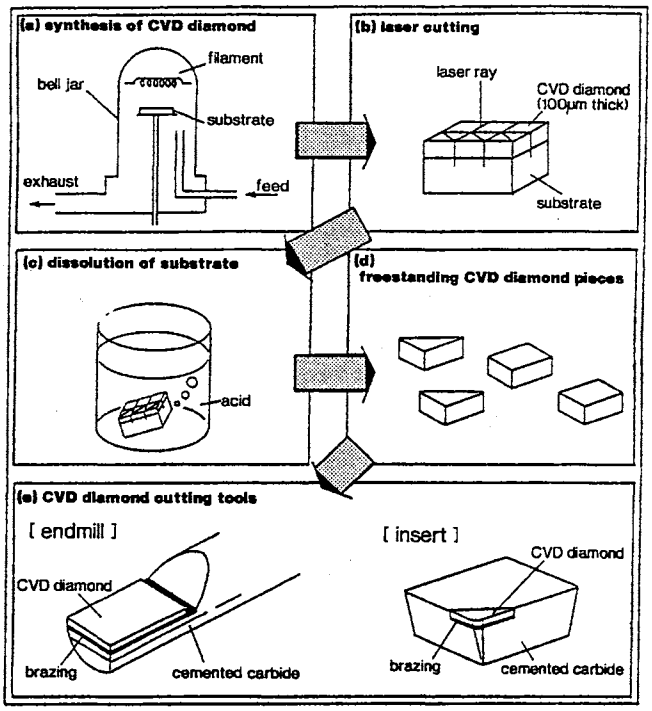

Figure 1.3 Production Process of Free Standing CVD Diamond Sheets Brazed to Cutting Tools (Yashiki et al., 1991)

Some Japanese investigators (Yashiki et al., 1991) reported the performance of CVD diamond in abrasion using a cleaning whetstone as a workpiece. They coated a tool with CVD diamond film (8 × 9 mm). Also polycrystalline (PCD) and single crystalline films by high pressure techniques were simultaneously tested at the same working conditions. The results are shown in Figure 1.4. Cleaning damage to CVD diamond is less than that of PCD, and CVD diamond showed the same resistance as single crystalline diamond. The costs analysis for three different diamond film products in this test is described in Table 1.3. The cost per bond (including regrinding) for both CVD diamond

tools and single tools is considerably lower than that of PCD. Single crystalline tools have the longest life time (8,000,000 individual bond) but high initial costs. CVD diamond and PCD tools show almost same life times, but CVD diamond tools have better performance as seen in Figure 1.4. Thus CVD diamond tools are best suited for medium-variety and medium-quantity or large-variety and small-quantity productions, while single crystalline diamond tools are most suited for mass production. Single crystalline diamond film can be produced by using CVD technologies.

Polycrystalline CVD diamond films are used in abrasive purposes. The most important property of diamond in these purposes is hardness (rigidity, high Young's modulus, etc.). Most polycrystalline CVD diamond films contain a certain amount of sp^2 bonds which means impurity. This impurity degrades diamond properties. However, small amounts of sp^2 in diamond film does not cause major detrimental effects on the antiwear performances of diamond. A certain degree of degradation of diamond hardness is acceptable in the antiwear performances. This greatly simplifies the development of abrasive applications of diamond films.

The main technical problems in the applications of CVD diamond films for abrasive purposes are: bonding free standing film to tool, adhesion of film to substrate (coating), rough surface of film, and large area of film. Bonding problems occur not only in CVD diamond films, but also in high-pressure synthesized diamond film. The bond strength has increased so far, and bonding has become a minor problem. The different thermal expansion coefficients of diamond film and substrate causes internal stress at the interface between diamond film and substrate during the synthetic process. This resulting internal stress leads to bad adhesion. Several treatments to solve adhesion problems have been recommended, and now some diamond-coated substrates are already able to achieve the required adhesion strength for acceptable performance. Because of the growth of faceted crystals in the direction normal to the substrate, the surface of polycrystalline CVD diamond is somehow rough. Sometimes, the resulting roughness is not acceptable for the

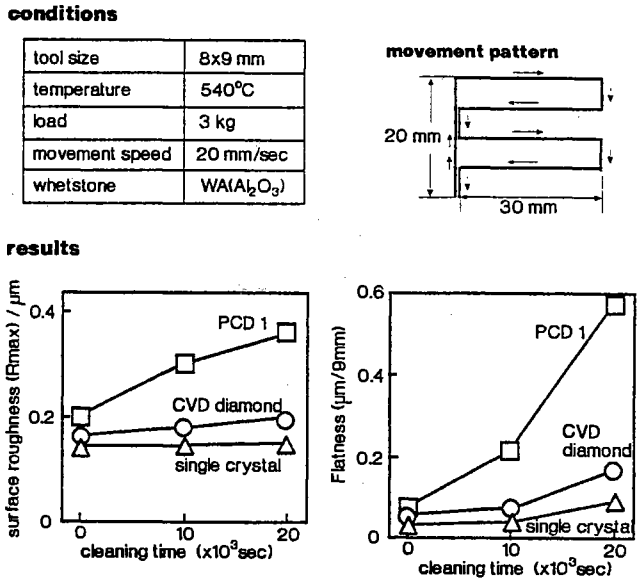

Figure 1.4 Influence of Cleaning Time of a TAB Tool on Surface Roughness and Flatness (Yashiki et al., 1991)

Table 1.3 Results of Tool Life Tests and Bonding Cost Analysis (Yashiki et al. 1991)

Tool Materials	CVD Diamond	Single Crystal	PCD1	PCD2
tool life ($\times 10^3$ shots)	600	2000	200	80
maximum regrinds		3	3	3
total tool life ($\times 10^3$ shots)	600	8000	800	320
tool price	1	2.5	1	1
regrinding price (PCD unit base)		2.5	1	1
bonding cost	1	1	3.2	2.9

better results of abrasive work. Thus the produced diamond films are to be grinned and polished, which results in a cost increase.

Pure diamond has very attractive properties required in electronic and electrical applications. As shown in Table A.5 in Appendix A, pure diamond easily outclasses the competing materials (silicon carbide, gallium arsenide, silicon) as semiconductors. Thus electronic applications have highlighted the potential areas such as semiconductors, motor control, automotive electronics, switched mode power converters, medical electronics, lighting aerospace electronics, etc.. However, a number of process steps is required to produce a diamond electronic device as described in Figure 1.5. The complete process cycle to produce diamond electronic devices has not been thoroughly attempted. There are only isolated reports concerning the fabrication of discrete diamond devices such as simple diode structures and transistors. CVD diamond films can be used in electrical areas such as high energy microwave amplifiers, pulsed lasers, high frequency/high power devices.

CVD diamond films do not settle a good market in electronic and electrical applications due to relatively high price and the lack of availability of lager sizes. Also, stress-free CVD diamond films are required. Moreover, high degree of purity is required in these applications compared to abrasive applications. Additionally, this fact causes costs to increase. Polycrystalline CVD diamond films degrade the excellent properties of pure diamond in electric and electrical applications because they have impurities, different surface crystal facets, different crystal orientation, internal defect structures, and different crystallite sizes (Field, 1979; Lux and Haubner, 1989). Thus homoepytaxial growth diamond films (single crystal quality) which is available in both CVD techniques and high pressure techniques, were applied in the areas of electric and electrical applications. In CVD technologies, homoepytaxial growth process requires diamond substrate. Thus producible films have limited size as small as few millimeter diameter, and the resulting costs are high. However, the performance were excellent: for example, the upper limit of

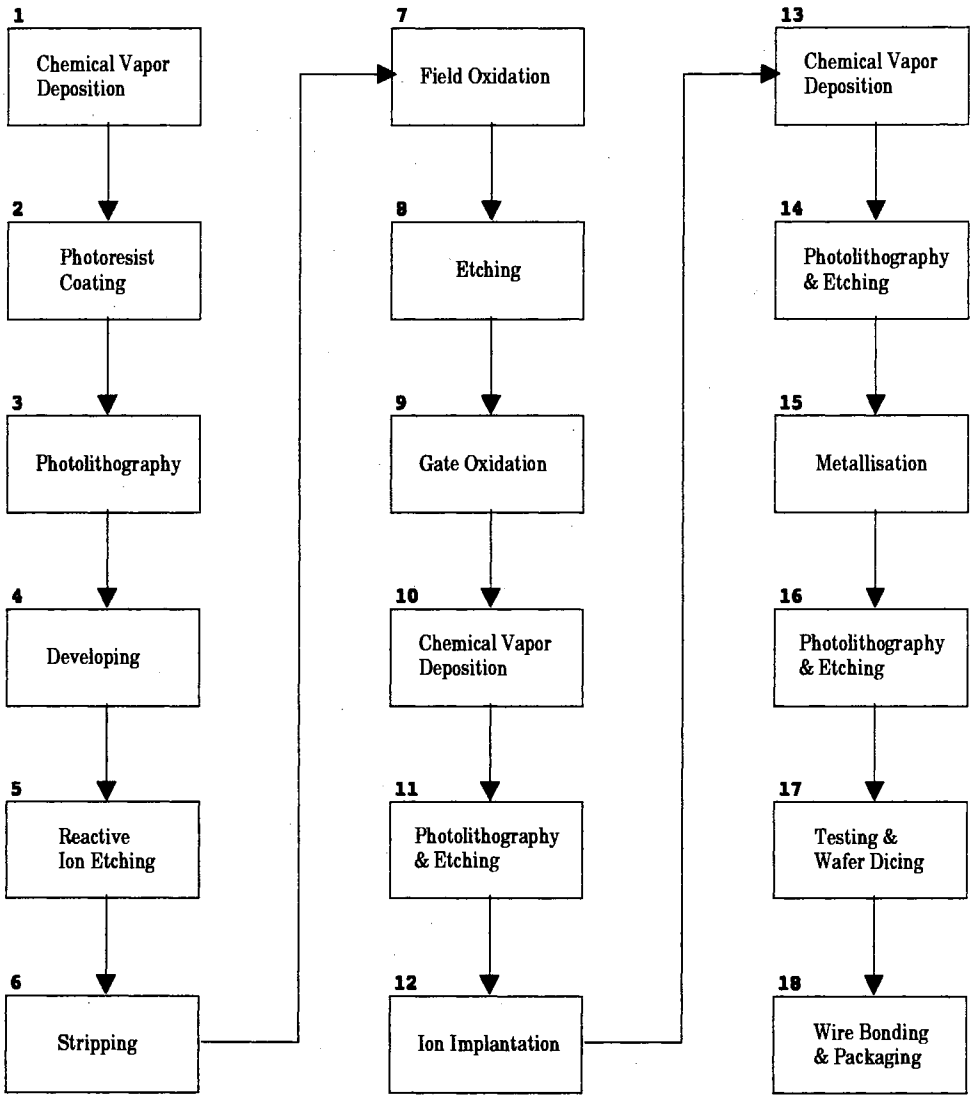

Figure 1.5 The Generic Process Steps Required to Produce a Diamond Electronic Device (Buckley and Collins, 1992)

working temperature of a transistor using diamond film increased significantly (Geis et al., 1987; Gildenblat et al., 1990). The costs of CVD films are decreasing from developments of technologies. Therefore, CVD diamond in electronic and electrical applications will be of widespread use, if large size film and high quality polycrystalline CVD films are available in future.

The typical thermal conductivity of PCD by high pressure techniques is about 5 W/cm-K, whereas CVD diamond reaches more than 15 W/cm-K. In addition, most PCD's are electrically conductive due to binder material, which prohibits its use as a heat sink for many electronics application. Thus CVD diamond is more suitable than PCD by high pressure techniques. CVD film is already entering the heat sink market and smart approaches for product integration rather than basic technological problems are the main problem in this sector. Cost and film size are major factors limiting the market for CVD diamond heat sink.

The potential market for CVD diamond products are shown in Figure 1.6. According to this estimate, thin film products (in situ CVD coatings) will account for $4500 million and free standing diamond products are expected to amount to $2000 million: total market of $6500 million. This estimate is based on the current market survey and expected technological developments. The final goal of CVD diamond synthesis is to produce a good quality polycrystalline diamond film with: quality close to that of single crystal (gem quality), large size (larger than 50 mm in diameter), and low cost. When these requirements are achieved, CVD diamond films will be used much more than the prediction as shown in Figure 1.6.

Among the developed methods of CVD diamond synthesis, oxy-acetylene combustion method is getting favorable attention due to its simplicity, high growth rate, low cost, and the possibility of producing large area coating. Diamond films produced by this method have relatively good quality and transparency. Several investigators (Bachmann and Enckevort, 1992; Lux and Haubner, 1989; Ghajar and Bang, 1993a; etc.) recommended oxy-acetylene combustion method as an efficient method among all CVD methods in the view of commercial and technical aspects. The cost of producing diamond film increases as a strong function of film dimension in all CVD methods since the cost of building experimental setup and the amount of supplied chemical gases increases. However, oxy-acetylene combustion method does not require rebuilding experimental

setup in order to produce large size of diamond film. Thus, the cost of producing large diamond film by this method is lower than any other CVD methods.

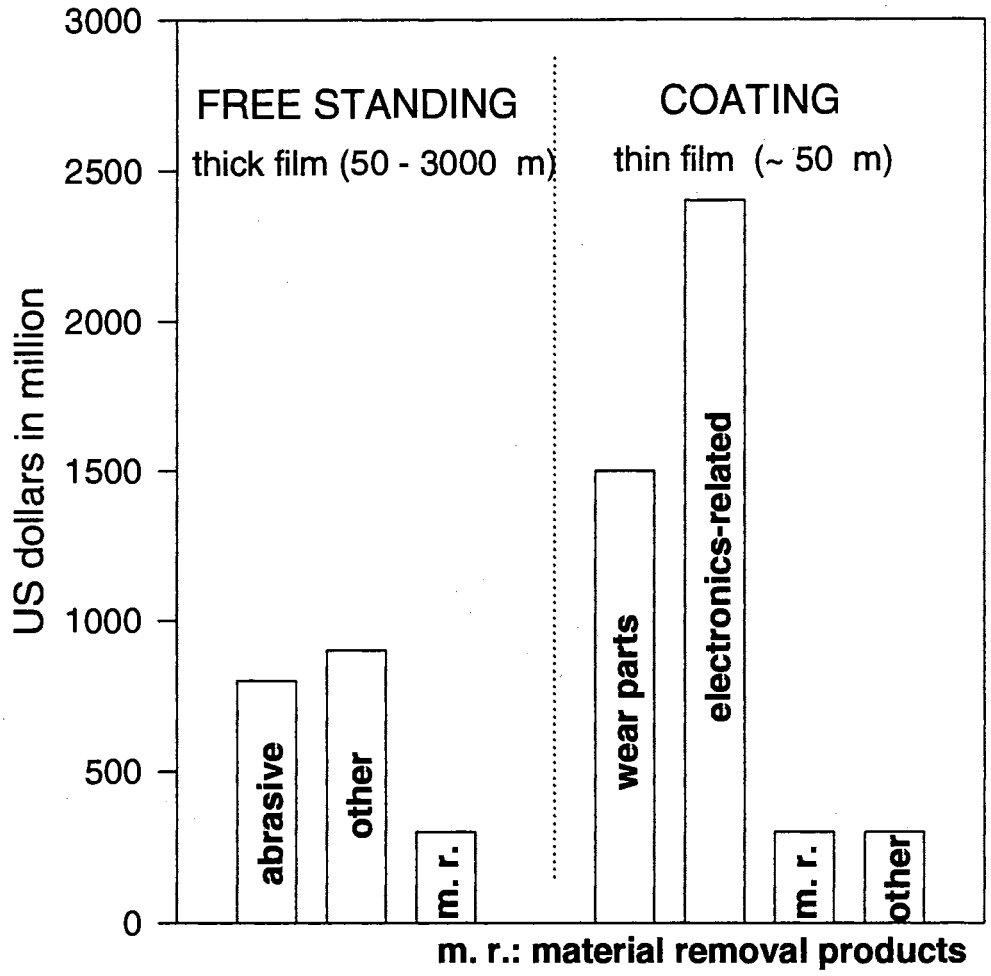

Figure 1.6 The Potential Market for CVD Diamond Products at the End of This Decade (Lux and Haubner, 1992)

The quality and morphology of the synthesized diamond films by oxy-acetylene combustion method depend on a variety of factors including the substrate temperature, gas flow ratio of oxygen to acetylene, and substrate position. Due to the nature of oxy-acetylene combustion flame, surface temperature of substrate varies in the radial direction. The substrate temperature profile, in turn, is influenced by such process variables as coolant flow rate, nozzle size, substrate position on heat sink, substrate position in combustion flame, and total flow rate of reactants (Ghajar and Bang, 1993a). The influence of these parameters on the substrate temperature profile and consequently the morphology and quality of diamond films in oxy-acetylene combustion method is yet to be fully exploited and is the focus of the present work.

A review of the literature is presented in the next chapter to provide proper perspective for the present work and to shed some light onto further contributions. Research needs, specific objectives, and the method of approach are also discussed therein.

CHAPTER II

LITERATURE REVIEW, RESEARCH NEEDS, OBJECTIVES AND METHOD OF APPROACH

In this chapter, a review of the work published in the open literature on diamond synthesis is presented. Then, shortcomings of previous works, objectives of the present work, and the method of approach are described.

2.1 History of Diamond Synthesis

The material presented in this section was partially obtained from the works by Angus and Hayman (1988), Backmann and Messier (1989), and Nandyal (1991).

Diamond synthesis started in the latter part of 19th century. The idea was to convert graphite directly into diamond at high pressure and high temperature-conditions where diamond is the thermodynamically stable form of carbon.

In 1880, Hannay claimed to have made diamond by heating a mixture of hydrocarbons, bone oil, and lithium at red heat in scaled wrought iron tubes. Some tubes were found to contain crystalline carbon like diamond. Carbon analysis of the crystals proved that the tubes contained 97.8% carbon. However, Hannay's experiments were very unreliable and present knowledge indicates that the temperatures used by Hannay and the reaction pressures in the tubes were too low for the synthesis of diamond.

In 1884, a French chemist by the name of Henri Moissan dissolved sugar-charcoal in molten iron and quenched the solution in cold water. This caused the carbon to crystallize under the high pressure generated by the contraction of the mass as it cooled. Moissan extracted transparent crystals from the metal. These crystals were reported to

have good optical properties and produced carbon-dioxide on combustion.

Later, Crookes, Parson and Hershey investigated Moissan's synthesis method. Parson had worked for thirty years using his own techniques as well as Moissan's to synthesize diamond, but the synthesized crystals turned out to be incombustible material indicating nondiamond.

During the 1940's, experimental attempts were based on the detailed knowledge of the carbon phase diagram with pressure and temperature (P-T equilibrium diagram of carbon) developed by Leipunskii, Liljeblad, Berman, Simon, and others (Bachmann and Messier, 1989; see Figure 2.1). Using the P-T equilibrium diagram of carbon, some research groups synthesized diamond successfully from graphite with high pressures (up to 50 kbar) and high temperatures (up to 1500 °C) : Allemanna Svenska Elektriska Aktiebolaget in Sweden in 1953 and General Electric in the U.S.A. in 1954.

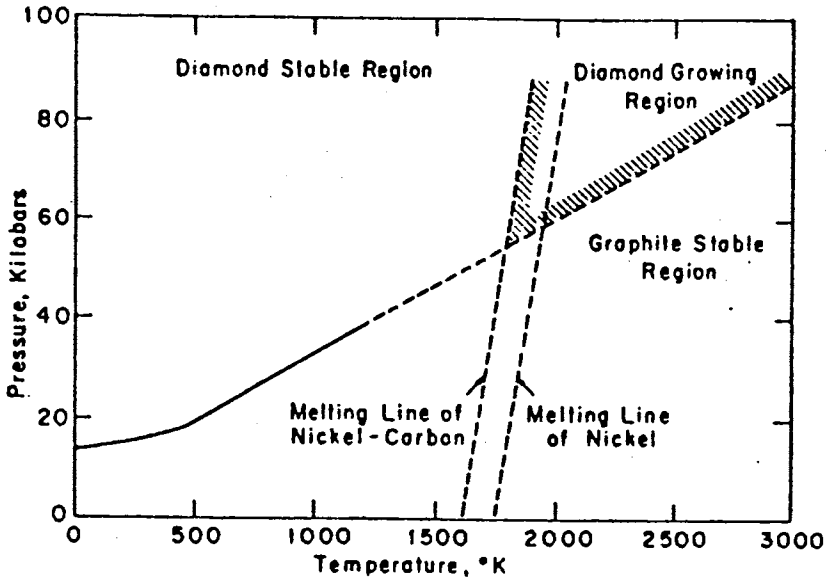

Figure 2.1 P-T Diagram of Carbon Showing the Diamond Stable Region (Bovenkerk et al., 1959)

In 1961, Decali of Stanford Research Institute and Jamieson from the University of Chicago synthesized diamond from graphite by means of shock wave at 300 kbar of pressure and 1200 °C of temperature. Today, industrial plants in many countries produce about 30 to 40 tons per year of synthetic diamond grit for abrasive use by one of these high-pressure methods (Bachmann and Messier, 1989).

However, big diamond grits often required for industrial uses, are usually prohibitively costly or totally unavailable. Today, advances in material science are showing ways to put a coating of diamond on many other, less-exotic materials, thereby imparting to them the beneficial properties of diamond (electronic and optical properties as well as hardness) as mentioned in the previous chapter.

Graphite is the stable form of carbon under normal atmospheric condition, while diamond is stable form of carbon at high pressure (see Figure 2.1). However, it is seen that graphite exists along with diamond under normal atmospheric condition, where diamond is metastable. This co-existence is possible because the activation energy between stable and metastable states is high enough to prevent the conversion of diamond (metastable) to graphite (more stable).

Though diamond is the metastable form of carbon at low pressure, this does not mean crystallization occurs at this condition. This is because the free energy of carbon in diamond is slightly higher than in graphite. However, metastable diamond can be formed from compounds such as methane, carbon-monoxide, carbon vapor, and other carbon containing gases, under kinetically controlled conditions. That is, the free energy of atomic carbon should be higher than that of carbon in diamond. Furthermore, if the free energy of carbon atoms decreases to an appropriate level, diamond can be crystallized (diamond synthesis at low pressure).

Eversole at the Union Carbide Corporation was the first to grow diamond successfully at low pressure, in the period of 1952 to 1953. At the same time period, Liander produced a synthesis of diamond at Allemanna Svenka Elektriska Aktiebulagat in

Sweden (ASEA). Eversole grew new diamonds on the pre-existing diamond nuclei, whereas ASEA synthesis started with nondiamond substrate. Eversole passed carbon containing gas (preferably with methyl group) over seed crystals at a temperature of about 1000 °C and a pressure of a few torr. New diamond was formed on the seeds until it was hampered by the accumulation of graphite, which was then removed by heating the diamond-deposited seed crystals in a hydrogen gas atmosphere at about 1000 °C and 50 atm. For continuous diamond growth, this deposition-cleaning cycle was repeated. The growth rate was extremely low, only a few Angstroms/hr.

Deryagin in the Soviet Union has had the longest sustained research efforts (since 1956) on diamond growth at low pressure. Deryagin's group performed theoretical investigations of the relative nucleation rates of diamond and graphite (Spitsyn and Deryagin, 1956; Deryagin and Fedoseeve, 1975; Deryagin et al., 1986). In the late 1960's, Angus and co-workers at Case Western Reserve University in the U.S.A. concentrated primarily on diamond deposition on diamond seed crystals from hydrocarbons and hydrocarbon-hydrogen mixture (Angus et al., 1968; Angus et al., 1971; Poferl et al., 1973; Chauhan et al., 1976). The growth rates were extremely low (0.001 μm/hr) until the mid-1970's. Diamond growth at low pressure had been achieved by many investigators (Aigenberg and Chabot, 1971; Spencer et al., 1976) since the mid-1970's. However, the growth rates were still low (less than 0.1 μm/hr).

The most significant initiative in recent years has been a large program in metastable diamond growth, started in 1974 at the National Institute for Research in Inorganic Materials (NIRIM) in Japan. In a series of remarkable papers starting in 1982, they described techniques for synthesizing diamond. But the growth rates were still low, only several micrometers per hour (microwave, DC charge, and hot filament methods).

At the 35th meeting of the Japanese Applied Physics conference in 1988, Hirose of Japan announced the synthesis of diamond using oxy-acetylene combustion flame in atmosphere . He reported remarkable growth rates as high as 100 μm/hr. This growth

rate was high enough to be practical and of commercial importance. This new method is very attractive, because it does not require a reaction chamber and a complicated experimental setup. In addition, it has the potential for a high deposition rate and a wide deposition area. Since 1988, several research teams in the U.S.A. have used and developed this method : Naval Research Lab., Materials Research Lab. at Pennsylvania St. University, Department of Electrical Engr. at Auburn University, School of Mechanical and Aerospace Engr. at Oklahoma St. University, Research Centers of General Electric and Lokheed Missiles and Space Company.

2.2 Introduction to CVD Diamond Synthesis

In the CVD diamond synthesis, atomic carbons from carbon-containing gas (carbon carrier) is deposited on a substrate surface via chemical reactions. Consequent diamond structures of these atomic carbons result in a diamond film. Most of the carbon carriers in CVD diamond synthesis are hydrocarbon compounds.

Atomic hydrogens are believed to have an important role in CVD diamond synthesis. Several Russian investigators (Spitsyn et al., 1981; Spitsyn and Bouilov, 1988) explained the role of hydrogen in CVD diamond synthesis. Atomic hydrogen, having a very high reactivity, etches away all solid carbon modifications except diamond. Furthermore, hydrogen in high concentration is supposed to chemically react with carbon's sp^3 bonds at the growing diamond interface, thus preventing a reaction with the linkage of sp^2 bonds which would lead to graphite. The carbon attachment during CVD growth takes place via carbon radicals (CH_3 is believed as a major radical in most CVD methods). The hydrogen bonded to the sp^3 carbon at the interface reacts with these carbon radicals arriving from the gas phase to form H_2 and simultaneously performs a chain linkage of the sp^3 bonds leading directly to the diamond lattice.

Thus, the general process of CVD diamond synthesis can be described by the following two chemical reactions proceeding simultaneously (see Figure 2.2):

1) thermal decomposition of the carbon carrier: it consists of a normal hydrocarbon chemical vapor deposition reaction.
2) etching reaction by the atomic hydrogen: it prevents the formation of all other solid carbon compounds except diamond.

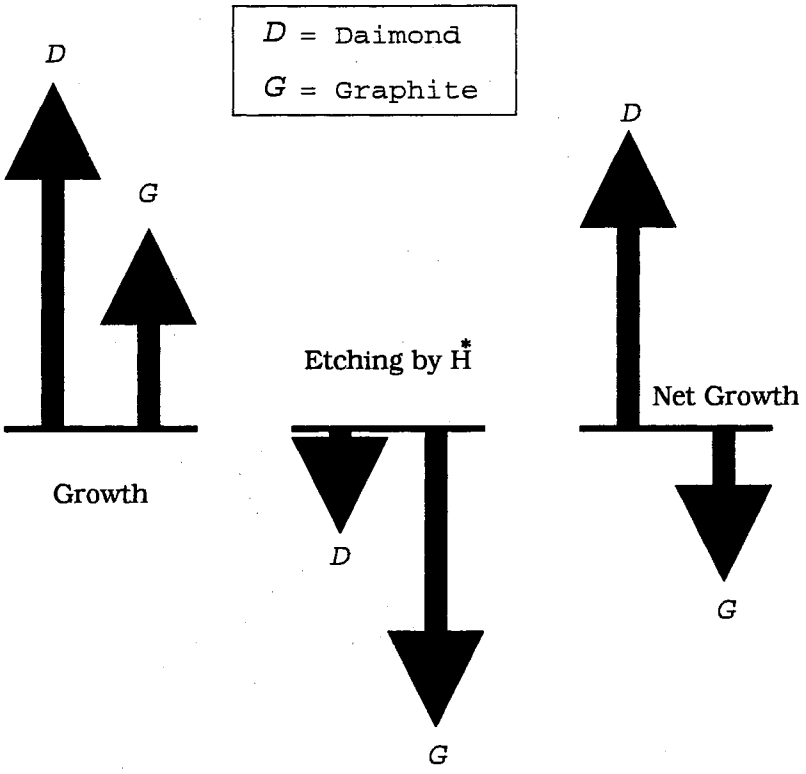

Figure 2.2 Relative Growth Rates, Etching Rates, and Their Differences of Daimond and Graphite During CVD Diamond Synthesis (Spitsyn and Bouilov, 1988; Lux and Haubner, 1989)

Atomic hydrogens are produced in the process of hydrocarbon decomposition or supplied directly into the reaction field. Rapid reaction of hydrocarbon is essential for a high growth of diamond film. This can be done by increasing the energy levels (or making the reactants very unstable) and concentrations of reactants (especially, the concentration of

atomic hydrogen).

Therefore, all CVD diamond synthesis methods at low pressure can be divided into three groups based on the activation principle for rapid reaction and supply of enough atomic hydrogen (Lux and Haubner, 1989):

1) Activation by high temperature:

Hot filament, Laser heating, Arc discharge, Arc plasma jet, and chemically induced hot gas flame (such as Oxy-acetylene combustion method)

2) Activation by electric or electromagnetic gas discharge:

Microwave and Radio frequency gas discharges, DC and AC glow discharges, and Plasma jets induced by RF, Microwave and DC

3) Combining the two principles:

Hot filament + Microwave, Hot filament + DC, and Electron assisted CVD

Also, these are categorized according to the specific technique for decomposing the carbon carrier gases and for producing atomic hydrogen simultaneously as shown in Table 2.1.

In the early days of CVD diamond synthesis, when diamond was grown on diamond seed (Eversol, 1962; Spitsyn and Deryagen 1956), carbon-monoxide-containing gas mixtures were common. Since Spitsyn reported the successful diamond growth on nondiamond substrate in 1981, mixtures of usually less than 5% methane in hydrogen have been used as reactants. Over the last five years, however, other carbon carrier gases, either undiluted or mixed with hydrogen, oxygen or noble gases, have been successfully applied to deposit diamond. Table 2.2 shows carbon carrier gases and their mixtures used successfully in CVD techniques. As shown in this table, most reactants are at least composed of carbon and hydrogen. Oxygen is frequently added, either directly or as an integral part of the carbon carrier.

Table 2.1 CVD Methods Categorized by Plasma Techniques
(Bachmann and Enckevort, 1992)

Thermal CVD	Thermal decomposition Chemical transport reaction Hot filament technique Oxy-acetylene torch Halogen-assisted CVD
DC plasma CVD	Low pressure DC plasma Medium pressure DC plasma Hollow cathode discharge DC arc plasma jets
RF plasma CVD	Low pressure RF grow discharge Thermal RF plasma CVD
Microwave plasma CVD	915 MHz plasma Low pressure 2.45 GHz plasma Atmospheric pressure 2.45 GHz plasma torch 2.45 GHz magnetized plasma 8.2 GHz plasma

Table 2.2 Reactants Used in CVD Methods (Bachmann et al., 1991)

Method	**Reactants**
Thermal Decomposition CVD	CO-H_2, CO-CO_2, CBr_4, CH_4
Hot Filament CVD	CH_3COCH_3-H_2
Combustion CVD	C_2H_2-O_2, C_2H_2-O_2-H_2
DC Plasma Jet CVD RF Plasma CVD	CH_4-H_2
Microwave CVD	CO-H_2, CH_4-CH_3COCH_3-O_2, C_2H_4, CH_4-H_2, CH_4-H_2-O_2, CH_4-CO_2-H_2, CH_4-CO-H_2, CH_4-H_2-H_2O, CO-CO_2-H_2, CO-H_2-O_2

The major CVD methods for diamond synthesis at low pressure will be presented and discussed next. Included in the discussion are reaction conditions, linear growth rates, size of coating area, quality of diamond films, advantages, and drawbacks of each method.

Analyses of film qualities are based on resulting Raman spectrums.

Thermal CVD Methods

The thermal decomposition method was the first developed CVD technique. In this method, carbon containing gases such as CBr_4, CI_4, CH_4, or CO were carried out at gas temperatures between 600 and 1200 °C. The substrate was a diamond seed in the early stage. The gas temperature was close to that of the substrate. The resulting linear growth rates were approximately 0.01 μm/h, which was too low for industrialization. Moreover, the products were contaminated by nondiamond carbons. The halogen-assisted CVD method was developed in 1991 by Hauge and his colleagues at Rice University (Patterson et al., 1991). Halogen gas is added in a gas mixture to support diamond formation. The linear growth rate was still low, but the gas mixture temperature was significantly reduced to as low as 200 °C. Thus, the halogen-assisted CVD method made it possible to use various substrate materials, mainly those with low melting points. However, the halogen-assisted CVD method is limited due to several problems associated with low growth rate and corrosion in the reactor.

The first breakthroughs towards industrially applicable processes in CVD diamond occurred when the substrate temperature and gas phase temperature were decoupled. In these cases (chemical transport reaction method, hot filament method, oxy-acetylene combustion method), the composition of the carbon carrier together with the formation of the atomic hydrogen used as an etching component, took place at a much higher temperature than the substrate temperature. Both the chemical transport reaction (CTR) and hot filament methods create a hot zone in the gas phase either by a hot graphite disk or by means of hot tungsten, molybdenum or tantalum wire. The temperarures of the hot disk and the hot filament are approximately 2000 °C and 2000-2400 °C, respectively. For both methods, the growth rates are in the order of 1 μm/h, which is 1-2 orders of magnitude higher than earlier thermal decomposition methods. Table 2.3 summarizes the

reaction conditions and results for typical hot filament CVD method, and process and setup are described in Figure 2.3.

Table 2.3 Summary of Hot Filament Method (Bachmann and Enckevort, 1992)

Substrate temperature (°C)	600 - 1050
Reactor pressure (mbar)	20 - 80
Total gas flow (sccm)	100 - 500
Filament temperature (°C)	2000 - 2400
Linear deposition rate (μm/hr)	0.3 - 8
Deposition area (cm^2)	2 - 100 (depending on filament structure)
Types of substrates	Si, Mo, silica, alumina, diamond, WC, SiAlON, other
Quality/crystallinity (Raman data)	+++ (filament metal co-deposited)
Uniformity/homogeneity	-/+ (mirrors filament shape)
Special remarks	Additional bias voltage affects quality and rate
Advantages of the method	Simple setup, large area possible
Drawbacks of the method	Filament stability can be a problem, metal contamination, higher oxygen concentrations difficult

- = bad quality; +++ = excellent quality.

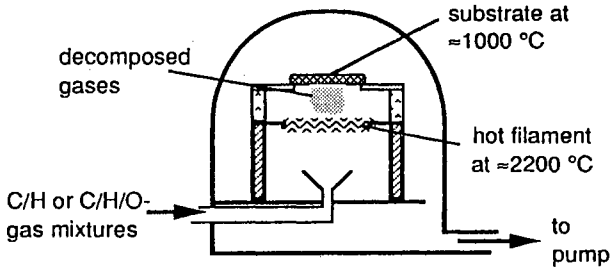

Figure 2.3 Schematic of Hot Filament Method (Bachmann and Enckevort, 1992)

Another big step in terms of increasing the linear growth rates of diamond was the introduction of the oxy-acetylene combustion method by Hirose of Japan in 1988. He used a mixture of roughly 50% acetylene and 50% oxygen to grow diamond film from an ordinary welding torch. High growth rates, up to 200 μm/h, have been reported (Snail and Hanssen, 1991). In this method, the hot gas mixture within the flame has a temperature range of 3000-3300 °C (Matsui et al., 1990). Table 2.4 includes the summary of reaction conditions and results, and Figure 2.4 shows the sketch of setup.

Table 2.4 Summary of Oxy-Acetylene Combustion Method. (Bachmann and Enckevort, 1992; Snail and Hanssen, 1991; Tzeng et al, 1991; Matsui et al, 1990)

Substrate temperature (°C)	400 - 1300 (cooling required!)
Reactor pressure (bar)	1
Total gas flow (sccm)	1000 - 2000
Flame temperature (°C)	3000 - 3300
Linear deposition rate (μm/hr)	10 - 200
Deposition area (cm^2)	≈ 0.5 (fixed torch, lager for moving torch)
Types of substrates	Si, Mo, silica, alumina, TiN, diamond, Al_2O_3, BN, WC, other
Quality/crystallinity (Raman data)	+ to +++ (high rate homoepitaxy!)
Uniformity/homogeneity	-
Special remarks	Rates and quality depend on nozzle used, distance from nozzle to substrate, turbulent flames differ from laminar
Advantages of the method	Simple setup, high rates
Drawbacks of the method	Control of substrate temperature difficult, inhomogeneous, contaminations, no gas recycling, small area

- = bad quality; +++ = excellent quality.

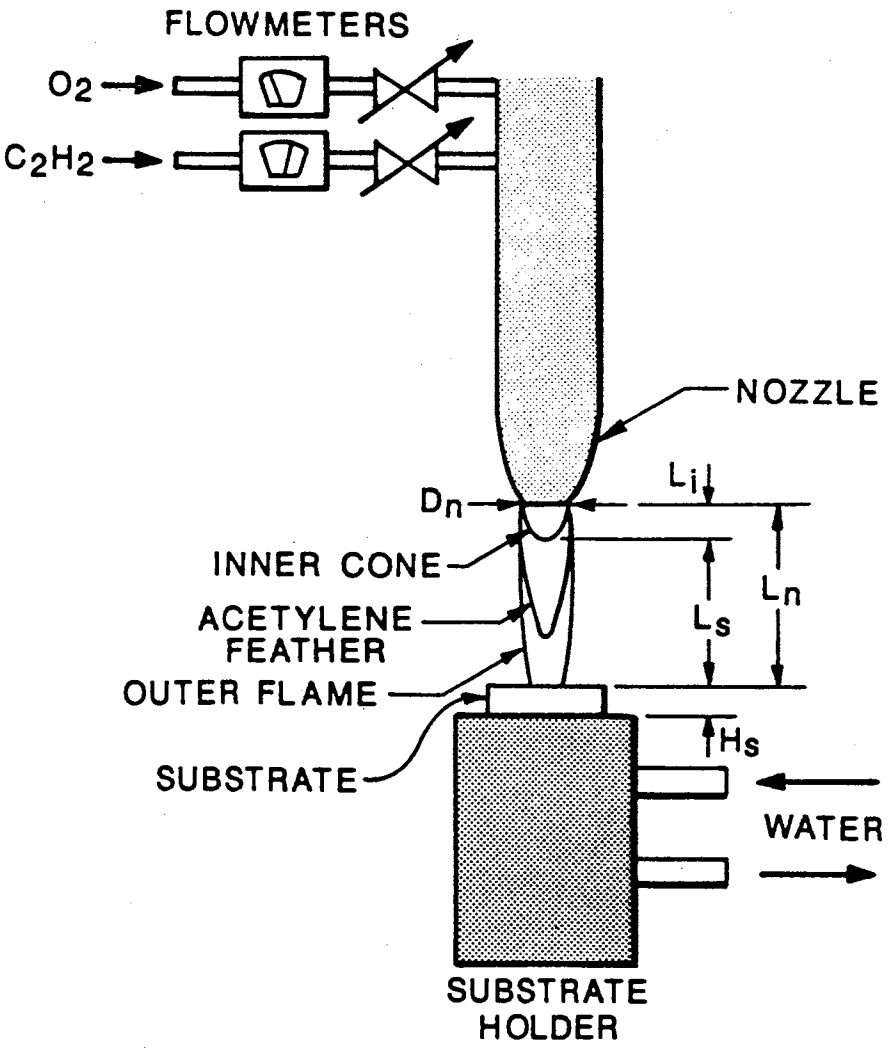

Figure 2.4 Schematic of Oxy-Acetylene Combustion Method

Direct Current (DC) Plasma CVD Methods

A DC plasma discharge is probably the simplest way to form an electrical discharge at low pressure in order to decompose hydrogen and the carbon carrier. The basic setup of low pressure DC plasma CVD method consists of an anode, cathode and substrate, where substrate is mounted onto the anode as shown in Figure 2.5. Due to the low temperature of gases in the plasma, the whole setup is usually mounted inside a furnace to reach the desired gas temperature (600-1000 °C). The discharge is formed between the cathode and anode. The low pressure DC plasma method can make a large area of diamond deposition (10 cm in diameter). However, the linear growth rates are lower than 0.1 μm/h, and the quality of the diamond film produced is not good (see Table 2.5).

Table 2.5 Summary of Low Pressure Direct Current (DC) Plasma Method (Bachmann and Enckevort, 1992)

Substrate temperature (°C)	600 - 1000
Reactor pressure (mbar)	20 - 40
Total gas flow (sccm)	100 - 200
Input power data (mA/cm^2; V)	40; 250 - 500
Linear deposition rate (μm/hr)	0.01 - 0.1
Deposition area (cm^2)	≈ 70
Types of substrates	Si, Mo, silica, alumina, diamond, other
Quality/crystallinity (Raman data)	0/+
Uniformity/homogeneity	++
Special remarks	Substrate needs to be mounted on anode to avoid amorphous carbon material
Advantages of the method	Simple setup, fairly large area
Drawbacks of the method	Low linear rates, poor quality (H-content; annealing necessary)

- = bad quality; +++ = excellent quality.

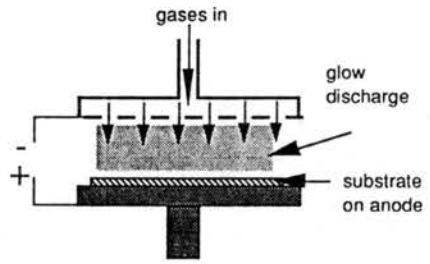

Figure 2.5 Schematic of Low Pressure DC Plasma Method
(Bachmann and Enckevort, 1992)

Medium pressure and low pressure DC plasma methods differ mainly in the reactor pressures: 200 mbar for the medium pressure method, and 20-40 mbar for the low pressure method. The medium pressure DC plasma CVD method was developed basically from the low pressure method, by increasing pressure to improve quality of the products and linear growth rate. To maintain a plasma under such conditions, it is necessary to increase the power fed into the system by increasing both the current density and the discharge voltage. This also results in a much higher gas temperature than that in the case of the low pressure method. Thus, the substrate has to be cooled rather than heated. Table 2.6 summarizes the reaction conditions and results of the medium pressure DC plasma CVD method. The gas temperature and linear growth rate depend on the DC charge current density (Suzuki et al. 1987): approximately 4000 °C and 20-130 μm/h for 4 A/cm^2 ,and 5300 °C and > 250 μm/h for 10 A/cm^2 as shown in Table 2.6. The main disadvantage of this method is the small area of diamond deposition (less than 1 cm^2).

Further increase of pressure in a DC plasma system lead to DC arc plasma and plasma jet CVD methods. The basic principles of this approach are illustrated in Figure 2.6. In these methods, gas temperatures higher than 5000 °C can be easily obtained. With DC arc plasma discharge CVD method, the highest linear growth rate (930 μm/h) was

achieved by Ohtake and Yoshikawa in 1990. In this approach, lower pressure in the reactor results in lower linear growth rate. Typical reaction conditions and results of DC arc discharge and plasma jet CVD methods are listed in Table 2.7. The main disadvantages in using these methods are: small area of diamond deposition, non-uniform thickness of produced film, contamination with amorphous carbons, and high cost due to construction of setup.

Table 2.6 Summary of Medium Pressure DC Plasma Method
(Bachmann and Enckevort, 1992)

Substrate temperature (°C)	600 - 900 (cooling required for P > 100 mbar)
Reactor pressure (mbar)	200
Total gas flow (sccm)	20 - 100
Input power data (A/cm^2 at 1 kV)	4 to > 10
Linear deposition rate (μm/hr)	20 - 130 at 4 A/cm^2; > 250 at 10 A/cm^2
Deposition area (cm^2)	< 1
Types of substrates	Si, Mo, alumina
Quality/crystallinity (Raman data)	+++
Uniformity/homogeneity	? (small area)
Special remarks	Substrate anode to avoid amorphous carbon; substrate cooling mandatory!
Advantages of the method	High rates
Drawbacks of the method	Small area

- = bad quality; +++ = excellent quality.

Radio Frequency (RF) Plasma CVD Methods

RF plasma methods use similar gas mixtures as the other methods, like DC plasma and microwave plasma methods. In low pressure RF glow discharge CVD method, the substrate has to be additionally heated in order to be at the desired temperature, about 900

°C. The linear growth rates are usually lower than 0.1 μm/h. Due to the severe contamination with non-diamond carbons, only diamond particles were produced rather than a complete diamond film. However, low pressure plasma systems lend themselves to a large setup (easy scale-up) and acceptance of three-dimensional substrate options. The reaction conditions, results, advantage, and drawbacks of this method are summarized in Table 2.8.

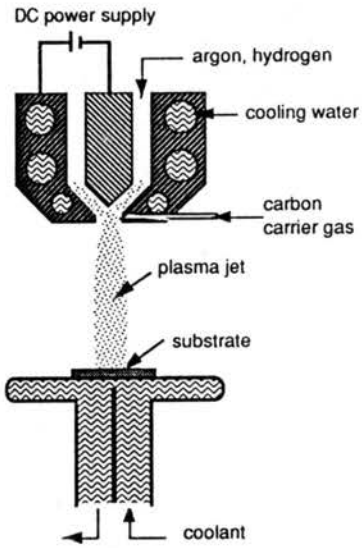

Figure 2.6 Schematic of Thermal DC Plasma Jet Method
(Bachmann and Enckevort, 1992)

Atmospheric pressure RF plasma system is shown in Figure 2.7. This method employs inductively coupled RF plasma operation. Such plasmas are typically created by inductively coupling 4 MHz RF power of 40-80 kW into a tubular silica reactor. The linear growth rates range form 120 to 180 μm/h and high quality diamond films can be achieved by atmospheric pressure RF plasma CVD method. The main problems of this method are to avoid contact with the plasma fireball whose temperature is up to 10000°C, and to stabilize the substrate temperature below 1100 °C, which prevents the growing

diamond film from being burnt away. These problems make this method uncommon. Table 2.9 summarizes the atmospheric pressure RF plasma CVD method.

Table 2.7 Summary of DC Arc Discharge and Plasma Jet Methods (Bachmann and Enckevort, 1992)

Substrate temperature (°C)	800 - 1100 (cooling required!)
Reactor pressure (mbar)	0.1 - 1000 (good quality only at P > 30 mbar)
Total gas flow (sccm)	3000 - 70000
Input power data (kW)	3 - 18 (Norton: megawatt)
Linear deposition rate (μm/hr)	25 at P < 100 mbar; 500 - 930 at high P)
Deposition area (cm^2)	< 2 (Norton; ≈ 90)
Types of substrates	Mostly Mo, Si, other
Quality/crystallinity (Raman data)	+++ (central part); - (periphery)
Uniformity/homogeneity	+++ to - depending on setup
Special remarks	Severe deformation observed for Si-substrates larger than the plasma beam; high power consumption, high flows
Advantages of the method	Extremely high deposition rates of up to 930 μm/hr
Drawbacks of the method	Small deposition area (except for stirred arc): contaminations (graphite and plasma gen. material); stability and temperature control; thickness and quality variations

- = bad quality; +++ = excellent quality.

Microwave Plasma CVD Methods

The diamond research group at NIRIM were the first to report the application of 2.45 GHz microwave plasma for diamond synthesis in 1983 (Kamo et al., 1983). Many of the experimental setups in use are similar to the apparatus originally described by Kamo et al. from NIRIM. Figure 2.8 shows three different setups of microwave plasma CVD methods. These systems employ reactor pressures of 20-150 mbar except that developed by Mitsuda et al. in 1989, which uses atmospheric pressure.

Table 2.8 Summary of Low Pressure RF Plasma Method
(Bachmann and Enckevort, 1992)

Substrate temperature (°C)	700 - 1000 (heating required)
Reactor pressure (mbar)	0.1 - 40
Total gas flow (sccm)	100 - 200
Input power data (W)	300 - 3000
Linear deposition rate (μm/hr)	< 0.1
Deposition area (cm^2)	-
Types of substrates	Si, silica, BN, alumina, Ni, diamond, other
Quality/crystallinity (Raman data)	- / +
Uniformity/homogeneity	-
Special remarks	Inductively and capacitively coupled plasmas used at frequencies between 0.4 and 13.56 MHz; higher pressures, higher power, high frequencies work better
Advantages of the method	Easy scale-up option, complex substrate shape option
Drawbacks of the method	Low rates, poor crystalline quality, contamination

- = bad quality; +++ = excellent quality.

The substrate size depends on the tube or reactor size. The system by Kamo et al. has a problem of severe contamination due to the plasma etching of the reactor wall. In the atmospheric pressure plasma system, the gas temperature and linear growth rate (~ 30 μm/h) are higher than in other systems (low pressure plasma) where the linear growth rates are 0.5-3.0 μm/h. However, the area of diamond deposition in atmospheric pressure microwave plasma torch method is smaller than that in other methods using low pressure.

The qualities of diamond produced by microwave plasma methods are fairly good. However, these methods need to increase the linear growth rate. The summary of these methods are shown in Table 2.10. In microwave plasma CVD methods, reactor pressure increase accompanied by higher power input (which causes higher gas temperatures), results in higher growth rate, similar to DC plasma CVD methods.

Table 2.9 Summary of Atmospheric Pressure RF Plasma Method (Bachmann and Enckevort, 1992)

Substrate temperature (°C)	≈ 700 - 1200 (cooling!)
Reactor pressure (mbar)	1
Total gas flow (sccm)	80000 - 100000
Input power data (kW)	6 - 60 at 4 MHz
Linear deposition rate (μm/hr)	120 - 180
Deposition area (cm^2)	< 3
Types of substrates	Mo
Quality/crystallinity (Raman data)	+++
Uniformity/homogeneity	-
Special remarks	Very hot plasma fireball, large amounts of diluting gas required (gas recycling!)
Advantages of the method	High deposition rates
Drawbacks of the method	Small deposition area; plasma stability and temperature control difficult; thickness and quality variations; poor adhesion

- = bad quality; +++ = excellent quality.

The major CVD methods of diamond synthesis at low pressure have been reviewed. All methods reviewed are compared in Table 2.11 with respect to linear growth rate, area of diamond coating, quality, substrates used, advantages, and drawbacks. The purpose of developing CVD methods for diamond synthesis is, without a doubt, to industrialize them. The required conditions for industrialization of CVD methods are (Bachmann and Enckevort, 1992; Buckley and Collins, 1992; Lux and Haubner, 1992):

1) low cost

2) good quality

3) production of large size of diamond films

4) production of diamond film at low temperature

5) reproducibility

6) film adhesion on a broad range of substrates

7) development of mass production-type setups

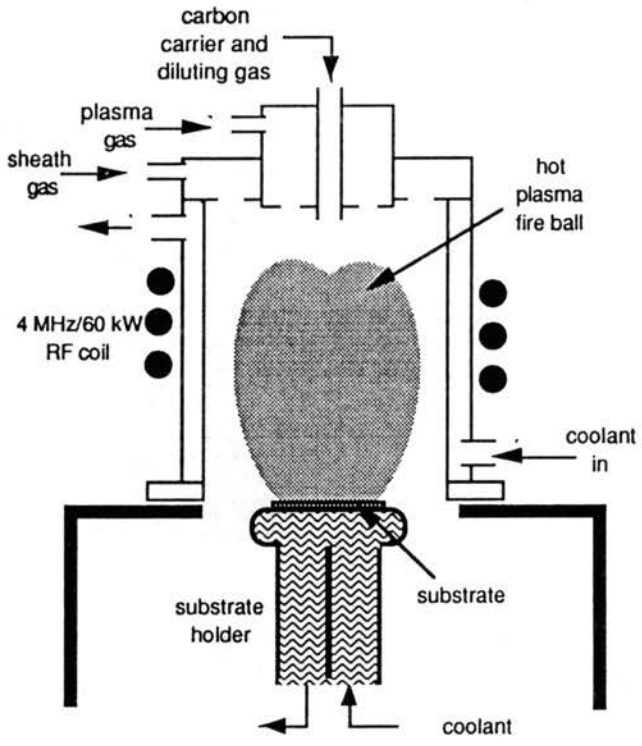

Figure 2.7 Schematic of RF Plasma Method (Matsumoto et al., 1987)

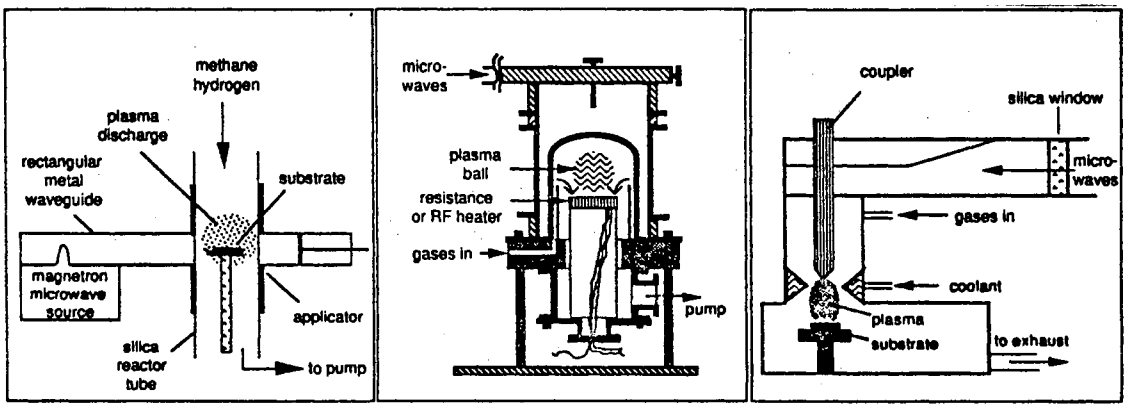

Figure 2.8 Schematic of Microwave Plasma Method. Left: original tubular reactor by Kamo et al. (1983). Middle: bell jar reactor by Bachmann et al. (1988). Right: microwave torch approach by Mitsuda et al. (1989)

Table 2.10 Summary of Low and Atmospheric Pressure Microwave Plasma Method (Bachmann and Enckevort, 1992)

Substrate temperature (°C)	350 - 1100 (optimum ≈ 1000 for C/H mixtures, ≈ 800 for C/H/O mixtures; low rates at low T)
Reactor pressure (mbar)	20 - 100
Total gas flow (sccm)	100 - 1000; 50000 for torch
Input power data (kW)	300 - 1500 at 2.45 GHz (5 kW for torch)
Linear deposition rate (μm/hr)	1 - 5; 10 - 30 for MW torch at 1 bar
Deposition area (cm^2)	≈ 30; 5 for MW torch at 1 bar
Types of substrates	Si, silica, alumina, graphite, Ni, soft glass, Ti, Ta, Si-nitride, SiC, SiAlON, WC, Pt, Cu, other
Quality/crystallinity (Raman data)	+++
Uniformity/homogeneity	+++ (low P)
Special remarks	Magnetized plasmas (ECR) at pressures of < 0.1 mbar result in lower rates and reduced quality
Advantages of the method	Very stable (operation over days); high quality material; uniform rates area not too small
Drawbacks of the method	Rates and area need to be improved

- = bad quality; +++ = excellent quality.

Table 2.11 Summary of Present Status of CVD Methods for Diamond Synthesis

Method	Results					
	Rate (μm/hr)	Area (cm^2)	Quality (Raman)	Substrate	Advantages	Drawbacks
Combustion method	30 - 100	< 2	++	Si, Mo, Tin	Simple	Area, Stability
Hot filament	0.5 - 8	> 250	+++	Si, Mo, silica, etc.	Simple, large area	Contaminations, stability
DC discharge (low pressure)	< 0.1	70	+	Si, Mo, silica, etc.	Simple, large area	Quality, rate
DC discharge (medium pressure)	20 - 250	< 2	+++	Si, Mo, alumina	Rate, quality	Area
DC plasma jet	930 (25)	< 2 Norton: 100	+++	Mo, Si	Rate, quality	Contaminations, homogeneity, stability
RF (low pressure)	< 0.1	Particles	- / +	Si, Mo, silica, BN, Ni	Scale-up	Quality, rate (contaminations)
RF (thermal, 1 atm)	180	3	+++	Mo	Rate	Area, stability, homogeneity
Microwave (0.9 - 2.45 GHz)	3 (at low P) 30 (high P)	100	+++	Si, Mo, silica, WC, etc.	Quality, stability	Rate, area
Microwave (ECR 2.45 GHz)	0.1	100	- / +	Si	Area, low P, low T	Quality, rate, (contaminations)

The linear growth rate is one of the most important factors related to the cost of CVD diamond production. It varies from method to method as seen in Table 2.11. The lowest growth rate is found in the thermal decomposition method which is not listed in this table (approximately 0.01 μm/h), and the highest is in the DC plasma arc discharge method (930 μm/h). In several cases, high growth rates seem to correlate with high total gas flow rate. However, reacting gas temperature is the most important factor influencing the linear growth rate, since chemical reactions rates are a function of temperature. A high energy level of reactants (unstable) is suitable for rapid chemical reactions. The energy level of chemical reactants is thermodynamically related to temperature if pressure is constant: higher temperature results in a higher energy level. Thus, we may expect theoretically high growth rate from high gas temperature. This expectation is proved by experimentation. For example, the gas temperature (higher than 5000 °C) of experiments by Suzuki et al. in 1987 and 1990 using DC plasma method, is higher than those in low pressure RF plasma and hot filament methods (lower than 3000 °C). The experiments by Suzuki et al. showed 20-250 μm/h of linear growth rate from only 20-100 sccm of total gas flow rate. This amount of total gas flow rate is small compared to reaction conditions

in the other methods (see Tables 11 and 6), but the linear growth rate is still higher. Figure 2.9 presents the relation between linear growth rate and gas temperature in CVD methods. Generally, higher gas temperature results in higher growth rate as shown in this figure. The effects of pressure, area of diamond deposition, and total gas flow rate are not considered. However, these parameters may also play roles in explaining some of the growth rate differences.

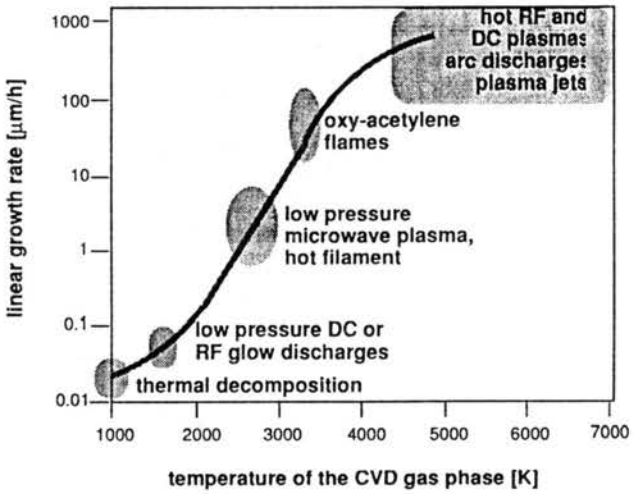

Figure 2.9 Relation of Linear Growth Rate to Gas Temperature (Bachmann et al., 1991)

It is almost impossible to produce perfect diamond as natural diamond of type II (the best diamond). The synthesized polycrystalline diamond film is considered the best quality if it is well facetted, pure, and binderless. However, diamond films produced by CVD methods contain different surface crystal facets, different crystal orientations, different grain sizes, internal defect structures, sp^2 bond (graphite) or amorphous carbons, and other imperfections and defects. They may have too rough a surface to be applied for certain areas. However, some techniques of smoothing film surface after deposition were developed (Jin, et al., 1992; Bogli et al., 1992). Degradation level or quality of produced

diamond depends on the CVD method (see Table 2.11) and the reaction conditions if the method is same. Properties of synthesized diamond strongly depend on its quality. Figure 2.10 shows dependency of thermal conductivity of diamond film produced by hot filament method (Baba et al., 1991) on reaction condition. Several diamond films produced under different CH_4 concentrations in H_2/CH_4 mixture, have different thermal conductivities: thermal conductivity decreasing with increasing CH_4 concentration as seen in Figure 2.10. This figure indicates that low concentration of CH_4 is necessary to produce a diamond film of high quality in hot filament CVD method. However, low concentration of CH_4 results in low linear growth rate.

Among the developed CVD methods, microwave plasma, hot filament, and DC plasma jet CVD methods are already industrialized (Diamonex Inc., Norton Company, Asahi Diamond Industrial Co., Sumimoto Electric Industries Ltd, etc.). However, these methods need to improve either growth rate or area of diamond coating for better industrialization. A lot of time and effort has been spent in developing these methods. That is the reason why these methods are more advanced than others.

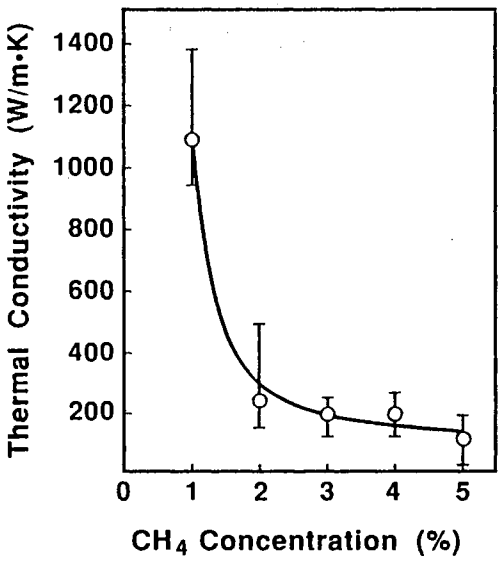

Figure 2.10 Thermal Conductivities for Diamond Films as a function of CH_4 Concentration (Baba et al., 1991)

There is an interesting formula to compare CVD methods based on the cost of diamond production, namely production efficiency (Bachmann and Enckevort, 1992). The production efficiency,η, is described as

$$\eta = (\text{growth rate} \times \text{deposition area})/\text{energy consumption}$$

According to this estimate, oxy-acetylene combustion CVD method is considered as an excellent method. This method has relatively high growth rate of up to 200 μm/h and surprisingly simple setup. A reaction chamber and complicated electronic equipment (such as power supplies) are not needed. If the cost for building the setup is accounted in calculating final production cost, oxy-acetylene combustion method is greatly favored for industrialization, compared to other methods.

As shown in Table 2.11, to remedy the shortcomings of the oxy-acetylene combustion CVD method, the area of diamond coating should be enlarged and the stability should be improved. The possibility of large area coating has already been demonstrated by Murakawa et al., 1989; Tzeng et al., 1991. Linear movement of combustion flame field and enlarging the combustion flame field by multiple nozzles were ideas for large area diamond deposition. Thus, additional setup for increasing the size of diamond film is simple and easily built with low cost. As to the stability of the oxy-acetylene method, it is caused when the levels of the reactant gases (oxygen and acetylene) in the tanks are low (Bang et al., 1994). Hence, the stability problem can be easily solved by avoiding the tanks with low amount of reactants. However, this exciting method has not yet been fully exploited; due to its short history (developed first in 1988). The present work was undertaken to make contributions to development of this method. A review of the literature on this method is presented in the next section. Then, some of the problems associated with oxy-acetylene combustion CVD method are addressed.

2.3 Current State of the Art

This section describes the results of literature survey on the mechanism of diamond

growth and roles of key parameters which influence the deposition, quality, and morphology of diamond film using oxy-acetylene combustion method.

Knowledge of experimental setup of oxy-acetylene combustion method helps to understand this method and the materials presented in this section. The experimental apparatus of oxy-acetylene method consists of a substrate (molybdenum, tungsten, silicon wafer ... etc.), a water cooled substrate holder or heat sink (usually copper block), a torch fitted with a brazing nozzle, and mass flow controllers for regulation of oxygen and acetylene flows as shown in Figure 2.4.

Temperature of flame close to the substrate is very high, about 3000-3200 °C at which diamond cannot be synthesized. Thus, cooling is required for the substrate. The substrate is mounted on the heat sink to be cooled via conduction and convection heat transfers by continuous coolant (water) flow. As mentioned in the last section, the substrate should be at a temperature less than 1300 °C for diamond growth. Therefore, control of substrate temperature is essential in this method, which requires reliable temperature measurements. In most experimental setups of this method, non-intrusive temperature measurements have been made, for example with a pyrometer.

The oxy-acetylene flame is sketched in Figure 2.4. Three regions are shown : the inner cone bounds O_2-C_2H_2 flame front, the C_2H_2 feather zone, where excess C_2H_2 burns with O_2 which diffuses into the flame from the surrounding air (only appears when mole ratio of C_2H_2 to O_2 which is supplied from a tank, is greater than one), and the outer flame, where CO and HO produced in the inner cone burns to produce CO_2 and H_2O. The substrate surface is exposed to the flame, and a diamond film is deposited on the substrate surface (only the area which meets the feather zone of flame). Several symbols are shown in Figure 2.4, such as D_n, L_i, L_n, L_s, and H_s. Their meanings are explained in the nomenclature section.

As mentioned in the previous section, atomic carbons and hydrogens are important to deposit diamond crystals in all CVD methods. Acetylene molecule consists of carbons

and hydrogens (C_2H_2). Thus, acetylene gas in the oxy-acetylene combustion method supplies atomic carbons and hydrogens simultaneously during combustion, and the free energies of these atoms are high enough because of high temperature as a result of combustion. Thus, rapid chemical reactions for diamond deposition is expected. The gaseous carbons are cooled on the substrate to a solid phase: deposition. Different types of solid carbons deposited, such as diamond, graphite, or amorphous carbons. Removal of nondiamond carbons is accompanied by atomic hydrogens as a result of etching as discussed in the section on introduction to CVD methods. In all the CVD methods, the produced sp^3-bonded carbons (diamond) tend to be partially transited to sp^2-bonded carbons(graphite) during the synthetic process (Spitsyn and Bouilov, 1988). However, atomic hydrogens are believed to inhibit the transition by forming a hydrogen layer on the surface of diamond crystal (Pate, 1985).

Oxygen is believed to play an important role in CVD diamond synthesis. The effect of O_2 on diamond synthesis was studied by Bachmann et al. in 1991, using other methods. They used CH_4-H_2-O_2 mixture to synthesize a diamond film by microwave plasma method. Sequent experiments with different fractions of O_2 in the mixture were conducted. They used the ratio of O_2 to CH_4-H_2-O_2 mixture to remark the existing degree of oxygen in the mixture. The ratio increased from zero, where the growth rate was about 0.5 μm/hr. The growth rate decreased with increasing oxygen flow rate, while the quality (purity) of resulting diamond film was improved. Finally, no diamond was synthesized beyond the 0.007 of O_2 to CH_4-H_2-O_2 mixture. Bachmann et al. concluded that oxygen removes (etches away) nondiamond carbons as well as diamond carbons at the surface of the diamond growing during the synthetic process. As shown by their experiments, excessive oxygen prevents net growth of diamond: no growth. Therefore, oxygen is another etching component like hydrogen in CVD diamond deposition.

The etching role of oxygen was also identified in the experiments by Sato and Kamo in 1989. They applied oxygen plasma onto a synthesized diamond. As a result,

existing nondiamond carbons were removed. In oxy-acetylene combustion method, diamond cannot be synthesized when the flow ratio of oxygen to acetylene , R, is greater than 1.0. However, the quality of produced diamond film at R close to 1.0 (still less than 1.0) is good. These tendencies can be explained by the etching role of oxygen in CVD diamond method.

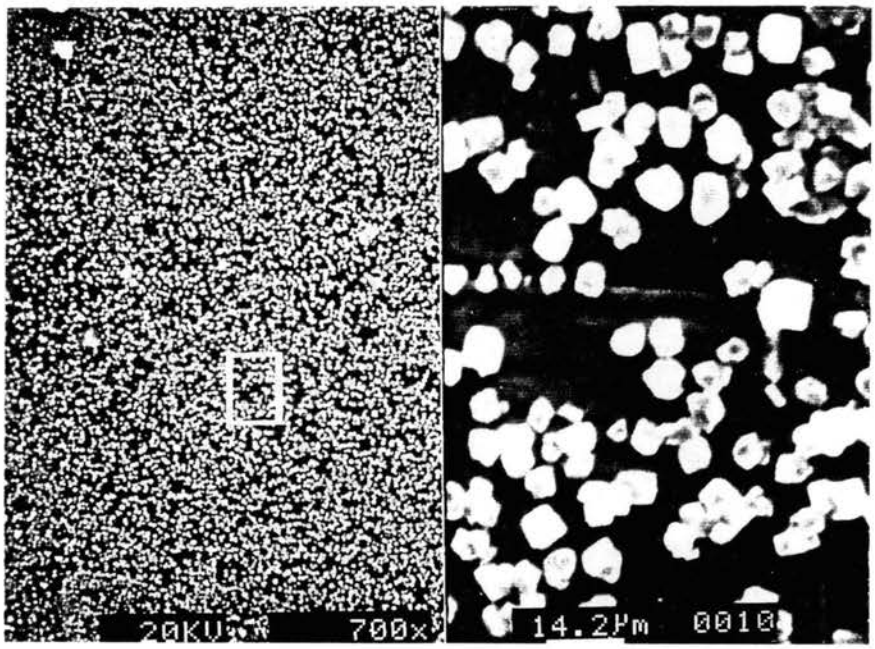

Figure 2.11 Random Distribution of Diamond Nuclei (from This Study)

There is no theory yet to explain nucleation of diamond because it includes complicated chemical reactions. Nuclei, however, seems to be prevented only if the carbon is too rapidly removed by diffusion resulting from etching or chemical reaction with substrate (carbide forming). The carbon atoms arriving from the gas phase at the substrate surface must exceed a certain minimum concentration at the solid/gas interface in order to reach and exceed the critical nucleus size (Joffreau et al., 1988a and b). Nuclei are randomly distributed as shown in Figure 2.11. Their number/surface (nucleation

density) strongly depends on the balance between the flux of incoming carbon atoms arriving at the substrate surface and the carbon diffusion rate. Furthermore, the carbon diffusion determines the distance between a nuclei and its immediate neighbors (Lux and Haubner, 1989).

Unfortunately, the mechanism of diamond growth in CVD method is not clear. However, the following stages of growth mechanism of polycrystalline diamond film on a nondiamond substrate can be distinguished (Joffreau et al., 1988c):

1) carbide and/or subcarbide layer formation

2) diamond nucleation on the carbide layer, and finally

3) growth of diamond crystals.

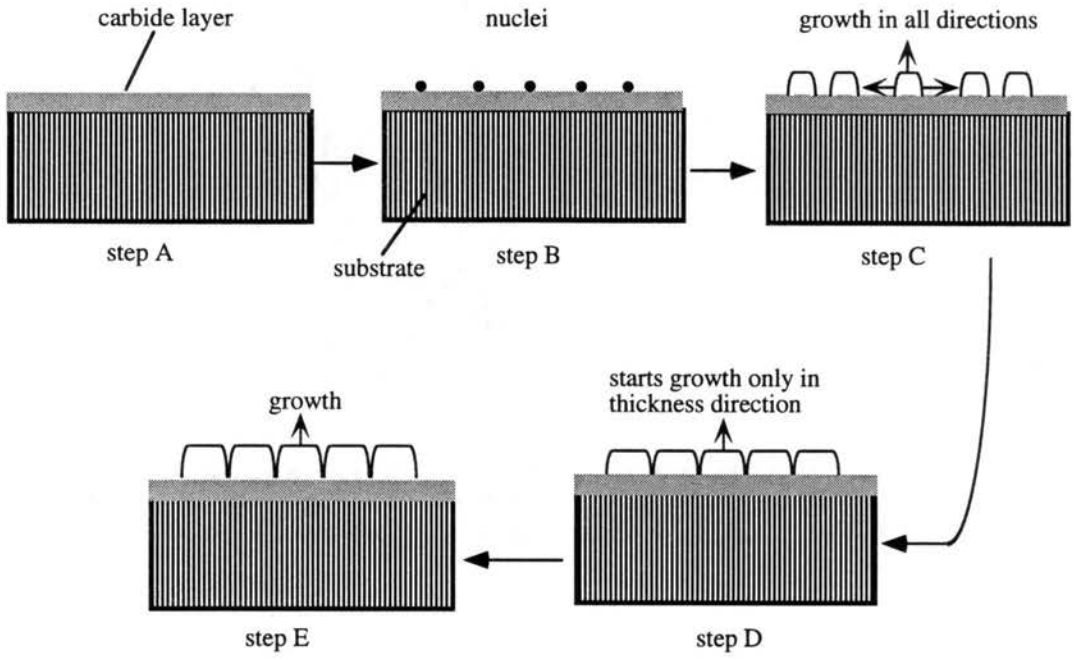

Figure 2.12 Growth Steps of Polycrystalline Diamond Film on Nondiamond Substrate

These stages are shown in Figure 2.12, where the growth of diamond crystals are described in three subdiagrams (C, D, and, E). Nuclei form either single or bicrystals

exhibiting re-entry corners, growth spirals and growth steps for easy atomic attachment in order to avoid secondary nucleation at the surface. Once a population of such individual crystals start to grow and the optimal nucleation density in accordance with the carbon diffusion rate at surface has established the minimum distance between the next neighbor, no further individual nuclei are formed. However, it has been shown that small crystal can be dissolved again during the early growth stages if the bulk diffusion rate of carbon into the substrate is high enough (Jeffreau et al., 1988a). The density of the nuclei is not so high that a layer can be formed directly. Thus, the individual crystals grow in all directions (see subdiagram C in Figure 2.12) until they touch and form the layer growth: two step growth. During this step of growth, the growth rate of the individual crystals in radial direction are much higher than that in layer-thickness direction. The linear growth rate in the layer-thickness direction is enhanced after formation of layer.

It is difficult to obtain an extremely thin diamond film (layer) because of the two step growth discussed above. This is the reason why the CVD method cannot produce a diamond film whose thickness is less than 1.0 μm. In order to produce very thin diamond films, the nucleation density should be significantly increased before the two step growth.

In the stage of carbide formation, its thickness is very small, believed to be in the order of 1 Angstrom. Thus, it is hard to detect the carbide layer by SEM (scanning electron microscope). However, XRD (X-Ray Diffraction) analysis can detect the existence of carbon layer over substrate surface rather than the thickness. In 1992, Polini et al. analyzed diamond crystals over a tungsten substrate prepared by microwave plasma method. CH_4 diluted in H_2 was used as a carbon carrier. They didn't make a complete diamond film. The produced diamond crystals were believed to be at the stage of carbide formation or nucleation of diamond. Figure 2.13 shows the results of XRD analysis by Polini et al. As shown in this figure, two different carbide phases (WC and W_2C) existed as well as diamond over the tungsten substrate. The portion of these carbide phases to the area of substrate surface have an increasing tendency with increasing substrate

temperature. However, carbide phases in the synthetic process using oxy-acetylene combustion method have not yet been discussed in the literature.

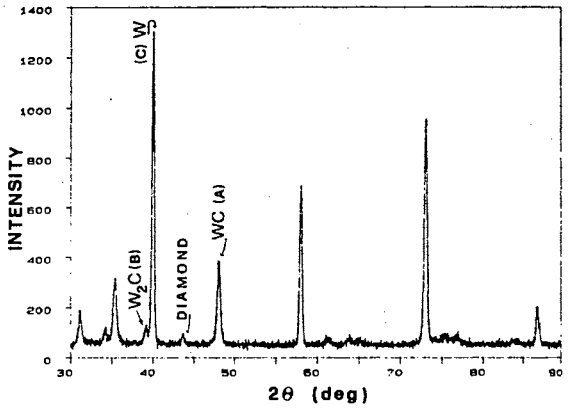

Figure 2.13 X-Ray Diffraction Spectrum over Substrate Surface at the Stage Before Diamond Growth Using Hot Filament Method (Polini et al., 1992)

Initial gas phase in the acetylene feather zone of flame contains simultaneously : 1) atoms, molecules, radicals and ions, which are growth components ; 2) other species which, due to their chemical activity or physical sputtering effects, promote the transition to the gas phase of any carbon condensing clusters with diamond like carbon and graphite (Matsui et al., 1989). Table 2.12 shows the gaseous components in the acetylene feather zone.

Table 2.12 Gaseous Components in Oxy-Acetylene Combustion Flame (Kosky and McAtee, 1989)

H	CH_4	C_2	C_3O_2
H_2	C_2H_4	C_3	O
CH	HO	C_4	O_2
C_2H	HO_2	C_5	O_3
CH_2	H_2O	CO	CHO
C_2H_2	H_2O_2	CO_2	CH_2O
CH_3	C	C_2O	C_2H_4O

Usually hydrocarbon molecules and radicals appear to be carbon precursors during diamond film crystallization, while atomic hydrogen and oxygen act as etching components. The ratio of the growth and etching fluxes will depend on the conditions of the process : temperature of the substrate, its nature (at the stage of the film formation) and composition of the gas phase.

Ravi and Joshi (1991), and Cappelli and Paul (1990) postulated that the growth of diamond crystals at high temperature and low pressure is related to the presence of oxidizing species in the flame near to the substrate. Oxidizing species (oxygen and its variants such as CO and OH radicals) perform the dual functions of etching and gassifying any nondiamond bonded phase formed during synthesis, as well as etching (or scratching) the diamond surface to create growth edges that can subsequently propagate laterally.

Matsui et al. (1989, 1990, and 1991) supported Ravi and Joshi, and Coppelli and Paul's postulation. They examined the feather zone of the flame with laser-induced flourescence and mass spectrometric techniques to measure the mole fraction of possible species. Their results were, CO and H_2 are the dominant species in the feather zone close to the substrate, and that C_2H_2 and C-containing radicals (C_2H_2, CH, C_n, n=1,2,3) are the minor species. They also did computer simulation to calculate the quantities of the species related to diamond deposition. The results of computer simulation in the case of R=0.91 and substrate temperature (T_S) = 1250 K, is shown in Figure 2.14. Finally, they concluded that assuming CH_3 to be the dominant precursor, the following chemical reactions occur at the film surface :

$$* + H \text{ ------> } H(ab) \quad (1)$$

$$H(ab) + H \text{ ------> } H_2 + * \quad (2)$$

$$H(ab) + H \text{ ------> } H_2(ab) \quad (3)$$

$$H_2(ab) + H \text{ ------> } H(ab) + H_2 \quad (4)$$

$$* + CH_3 \text{ ------> } C(\text{diamond}) + H(ab) + H_2 \quad (5)$$

$$* + C \text{ ------> } C(\text{graphite}) \quad (6)$$

$$C(graphite) + 4H\text{------}> CH_4 + * \quad (7)$$

$$C(graphite) + O\text{------}> CO \quad (8)$$

$$C(graphite) + OH\text{------}> H(ab) + CO \quad (9)$$

where * denotes the dangling bond, and H(ab) and H_2(ab) are H-absorbed and H_2-physisorbed sites on the growing diamond surface respectively (Matsui et al., 1991).

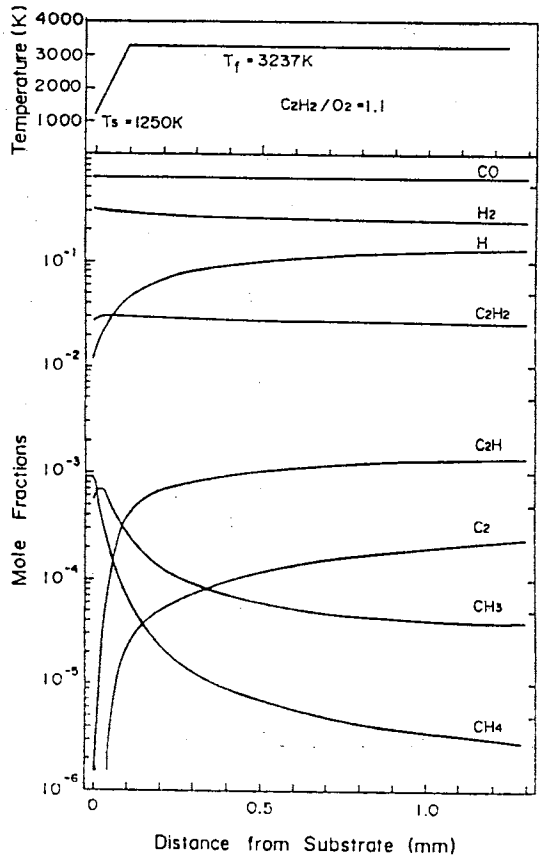

Figure 2.14 Concentration Profiles in Feather Flame Calculated from Computer Simulation for R = 0.91 and T_S = 1250 K (Matsui et al., 1991)

To explain the occurrence of the above chemical reactions on the growing diamond surface, Pate's postulation should be reminded: a hydrogen layer is formed on the

surface of diamond growing during the synthetic process. Actually, this postulation is accepted to be true. If there are too many atomic hydrogens attached to diamond carbons via dangling bond (* in above equations), graphitization becomes significant. Hydrogen coverage H(ab) may be determined by the balance between the addition of a hydrogen atom to the dangling bond: Equation (1), and the subtraction of hydrogen atoms: Equation (2). This subtraction is shown in Figure 2.15. The attached hydrogen on the diamond surface can be recombined by the reactions described in Equations (3) and (4). But these recombinations have low possibility, approximately 1.0% (Matsui et al., 1990). Among the chemical reactions described in Equations (1)-(4), the activation energy of Equation (2) was proved to be the smallest (Huang et al., 1988).

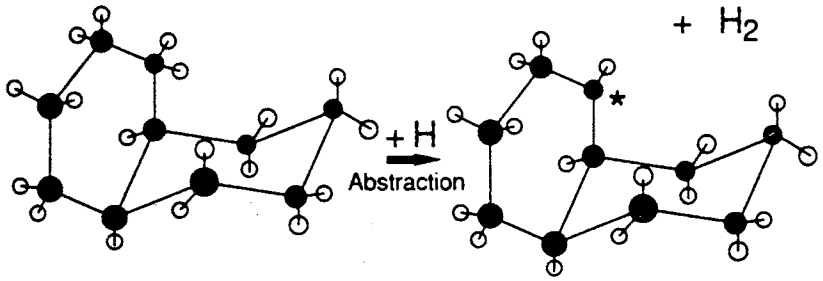

Figure 2.15 Diagram of Atomic Hydrogen Subtraction from Diamond Surface (Peploski et al., 1992)

Equations (5)-(9) are related to atomic carbons, either diamond or nondiamond. Assuming a CH_3 radical as a diamond precursor, it is chemisorbed on the dangling bond. Then, diamond crystal is produced: Equation (5). Other carbon radicals (represented by C) are also chemisorbed on the dangling bond to form graphite carbons: Equation (6). However, the resulting graphite carbons are quickly etched by hydrogen and oxygen atoms: Equations (7) and (8). Then, CH_4 and CO are produced. Also, graphite carbon disappears by reaction with an oxygen radical, OH: Equation (9). Thus, Equations (5)-(9)

explain well the mechanism of diamond growth (deposition and etching) by oxy-acetylene combustion method. Through this section, it is clear that acetylene and oxygen supply enough growth components (hydrocarbon radicals) and etching components (atomic hydrogen and oxygen radical) for themselves.

It has been documented by several investigators that the growth of diamond by oxy-acetylene combustion method is dependent on three key parameters. These are substrate temperature, O_2/C_2H_2 ratio, and the distance between inner cone of flame and substrate. These parameters are dependent on each other. However, the optimal conditions vary with investigators since the specific purposes of each experiment and the dimensions of each experimental setup were different. Table 2.13 shows the optimal conditions for the diamond growth on a nondiamond substrate using oxy-acetylene combustion method by some of the investigators.

Table 2.13 Optimal Conditions of Key Parameters in Oxy-Acetylene Combustion Method

INVESTIGATORS	T_S (°C)	L_S (mm)	O_2/C_2H_2	PRODUCTS
Hirose and Amanuma (1990)	500 - 750		0.9 - 1.0	transparent film
Yarbrough et al. (1989)	950	1	0.89	clean film
Cappelli and Paul (1990)	900	11	0.9	well faceted crystals
Nandyal (1991)	850	2	1.0	octahedral crystals

The gaseous atomic carbons and carbon radicals (hydrocarbons) in the acetylene feather zone of the combustion flame, have a high level of free energy because of high temperature (approximately 3000 °C). The carbons should be cooled to form a solid state via heat dissipation to substrate. The types of resulting solid carbons are decided by the substrate temperature (T_S): diamond, graphite, or amorphous carbon. Thus, T_S is very

important for the diamond synthesis in oxy-acetylene method as well as other CVD methods. The substrate temperature depends on the flow rate of coolant in the heat sink, the substrate-heat sink distance (H_S), the substrate-inner cone distance (L_S), nozzle size, and total flow rate of mixed gas ($C_2H_2 + O_2$). However, there has been no study of the influences of these parameters on the substrate temperature before the present study.

Kosky and McAtee (1989) found that formation of solid carbons from gaseous carbons by condensation is dependent on the flow ratio, R, of O_2 to C_2H_2. Figure 2.16 is a graph of the maximum substrate temperature locus at which solid carbon can form. In fuel rich flames, $R < 1.0$, solid state carbon will deposit on the substrate from low to high temperature. The etching-deposition boundary is very steep near $R = 1.0$ and for a given flame stoichiometry, relatively small substrate temperature changes will control whether a deposit is produced or an existing deposit is etched away.

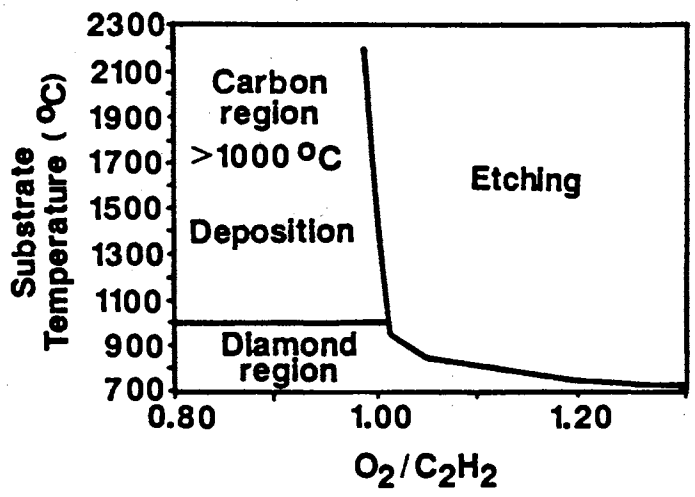

Figure 2.16 Maximum Temperature for Carbon Deposition at 1 Bar as a function of the Flame Stoichiometry (Kosky and McAtee, 1989)

If the substrate temperature is too low, then the energy level of gaseous carbon decreases to that of graphite due to more heat dissipation to substrate than desired (heat dissipation to substrate is proportional to the temperature difference between gas and

substrate). In this case, diamond can not be deposited. Thus, there exists a lower limit of substrate temperature below which diamond can not be deposited. However, the reported lower limits of T_S were not consistent. For example, Hirose and Amanuma (1990) and Hannsen et al. (1988) showed 370 °C and 650 °C respectively, as the lower limit of T_S for diamond synthesis using oxy-acetylene combustion method. The upper limit of T_S for diamond synthesis is related to hydrogen. Pate (1985) has shown that diamond surfaces are normally hydrogenated during CVD synthesis process, but lose this layer at 1000° C (desorption of atomic hydrogen). Then, the subsequent reconstruction and graphitization of diamond surface occur. Matsumoto and co-workers (1979, 1981) found the desorption peak from pre-hydrogenated diamond surface to occur at temperatures of 900 to 1050 °C. Also, they have shown the evolution of graphite, i.e. sp^2 bonding, at the expense of diamond, i.e. sp^3 bonding, at a temperature higher than 1200 °C. The upper limits of T_S on nondiamond substrate reported by most investigators in oxy-acetylene combustion method, are in good agreement (not higher than 1200 °C) with a few exceptions (Matsui et al., 1990 and Komanduri et al., 1990). However, it varies with gas flow ratio (Hanssen et al., 1991).

Hirose and Amanuma (1990) made a map of carbon deposition on nondiamond substrates (TiN, Mo, Si, Al_2O_3) by oxy-acetylene combustion method, in terms of substrate temperature and gas flow ratio, O_2/C_2H_2, as shown in Figure 2.17. This figure shows a wide temperature range for diamond deposition (370 to 1200 °C) depending on gas flow ratio. When gas flow ratio is close to 1.0, the temperature range for diamond deposition is the widest (370-1200 °C). This temperature range decreases with decreasing gas flow ratio. Finally, no diamond is deposited at $R < 0.7$ regardless of the temperature. In this case, amorphous carbon, graphite, or soot can be deposited on the substrate. The temperature range for the deposition of transparent diamond film (high quality diamond, H.Q.D) is smaller (500-750 °C), depending on the gas flow ratio. Hirose and Amanuma pointed out that diamond crystal can not be synthesized in an oxygen-rich flame, i.e. R >

1.0, because of a strong etching reaction on the diamond surface.

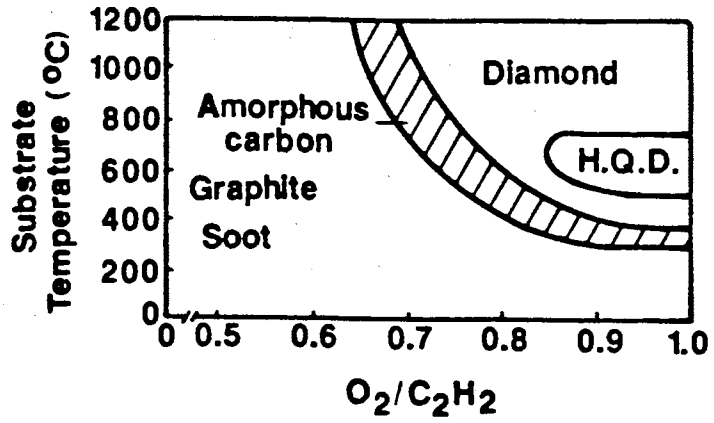

Figure 2.17 Map of Carbon Deposition with Oxy-Acetylene Combustion Method (Hirose and Amanuma, 1990)

The dominant morphologies of diamond crystals by CVD methods are cubic {100} and octahedral {111} surfaces with a rare {110} surface (Matsumoto et al., 1982a; Kamo et al., 1983; Matsumoto and Matsui, 1983). Multiple twinned and cubo-octahedral exhibiting both {100} and {111} surfaces are also common. Octahedral surfaces are rough while cubic faces are smooth since they are parallel to the substrate surface. Also, {100} textured films have a good transparency. In the high-temperature high-pressure synthesis of diamond films, a cubic habit is observed at a low temperature range and octahedral habit at a high temperature range. This phenomena is also observed in microwave plasma CVD method (Kobashi et al., 1988). However, a different tendency was found in chemical transport reaction and hot filament methods (Spitsyn et al., 1981; Matsumoto et al., 1982b; Clausing et al., 1992). That is, a cubic habit at high temperature and a octahedral habit at low temperature. Ravi and Joshi (1991) observed the morphology of diamond films produced by oxy-acetylene combustion method. The

resulting morphology was a strong function of substrate temperature with temperature below 1000 °C resulting in octahedral habit, and with temperature above 1000 °C resulting in cubic habit. They did not report the gas flow ratio, R, of oxygen to acetylene. Ravi and Joshi's results correspond with Matsui et al.'s (1990) report about the temperature for cubic habit. Matsui et al. reported that {100} oriented diamond crystals were dominant at 1330 °C, and were degraded at the temperature of 1480 °C due to graphitization. The results by Ravi and Joshi are contradictory to Hirose and Amanuma's (1990) conclusion that the optimal substrate temperature is in the range of 500-750 °C for the deposition of transparent diamond films. Transparent diamond films are {100} (cubic habit) textured.

Hanssen et al. (1991) and Carrington et al. (1989) showed the dependency of faceted diamond crystals on the substrate temperature (T_S) and gas flow ratio (R). Figure 2.18 shows the results. They observed ball-like structures at R less than 0.9 and well faceted crystals (octahedral, cubo-octahedral, and cubic habits) between 0.9 and 1.08 depending on substrate temperature. The temperature range for well-faceted crystals was 650 to 850 °C at R= 0.9 and 700 to 1150 °C at R = 1.05, showing the expansiveness of the temperature range with increasing R (see Figure 2.18). Beyond R= 1.1 no diamond crystal was seen. They classified the deposit morphologies into three categories: ball-like, faceted structure, and intermediate structure (a cauliflower-like structure).

Recently, Nandyal (1991) showed the results of his experiments about the effects of R on morphology. He made octahedral morphology at R = 0.94 and T_S = 850 °C and cubic morphology at R = 1.0 and T_S = 850 °C. One of his results is that a cubic morphology can be produced at R = 1.0. Thus, gas flow ratio is very important in the morphology of diamond film produced by oxy-acetylene combustion method, as well as substrate temperature. In addition, from his experiments for morphological study, Nandyal insisted that a cauliflower structure of diamond is a precursor growth feature for well-faceted structures such as octahedral, cubo-octahedral, and cubic morphologies.

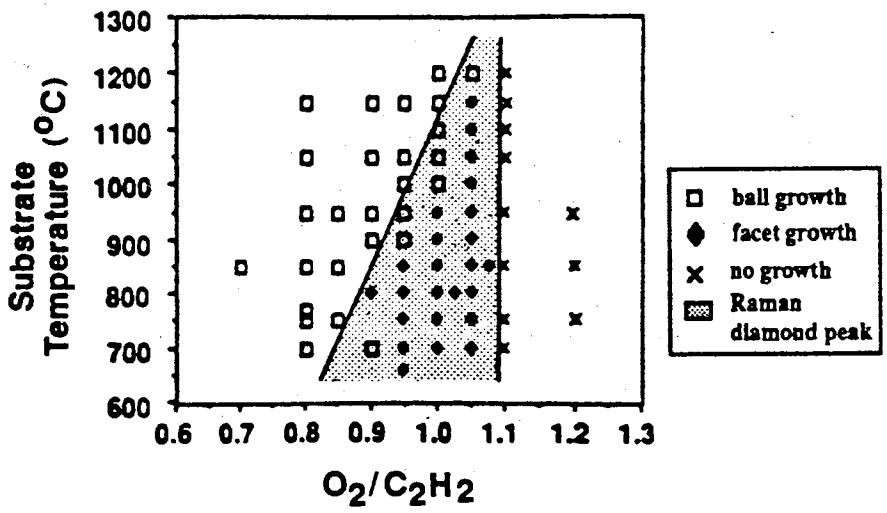

Figure 2.18 Carbon Growth Morphology as a Function of Oxygen to Acetylene Ratio and Substrate Temperature (Hanssen et al., 1991)

Growth of diamond film in the combustion flame is a result of chemical reactions of the growth species such as carbon radicals and etching species such as atomic hydrogen and HO, as mentioned before. All chemical reactions related to the diamond growth occur at the surfaces of diamond crystals which are surrounded by a thin viscous boundary layer of the combustion flame impinging on the substrate surface. The delivering rate of the growth and etching species to the diamond surface from the flame during the synthetic process depends on the transport coefficient of mass (mass diffusion coefficient). Thus, the transport coefficient of mass in the boundary layer plays an important role in the oxy-acetylene combustion method. Generally, magnitudes of transport properties (mass, momentum, and energy) of a flowing fluid are associated with the type of flow regime such as laminar, transition, and turbulent. In the oxy-acetylene combustion method, the premixed gas ($O_2 + C_2H_2$) flows inside the nozzle (pipe flow), then the flow type changes to an impinging round jet flow after the nozzle exit. The flow regime of the round jet flow can be decided by the Reynolds number, Re, based on the nozzle diameter at the nozzle

exit given by

$$Re = \rho V D_n / \mu \qquad (10)$$

where V is the average fluid velocity; D_n is the inside diameter of the nozzle; ρ is the density of fluid; and μ is the absolute viscosity of fluid. For Reynolds numbers less than 2300, the fluid flow in the tube is classified as laminar, where the viscosity of fluid dominates the motion of the flow. As Reynolds number increases from 2300 to 10000, the flow becomes progressively more turbulent (transition regime). For Reynolds number higher than 10000, the flow is classified as turbulent, where the inertia force of fluid dominates the motion of the flow. In turbulent flow, the transport properties are larger than in laminar flow, due to the turbulent eddies. In the previous works reviewed so far in this section, the fluid flows were considered to be laminar.

Snail and Craigie (1991) produced diamond films on molybdenum substrate in turbulent flame. They calculated Reynolds number at the nozzle exit by Equation (10). Room temperature (300 K) was used in evaluating density and absolute viscosity. They used two different mixed gas flow rates with R = 1.08. The resulting Reynolds numbers were 5900 and 12200. The observed combustion flame with Reynolds number of 12200, was turbulent since it had a feather brush that was rounding and blurring before the feather zone. However, in the other case (Re = 5900), the observed combustion flame was shown to be laminar. It had three different zones (inner cone, feather, and outer flame, see Figure 2.4) indicating a laminar flame. The temperature of the premixed gas increases suddenly just after the nozzle exit, due to the combustion reaction. In most gases, the absolute viscosity and density decreases with increasing temperature. Therefore, the actual Reynolds number of the impinging jet flow of mixed gas in oxy-acetylene combustion method, is lower than that calculated at the nozzle exit with the assumption of room temperature. Thus, it is noted that the actual Reynolds number in Snail and Craigie's work, was lower than 2300 even if the calculated Reynolds number with assumption of room temperature was 5900.

(a)

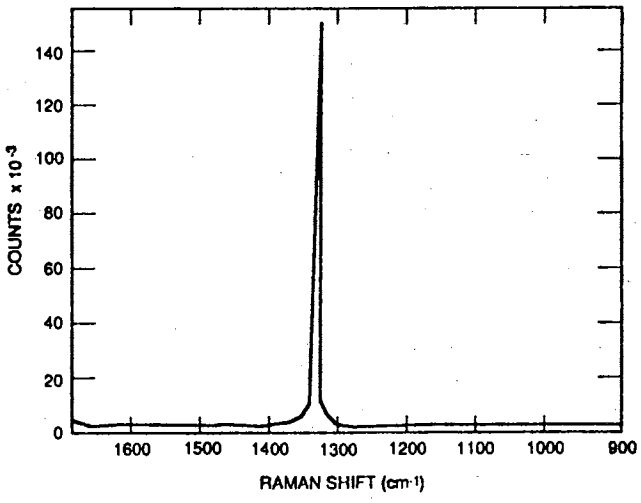

(b)

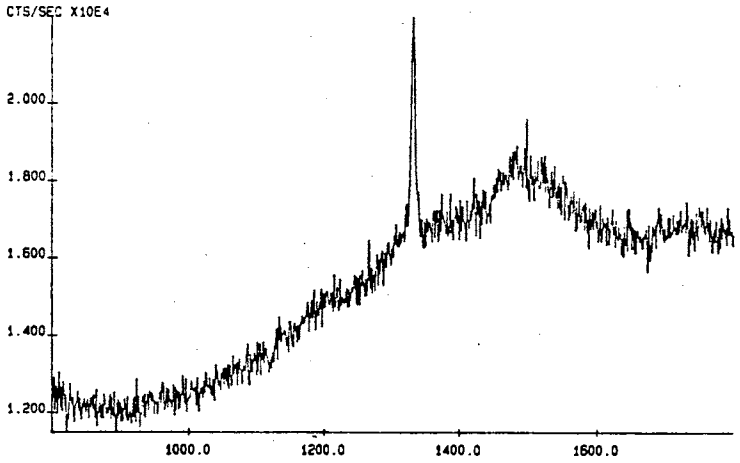

Figure 2.19 Raman Spectra of Diamond Films Produced by Oxy-Acetylene Combustion Method, (a) by Snail and Craigie, 1991; (b) by Nandyal, 1991

After Snail and Craigie (1991), several investigators (Glesener et al., 1991; Snail et al., 1992) at the Naval Research Laboratory produced diamond films on diamond seeds in a turbulent flame. The reported growth rates were in the range of 10 - 30 μm/h. These growth rates are lower than those in laminar flame (up to 200 μm/h). However, the quality of diamond film produced in a turbulent flame improved significantly. The results

of Raman spectra of a polycrystalline diamond film grown in turbulent flame by Snail and Craigie, and that grown in laminar flame by Nandyal (1991) are shown in Figure 2.19. Typically, diamond films produced by CVD methods have peaks at 1400 - 1600 cm^{-1} due to nondiamond carbons in addition to the peak at 1332 cm^{-1} due to diamond (see Figure 2.19-b). However, diamond film grown in a turbulent flame shows only one sharp peak at 1332 cm^{-1} indicating the natural diamond quality (see Figure 2.19-a). Snail and Craigie examined the transparency of the film grown in a turbulent flame by using a spectrophotometer. The results showed a high degree of transmittance throughout the UV (ultra violet), visible, and near IR (infrared). The diamond film was transparent enough to observe the substrate through the individual crystals with an optical microscope. Also, one can read newsprint through the diamond film.

In a turbulent flame, the premixed gas flow rate is higher than that in laminar flow with same nozzle size. Also, the mass diffusion coefficient is high, thus more chemical species (for growth and etching) are supposed to be transported to the substrate surface. Therefore, one may expect higher diamond growth rate in a turbulent flame than in a laminar flame. But, as discussed in the previous paragraph, the results are contradictory to our expectation from the consideration of fluid dynamics. Even though more chemical species are transported in a turbulent flame, a higher growth rate results from a laminar flame. This implies that the ratio of growth to etching species dictates the growth rate of diamond film as discussed earlier in this section. It is believed that the flux of growth and etchant species is altered in the increasing direction of the ratio of etchant to growth (growth species are shifted to etching species), in going from laminar to turbulent conditions (Snail and Craigie, 1991; Snail et al., 1992). The resulting small ratio of growth to etching species can be explained by the lower growth rates and better quality of diamond films grown in a turbulent flame than those in a laminar flame. Kondoh et al. (1991) support the reason of small growth rate in a turbulent flame. They conducted a series of experiments using hot filament CVD method for the study of diamond growth

rate in CVD methods. Finally, they suggested that diamond growth in CVD methods may be limited by surface reactions such as growth and etching. Moreover, Matsui et al. (1989) gave another clue for explaining growth rate. In experiments of diamond synthesis with a laminar flame, they reported that the diamond growth rate was roughly proportional to the premixed gas flow rate up to a certain value, and then independent of the flow rate above that value.

Sometimes, in the oxy-acetylene combustion method, large single diamond crystals were found as pedestals on diamond films which consisted of a number of small and continuous crystals (Bang, 1992). Also, these large crystals (up to 350 μm) were observed at the Naval Research Laboratory (Snail and Hanssen, 1991). These crystals typically have {100} oriented faces. Thus, the surfaces are very smooth and these crystals proved to be indistinguishable from natural diamond (Vardiman et al., 1989). During the synthetic process, large diamond pedestals are regarded to be thermally isolated from the substrate since the thermal conductivity of diamond is very high and their top surface areas are very small, less than 0.1 mm^2. Thus, their temperatures are believed to be higher than the substrate since these are at a thermally equilibrium state in the high-temperature flame. Capelli and Paul (1990) have used an energy balance argument to show that diamond crystals in oxy-acetylene combustion flame would equilibrate above 1200 °C if thermally isolated from the substrate. Thus they conclude that large crystals cannot be grown in a flame because graphite nucleation and growth occur at these high temperatures. However, Lander and Morrison (1966) suggested that the mobility of carbon atoms on the diamond surface may be sufficient to permit the homoepitaxial growth of diamond in the temperature range of 900 - 1400 °C, if graphitization is prevented by expansive atomic hydrogens.

The Naval Research Laboratory measured the temperatures of the thermally isolated large single crystals (up to 100 μm) using a two color pyrometer. The measured temperatures were higher than 1250 °C (the limit of the instrument), whereas the substrate

was at 900 - 1000 °C. Thus, it was clear that large single crystals can be produced by oxy-acetylene combustion method at temperatures higher than 1250 °C, regardless of the arguments about temperature limit for diamond growth. The first condition to produce large single crystals was the preparation of a base, thermally isolated from the substrate. Snail and Hanssen (1991) used small natural diamond seed (1.5mm of diameter, 0.5mm of thickness) as this base. They produced single crystal diamond films (homoepitaxial growth of diamond) on the diamond seed in laminar flames at temperatures of 1150 - 1500 °C and R of 1.03 -1.05. The diamond seed was brazed to molybdenum rod before deposition. The thickness of the produced diamond films were up to 160 μm, and the growth rates were very high, in the range of 100 - 200 μm/h. From the examinations with the Raman spectra and X-ray diffraction techniques, these films were almost identical to the natural diamond, i.e. gem quality. The temperatures of the diamond seed (up to 1500 °C) were the highest among those reported in the literature, regardless of the types of CVD methods. From Snail and Hanssen's works, it looks possible in the near future to produce large single crystals (1 - 10 carats) which are not readily available from natural source. Also, the cost for producing them is not expensive. These large single crystals can be applied to high power electronic devices.

Janssen et al. (1990) also produced single crystalline diamond films (homoepitaxial growth) on diamond seeds in laminar flames. The dimensions of the diamond seeds are believed to be about 2mm × 2mm with thicknesses of 0.25mm and 0.07mm. The temperatures of the diamond seeds were 800 - 1000 °C which were lower than those in Snail and Hanssen's experiments. The gas flow ratio (R) was 1.15 and growth rate was about 50 μm/h. This value of R is higher than 1.0 which is believed to be the upper limit of R for diamond synthesis using oxy-acetylene combustion method (Hirose and Amanuma, 1990). Actually the reported limits of R vary with investigators. Japanese investigators insisted 1.0 as the upper limit of R for diamond synthesis. Some higher values were considered by other investigators: 1.3 by Carrington et al. (1989), 1.1 by

Hanssen et al. (1991), and 1.02 by Nandyal (1991). However, the appropriate value of R for diamond synthesis is dependent on the accuracies of gas flow controllers, mixing efficiency in the torch, and the rate of ambient air entrainment.

Oakes et al. (1991) studied the effects of hydrogen addition to O_2-C_2H_2 flame. They used hydrogen in two different ways; in the first method, the O_2/C_2H_2 ratio was fixed at 1.03 and hydrogen was added to the flame. In the second method, the ratio $O_2/($ $C_2H_2 + H_2)$ was fixed at 1.03 and hydrogen was substituted for acetylene. It was observed that the diamond growth density decreased significantly as the ratio (H_2/C_2H_2) exceeded 0.25. However, there was a remarkable improvement in diamond quality as a result of hydrogen addition.

The mole fractions of species in the feather zone of flame are dependent on the distance from the nozzle as well as the radial direction (Matsui et al., 1990; Tzeng et al., 1989; Ravi and Joshi, 1991). The cross sectional area of diamond film is also dependent on the distance from the nozzle-tip. Therefore, substrate position in a flame decides the film deposition area and growth rate. Oakes et al. (1991) showed that the growth of diamond film varies with position of substrate (see Figure 2.20). The growth density (nucleation or crystal density) in this figure has a different profile in the radial direction from the center of film, as the distance from the inner cone of flame to the substrate surface increases from 3.0 to 9.0 mm. The crystal density is very low at the center region (1 mm diameter) with a distance of 3 mm, and also very low at the annulus region (radius from center is greater than 1.5 mm) with a distance of 9.0 mm. The description in Figure 2.20 indicates that the mole fractions of carbon containing gas changes in the axial direction as well as the radial direction. But, Oakes et al. did not report the substrate temperature and the gas flow ratio of oxygen to acetylene.

Some investigators (Komanduri et al., 1990; Hanssen et al., 1991; Yarbrough et al., 1989) have pointed out the importance of substrate position with respect to the feather zone. Nevertheless, no detailed study of the influence of substrate position in the flame on

diamond deposition was reported.

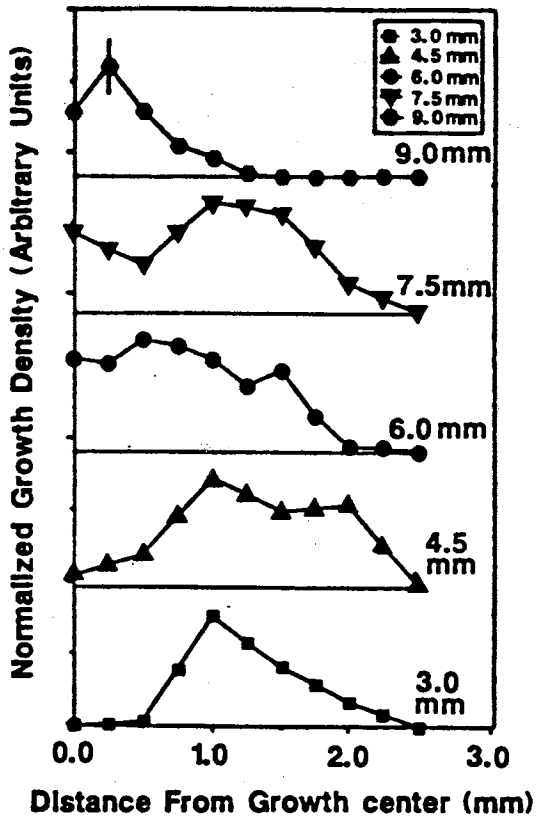

Figure 2.20 Normalized Diamond Growth Density vs. Position Along a Growth Radius on Substrate for Various Substrate-Inner Cone Distance (Oakes et al., 1991)

Table 2.14 Conversion Chart for Nozzle Number

Nozzle Number	Diameter of Nozzle at Exit (mm)
1	0.939
2	1.067
3	1.270
4	1.613
5	1.930
6	2.184
7	2.489
8	2.705
9	2.946
10	3.569
11	3.797

Nozzle size and flow rate of premixed gas (O_2 + C_2H_2) are also important parameters to oxy-acetylene combustion method. These parameters are related to the combustion field. Different values of these parameters change the flame length and shape (Plumley, 1939 and Geary, 1980). As nozzle size increases with constant flow rate of premixed gas, the flame becomes wider and shorter. When the flow rate of premixed gas increases with the nozzle size fixed, the flame becomes wider and longer. Thus, heat flux to the substrate surface depends on these parameters. Furthermore, heat flux is decisive to substrate temperature. Substrate temperature has been emphasized by many investigators since it effects the morphology of diamond film and graphitization of diamond, as discussed in this section so far. Therefore, nozzle size and flow rate of premixed gas are very important in oxy-acetylene combustion method. However, most investigators did not pay attention to these parameters. Some investigators reported the nozzle number to represent nozzle size, while others used the diameter of nozzle. Table 2.14 shows the nozzle numbers and their equivalent diameter sizes.

From the literature survey, substrate materials used in CVD methods can be divided into the following two groups :

metal group : Ti, Ta, Mo, W, Pt, Cu, TiC, Hf, Nb, Al_2O_3, W, WC, WC-Co alloy, Ni, TiN

nonmetal group : Si, Bn, SiC, sillica glass

Joffreau et al. (1988c) examined the refractory metals (Ti, Hf, Nb, Ta, Mo, W) as substrate materials by using hot filament method. They concluded that all refractory metals can be used as a substrate even though the diamond grain size and the diamond nucleation density are dependent on the substrate material; molybdenum showed the highest nucleation density and smallest grain size. Also, the dependency of grain size on substrate material was studied by Lee et al. (1990). It was reported that Fe, Ni, and Co cannot be substrate materials in DC plasma jet CVD method (Koshino et al., 1988). However, Lee et al. suggested Ni as one of the good substrate materials. Thus, substrate

material may depend on the type of CVD method. Many investigators in oxy-acetylene combustion method used Si and Mo as the substrate. No matter what type of substrate is used, the surface should be polished well and cleaned chemically. Scratching the surface of the substrate using a diamond paste (1 - 6 μm) before diamond deposition, is believed to be desirable for increasing the nucleation density of diamond and improving the adhesion of diamond film to substrate (Avigal, 1992; Hanssen et al., 1991). However, heavy scratching tends to lift off the film from substrate and sometimes breaks apart the film upon cooling. Cementing carbide to the substrate and coating silicon to the substrate as well as scratching the surface, have been used to improve adhesion of the film to the substrate (Carrington et al., 1989).

Oakes et al. (1991) recently measured the substrate temperature profile under typical growth conditions using a thermal imaging camera (see Figure 2.21), and compared it with the observed inhomogeneities in the diamond crystallite quality. They concluded that the temperature profile on a substrate is one physical property which could contribute to this inhomogeneity.

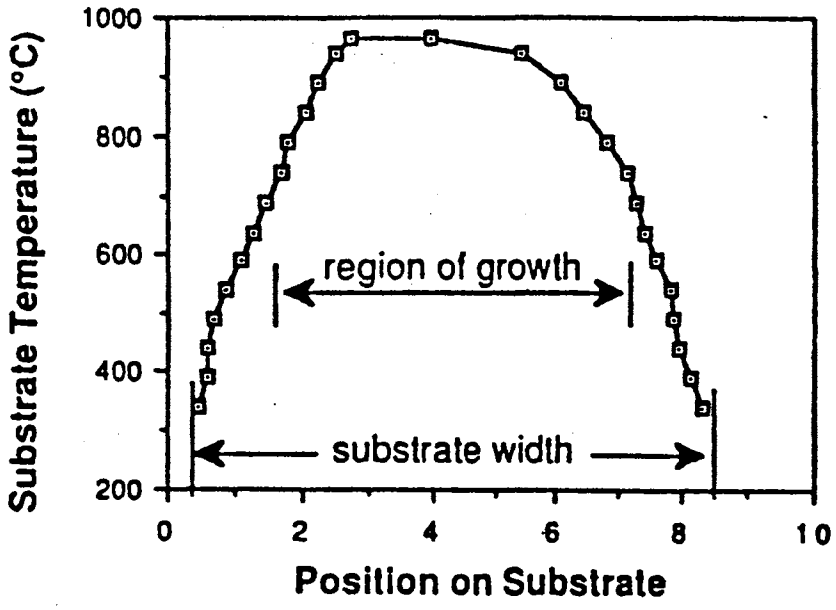

Figure 2.21 Substrate Temperature Profile Measured with Thermal Imaging Camera (Oakes et al., 1991)

More recently, Nandyal (1991) observed that the morphology of the produced diamond film varies in the radial direction from the center of the film as shown in Figure 2.22. This figure shows four distinct radial zones of a diamond film with each zone having a different morphology. However, the substrate temperature profile in the radial direction for these observations were not reported. It should be noted that prior to the present study, Figure 2.21 was the only information available in the literature on the substrate surface temperature distribution.

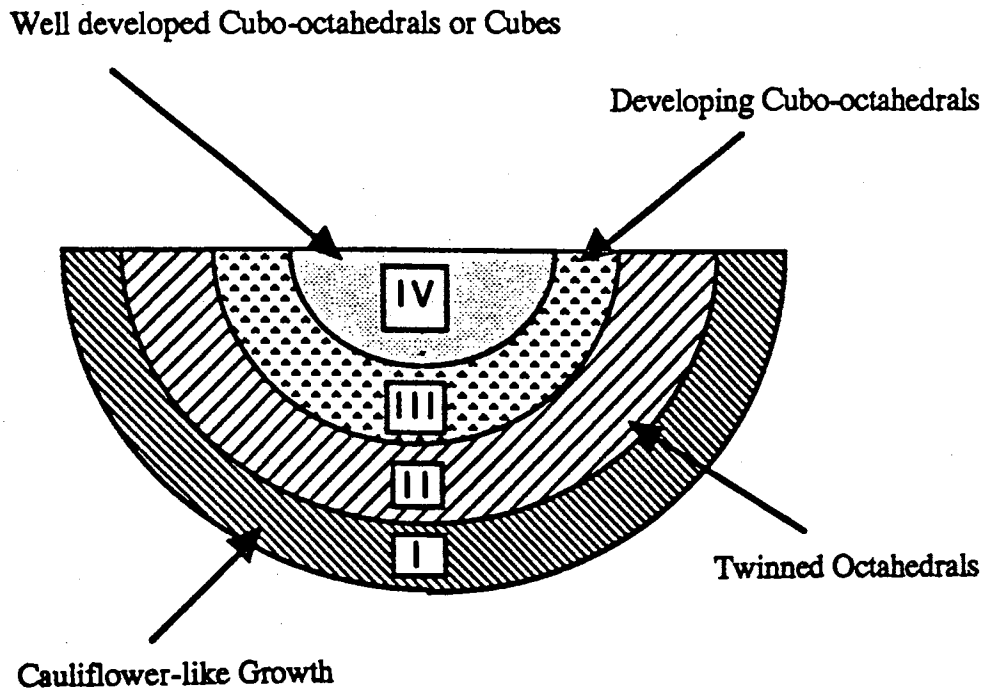

Figure 2.22 Morpholgy Distribution on a Diamond Film Produced by Oxy-Acetylene Combustion Method (Nandyal, 1991)

The majority of investigators using oxy-acetylene combustion method have used a noncontact temperature measurement instrument (pyrometer) to measure the substrate temperature. The accuracy of pyrometer is associated with the emittance calibration of the object whose temperature is being measured. Also, the temperature measurements by the pyrometer are influenced by the target size, area of focus, changes of target emissivity with deposition of diamond film, distance between the target and the pyrometer, and the surroundings. Choi et al. (1992) reported temperature measurement error using the pyrometer during diamond deposition. They observed that the temperature measurement error was induced by emittance variations with changing film thickness during the film growth process. In addition, the pyrometer ,due to its inherent limitations, can only detect the average temperature of the target area, not the temperature of a specified point. Most investigators have claimed the measured temperature to be the center temperature of the substrate surface. Furthermore, the area detected by a pyrometer varies with the working distance from the pyrometer to the target. For a typical pyrometer used in most of these experiments (Williamson 8000 series), the smallest target diameter is about 0.64 cm at a distance of 46 cm from the pyrometer. Thus, the reported temperature is actually the average surface temperature of the detected area and not the temperature at a point and could have been influenced by a number of uncontrollable external factors. Moreover, the flame temperature varies with the radial direction as well as with the propagation direction (axial direction). Therefore, the single substrate temperatures reported by almost all of the investigators cannot be the representative of the substrate surface temperature as long as temperature gradients exist on the substrate surface.

The previous works of the investigators using the oxy-acetylene method have been presented with respect to the key parameters (the substrate temperature, the gas flow ratio, and the distance between the substrate and inner cone of flame) and other parameters. A brief summary of the important previous investigations on oxy-acetylene combustion method is shown in Table 2.15. This table outlines specifics about the

Table 2.15 Summary of Previous Works Related to Oxy-Acetylene Combustion Method

YEAR	INVESTIGATORS	SUBSTRATE	SUBSTRATE TEMP.(°C)	SUBSTRATE POSITION(mm)	O_2/C_2H_2	FLOW RATE (l/min)	GROWTH (μm/hr)	EQUIPMENTS	NOZZLE (mm)	REMARK
1988	Hirose & Kondoh						100 - 200			
1988	Yazu et al.						- 100			
1988	Hanssen et al.	Si, BN, No, Nb, TiC	650 - 1200	1 from inner cone	0.8 - 1.5	$O_2 + C_2H_2$: 2.0	- 60	SEM, Pyrometer, Raman Spectroscopy, X-ray diffraction		
1989	Matsui et al.	WC	627 - 1227	10 - 50 from nozzle	0.78 - 1.5	C_2H_2 : 3.2	- 100	SEM, Pyrometer, Raman Spectroscopy, Mass spectrometry		Upwind flame
1989	Murakawa et al.	WC-Co alloy	1000 - 1100	20 from nozzle	0.89	O_2 : 10.0 C_2H_2 : 11.2	80 - 100	SEM, Pyrometer		Long substrate
1989	Carrington et al.	Si, Si coated Mo	700 - 1200	1 - 2 from inner cone	0.8 - 1.3	$O_2 + C_2H_2$: 2.3 - 3.0		SEM, Pyrometer, Raman Spectroscopy, X-ray diffraction		
1989	Yarbrough et al.	Si	800 - 1100	5 - 35 from nozzle	0.85 - 1.1	$O_2 + C_2H_2$: 1.8 - 3.0	- 60	SEM, Pyrometer, Raman Spectroscopy	0.66 0.97	
1989	Kosky & McAtee	Si	1070 & 1080		1.08 & 1.09	$O_2 + C_2H_2$: 2.0		SEM, Pyrometer, Raman Spectroscopy, X-ray diffraction		
1990	Matsui et al.	Si	827 - 1477	10 from nozzle	0.9 - 1			SEM, Pyrometer, Raman Spectroscopy, Color thermometer		Inclined angle of flame (30 - 90°)
1990	Hirose & Amanuma	TiN, Mo, Si, Al_2O_3	370 - 1200		0.7 - 0.89		- 50	Raman Spectroscopy, X-ray diffraction, IR rad. thermometer	0.94	
1990	Cappelli & Paul	Si	800 - 1200	11 from nozzle	0.6 - 1.4			Mass spectrometer, Pyrometer		
1990	Tzeng et al.	Si	500 - 800	several mm from nozzle	0.8 - 0.99	$O_2 + C_2H_2$: 2.0	20 - 40	SEM, Pyrometer	1.2	70° of flame inclined angle
1990	Komanduri et al.	SC (D=6.25mm)	850 - 1450	6.9 - 30	1		50 - 150	SEM, Pyrometer	1.07	
1990	Ravi and Koch	Mo	780		0.9			SEM, Pyrometer		Two stages of process(R=0.75 ~0.8 & 0.9)
1990	Janssen et al.	Natured diamond	800 - 1000		1.15	O_2 : 1.5 C_2H_2 : 1.3	50	SEM, Pyrometer, Raman Spectroscopy, X-ray diffraction, Spectrophotometer	1.07	

Table 2.15 cont.

1990	Hoff et al.	Mo (D=9.52mm)	780		1.02	$O_2 + C_2H_2$: 5.0	18	SEM, Raman Spectroscopy, Transmission, Electron microscopy		Comparison of HF, MW, combustion
1991	Hanssen et al.	Mo (D=9.25mm)	660 - 1050		0.7 - 1.2	$O_2 + C_2H_2$: 3.0		SEM, Pyrometer, Raman Spectroscopy, Optical microscopy		
1991	Oakes et al.	Si (8 by 8mm)	650 - 1050	3 -9 from inner cone	*	O_2 : 1.7	- 140	SEM, Thermal imaging camera, Ramam Spectroscopy	0.89	
1991	Tzeng et al.	Mo (D=20mm)	800		0.9 - 1.0		9 - 20	SEM, Pyrometer, Raman Spectroscopy, Photoluminescence, spectroscopy	1	Multiple nozzles
1991	Ravi & Joshi	Mo	700 - 1100				- 50	SEM, Pyrometer		
1991	Nandyal	Mo	750 - 1100	1 - 8 from inner cone	0.9 - 1.1	C_2H_2 : 1.5 - 4.0		SEM, Pyrometer, Raman Spectroscopy	0.94 - 1.61	$O_2/C_2H_2 = 1$ for good diamond film
1991	Snail & Craigie	Mo (D=9.52mm)	900		1.08 turbulent		10	SEM, Pyrometer, Raman Spectroscopy, Spectrophotometer	0.89 & 1.85	Good transparency
1991	Glesener et al.	Mo (D=10.25mm)	980 - 1020		1.07 turbulent	O_2 : 6.47 C_2H_2 : 6.005		SEM, Pyrometer, Raman Spectroscopy	1.85	Component of Schottky diode
1991	Snail & Hanssen	Natured diamond (D=1.5mm)	1150 - 1500		1.03 - 1.05		100 - 200	SEM, Pyrometer, Raman Spectroscopy, X-ray diffraction, Optical microscope		Single crystal quality
1991	Matsui et al.				0.83 - 1.0			SIT camera		Study of combustion flame
1992	Snail et al.	Natured diamond (D=1.5mm)	1200 - 1300	1 from inner cone	1.03 turbulent	O_2 : 10.42 C_2H_2 : 10.08	26 - 31	SEM, Pyrometer, Raman Spectroscopy, Optical microscope, Spectroscopy, AFM	1.85	Good quality over whole area
1992	Golozar et al.	Mo (D=5 & 10 mm)	600 - 1200		0.91	O_2 : 1.0 C_2H_2 : 1.1 & 1.4		SEM	1.0	Two stages of process (R = 0.71 & 0.91)
1993	Zhu et al.	Mo Plate (12×12mm)	875	3-4 from nozzle	1.0	O_2 : 1.32		SEM, Pyrometer, Raman Spectroscopy, X-ray diffraction		Multiple nozzle

Table 2.15 cont.

1994	McClure et al.	Si	650	10 & 15 from nozzle	0.97	$O_2 + C_2H_2$: 4.0		SEM, Pyrometer, AES, XPS		Two stages of process (R = 0.93 & 0.97)

*: $O_2/C_2H_2 = 1.03$ & $H_2/C_2H_2=0.1$

$O_2/C_2H_2 = 1.03$ & $O2/(O_2 + C_2H_2)=1.03$

AFM = Atomic Force Micrograph

HF = Hot Filament

MW = Microwave

AES = Augar Electron Spectroscopy

XPS = X-ray Photoelectron Spectrum

equipment used in addition to typical experimental setup, the parameters and techniques used by each investigator(s), and the variables measured.

2.4 Shortcomings of Previous Works

The main purposes of the past investigations on the oxy-acetylene combustion method were to reveal some parameters influencing the quality of diamond films and produce diamond films of good quality. From the works of investigators discussed in the previous section, it is evident that in oxy-acetylene combustion method there are at least three apparent primary parameters which influence the deposition and growth rate of good quality diamond films. These parameters are the substrate temperature, the gas flow ratio of oxygen to acetylene, and the substrate position in the combustion flame. Although there is agreement among investigators on the role of these parameters, there is disagreement on the range of these parameters. The variation in the reported range of these parameters is quite large, considering the fact that the experimenters basically used the same type of experimental setup and had the same objective (producing good quality diamond). The reasons behind these differences could be attributed to inaccurate substrate temperature measurement and lack of consideration of the role of some secondary parameters. For example, the coolant flow rate, the flow rate of premixed gas, substrate position in heat sink, and the nozzle size also play an important role in oxy-acetylene combustion method.

Diamond films should have uniform morphology, uniform crystal size, uniform and high crystal nucleation density, and uniform thickness to be of good quality. Type of particular morphology, certain magnitude of grain, and thickness of diamond film depend on the application (heat transfer, tribology, chemical insulation, etc.). As to controlling the thickness of a diamond film, it is mainly associated with the diamond growth rate and the time for the synthesis process. Although producing a uniform thickness diamond film is not easy, some techniques have been suggested to make the uniform thickness after

deposition (Bogli et al., 1992; Jin et al., 1992). As discussed in the previous section, it is evident that substrate surface temperature and gas flow ratio effect diamond deposition, and crystal structure (morphology) of the deposited film. However, it was pointed out in the previous section that temperature gradients exist on the substrate surface.

The oxy-acetylene combustion method is not yet fully studied due to its short history. Thus, there are many shortcoming and unanswered questions associated with the previous works of investigators. These are:

1. The effect of substrate temperature on the morphology of diamond films and crystals is a subject of controversy. One group(Ravi and Joshi, 1991; Tzeng et al., 1990; Nandyal, 1991) concluded that a cubic habit ({100} orientation) predominates at high substrate temperature, while octahedral faces ({111} orientation) result at low substrate temperature. However, another group(Kobashi et al., 1988; Zhu et al., 1989) assert the opposite. Even in the same group, the limits of substrate temperature to cubic and octahedral morphology are different. Ravi and Joshi (1991) insisted that octahedral morphology were found at below 1000 °C, and cubic morphology at above 1000 °C. But, Nandyal (1991) observed cubic morphology at 850 °C. The morphology of diamond crystals is very important to diamond film application. Therefore, clear conclusion about the morphology of diamond crystals with respect to substrate temperature is required.

2. The upper limit of substrate temperature for diamond deposition during synthetic process is not clear. Hanssen et al. (1991) showed that the upper limit of substrate temperature for diamond deposition was below 1200 °C. However, Nandyal (1991) observed diamond films at 1300 °C.

3. In reviewing existing literature, the majority of investigators have used pyrometer to measure the substrate temperature. Pyrometer can detect the average temperature of a certain area. The target area varies with the distance between pyrometer and target as mentioned in the previous section. The flame temperature varies with radial direction as well as with propagation direction(axial direction). Thus, the substrate surface

temperature should vary with radial direction in nature. However, most investigators reported a single value for the temperature of the substrate surface. As shown in Figure 2.21, there exists temperature gradient over the substrate surface (Oakes et al., 1991). Nandyal (1991) showed the radial dependency of morphology of diamond crystals (see Figure 2.22). That phenomena is considered as the result of temperature gradient over the substrate surface. Also, it was reported that temperature measurement error from pyrometers is caused due to the emittance variation with film thickness change during diamond deposition process (Choi et al., 1992). Therefore, it is necessary to measure accurately the radial temperature distribution of substrate surface to study the radial morphology distribution in diamond films produced by oxy-acetylene combustion method.

4. In the previous works, no attention has been given to the heat transfer in cooling the substrate. The temperature profile (shape and magnitude) at the substrate surface can be directly influenced by the secondary parameters, such as coolant flow rate, nozzle size, substrate position in the combustion flame, total flow rate of mixed gas(acetylene + oxygen), and the substrate position on heat sink. These parameters are related to the heat transfer in the heat sink and substrate. To make relatively uniform morphology of diamond film, it is desirable to reduce temperature gradient over the substrate surface. Therefore, it is necessary to study the secondary parameters which influence substrate surface temperature profile.

5. The study of such key parameters of oxy-acetylene combustion method as substrate temperature, gas flow ratio of oxygen to acetylene, and substrate position in the combustion flame has been reported since 1988. These key parameters are dependent on each other. However, only the partial roles of the key parameters without combination have been explained in the previous works. Moreover, full information about each experimental condition (the values of key parameters, substrate surface temperature distribution, nozzle size, substrate size, etc.) is not available.

2.5. Statement of Objectives

Oxy-acetylene combustion method has been proved to be (potentially) a very efficient technique for producing diamond films, compared to other CVD methods discussed in Section 2.2 of this chapter (see Table 2.11). Due to increasing demand for the production of diamond films, this method needs to be industrialized to take advantage of its potential. However, the literature review presented in this chapter revealed several areas that need to be researched for this method to be ready for industrialization. These areas were discussed in the previous section. This study was undertaken to make a step forward to the industrialization of the oxy-acetylene combustion method in diamond synthesis by developing guidelines on producing a good-quality diamond film.

The specific objectives of this study are :

1. Study the influence of coolant flow rate, nozzle size, flow rate of mixed gas (acetylene + oxygen), substrate position in the combustion flame, and substrate position on the heat sink, on the substrate surface temperature profile.

2. Study the dependencies of morphology and quality of diamond film produced by the oxy-acetylene combustion method on the substrate temperature and the secondary parameters such as the nozzle size and flow rate of the mixed gases.

3. Predict the resulting quality and morphology of diamond film from certain experimental or operating conditions of the oxy-acetylene combustion method (without producing a diamond film) using the results from the previous two specific objectives. This requires prediction of temperature distribution at the substrate surface which influences quality and morphology of diamond film produced by this method.

4. Finally, develop guidelines for the operating conditions of the oxy-acetylene combustion method for producing a desired-quality diamond film with the desired morphology, and to design a better setup for this method for producing higher quality diamond films.

2.6 Method of Approach

The following six tasks were planned to meet the objectives of this study:

1. Construction and instrumentation of the substrate and heat sink based on the proposed design discussed in the next chapter.

2. Systematic experimentation of temperature measurements to determine the influences of

   coolant flow rate

   nozzle size

   substrate position on heat sink

   substrate position in combustion flame

   total flow rate of mixed gas(oxygen and acetylene)

on the substrate surface temperature profile.

3. Producing diamond films by the oxy-acetylene combustion method and analyzing them with respect to quality components such as grain size, nucleation density, film size, and morphology with the aid of SEM (scanning electronic microscope). The effects of the primary and secondary parameters on the morphology and quality of the produced diamond films are studied in this step.

4. Development of an analytical (mathematical) model for the heat transfer in the heat sink and substrate based on the heat conduction equation.

5. Development of a numerical model for the heat transfer in the heat sink and substrate from the analytical model developed in the previous step. This includes developing a computer code and comparing the results to the experimental data.

6. Development of guidelines to the industrialization of the oxy-acetylene combustion method based on the results from steps 2 through 5. This includes the optimal conditions of the parameters for the synthesis of good quality diamond films as well as the conditions required to synthesize a diamond film using oxy-acetylene combustion method.

CHAPTER III

EXPERIMENTAL SETUP, FACILITIES AND PROCEDURES

The typical experimental apparatus of oxy-acetylene combustion method was shown in Figure 2.4. In order to perform the type of experiments to meet the objectives of this study, the substrate and substrate holder (heat sink) were redesigned. This chapter describes mainly the experimental setup, facilities, and procedures.

3.1 Thermocouples

Thermocouples are desirable for the temperature measurement at specified points. The size of thermocouples should be considered as well as the upper working temperature limit. There are two styles of thermocouples- probes and wires. Both styles should not be exposed to a combustion flame since the strong oxidizing agents in the combustion flame cause unrecoverable damage to the thermocouples. The available size of probe thermocouples from commercial products is not adequate for temperature measurement at small areas. Therefore, wire style thermocouples were selected for the substrate temperature measurements. These thermocouples were mounted inside the substrate to provide protection from the flame.

There are four types of thermocouples for high temperature measurements (up to 2200 °C). Table 3.1 shows the four types of unsheathed thermocouples with respect to maximum working temperature, error, response time, and diameter of bare wire required for the measurement of temperatures higher than 1000 °C. In this study, thermocouples were used to measure the temperature distribution at the substrate surface. Thus, many

thermocouples should be used to measure the temperatures at different locations in the substrate. Consequently a small size of thermocouple is required. Thermocouples with small wire diameter have quick response time to give temperatures as shown in Table 3.1. Therefore, the favorable thermocouple used for this study was small diameter bare wire. Among the four types of unsheathed thermocouples in this table, C-type has the highest maximum working temperature with the smallest required diameter of bare wire. However, the datalogger available for these experiments (Electronic Controls Design Model 5100) could not accept C-type thermocouple wires. B-type has the second highest working temperature limit of 1650 °C as seen in Table 3.1. The lower limit of the working temperature in B-type thermocouple is 300 °C. The temperature range to be measured was 500 to 1500 °C which was in the working temperature range of B-type thermocouple. The required minimum diameter of B-type thermocouple wire for the temperature range of this study is smaller than R and S type as listed in Table 3.1. Thus the B-type thermocouple was chosen to measure the substrate surface temperature. For the coolant (water) temperature measurements, the T-type thermocouple was used (working temperature range of -270 to 350 °C).

Table 3.1 Unsheathed Thermocouples for High Temperatures
(ASTM, 1970 and OMEGA, 1987)

Type	Max. Temp.	Error	Required Size	Response Time
R, S	1450 °C	±1%	D ≥ 0.381 mm	2.6 sec for D=0.254 mm
B	1650 °C	±1%	D ≥ 0.254 mm	4.3 sec for D=0.381 mm
C	2200 °C	±1%	D ≥ 0.254 mm	12.3 sec for D=0.81 mm

3.2. Substrate

There are two groups of substrate materials (either rod or sheet) as mentioned in the previous chapter :

metal group (either rod or sheet): Ti, Ta, Mo, W, Pt, TiC, Hf, Nb, Al_2O_3

nonmetal group: Si, Bn, Sic, silica glass

To select the proper substrate material for this study, the following aspects were considered:

1) repeatability of experiments, no change of substrate characteristics with each heat cycle
2) ease of installation of thermocouples
3) high thermal conductivity for relatively uniform temperature distribution
4) high melting point (above 1800 °C)

From the first aspect, rod type of substrate was chosen because sheet type causes the thermal resistance at the interface between sheet and contacting substrate holder. To install a set of thermocouples in the substrate, drilling a number of small diameter holes(about 1.7 mm) was required. Thus the metal materials are better to be a substrate since the metal materials are easier than nonmetal materials to drill holes in. Also, the metal materials have high thermal conductivities. Among the metal materials, copper cannot be used for substrate since its melting point is less than the upper temperature limit in the proposed experiments, 1500 °C. Tungsten and molybdenum are used widely in oxy-acetylene combustion method. Since the hardness of tungsten is greater than molybdenum (tungsten is hard to drill), molybdenum rod was chosen as the substrate material. The size of molybdenum rod used as a substrate was 12.7 mm in diameter and 31.75 mm in height.

3.3. Experimental Setup and Facilities

A modified version of the typical experimental setup (see Figure 2.4) was used for the experiments of this study. In order to carry out the experiments to meet the objectives of this study, the substrate and the substrate holder(heat sink) were redesigned. Figure 3.1 shows an overall schematic of the experimental setup used in this study. As shown in the figure, the substrate (molybdenum screw with installed thermocouples) of 12.7 mm in

diameter and 31.75 mm in height, is mounted at the center of a water-cooled copper block(heat sink) to be cooled via conduction heat transfer through copper block and convection heat transfer by continuous coolant (water) flow. The copper block was 101.6 mm in diameter and 25.4 mm in height with a threaded center hole diameter of 12.7 mm (same as the substrate). Figure 3.2 shows the details of the copper block(heat sink). Coolant (water) flows inside the copper block to dissipate heat from the substrate and upper surface of the copper block. The coolant flow rate was monitored using a calibrated rotameter with full scale (0.5 - 4.0 l/min) accuracy of ±2% and the full scale repeatability of ±1%. The inlet and exit temperatures were monitored with two T-type thermocouples. Calibration of the T-type thermocouples showed an accuracy of ±0.5 °C.

One of the primary objectives of this study was the accurate determination of substrate surface temperature distribution. As discussed in the previous chapter, pyrometers do not provide an accurate and realistic temperature distribution of the substrate surface. Therefore, for this study thirteen B-type thermocouples with the distribution shown in Figure 3.3 were used. A numerically controlled milling machine (Bridgeport Model Interact 412 with controller Heidenhain TNC 151) was used to drill thirteen 1.7 mm diameter holes on the back of the molybdenum substrate to a depth of approximately 0.5 mm below the substrate surface. A control program for drilling was developed using a language call 'DIALOGUE'. This program moves the substrate as a workpiece to each hole center, and controls the rpm and the drilling feed rate. Cobalt and high speed steel drill bits (size #51, 1.7 mm diameter) were used for drilling holes. Unsheathed fine gage thermocouples with a bead diameter of approximately 0.63 mm and a wire diameter of 0.254 mm placed in ceramic insulators of 1.6 mm in diameter (OMEGA TRX 164116) were inserted through the drilled holes in the back of the substrate (see Figure 3.1). To maintain a good contact between the thermocouple beads and the substrate, a specially designed spring-loaded thermocouple holder plate was used. The temperature stations #1 to #13, refer to Figure 3.3, were monitored with B-type

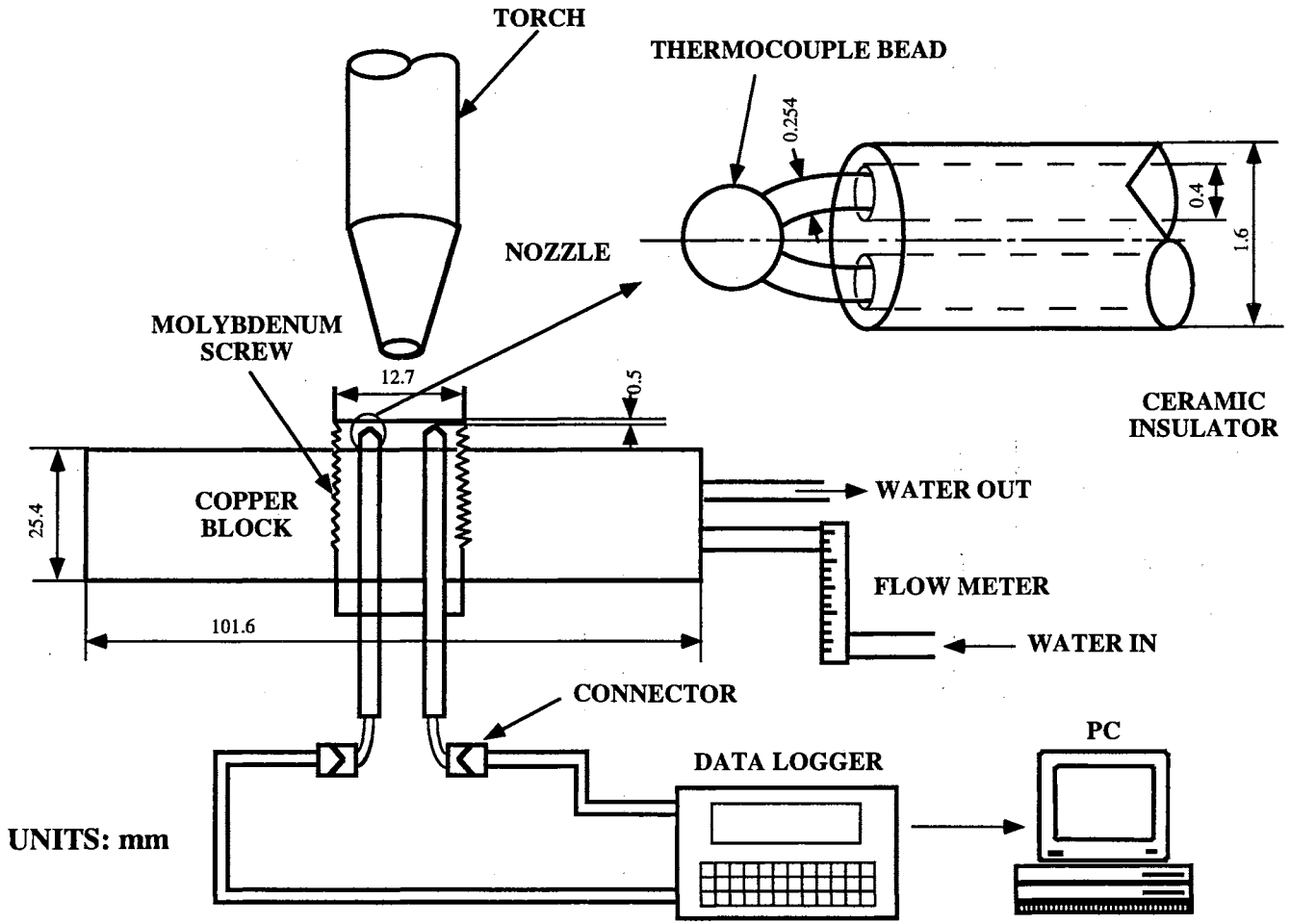

Figure 3.1 Schematic of Overall Experimental Setup

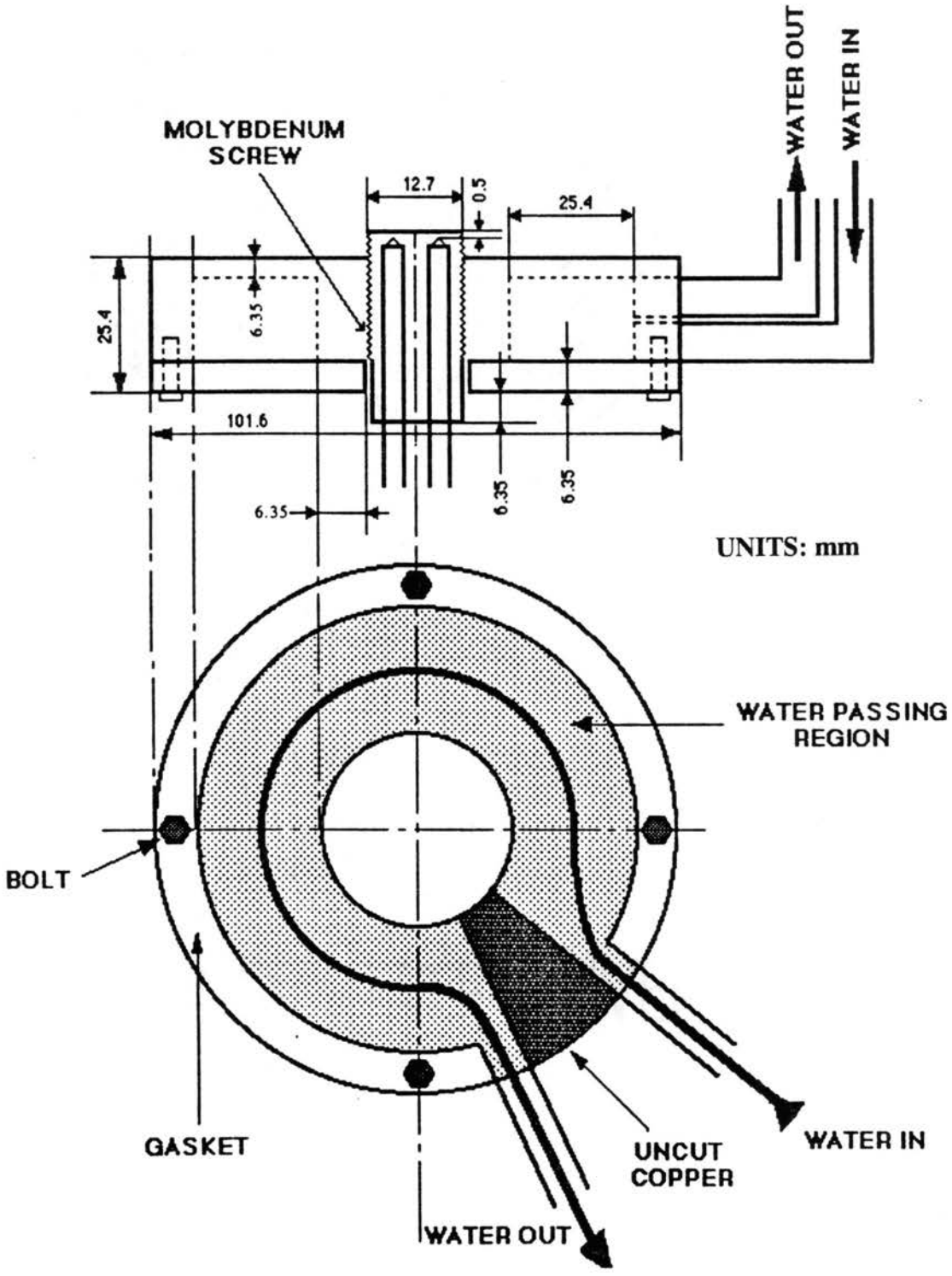

Figure 3.2 Schematic of Copper Block (Heat Sink)

DISTANCE FROM CENTER, mm	THERMOCOUPLE STATION NO.
0.0	1
2.0	2, 3, 4, 5
3.0	6, 7, 8, 9
4.0	10, 11, 12, 13

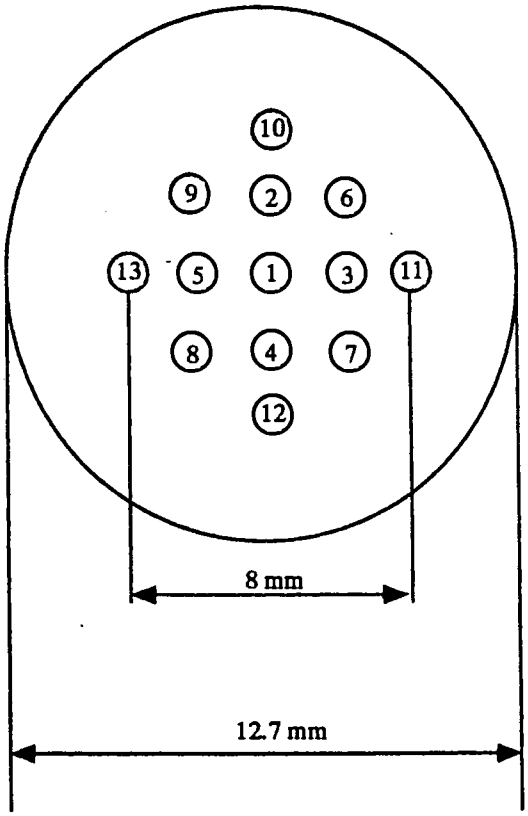

Figure 3.3 Distribution of Thermocouples in Substrate

thermocouples (OMEGA P30R-010) which have a temperature limit of 1650 °C and a response time of about 2.6 seconds. As shown in Figure 3.1, the thermocouples were monitored with a datalogger (Electronic Controls Design Model 5100, see Appendix B for detailed specifications) interfaced with a personal computer. Steady state temperature readings were taken at 30 second intervals. All temperature readings were stored in the hard drive of the personal computer, then divided by the run time to give the average temperature for each thermocouple station. Calibration of the thermocouples showed an accuracy of ±1% of the reading for the B-type thermocouples.

Mass flow meters (MKS Model 2259C) were used to meter the gas flow rates of oxygen and acetylene. A mass-flow programmer (MKS Model 147B) was used to program the flow rates desired and control the individual mass flow meters. Detailed specifications of the mass flow meters and mass-flow programmer are given in Appendix B. Welders-grade acetylene (99.6% purity grade) and high-purity oxygen (99.9% purity grade) were used as the reactant gases. The torch was mounted on a translation stage for accurate and repeatable positioning of the torch relative to the substrate. Single-hole brazing nozzles (#1, #2, and #4; see Table 2.14) were used in the experiments.

As the diamond crystallites in the films are of the order of microns in size, a scanning electron microscope (SEM) was used for the morphological studies. For this purpose an ISI-ABT32 digital SEM with a resolution of 5 nm was used. The SEM also has a built-in polaroid camera for taking micrographs of the specimens. Before a diamond film was examined on SEM, a thin coating of gold-palladium was deposited on the film surface. A Ladd SC502 vacuum sputter coater was used to coat the diamond films.

3.4 Experimental Procedures

All experiments for temperature measurements and diamond film synthesis were conducted with the centerline of the combustion flame perpendicular to the substrate surface under normal atmospheric pressure conditions (101.3 kPa). Oxygen and acetylene

cylinder pressures (P_{O_2} and $P_{C_2H_2}$) were constant during each experiment. The gage pressures of oxygen and acetylene in the cylinders were 1013 kPa and 506.5 kPa, respectively in the experiments of temperature measurements to study parametric effect on the substrate temperature profile, and 2026 kPa and 1013 kPa in the experiments of diamond synthesis. The ratio of oxygen to acetylene flow rates, R, was fixed at 0.98, but flow rates of oxygen and acetylene varied in the experiments. Table 3.2 shows ranges of several process parameters, such as flow rates of oxygen and acetylene, nozzle size, coolant flow rate, substrate-heat sink distance, and substrate-inner cone distance, used in the experiments. Accuracies in controlling the flow rates of oxygen, acetylene, and coolant were ±0.04 l/min, ±0.08 l/min, and ±2% of the settling, respectively (refer to Section D.2 of Appendix D).

Table 3.2 Ranges of Process Parameters Used in the Experiments

Parameters	Range	
	Temperature Measurements only	Diamond Film Synthesis with Temperature Measurements
Q_{O_2} (l/min)	2.0 ~ 3.5	2.0 ~ 3.0
$Q_{C_2H_2}$ (l/min)	2.04 ~ 3.57	2.04 ~ 3.06
Q_c (l/min)	0.76 ~ 2.46	0.76 ~ 2.46
D_n (mm)	0.939 ~ 1.613	0.939 ~ 1.067
H_s (mm)	4 ~ 9	2 ~ 7
L_s (mm)	2 ~ 10	4 (fixed)

The substrate surface was polished well (roughness was within ±4.0 μm), then it was scratched with six-micrometer diamond paste to enhance the nucleation of diamond and cleaned by methanol before each experiment. Scratching the substrate surface was done even in the experiments of temperature measurements. The scratching for each experiment was repeated the same way to ensure nearly the same initial substrate surface

condition. When the substrate was ready for experiment, the substrate was mounted on the heat sink with a desired substrate-heat sink distance by rotating the substrate (molybdenum screw), then the torch with the desired nozzle size was positioned perpendicular to the substrate surface. Further steps are:

- Open the valve of the coolant and adjust the desired amount of the coolant flow rate.
- Open the two mass flow meters for oxygen and acetylene.
- Program the desired flow rates of oxygen and acetylene using the keyboard in the mass flow programmer.
- Open the valves of oxygen and acetylene containers (tanks) and adjust P_{O_2} and $P_{C_2H_2}$ using regulators connected to each tank.
- Place a metal plate over the substrate and heat sink to protect the system from the combustion flame.
- Open the two valves connected to the torch (one is for oxygen, and the other is for acetylene).
- Generate combustion flame using a lighter (fire starter).
- When the flow rates of oxygen and acetylene shown on the monitor of the mass flow programmer reach the desired rates, remove the metal plate positioning over the system. Then, control the torch position to have the desired substrate-inner cone distance by rotating the screw on the torch holder.
- Run the program (software supplied by the datalogger company) for the temperature data acquisition system. Temperature data are shown on the datalogger monitor and stored in the hard drive of the personal computer.

After completion of the experiments, the two valves on the torch and those on the gas containers were closed. However, the two valves on the torch should be open again for about 15 minutes to remove the resident oxygen and acetylene in the line after taking the

substrate from the system. It is noted that the mass flow programmer should be always on since it requires at least two days to be on working status after turning on. The synthesized diamond films from the experiments were studied with respect to morphology and quality using a scanning electron microscope.

To ensure reproducibility of the results, the initial conditions of the experiments were carefully controlled and each experiment was repeated two or three times. The results of these runs compared very well. It is interesting to note that during the reproducibility runs it was discovered that when the amount of oxygen or acetylene in the cylinder was low, the combustion flame became unstable due to flow fluctuation and the results were not reproducible. Unstable flame causes a continuous change in the chemical reactions associated with growth and etching processes. However, the results reported in this study were reproducible and were obtained with stable combustion flame.

CHAPTER IV

BACKGROUND OF COMPUTER SIMULATIONS

The literature survey revealed that no attempt has been made to predict the temperature profile at the substrate surface. Although the effect of the substrate surface temperature on the morphology and quality of diamond films is a subject of controversy, every investigator in the oxy-acetylene combustion method arrived at the same conclusion that the substrate surface temperature plays an important role in the morphology and quality of diamond films. Using the experimental results of the dependencies of the morphology and quality of diamond films on the substrate surface temperature, prediction of the substrate surface temperatures helps in prediction of the resulting morphology and quality of diamond films from certain operating conditions. Furthermore, it can help in developing guidelines for the operating conditions of the oxy-acetylene combustion method for producing a desired quality diamond film with the desired morphology, and in designing a better setup for this method for producing higher quality diamond films.

Heat transfer in the system (substrate and heat sink) was properly modeled mathematically and numerically for the prediction of the substrate surface temperatures. Since the governing equation (to be discussed later) in the mathematical heat transfer modeling could not be solved directly, a computer code was developed based on the numerical heat transfer modeling. These are presented in the following sections.

4.1. Mathematical Modeling

The heat transfer from oxy-acetylene combustion flame into the substrate and heat sink was modeled to examine the several parameters influencing the substrate surface temperature distribution. The actual experimental setup modeled in this study is shown in Figure 3.1. As depicted in this figure, the oxy-acetylene combustion flame impinges perpendicularly on the substrate and heat sink, and the combustion characteristic is two-dimensional (axial and radial directions). A threaded molybdenum rod of 12.7 mm in diameter and 31.75 mm in length was used as a substrate. A diamond film is deposited on the upper substrate surface which is surrounded by the oxy-acetylene combustion flame. A cylindrical copper block (101.6 mm in diameter and 25.4 mm in height) was used as a heat sink. The heat sink has coolant flowing in the radial direction through a rectangular shaped region (25.4 × 12.7 mm). Most of the heat transferred from the combustion flame to the heat sink and substrate is eventually dissipated into the flowing coolant via convection heat transfer. The main heat transfer mechanism in the heat sink and substrate is by heat conduction. The heat sink was designed to have relatively two-dimensional heat dissipation into the coolant as shown in Figure 3.2. Thus, the conduction heat transfer in the heat sink and substrate can be simplified to be two-dimensional. The system (heat sink and substrate) exhibits an axisymmetric condition.

The two-dimensional conduction heat transfer for the system may be represented as a partial differential equation in cylindrical coordinates. Assuming steady state and constant thermal conductivity, the partial differential equation has the following form:

$$\frac{\partial^2 T}{\partial r^2}+\frac{1}{r}\frac{\partial T}{\partial r}+\frac{\partial^2 T}{\partial x^2}+\frac{S}{k}=0 \qquad (11)$$

where, T is temperature field of the system, $T=T(x, r)$; k is the thermal conductivity of the medium where heat is transferred by conduction (heat sink and substrate); and S is the source term (internal heat generation term per unit volume), which in this case is represented by the heat dissipation into the coolant inside the heat sink.

Free convection boundary conditions can be applied on the vertical cylindrical surface and the flat bottom surface of the heat sink. The convection boundary condition should be expressed in an equation for the boundary temperature in order to solve the whole temperature field (T) of the system in Equation (11). From the definition of the average convection heat transfer coefficient, the free or forced convection heat transfer (heat flux) can be expressed as

$$q''_{conv} = \bar{h}(T_\infty - T_B) \tag{12}$$

where, q''_{conv} is the heat flux across the boundary via free or forced convection; T_B is the temperature at the boundary where heat is transferred via convection; and T_∞ is the ambient fluid temperature.

The average free convection heat transfer coefficient in free convection on a vertical cylinder can be obtained from the well known correlation of Churchill and Chu (1975) for a vertical plate when the ratio of the diameter to the height meets the following restriction (Sparrow and Gregg, 1956):

$$\frac{D}{L} \geq \frac{35}{\left[\frac{Ra_L}{\mathrm{Pr}}\right]^{1/4}} \tag{13}$$

where D and L are the diameter and height of cylinder, Pr is the Prantdl number of ambient fluid (air), and Ra_L is the Rayleigh number expressed by

$$Ra_L = \frac{g\beta(T_w - T_\infty)L^3}{\nu\alpha}$$

where, g is the gravitational acceleration; β is the volumetric thermal expansion coefficient of ambient fluid (air); T_W is the temperature of the surface exposed to free convection; T_∞ is the ambient fluid (air) temperature; ν is the kinematic viscosity of ambient fluid (air); and α is the thermal diffusivity of ambient fluid (air). All properties of air such as β, ν, α, and Pr used in calculating Ra_L were evaluated at the film temperature of $(T_W + T_\infty)/2$.

All experiments conducted in this study satisfied the condition of Equation (13). Thus, the average heat transfer coefficient, $\bar{h}$, related to the free convection on the cylindrical surface of the heat sink can be calculated by the following nondimensional correlation (Churchill and Chu, 1975).

$$\overline{Nu_L} = 0.68 + \frac{0.67 Ra_L^{1/4}}{\left[1+(0.492/\mathrm{Pr})^{9/16}\right]^{4/9}} \qquad (0 < Ra_L < 10^9) \tag{14}$$

where, $\overline{Nu_L}$ is the average Nusselt number based on the height of the cylinder (L), defined as $\overline{Nu_L} = \bar{h}\,L/k$. Again, all experiments conducted for this study satisfied the range of Ra_L in Equation (14). The average heat transfer coefficient related to the free convection on the bottom surface of the heat sink can be calculated by the following nondimensional correlation (Goldstein et al., 1973).

$$\overline{Nu_{Lc}} = 0.54 Ra_{Lc}^{1/4} \qquad (10^4 < Ra_{Lc} < 10^7) \tag{15}$$

The convection heat transfer characteristic length (L_c) in Equation (15) is defined as the ratio of plate surface area to the plate perimeter. Again, the restricted range of Ra_{Lc} in Equation (15) was satisfied in the all experiments conducted for this study.

The heat transfer mechanism of the heat dissipation into the coolant (water) inside the heat sink is forced convection. In the experiments conducted for this study, the temperatures of the coolants entering and exiting the heat sink were monitored with two thermocouples. Using these temperatures, the heat dissipation rate into the coolant, q_c, was determined by the following equation:

$$q_c = Q_c \rho\, c_p (T_{out} - T_{in}) \tag{16}$$

where, Q_c is the volumetric flow rate of coolant; ρ is the density of coolant; c_p is the specific heat of coolant; T_{in} is the coolant temperature entering heat sink; and T_{out} is the coolant temperature leaving heat sink. The heat dissipation rate into the coolant can be expressed in terms of the average convection heat transfer coefficient by Equation (12). However, the heat transfer coefficient in the forced convection inside a duct is strongly

dependent on the flow regime (laminar, transition, or turbulent) and the configuration of the fluid flowing region. In most of the conducted experiments, the coolant flow inside the heat sink was laminar. The configuration of the coolant flowing region in the heat sink is a 360° bend as shown in Figure 3.2. There is no correlation or data for the average heat transfer coefficient of the coolant corresponding to the given conditions of the coolant flowing inside the heat sink. However, the combination of the results from Wilbuswas (1966) and Boelter et al. (1948) may give the appropriate average heat transfer coefficient of the coolant inside the heat sink. The estimation of the average heat transfer coefficient of the coolant is discussed in Section D.1 of Appendix D.

One of the main purposes of this part of the study was the determination of heat flux distribution at the substrate surface. Heat transfer from the flame to the substrate surface is carried out by convection and radiation. Using the total heat transfer coefficient, heat flux, q_s'', at the substrate surface can be expressed by

$$q_s'' = h_t(T_f - T_s) \tag{17}$$

where, h_t is the total heat transfer coefficient which is the sum of heat transfer coefficients by convection and radiation (h_t varies in the radial direction); T_f is the temperature of flame over the substrate surface (acetylene feather zone flame), about 3000 °C (Matsui et al., 1990); and T_S is the substrate surface temperature which varies in the radial direction. The distributions of the total heat transfer coefficient (h_t), surface heat flux (q_S''), and substrate temperature (T_S) were determined by the computer simulation. The oxy-acetylene combustion flame over the upper surface of the heat sink transfers heat into the heat sink via convection and radiation as in over the substrate. The resulting heat flux at the upper surface of the heat sink can be expressed by Equation (17). In this case, T_f is the outer flame temperature which is about 1500 °C (Plumley, 1939). The total heat transfer coefficient (h_t) at the upper surface of the heat sink is assumed to be relatively uniform compared to that at the substrate surface.

The threaded area of the substrate and the region of the upper surface of the heat sink, which is close to the substrate, are not in contact with the combustion flame. The heat transfer from the flame to these regions in the system can occur by the combination of radiation and conduction, rather than convection since the air between these regions and the flame is stationary. The resulting heat flux, q''_{r+c} in this case can be expressed as follows:

$$q''_{r+c} = \sum G'' - \varepsilon\sigma T_w^{\,4} + k_a \left.\frac{\partial T_a}{\partial x}\right|_{at\ surface} \qquad (18)$$

where, G'': any kind of irradiation absorbed per unit surface area

ε : emissivity of the wall where radiation heat exchange occurs

σ : Stefan-Boltzmann constant (5.67×10^{-8} W/m^2·K^4)

k_a, T_a : thermal conductivity and temperature of the air between the threaded area of the substrate and the upper heat sink surface and their neighboring flame

x : radial or axial direction depending on the heat transfer direction

T_w: temperature of the surface exposed to both convection and radiation heat transfers (the threaded area of the substrate and upper heat sink surface close to the substrate)

The terms related to the radiation heat transfer in Equation (18) are discussed and expressed in terms of temperatures of the flame, heat sink, and substrate in Section C.1 of Appendix C.

4.2. Numerical Modeling

The main governing equation for the heat conduction in the heat sink and substrate was solved using a computer code employing the control-volume approach developed by Patankar (1991). When the control-volume method is applied for heat transfer, the

resulting discretization equations represent the conservation of energy for each control volume in the calculation domain. The solutions obtained by the control-volume method give a very good overall balance of energy for the whole calculation domain.

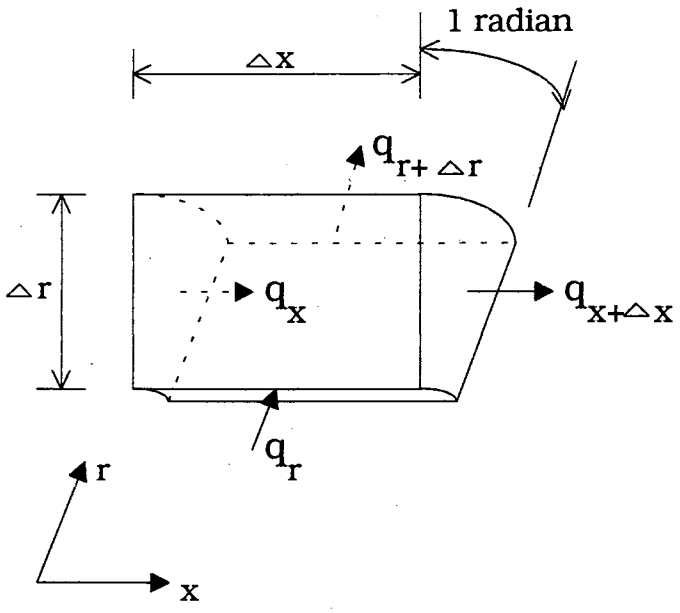

Figure 4.1 Schematic of Control Volume for Two-Dimensional Conduction Analysis in Cylindrical Coordinates (x, r)

The heat transfer in the system was simplified to be two-dimensional (axial and radial directions) in cylindrical coordinates. Figure 4.1 shows a control volume in cylindrical coordinates, where the control volume has dimensions of Δx and Δr with the unit radian in the θ-direction. When the energy balance in two-dimensional and steady state conduction heat transfer is applied to the control volume, the following equation should be satisfied in the control volume.

$$q_r - q_{r+\Delta r} + q_x - q_{x+\Delta x} + \bar{S}\Delta V = 0 \qquad (19)$$

where, q's are the heat transfer rate via conduction across the control volume surfaces (subscript specifies the corresponding control volume surface); Δx and Δr are the thicknesses in the axial and radial directions, respectively; $\overline{S}$ is the average heat generation rate in the control volume; and ΔV is the volume of the control volume [$\Delta V = \Delta r \Delta x r(1)$]. The heat transferred into or from the control volume is carried out by heat conduction. Then, the heat transfer rates across the control volume surfaces can be expressed as

$$q_i = -kA_i \frac{\Delta T}{\Delta x_i} \tag{20}$$

where, subscript i is the direction of heat flow; k is the thermal conductivity of the control volume; A is the area of the control volume surface perpendicular to the heat flow direction; Δx is the distance between the centroids of two neighboring control volumes which have a common control volume surface (heat flow across this surface); and ΔT is the temperature difference between two neighboring control volumes.

The source term, $\overline{S}$ in Equation (19) may depend on the temperature of the control volume. Symbolizing T_p as the representative temperature for the control volume, the source term in the control volume can be expressed linearly with respect to T_p as

$$\overline{S} = S_c + S_p T_p \tag{21}$$

where S_c and S_p are constants. When the source term is not dependent on the temperature, S_p becomes zero. One control volume in the calculation domain except boundaries has four neighboring control volumes which have the common control surfaces of the control volume. Using the representative temperature of these four neighboring control volumes for expressing ΔT in Equation (20), the two-dimensional heat conduction equation [Equation (11)] with steady state and constant thermal conductivity can be reduced to the following discretization equation for all control volumes in the calculation domain except those on the boundary.

$$a_p T_p = \sum a_{nb} T_{nb} + b \tag{22}$$

where, a_p is the coefficient of T_p in the discretization equation of the temperature field which is related to control volume dimension such as Δr and Δx, and S_p; T_{nb} and a_{nb} are the representative temperatures of the neighboring control volumes and their coefficients in the discretization equations for the neighboring control volumes; and b is the constant term related to S_c and control volume dimension.

Equation (22) is applied for the discretization equations of heat conduction at the control volumes around internal grid points in the calculation domain. Now, the discretization equations at the control volumes on the boundaries in the calculation domain are needed to calculate the temperature fields of the whole calculation domain. The boundary condition may be a known surface temperature, known surface heat flux, or convective surface. At the boundary grid points, half control volumes are used, whereas regular control volumes are used at the interior grid points. If the boundary temperatures are given, then we have enough algebraic equations for the unknown temperatures at the interior grid points.

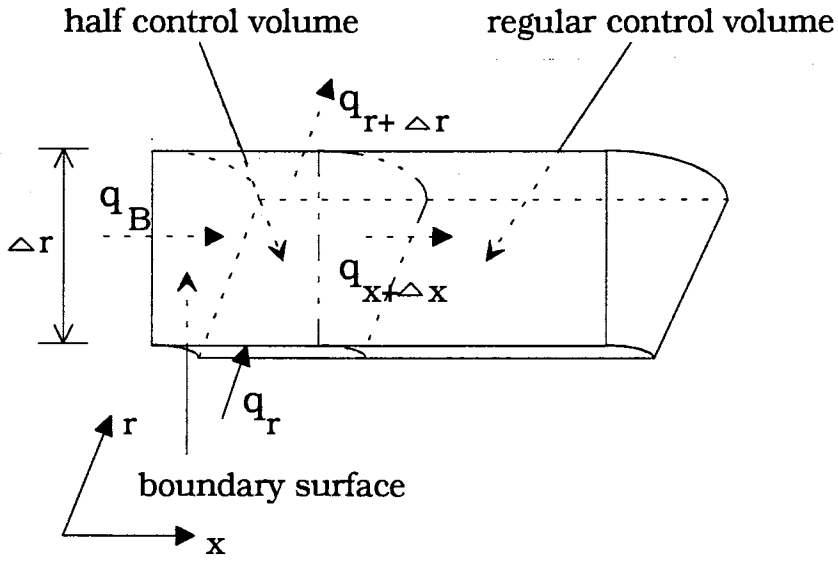

Figure 4.2 Schematic of Half Control Volume on the Left Boundary for Two-Dimensional Heat Conduction in Cylindrical Coordinates (x, r)

When, however, the boundary temperatures are not given, more discretization equations at the control volumes on the boundary should be set using the given boundary conditions. In this study, the boundary conditions are convective surfaces rather than known temperatures. Figure 4.2 shows the half control volume on the left boundary and adjacent regular control volume. Applying an energy balance in the half control volume, we get the following equation.

$$q_B - q_{B+\Delta x} + (S_C + S_p T_B)\Delta V = 0 \tag{23}$$

where, q_B is the heat flow rate across boundary surface of the half control volume; $q_{B+\Delta x}$ is the heat flow rate across the right half control volume surface; and T_B is the boundary temperature (unknown). The source term was expressed as a linear function of T_B in Equation (23). The term, $q_{B+\Delta x}$ can be expressed with boundary temperature and the temperature of the neighboring (regular) control volume using Equation (20). When convective heat transfer boundary is applied, the term, q_B can be expressed by a linear function of the boundary temperature, T_B as

$$q_B = A_B (f_c + f_p T_B) \tag{24}$$

where f_C and f_p are the coefficients in the linear expression and A_B is the area of the boundary surface of the half control volume. For the convective surface boundary conditions, the heat flow rate into the boundary surface of the half control volume, q_B, has the following expression using the average convective heat transfer coefficient, $\bar{h}$, and the surrounding fluid temperature, T_∞.

$$q_B = \bar{h} A_B (T_\infty - T_B) \tag{25}$$

which implies

$$f_c = \bar{h} T_\infty \text{ and } f_p = -\bar{h} \tag{26}$$

Substituting Equations (26) and (24) into (23), the discretization equations of heat transfer for the half control volumes on the convective surface boundary condition can be obtained.

Figure 4.3 shows the computational domain representing a vertical half-section of the system bounded by the axis of the system on the bottom, cylindrical surface of heat sink on top, substrate surface and the inactive domain on the right, and the plane surface of the heat sink on the left. Since the system is symmetric about a plane passing through the axis of the system, only half of the system was considered in order to minimize the computational task. Comparing the schematic of the experimental setup shown in Figure 3.1 to that of the computational domain shown in Figure 4.3, the computational domain is the upper half of the experimental setup rotated clockwise by 90°. The thermal conductivity of the inactive domain in the computational domain was set to zero. Thus, the boundary conditions of the inactive domain do not affect the temperature field of heat sink and substrate. The boundary conditions of the top and left sides of the computational domain were set as the convective surfaces, whereas the bottom boundary condition was set to a known surface heat flux of zero (adiabatic condition). The average heat transfer coefficients at the top and left sides of the computational domain, were calculated by Equations (14) and (15), respectively.

The heat flux, q_c'', from the copper block to the coolant inside the heat sink is expressed by

$$q_c'' = \bar{h}(T_c - T_B) \tag{27}$$

The interface of the copper block and coolant inside the heat sink is enlarged in Figure 4.3. The heat conduction from B to P in this figure, where P is the center of the control volume at the copper block adjacent to the coolant, gives

$$q_C'' = \frac{k_{cu}}{\delta}(T_B - T_p) \tag{28}$$

where δ is the half thickness of the control volume (in the direction of the heat flow into coolant), and k_{cu} is the thermal conductivity of copper. Eliminating T_B between Equations (27) and (28), q_C'' can be expressed in terms of T_C and T_p as follows

$$q_c'' = \left[\frac{1}{\bar{h}} + \frac{\delta}{k_{cu}}\right]^{-1}(T_c - T_p) \tag{29}$$

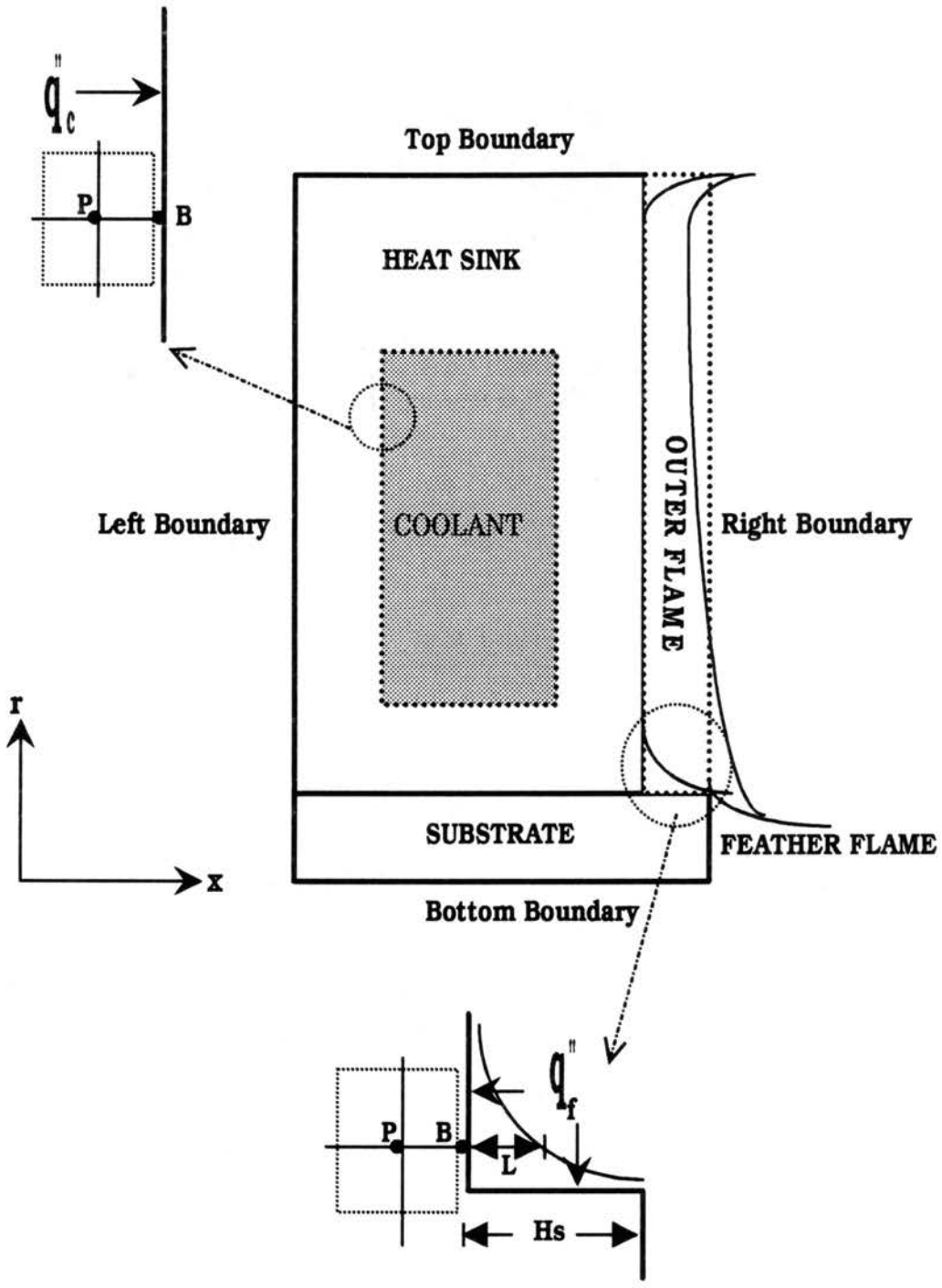

Figure 4.3 Schematic Diagram of Computational Domain

Considering the heat loss to the coolant as a source term in heat conduction equation, an extra heat source due to cooling by coolant can be added to the source term in Equation (11). From Equation (29), the extra source term, when expressed on a unit-control basis, becomes

$$\overline{S}_{extra} = \frac{A}{\Delta V}\left[\frac{1}{\overline{h}} + \frac{\delta}{k_{cu}}\right]^{-1}(T_c - T_p) \tag{30}$$

where A is the area through which heat flows into the coolant and ΔV is the volume of the control volume. Expressing Equation (30) in the form of Equation (21), $S_{c,extra}$ and $S_{p,extra}$ become

$$S_{c,extra} = \frac{A}{\Delta V}\left[\frac{1}{\overline{h}} + \frac{\delta}{k_{cu}}\right]^{-1} T_c \tag{31-a}$$

$$S_{p,extra} = -\frac{A}{\Delta V}\left[\frac{1}{\overline{h}} + \frac{\delta}{k_{cu}}\right]^{-1} \tag{31-b}$$

At the upper surface of the heat sink which is in contact with the combustion flame, the heat transfer from the flame can be treated as an extra heat source in the same manner as in the treatment of cooling by the coolant.

In the region of the threaded area of the substrate and the upper surface of the heat sink which is close to the substrate (the region enlarged in Figure 4.3), the heat transfer from the flame was characterized by conduction and radiation as expressed in Equation (18). This combined heat transfer was treated as an extra heat source in the computational task. From Equations (31), however, the extra source term does not have a linear expression with temperature, such as Equation (21). Patankar (1991) suggested an approximate lineariztion of nonlinear source term as follows

$$\overline{S} = \overline{S}^* + \left[\frac{d\overline{S}}{dT_p}\right]^*(T_p - T_p^*) \tag{32}$$

where T_p is the unknown temperature to be calculated in computational tasks and superscript * is the initial guess or the value obtained from the previous iteration in the

numerical procedure. Comparing this equation to the linear formula of source term as in Equation (21), $S_{c,extra}$ and $S_{p,extra}$ are

$$S_{c,extra} = \overline{S}^* - \left[\frac{d\overline{S}}{dT_p}\right]^* T_p^* \tag{33-a}$$

$$S_{p,extra} = \left[\frac{d\overline{S}}{dT_p}\right]^* \tag{33-b}$$

The heat flux in this case is given by Equation (18). The term $(\partial T_a/\partial x)_{at\ surface}$ in Equation (18) is approximated as $(T_f - T_p)/L$, where L is the distance from the flame to the surface of the control volume where heat is transferred from the flame via conduction and radiation as shown in Figure 4.3. The appropriate radiation equations are developed in Section C.1 of Appendix C. After substitution of Equations (C.9) and (C.10) in Appexdix C into Equation (18), applying the resulting equations to Equations (33-a) and (33-b) results in

for the threaded area of the heat sink

$$S_{c,extra} = \frac{A_p}{\Delta V_p}\varepsilon_p\varepsilon_f\sigma T_f^4[F_{pf} + \sum_i (A_i - \sum_j A_j F_{ji})(1-\varepsilon_i)\frac{F_{pi}}{A_i}] + \frac{A_p}{\Delta V_p}\varepsilon_p \sum_i (\varepsilon_i \sigma T_i^4 F_{pi})$$

$$+ \frac{A_p}{\Delta V_p}\varepsilon_p \sum_j [A_j\varepsilon_j\sigma T_j^4 \sum_i (1-\varepsilon_i)\frac{F_{pi}}{A_i}F_{ji}] + \frac{A_p}{\Delta V_p}(T_f\, k_a/L) + \frac{A_p}{\Delta V_p}(3\varepsilon_p\sigma)(T_p^*)^4 \tag{34-a}$$

$$S_{p,extra} = \frac{A_p}{\Delta V_p}[-3\varepsilon_p\sigma(T_p^*)^3 - k_a/L] \tag{34-b}$$

for the heat sink

$$S_{c,extra} = \frac{A_p}{\Delta V_p}\varepsilon_p\varepsilon_f\sigma T_f^4[F_{pf} + \sum_j (A_j - \sum_i A_i F_{ij})(1-\varepsilon_j)\frac{F_{pj}}{A_j}] + \frac{A_p}{\Delta V_p}\varepsilon_p \sum_j (\varepsilon_j \sigma T_j^4 F_{pj})$$

$$+ \frac{A_p}{\Delta V_p}\varepsilon_p \sum_i [A_i\varepsilon_i\sigma T_i^4 \sum_j (1-\varepsilon_j)\frac{F_{pj}}{A_j}F_{ij}] + \frac{A_p}{\Delta V_p}(T_f\, k_a/L) + \frac{A_p}{\Delta V_p}(3\varepsilon_p\sigma)(T_p^*)^4 \tag{35-a}$$

$$S_{p,extra} = \frac{A_p}{\Delta V_p}[-3\varepsilon_p \sigma (T_p^*)^3 - k_a / L] \qquad (35\text{-b})$$

where A_i, A_j : areas of control surfaces in i (heat sink) and j (substrate) directions, respectively (see Figure C.1 in Appendix C)

F_{pi}, F_{pj} : configuration factors, the fractions of the radiative energy leaving the surface of the considered boundary control volume (p) that arrive at i and j control surfaces, respectively

The development of the numerical heat transfer modeling for the substrate and heat sink has now been given. This modeling can be summarized by the three parts given below.

For the first part, the control-volume approach was used as a numerical scheme to solve the partial differential heat conduction equation given by Equation (11). Equation (22) gives the general form of the discretization equation for all control volumes in the computational domain except those boundaries that are convective surfaces or have known heat fluxes.

The second part of the numerical modeling concerned the treatment of those boundaries having convective surfaces or known heat fluxes. The numerically modeled equations for these portions of the computational domain are given by Equations (23) through (26).

The last part of the numerical modeling concerned the source terms. Recall, that both the heat transfer to the heat sink and threaded area of the substrate by convection, radiation, and conduction from the flame and the heat dissipation into the coolant by forced convection were treated as source terms. These source terms were then numerically modeled by Equations (27) through (35).

To solve the general discretization equation of heat conduction , Equation (22), a computer code called 'CONDUCT' was used in the computer simulations of this study. CONDUCT was developed by Patankar (1991) for the solution of two-dimensional partial differential equations of heat conduction type such as Equation (11). CONDUCT was designed to employ three coordinate systems: cartesian, axisymmetric and polar coordinates. It provides the general calculation scheme using the control-volume approach. For the treatments of convective surface boundary and source terms included in the numerical heat transfer modeling of the system, a computer code called 'SUBTEMP' was developed based on the discussions presented in this section. SUBTEMP provides the problem specifications of the given situations in this study such as the geometry, grid system, material properties, desired output, and the treatments of boundary conditions and source terms. SUBTEMP was designed to communicate with CONDUCT. Separate runnings of SUBTEMP and CONDUCT do not make any sense in the prediction of the temperature field of the system, and are not possible since they are not complete computer codes by themselves. For the computational simulations, SUBTEMP and CONDUCT were linked together during the compilation process. Only the executable file generated by linking SUBTEMP and CONDUCT can be used for the computer simulations. Both SUBTEMP and CONDUCT were written in FORTRAN. The text files of SUBTEMP and CONDUCT are included in Appendix E.

4.3. Procedure for Computer Simulations

The temperature field of the system consisting of the heat sink and substrate including the substrate surface temperatures can be simulated by running the executable file from SUBTEMP and CONDUCT. The boundary conditions and supporting data such as heat transfer coefficient, known boundary temperature, or heat flux should be specified in SUBTEMP before its linking with CONDUCT. The bottom boundary condition can be easily specified as zero heat flux (adiabatic condition) since bottom boundary is an

axisymmetric line (see Figure 4.3). The top and left boundaries are exposed to the ambient air. Thus, they have convective surfaces. The corresponding average heat transfer coefficients at the top and left boundaries can be estimated by Equations (14) and (15), respectively. Equations (14) and (15) require properties of air, such as volumetric thermal expansion coefficient, kinematic viscosity, thermal diffusivity, and boundary and ambient temperatures. For providing accurate input data into the computer code, temperatures at the top and left boundaries were monitored with T-type thermocouples during actual experiments. However, the boundary temperature measurements were not necessary for all the computer simulations, which will be discussed in the next chapter. For the treatment of heat dissipation into the coolant, the average heat transfer coefficient of the coolant is required for the computer simulations. The heat transfer coefficient of the coolant could be estimated using coolant flow rate. A detailed procedure for the estimation of the average heat transfer coefficients at the top and left boundaries, and coolant heat transfer coefficient is described in Section D.1 of Appendix D.

The right boundary (substrate surface) is still left to be specified. It should be one of the three conditions: known heat flux, convective surface, or known temperature. The known heat flux can not be applied for the right boundary condition since the heat flux was not available from the experiments. Also, the convective surface can not applicable at this stage. The substrate surface temperatures could not be obtained from the experiments. Only the substrate temperatures at 0.5 mm below the surface are available from the experiments at this stage. To make the computer simulations possible, an assumption was needed to be made in order to be able to use the substrate surface temperatures measured in the experiments. For this purpose it was assumed that the substrate temperature profiles (shape) at the substrate surface and at 0.5 mm below the surface are similar to each other except in magnitude. This assumption was based on the fact that the heat transfer rate in the radial direction in the 0.5 mm thickness region (from the substrate surface) of the substrate is negligible compared to that in the axial direction.

Considering that the amount of the heat transfer rate to the substrate surface from the combustion flame via convection and radiation is much more than that to the threaded area of the substrate (0.5 mm thickness region) from the flame through the air via radiation and conduction (see Figure 4.3), the assumption for the computer simulations seemed to be reasonable. This assumption will be verified in the next chapter. Using this assumption, the total heat transfer coefficient (h_t) distribution at the substrate was calculated from running the executable file. Then, the calculated h_t distribution was used for the actual computer simulations for the prediction of the temperature field of the system including the substrate surface temperatures. The specific steps to determine the total heat transfer coefficient distribution at the substrate surface were:

1) Run the executable file from SUBTEMP and CONDUCT with the measured substrate temperatures at 0.5 mm below the surface as the temperatures at the substrate surface in the computational domain. At this step, the left boundary (substrate surface) condition was the known temperature. The average total heat transfer coefficient at the upper surface of the heat sink (required for running the executable file) was not known. However, this coefficient could be obtained at this step by updating the initial guess until the resulting heat dissipation rate into the coolant was in agreement with that from the experiments. The resulting temperature field from this step obviously would be lower than the actual temperature field since the temperatures used for the substrate surface were lower than the actual temperatures.
2) Assuming that the substrate temperature profile (shape) at the substrate surface and at 0.5 mm below the surface are similar to each other except in magnitude, adjust the temperatures at the substrate surface obtained from the first step by the temperature differences between substrate surface and 0.5 mm below the surface.
3) Run the executable file again with the adjusted substrate surface temperatures. At the end of this step, the code calculates distribution of total heat transfer

coefficients, h_t, as well as the temperature field of the system. At the end of this step we are ready for the actual simulations.

The reasonability of these three steps will be discussed in the next chapter by comparing the results from the three steps with the experimental results. The average total heat transfer coefficients at the upper surface of the heat sink obtained at the first step were used in the actual computer simulations. The deviations of the heat dissipation rates into the coolant calculated at the first step were less than 2% compared to the results from experiments.

The total heat transfer coefficient (h_t) distribution at the substrate surface is related to the combustion characteristics of the flame. The combustion characteristics (flame shape) are dominated by several parameters such as the nozzle size, flow rates of oxygen and acetylene. The heat release rate per unit volume inside the flame varies in the radial and axial (flame propagation) directions. Thus, h_t distribution at the substrate surface is dependent on the nozzle size, flow rates of oxygen and acetylene, substrate position in the flame. Then, we could reach a conclusion that the change in h_t distribution at the substrate surface is negligible with the variation of the operating parameters in the oxy-acetylene combustion method which do not change the combustion characteristics, such as the coolant flow rate (Q_C) and the substrate-heat sink distance (H_S) as long as the parameters influencing the combustion characteristics are kept constant. Using this idea, the computational code was used to predict the temperature field of the system (substrate and heat sink) for different Q_C and H_S values.

Using the computer simulations, the substrate surface temperatures could be calculated using the measured substrate temperatures at 0.5 mm below the surface. Also, heat flux distribution at the substrate surface can be calculated from the computer simulations. Additionally, the results from the computer simulations can help in studying the effects of Q_C and H_S on the substrate surface temperature.

As to the grid system, a nonuniform grid was used in the computational domain: 22 and 21 control surfaces in the x and r directions, respectively. The maximum allowable grid system in CONDUCT and SUBTEMP is 48 control surfaces in each direction. In selecting the proper numbers of control surfaces in each direction, finer grid points at the substrate was used compared to those at the heat sink since the heat flux at the substrate surface from the flame is large and varies in the radial direction. See the printout of a sample output from the computer simulations listed in Section E.4 of Appendix E for the locations of the grid points. From testing the dependence of resulting temperature field of the system on the grid system, the temperature field of the system resulting from the selected grid system (22 and 21 control surfaces in the x and r directions, respectively) was fairy identical to that resulting from the grid system which has more control surfaces in each direction. The boundary conditions of the computational domain discussed above and several properties used in the computer simulations are listed in Tables 4.1 and 4.2, respectively. The capability of the developed computer codes, SUBTEMP, and CONDUCT by Patankar, for the prediction of the temperature field of the system will be discussed in the next chapter.

Table 4.1 Boundary Conditions in Computational Domain

	Boundary Conditions
Bottom	adiabatic (no heat flux)
Right	1. known surface temperature 2. convective surface
Top	convective surface
Left	convective surface

Table 4.2 Properties Used in Computational Simulations
(Incropera and De Witt, 1990)

	Properties	
Materials	Thermal conductivity (W/mm-K)	Emissivity
Copper (substrate)	0.39	0.5
Molybdenum (heat sink)	0.12	0.8
Hot air around substrate	0.0000821	
Silicon gasket	0.001715	

CHAPTER V

RESULTS AND DISCUSSION

In this chapter, the results from the experiments and computer simulations conducted for this study are presented and discussed. The results and discussion are divided into three sections based on their specific objectives: parametric effects on the substrate temperature profile; effect of substrate temperature on morphology and quality of diamond films; and prediction of substrate temperature profile. Once the results have been presented, guidelines for diamond film synthesis by the oxy-acetylene combustion method are provided in Section 5.4.

5.1. Parametric Effects on the Substrate Temperature Profile

Table 5.1 shows a sample of the temperature readings, obtained by the data acquisition system, from the thirteen thermocouples used in the substrate for a typical oxy-acetylene combustion experiment. For distribution of the thermocouples refer to Figure 3.3. From the tabulated data it is evident that the substrate temperature profile is symmetric about the center of the surface. The four temperature readings obtained at the same radial distance from the center but at different locations are very close to one another and the variations are within the accuracy of the thermocouples used which is ± (1% of the reading temperature + 1°C), see Section D.2 in Appendix D. For this reason only four of the thirteen thermocouples were chosen for reporting the substrate surface temperature distribution under different experimental conditions. The remainder of the thermocouples were used for checking the symmetric nature of the profile. The

temperature profiles presented in this section (see Figures 5.1 to 5.6) are based on the thermocouples at stations 1, 2, 7, and 10, refer to Figure 3.3.

As discussed in Chapter II, the substrate surface temperature distribution is influenced by a variety of factors including the oxygen and acetylene flow rates, substrate position in combustion flame, substrate position on heat sink, coolant flow rate, and nozzle size. The influence of these parameters on the substrate temperature profile is shown in Figures 5.1 to 5.6. The presented experiments were conducted with the centerline of the combustion flame perpendicular to the substrate surface (see Figure 3.1), constant ratio of oxygen to acetylene flow rates (R = 0.98), and constant oxygen and acetylene cylinder pressures (P_{O_2} = 68.9 kPa and $P_{C_2H_2}$ = 34.5 kPa in gauge pressures). Other experimental conditions specific to a particular experimental run are shown on the figures. The heat transfer rate (q_c) labeled on each temperature curve (see Figures 5.1 to 5.6) needs further explanation. The term expresses the heat dissipation rate to the cooling water inside the heat sink. The heat dissipated to the coolant was transferred from the combustion flame through the substrate and heat sink. The heat dissipation rate to the coolant was determined from an enthalpy balance on the cooling water as expressed by Equation (16). The accuracy of q_c calculated by Equation (16) was about ±1% (refer to Section D.2 of Appendix D).

Table 5.1 Sample Thermocouple Temperature Data

DISTANCE FROM CENTER, mm	THERMOCOUPLE STATION NO.	TEMPERATURE (°C) FOR EACH STATION
0.0	1	560.3
2.0	2, 3, 4, 5	542.5, 541.5, 543.3, 543.7
3.0	6, 7, 8, 9	537.2, 538.7, 539.0, 538.3
4.0	10, 11, 12, 13	524.4, 524.3, 523.1, 524.6

The effect of oxygen and acetylene flow rates (Q_{O_2} and $Q_{C_2H_2}$) on the substrate surface temperature distribution for three different gas flow rates is shown in Figure 5.1. An increase in the gas flow rate increases the length of the inner cone (L_i), and results in a higher rate of heat transfer from the flame to the substrate surface. This high rate of heat transfer to the substrate surface causes an increase in the substrate temperature distribution and is supported by the increase in the heat dissipation rate to the coolant (q_c) as indicated on Figure 5.1. From the results shown, a fifty percent increase in the gas flow rates is accompanied by roughly a 120 °C increase in the substrate surface temperature. However, the resulting temperature profiles are all fairly similar in shape. In these experiments the substrate height (H_S) and the distance between the substrate surface and the inner cone (L_S) were fixed. However, the distance between the surface of the substrate and the tip of the nozzle (L_n) had to vary due to variation in L_i.

Figure 5.2 shows the influence of substrate-inner cone distance (L_S) on the substrate temperature profile for four different cases. The resulting temperature profiles are very similar in shape. However, the magnitude of the temperature decreases with an increase in the substrate-inner cone distance. That is, the smaller the distance from the inner cone in the combustion flame, the higher the surface temperatures. These higher substrate surface temperatures are believed to be due to the higher heat release rate per unit volume in the feather flame zone as it is closer to the inner cone (see Figure 3.1). The feather zone temperature is a function of both the radial direction and the flame propagation direction. As the substrate is moved away from the inner cone, the substrate surface temperature decreases. However, from the presented results it appears that there is a limit to this decrease of substrate surface temperature. The temperature drop from L_S = 6 to 10 mm is very small, indicating that for the conditions of Figure 5.2 any further increase in L_S would not change the temperature levels significantly.

Another interesting aspect of results presented in Figure 5.2 has to do with the values of heat dissipation rate to the coolant (q_c). These values behave opposite of what

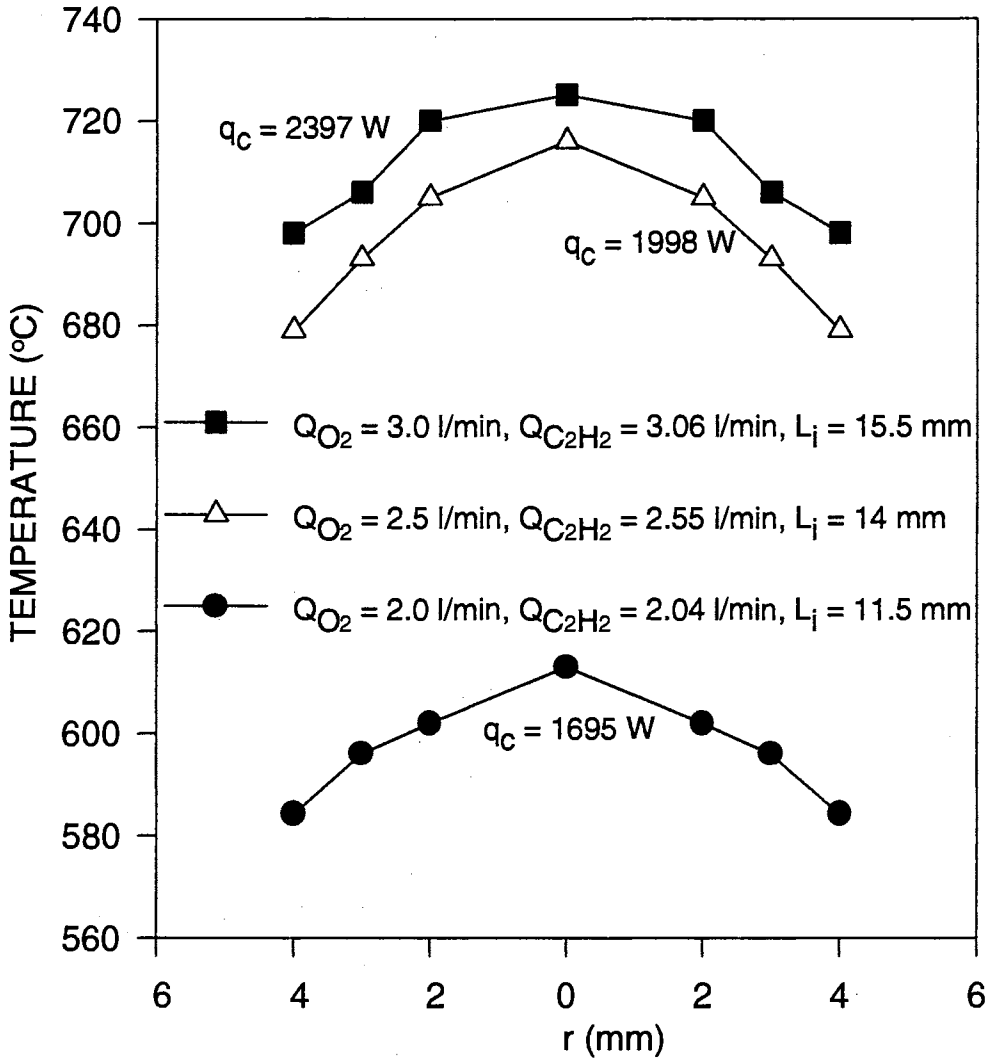

Figure 5.1 Effect of O_2 and C_2H_2 Flow Rates on the Substrate Temperature Profile: D_n = 0.939 mm, H_s = 7 mm, L_s = 4 mm, Q_c = 1.33 l/min

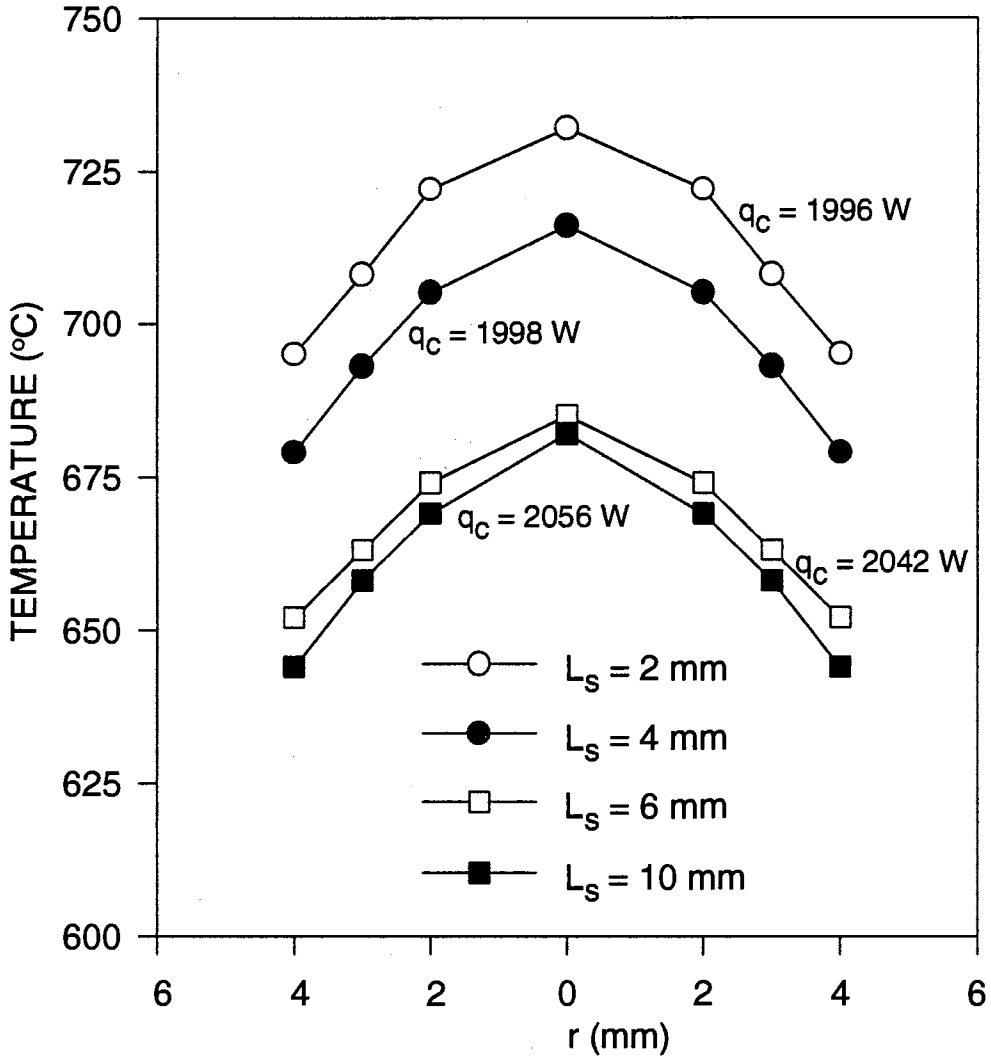

Figure 5.2 Effect of Substrate-Inner Cone Distance on the Substrate Temperature Profile: D_n = 0.939 mm, H_S = 7 mm, L_i = 14 mm, Q_C = 1.33 l/min, Q_{O_2} = 2.5 l/min, $Q_{C_2H_2}$ = 2.55 l/min

was reported for the results of Figure 5.1. In this case, the coolant heat transfer rates increase with decreasing substrate surface temperature. This is due to steep temperature gradients in the radial direction which gives rise to heat transfer by conduction in the radial direction. This large radial conduction causes an increase in the rate of heat transfer by convection from the heat sink (copper block) to the surroundings. Therefore, for small substrate-inner cone distances, there is less transfer of energy between the substrate and the cooling water.

The effect of substrate-heat sink distance (H_S) on the substrate temperature distribution is shown in Figure 5.3 for three different cases. An increase in the distance between the substrate and the heat sink results in an increase in the substrate surface temperature. This increase in temperature is due to less heat conduction through the heat sink (copper block) because of reduced contact area between the substrate and the heat sink. The shape of the temperature profiles shown in Figure 5.3 are generally similar. However, the comparison of the two close temperature profiles at H_S = 7 and 9 mm shows considerably less radial temperature gradient for the case with H_S = 9 mm. This flatness of the temperature profile is due to additional heat transfer to the exposed threaded surface area of the substrate rod by radiation and conduction from the surroundings. As the distance H_S decreases, the temperature gradient in the radial direction should increase.

Figure 5.4 shows the influence of coolant flow rate (Q_C) on the substrate temperature profile for four different cases. As shown, higher coolant flow rates produce lower substrate surface temperatures. The temperature profiles presented in the figure show an increase in the radial temperature gradient with an increase in the coolant flow rate. Variations of the coolant flow rate and the substrate-heat sink distance do not cause any change in the combustion characteristics of the flame. However, the substrate surface temperature profile is influenced by these parameters as shown in Figures 5.3 and 5.4. Comparing these two figures, the variations in the substrate-heat sink distance have more

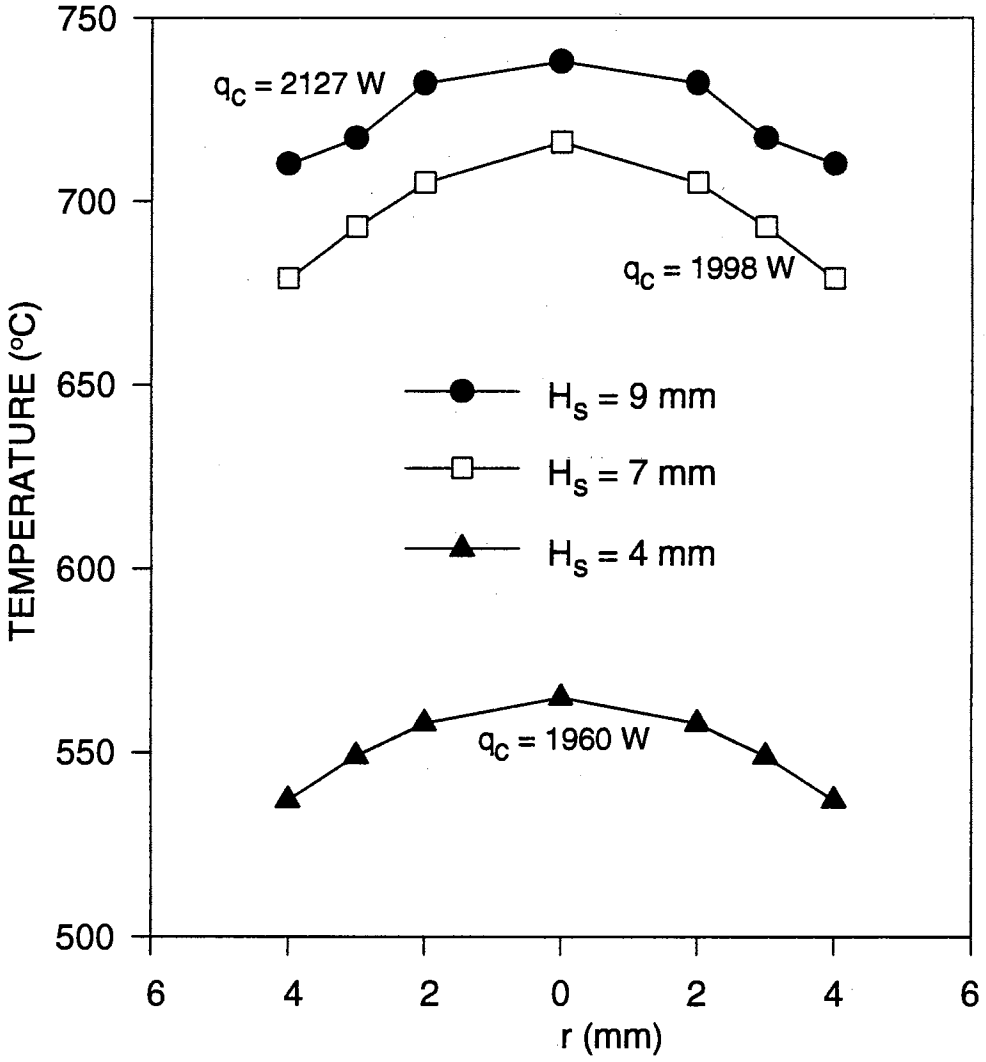

Figure 5.3 Effect of Substrate-Heat Sink Distance on the Substrate Temperature Profile: D_n = 0.939 mm, L_s = 4 mm, L_n = 18 mm, Q_c = 1.33 l/min, Q_{O_2} = 2.5 l/min, $Q_{C_2H_2}$ = 2.55 l/min

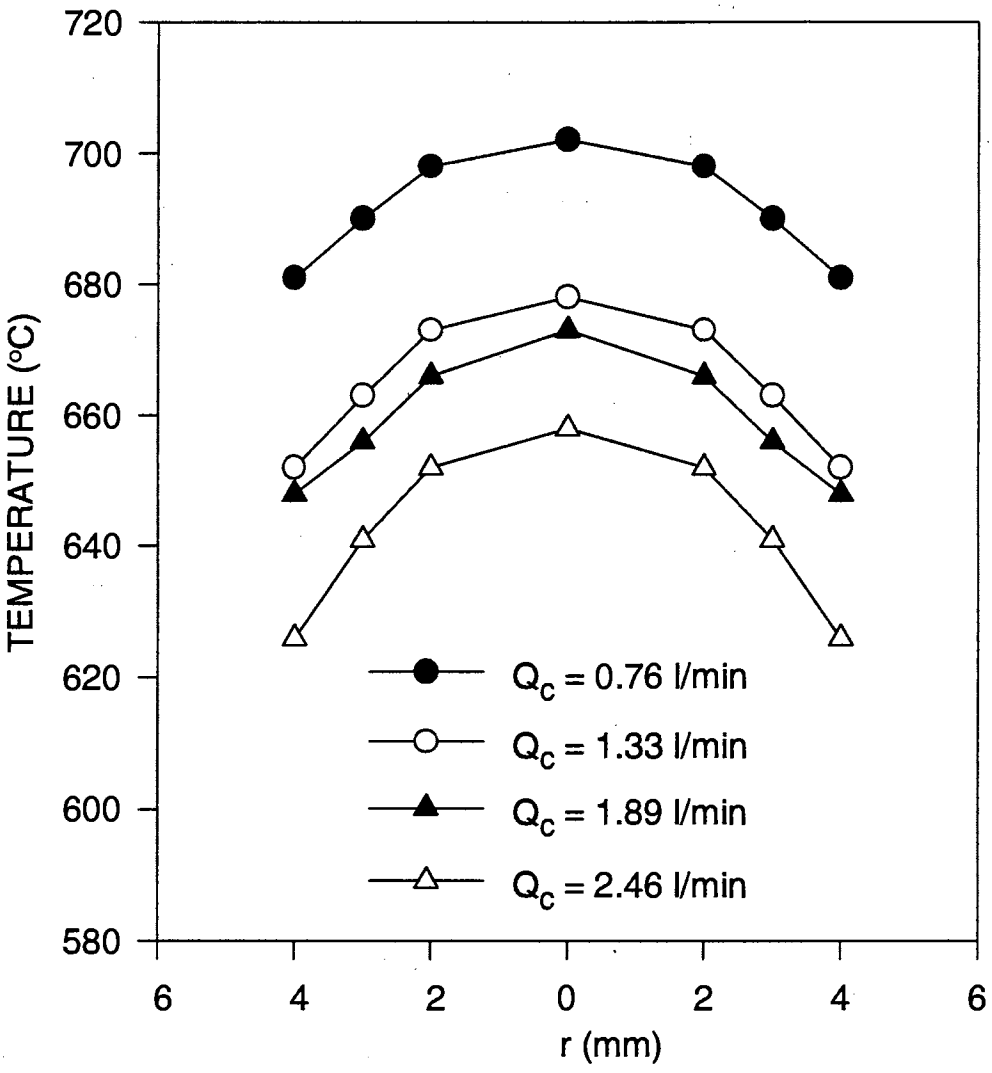

Figure 5.4 Effect of Coolant Flow Rate on the Substrate Temperature Profile: D_n = 1.067 mm, H_S = 7 mm, L_S = 4 mm, L_n = 17 mm, Q_{O_2} = 2.5 l/min, $Q_{C_2H_2}$ = 2.55 l/min

influence on the substrate surface temperature profile than the variations in the coolant flow rate.

The effect of nozzle diameter (D_n) on the substrate temperature distribution for three different nozzle diameters is shown in Figure 5.5. An increase in the nozzle diameter is accompanied by a decrease in the length of the inner cone (L_i) and a widening of the feather zone. Thus, for a small diameter nozzle the heat flux distribution from the flame is more concentrated on the center region of the substrate surface, causing higher substrate surface temperatures. For the largest nozzle diameter used in these experiments, the resulting substrate temperature is fairly uniform. This is due to wide and relatively uniform distribution of flame heat flux over the entire substrate surface.

The results presented in Figures 5.1 to 5.5 clearly show that changes in the rates of heat transfer from the substrate and the heat sink caused by variations in several parameters, influence the shape and the magnitude of the substrate surface temperature distribution. The produced synthetic diamond crystals (films) by the oxy-acetylene combustion method should have uniform morphology in the radial direction. For this purpose, a relatively uniform temperature distribution across the substrate surface is desirable. That is, the radial temperature gradient across the substrate should be minimized. Another requirement for successful application of this method is the magnitude of substrate surface temperature. For well faceted diamond films, substrate surface temperatures greater than 500 °C are required (Hirose and Amanuma, 1990). Figure 5.6 shows that by appropriate combination of the parameters which influence the substrate surface temperature distribution, the desired conditions for producing good quality diamond films with uniform morphology (i.e., uniform substrate temperature profile at temperatures greater than 500 °C) can be developed. The second temperature profile in Figure 5.6 shows that only one of the conditions for successful application of diamond synthesis was met. In this case, the temperature levels are high enough to produce transparent diamond films according to Hirose and Amanuma. However, the

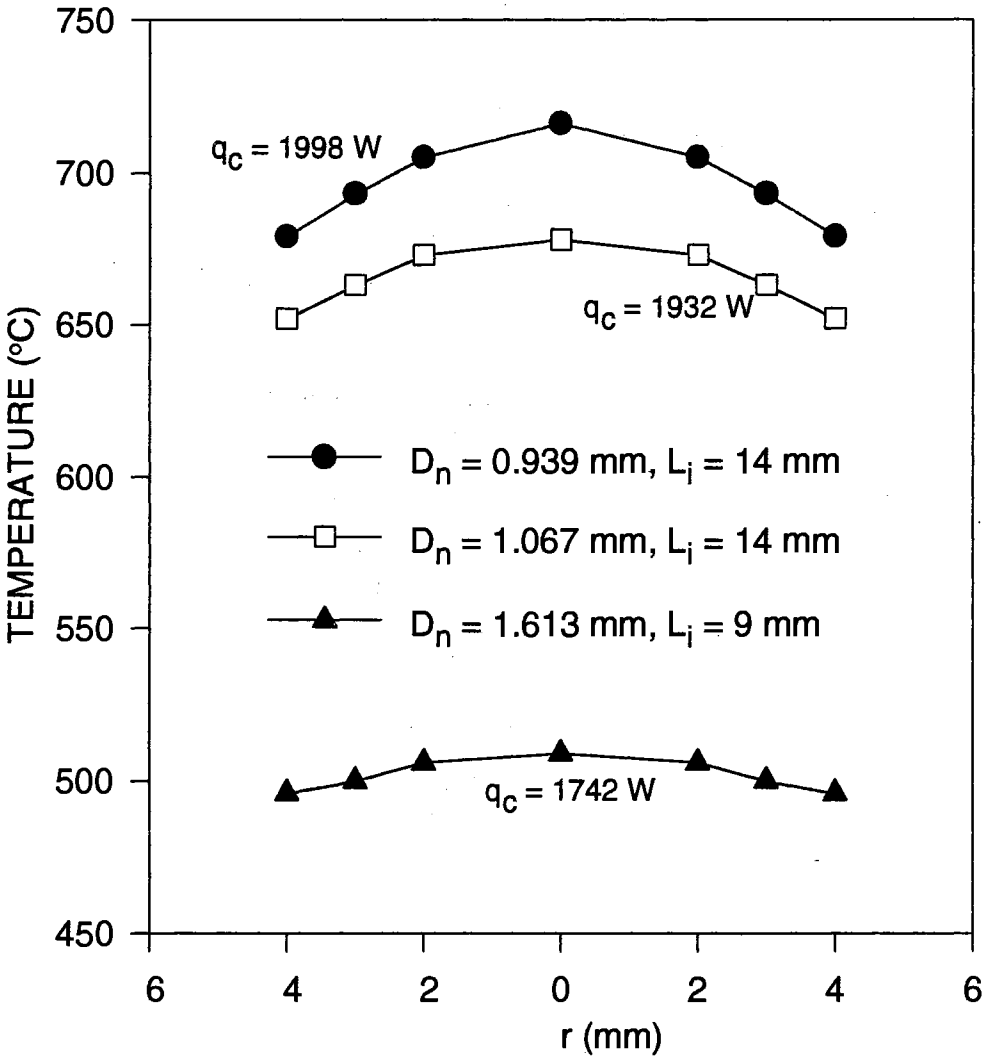

Figure 5.5 Effect of Nozzle Diameter on the Substrate Temperature Profile: H_S = 7 mm, L_S = 4 mm, Q_C = 1.33 l/min, Q_{O_2} = 2.5 l/min, $Q_{C_2H_2}$ = 2.55 l/min

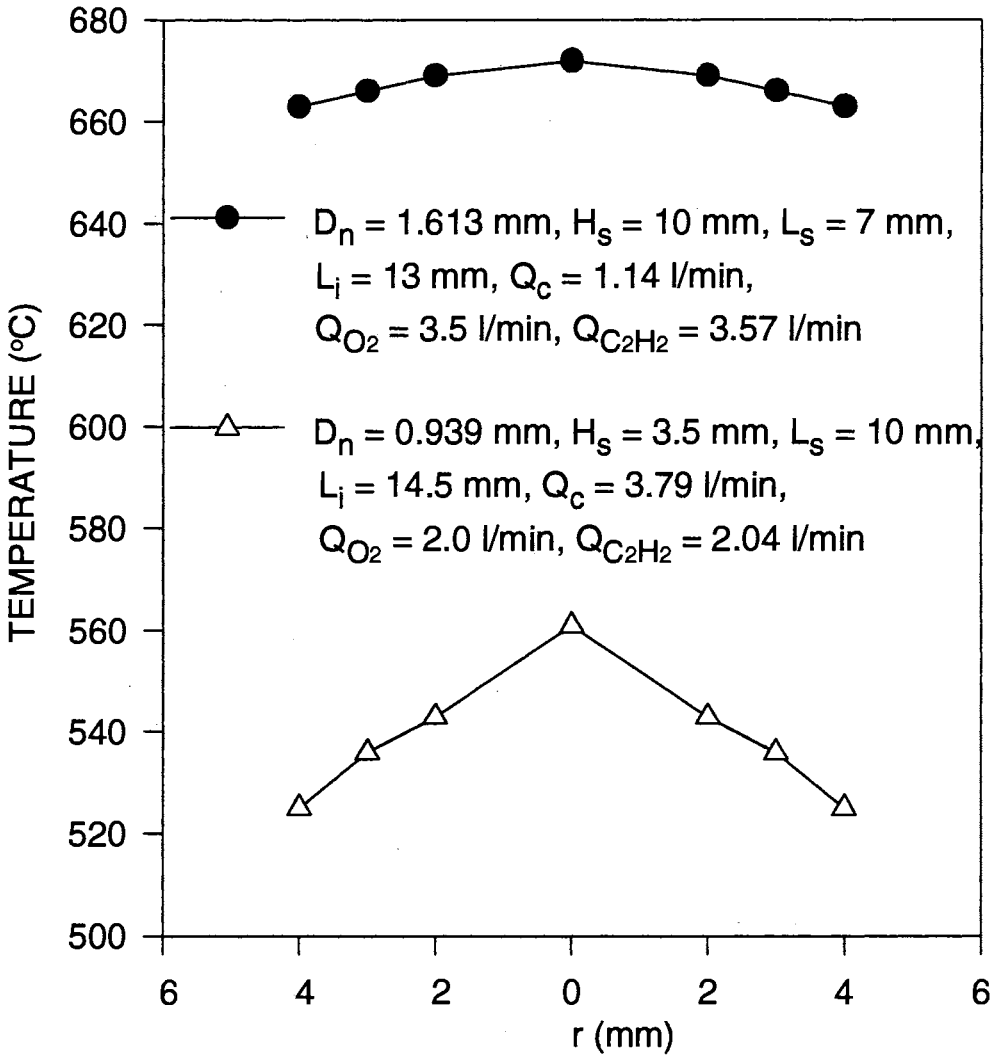

Figure 5.6 Effect of Several Parameters on the Substrate Temperature Profile

substrate surface temperature distribution is not uniform. Therefore, due to large radial temperature gradients, the morphology of the diamond film would not be uniform in the radial direction. This emphasizes the importance of the knowledge of radial distribution of the substrate surface temperature for correct application of this method.

5.2 Effect of Substrate Temperature on Morphology and Quality of Diamond Films

A characteristic of the diamond films synthesized by CVD methods is that it has a well-defined crystal habit, which depend on the experimental conditions. Matsumoto and Matsui (1983) have observed that the morphology of CVD diamond crystals is dominated by cubic and octahedral habits. Figure 5.7 shows the typical crystal structures of diamond films produced by the oxy-acetylene combustion method. All of the diamond crystal structures shown in this figure were found through the experiments conducted in this study.

Results of five selected experiments will be presented here. They are referred to as EXP1 through EXP5. EXP1 and EXP2 used a larger nozzle (D_n = 1.067 mm), while the others used a smaller nozzle (D_n = 0.939 mm). The experiments were conducted with the centerline of the combustion flame perpendicular to the substrate surface, and constant oxygen and acetylene cylinder (gauge) pressures of 137.9 and 68.9 kPa, respectively. The ratio of oxygen to acetylene flow rates, R, was fixed at 0.98, but oxygen flow rate, Q_{O_2}, varied from 2.5 to 3.13 l/min. The inner cone-substrate distance, L_S, was kept at 4 mm throughout the experiments. The coolant flow rate, Q_C, was varied from 0.76 to 2.46 l/min, and the heat sink-substrate distance, H_S, was varied from 2 to 7 mm. The specific experimental conditions used for the five experiments are tabulated in Table 5.2 (for description of the parameters listed refer to the nomenclature section). Before placing the substrate into the O_2-C_2H_2 combustion flame for the deposition of diamond film, the substrate surface was scratched with six-micrometer diamond paste and cleaned by methanol. Scratching the substrate surface with diamond is found to facilitate the

Ball-Like Structure

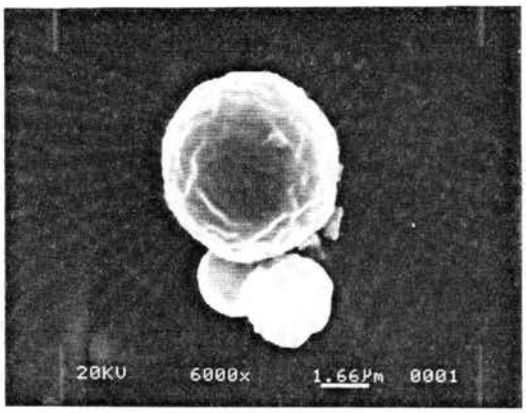

Cauliflower Structure

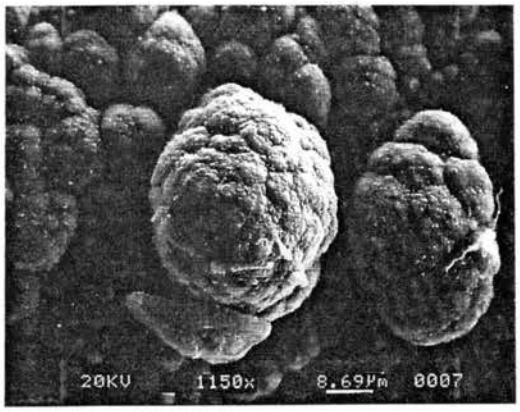

Octahederal Structure

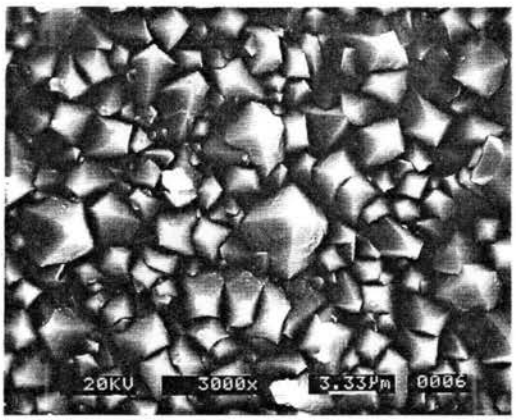

Cubo-Octahederal Structure

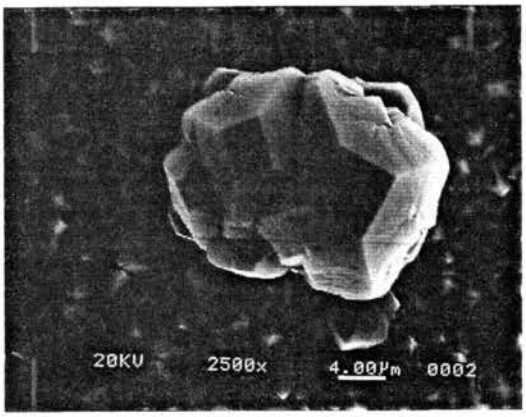

Cubic Structure

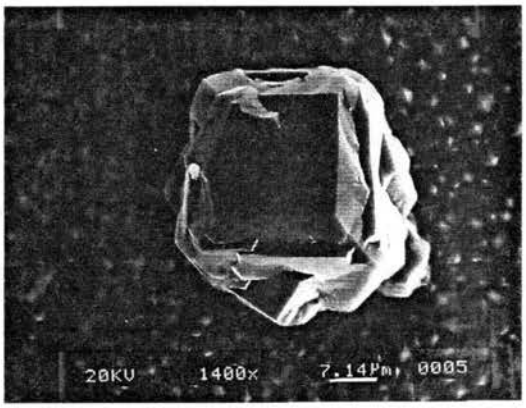

Figure 5.7 Typical Diamond Crystal Structures Produced by the Oxy-Acetylene Combustion Method

diamond nucleation. The scratching for each experiment was repeated the same way to ensure nearly the same initial substrate surface condition. In Figures 5.8 to 5.15, along with the substrate surface temperature profiles, a number of scanning electron micrographs of the diamond films are presented. In the micrographs, two different magnifications of 700 and 7000 times were used.

To ensure reproducibility of the results, the initial conditions of the experiments were carefully controlled and each experiment was repeated two or three times. The results of these runs compared very well. It is interesting to note that during the reproducibility runs it was discovered that when the amount of oxygen or acetylene in the cylinder was low, the combustion flame became unstable due to flow fluctuation and the results were not reproducible. Unstable flames cause a continuous change in the chemical reactions associated with growth and etching processes. However, as mentioned before, the results reported in this study were reproducible and were obtained with stable combustion flames.

Table 5.2 Experimental Conditions for Diamond Synthesis

Experiments	D_n (mm)	Q_{O_2} (l/min)	$Q_{C_2H_2}$ (l/min)	H_S (mm)	L_n (mm)	Q_C (l/min)	t_d (min)
EXP1	1.067	2.5	2.55	7	17	0.76	110
EXP2	1.067	2.5	2.55	7	17	2.46	110
EXP3	0.939	3.0	3.06	7	16	1.13	60
EXP4	0.939	3.0	3.06	2	16	1.13	60
EXP5	0.939	3.13	3.19	7	15	1.13	50

EXP1: Figure 5.8 shows the morphology and substrate temperature distribution in the radial direction. It should be noted that due to the experimental limitations the substrate temperature profile was measured up to a radius of 4 mm from the center of the substrate (see Figure 3.3). As shown in the figure, there is a cauliflower crystal structure at the center of the produced diamond film ($T_S \approx 781$ °C). At this region

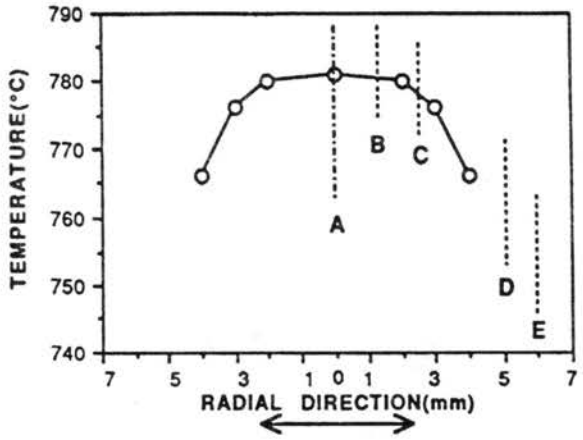

A: r = 0 mm, T_S = 781 °C

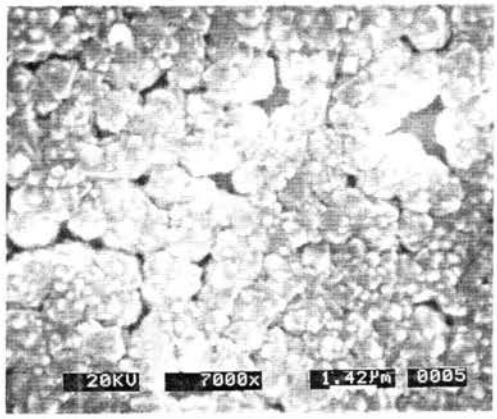

B: r = 1.3 mm, T_S = 780 °C

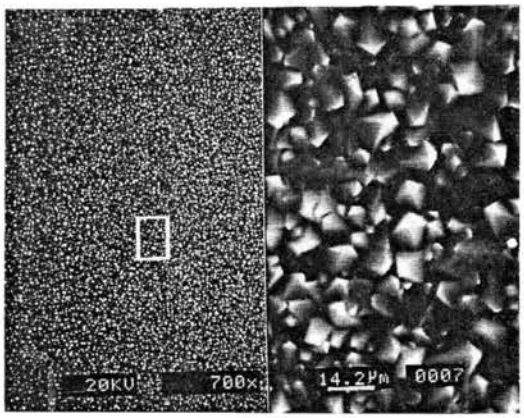

C: r = 3.5 mm, T_S = 771 °C

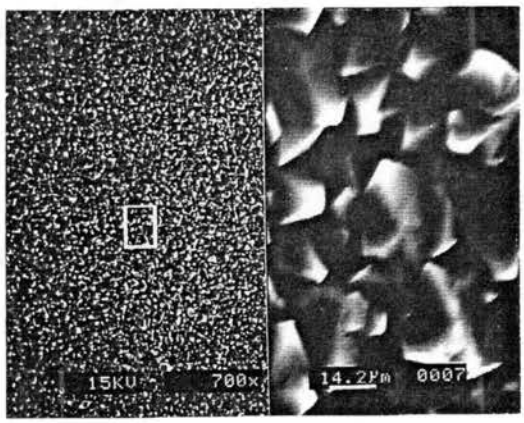

D: r = 5 mm

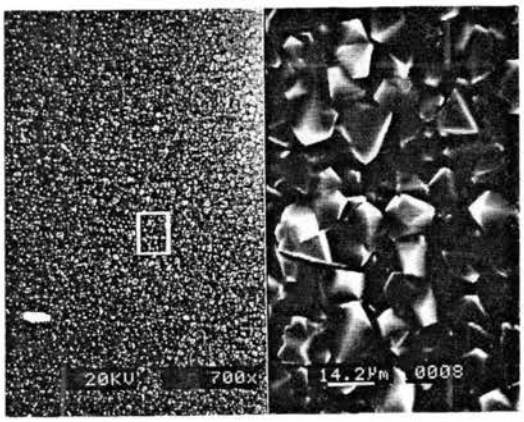

E: r = 6 mm

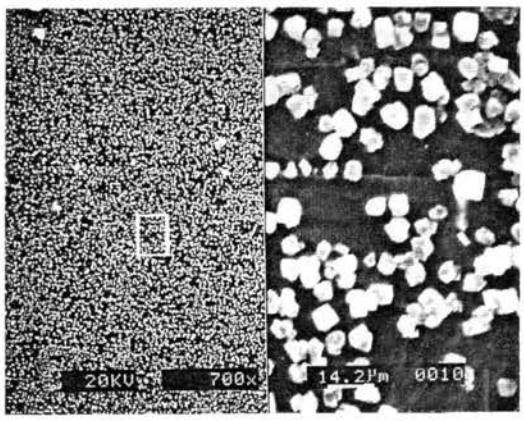

Figure 5.8 Substrate Temperature Profile and Optical Observation of the Film for EXP1

there are also some small areas where crystals have not grown. At r = 1.3 mm ($T_S \approx 780$ ° C), an octahedral crystal structure is observed. At that radius, the length of a side of square base, L_b, is less than approximately 0.8 μm. The film has this type of morphology for a radius up to 5 mm, except at the center. Also, the sizes of the octahedral crystals are different in the radial direction. L_b varies up to 1.4 μm at r = 3.5 mm ($T_S \approx 771$ °C), and varies up to 1.0 μm at r = 5 mm. Examining the micrographs at each radius, the grain size seen at r = 3.5 mm is relatively uniform compared to others.

For a radius greater than 5 mm, the micrograph in Figure 5.8 shows empty areas, which means the nucleation density is very low in this region. This is more pronounced at the edge of the film (r = 6 mm). The diameter of this film was approximately 12 mm.

In summary, an octahedral crystal structure is the dominant morphology with larger grains at r = 3.5 mm and smaller grains at the center and edge. Empty areas (low nucleation density) become prominent at the edge of the film, which is common through all the experiments conducted in this study.

EXP2: The conditions of this experiment were identical to EXP1, except that the coolant flow rate was increased from 0.76 l/min to 2.46 l/min. The resulting temperature levels for EXP2 are lower than those of EXP1.

From the micrographs in Figure 5.9, the produced film has a ball-like crystal structure at the center ($T_S \approx 744$ °C) with very low nucleation density. A cauliflower crystal structure is seen at r = 1 mm ($T_S \approx 743$°C) while the dominant morphology at r > 1 mm is an octahedral crystal structure. The nucleation density is low at r > 4 mm ($T_S \approx$ 718 °C at r = 4 mm). The diameter of this film was 9.5 mm which is smaller than the resulting film from EXP1.

A comparison of results for EXP1 and EXP2 is shown in Figure 5.10. The temperature profile for EXP2 has a higher temperature gradient at the edge due to higher coolant flow rate. Thus, more heat dissipation occurs in the radial direction to the heat

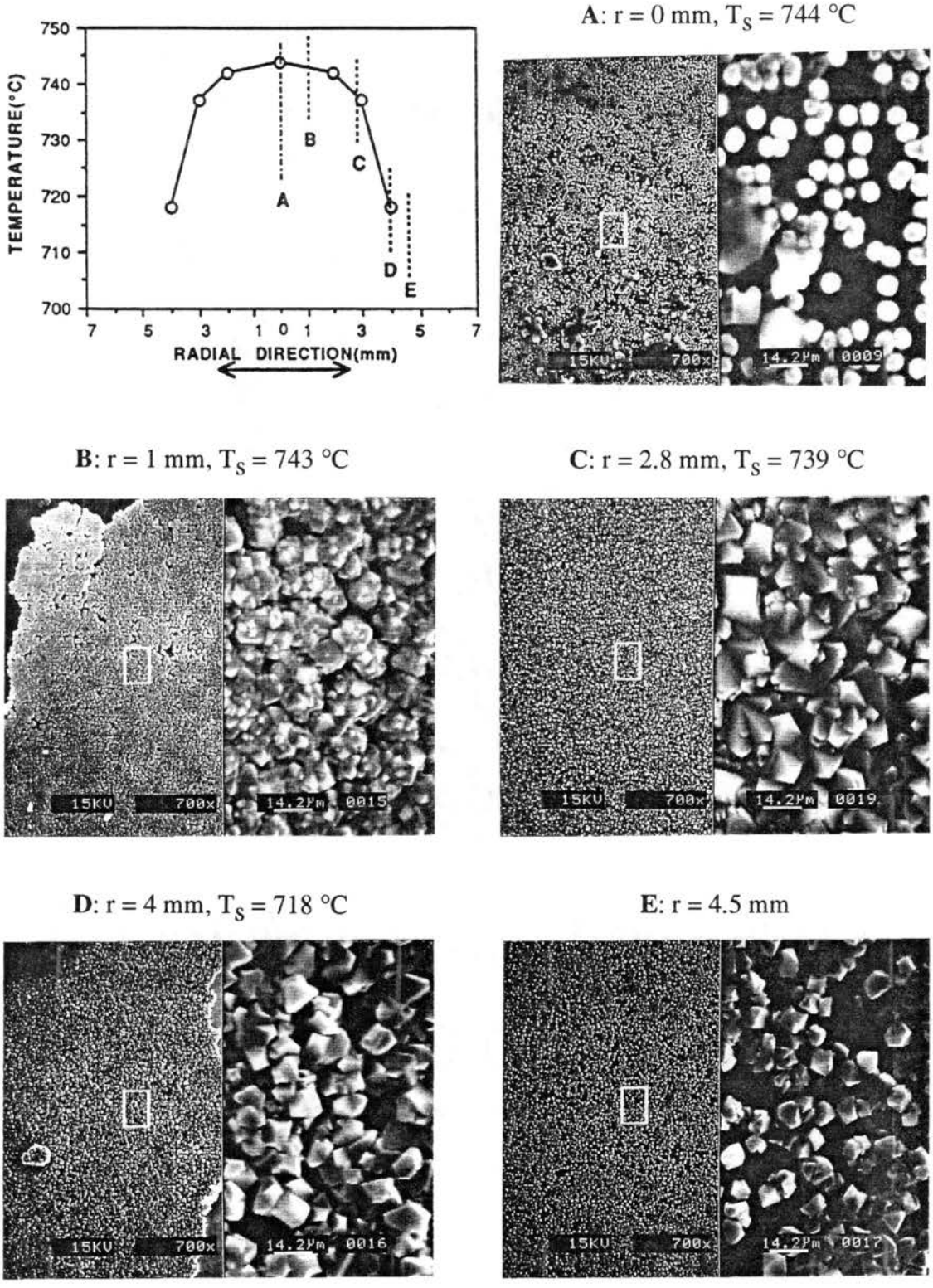

Figure 5.9 Substrate Temperature Profile and Optical Observation of the Film for EXP2

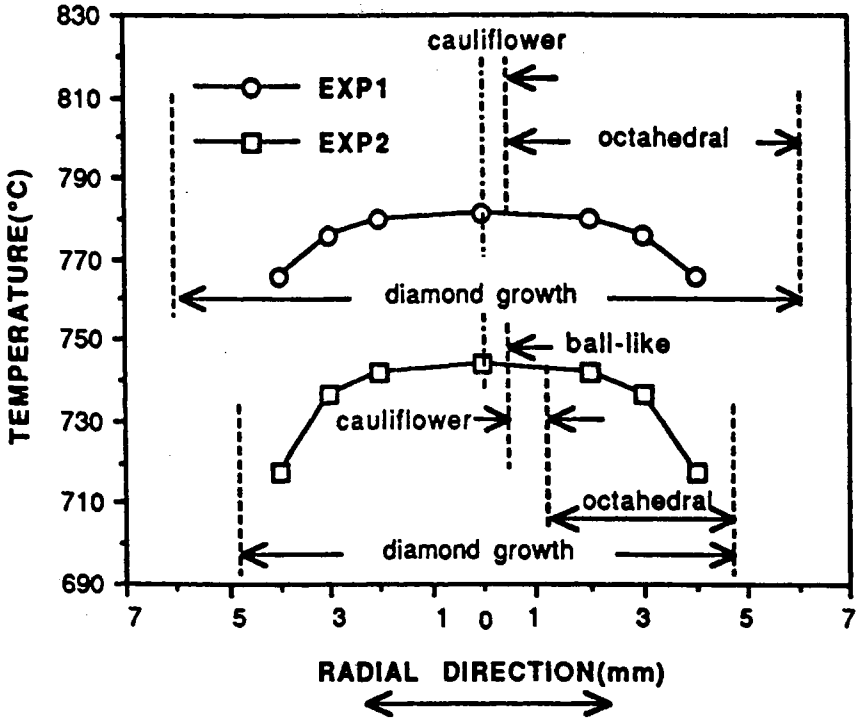

Figure 5.10 Comparison of Substrate Temperature Profiles and Film Morphologies for EXP1 and EXP2

sink, resulting in lower temperatures for EXP2. These lower temperatures in the radial direction cause a smaller diameter of diamond film, D_f, to be produced. The value of D_f for EXP2 is 2.5 mm smaller than D_f for EXP1. Experimentation at a fixed value of R = 0.98 showed that below about 680 °C diamond crystals cannot be produced. The temperature levels for EXP2 drop below the lower temperature limit at approximately r > 4.8 mm. Thus, the diameter of the diamond film was limited to 9.5 mm.

The manner in which the morphology is distributed is also affected by the temperature profile. The dominant morphology is an octahedral crystal structure. However, a cauliflower crystal structure was found at the center for EXP1, while a ball-like crystal structure with low nucleation density was seen at the center for EXP2.

EXP3: The results of this experiment are shown in Figure 5.11. The nozzle diameter is 0.939 mm which is smaller than what was used for EXP1 and EXP2. Also, the temperature levels are much higher than EXP1 and EXP2.

Two different groups of grain sizes are present at the center ($T_S \approx 938$ °C). The group of small grains have an octahedral structure and the group of large grains consist of multifold twinned crystallites with octahedral and cubo-octahedral structures as shown in Figure 5.11. The portion of small grains decreases in the radial direction from the center. Large size grains are dominant at r > 1.5 mm ($T_S \approx 923$ °C at r = 1.5 mm, $T_S \approx 899$ °C at r = 4 mm). In this region, the large grains have the same crystallite structure as described at the center. At each radius, the nucleation density is uniform and high. The distribution of grain size is smaller at the center and the edge, while larger in the region in between. The largest grain size is seen at r = 2 mm. The diameter of diamond film, D_f, was 9.0 mm. The reason diamond film is not produced over the entire substrate diameter (12 mm) is due to the smaller nozzle diameter. A smaller D_n causes a smaller acetylene feather diameter which reduces the diamond deposition area.

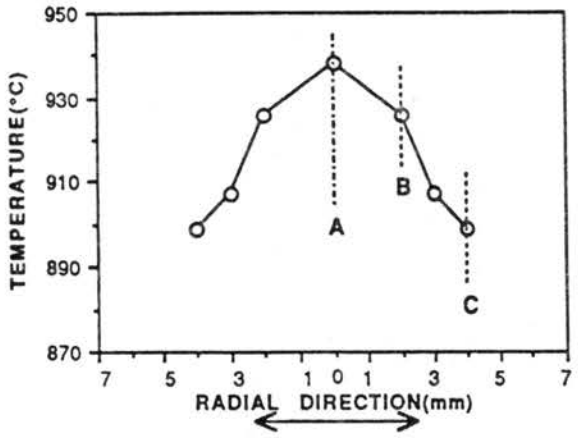

A: r = 0 mm, T_S = 938 °C

Side View at A

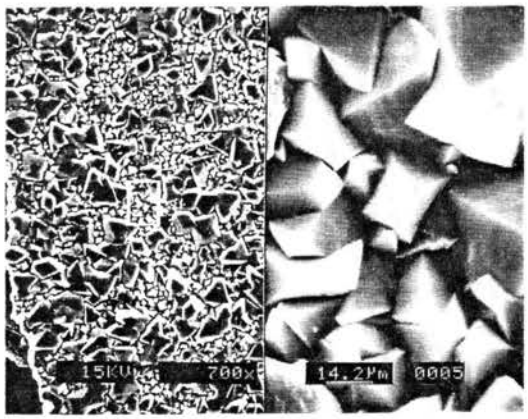

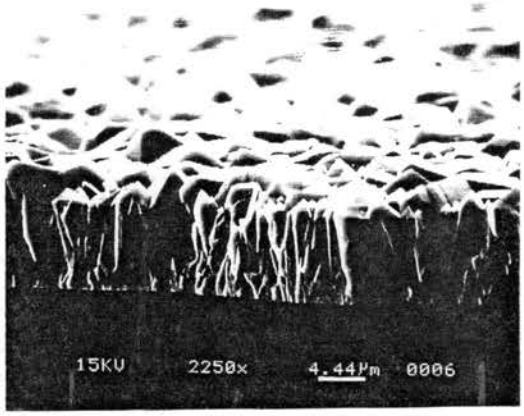

B: r = 2 mm, T_S = 926 °C

C: r = 4 mm, T_S = 899 °C

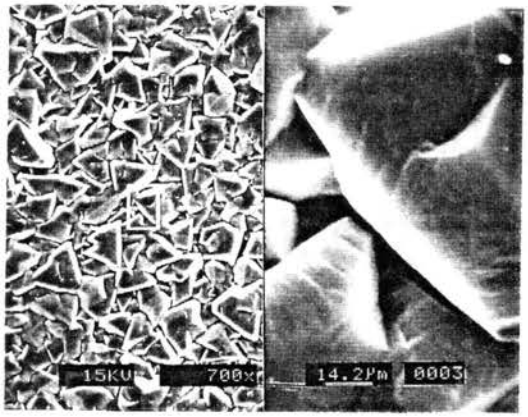

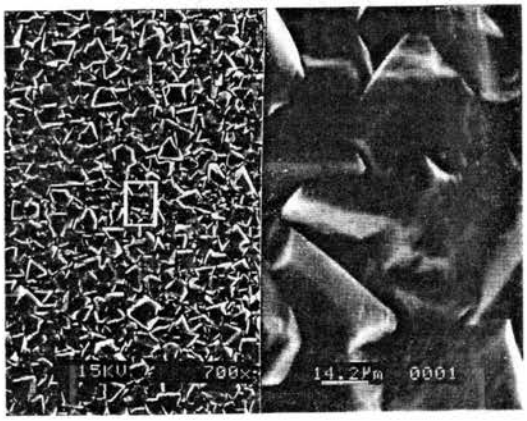

Figure 5.11 Substrate Temperature Profile and Optical Observation of the Film for EXP3

EXP4: The conditions in this experiment are the same as in EXP3, except the distance from the top of the substrate to the heat sink, H_S, is decreased from 7 mm to 2 mm. The resulting temperature profile ($T_S \approx 722$ °C at the center, $T_S \approx 676$ °C at r = 4 mm) and morphology are shown in Figure 5.12. The morphology is similar to what is seen in Figure 5.11 for EXP3 (a single octahedral structure and multifold twinned crystallites with octahedral structure and a small presence of cubo-octahedral structure).

The largest grain size is seen at r = 2 mm ($T_S \approx 719$ °C). The distribution of grain size is also similar to EXP3, smaller at the center and edge and larger in the region in between. The diameter of the produced diamond film, D_f, was approximately 7.5 mm.

A comparison of the results for EXP3 and EXP4 is shown in Figure 5.13. Lowering the value of H_S from 7 mm to 2 mm has an extreme effect on the temperature profile for EXP4. The difference in temperature at each radius is about 220 °C. As was the case for EXP2, as the temperature is lowered the diameter of the diamond film decreases. If the temperature drops below the lower limit of 680 °C, no film will be produced. As seen in Figure 5.13, the temperature profile for EXP4 drops below 680 °C at the same radius where diamond crystal is no longer seen. The morphology for EXP4 is similar to EXP3, except that there is more of a presence of the cubo-octahedral crystals in EXP3. The dominant morphology in EXP4 is an octahedral structure. Also, the grain size in EXP3 is larger than the grain size in EXP4. The value of L_b ranges up to 10 μm for EXP3 and up to 4 μm for EXP4.

EXP5: The same conditions exist for EXP5 as for EXP3, except that the gas flow rates (Q_{O_2} and $Q_{C_2H_2}$) were increased. The gas flow ratio was kept the same as for all the previous experiments (R = 0.98). The temperature profile ($T_S \approx 1059$ °C at the center, $T_S \approx 1023$°C at r = 4 mm) and morphology are shown in Figure 5.14.

Well developed cubo-octahedral structure and multifold twinned crystallite with octahedral and cubo-octahedral structures are found at each radius, except at the center

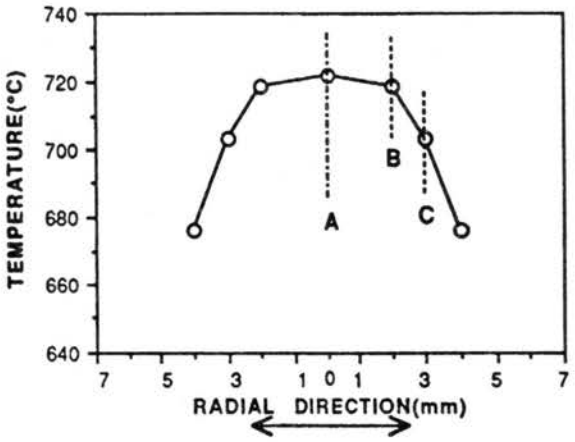

A and **C**: r = 0 mm, T_S = 720 °C (**A**)
r = 0 mm, T_S = 703 °C (**C**)

B: r = 2 mm, T_S = 713 °C

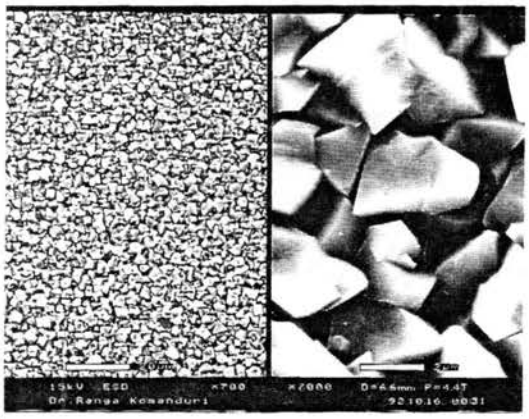

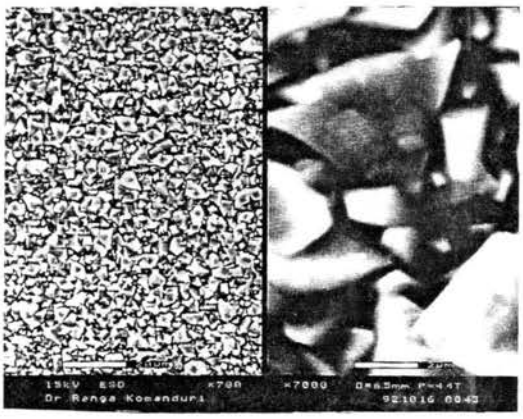

Figure 5.12 Substrate Temperature Profile and Optical Observation of the Film for EXP4

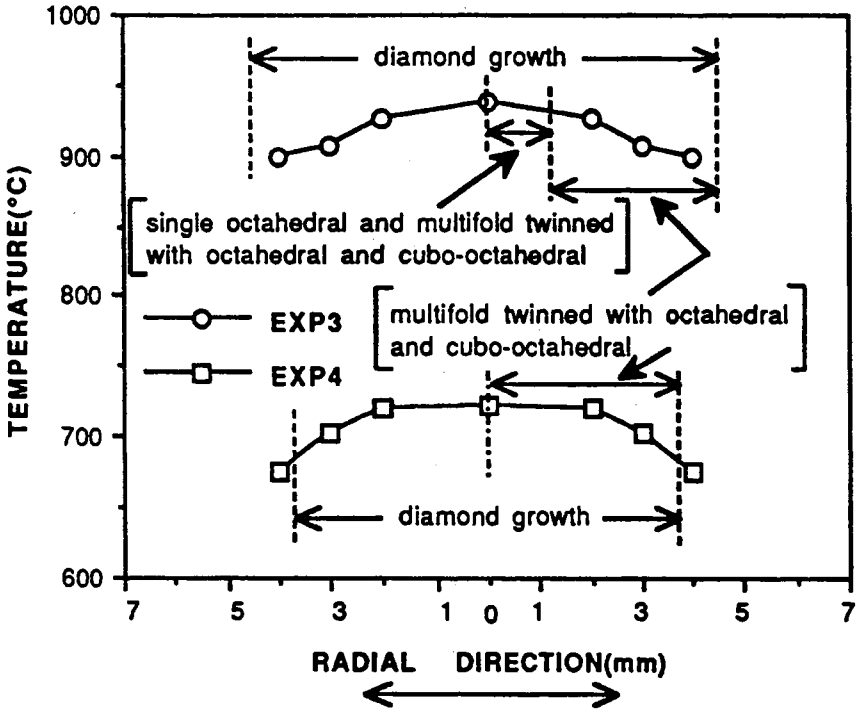

Figure 5.13 Comparison of Substrate Temperature Profiles and Film Morphologies for EXP3 and EXP4

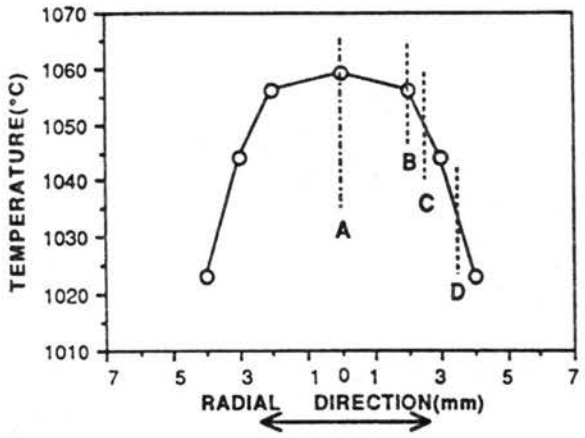

A: r = 0 mm, T_S = 1059 °C

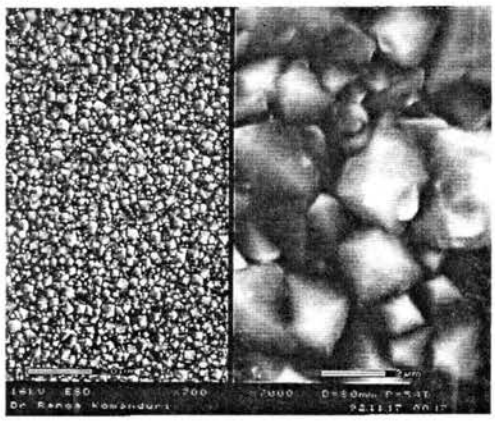

B: r = 2 mm, T_S = 1056 °C

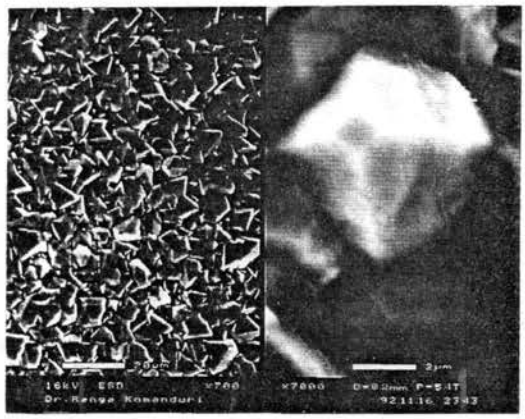

C: r = 2.5 mm, T_S = 1050 °C

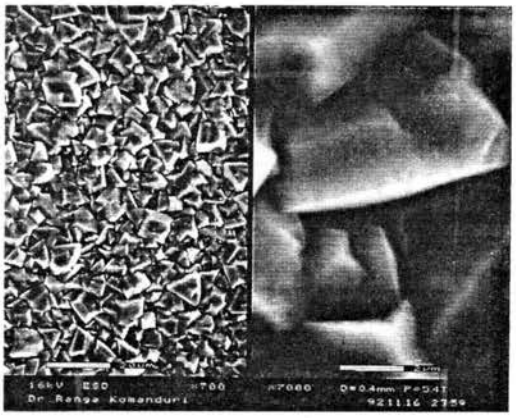

D: r = 3.5 mm, T_S = 1033 °C

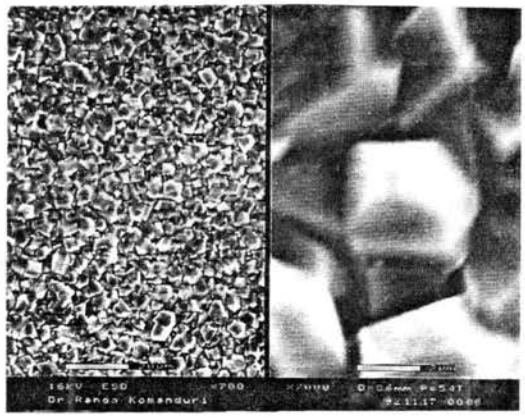

Figure 5.14 Substrate Temperature Profile and Optical Observation of the Film for EXP5

where an octahedral structure is present. The distribution of grain size is similar to all the previous experiments; smaller at the center and edge and larger in the region in between. The smaller grain size L_b seen at the center varied up to 4 μm while the larger grain at r = 2 mm ($T_S \approx 1056$ °C) varied up to 9 μm. The diameter of the produced diamond film was approximately 10 mm.

A comparison of the results for EXP3 and EXP5 is shown in Figure 5.15. The temperature levels for EXP5 exceed 1000 °C and are higher than EXP3. The higher temperatures are due to the high gas flow rates. A cubo-octahedral structure shows up more in the morphology distribution on the resulting diamond film from EXP3 compared to the previous lower temperature experiments. Also, this structure is the dominant morphology in EXP5. This indicates that the cubo-octahedral structure begins to be produced at a higher temperature (around 900 °C) and becomes the dominant morphology at temperatures above 1000 °C. The diameter of diamond film (D_f = 10 mm) for EXP5 was larger than that of EXP3 (D_f = 9 mm) due to the change in gas flow rates. An increase in the gas flow rate increases the diameter of the acetylene feather. Thus more substrate area is covered by the acetylene feather causing a larger diameter of diamond film.

A brief analysis of the diamond films produced by the five experiments and the resulting substrate surface temperatures, are shown in Table 5.3 (for description of the parameters listed refer to the nomenclature section). The table summarizes the results of EXP1 through EXP5 shown in Figures 5.8 through 5.15 with respect to the film size (D_f), grain size (L_b), observed morphology, and the measured substrate surface temperature. All parameters influencing substrate surface temperature profile and diamond film quality can be divided into two groups of internal and external parameters. Change of internal parameters such as D_n, Q_{O_2}, $Q_{C_2H_2}$, and R causes change in the combustion field. As shown in Table 5.3, diamond grain size increases with increasing substrate surface

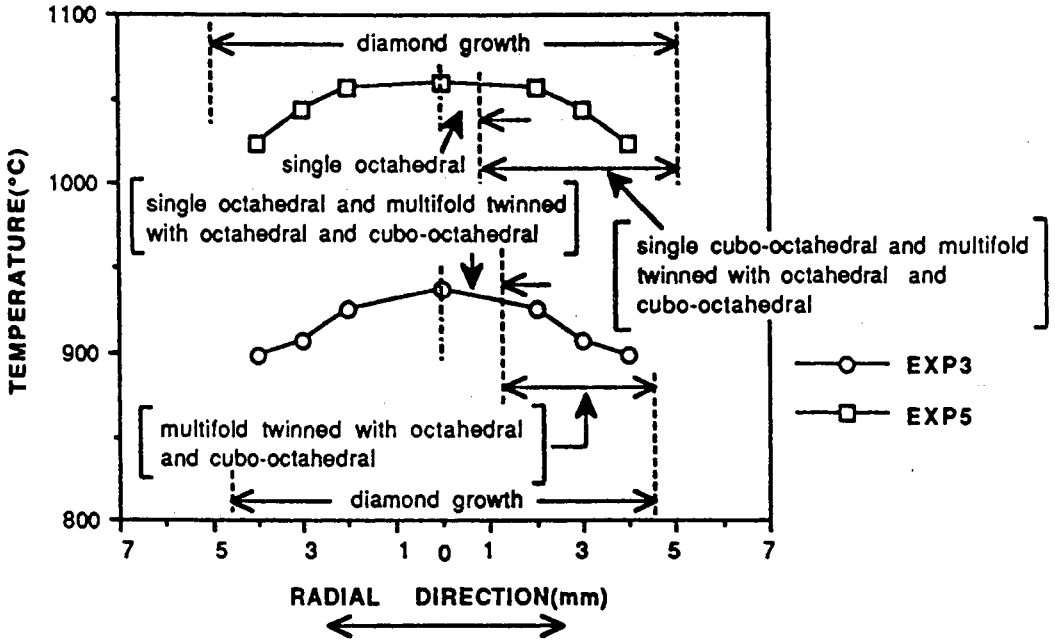

Figure 5.15 Comparison of Substrate Temperature Profiles and Film Morphologies for EXP3 and EXP5

temperature by change of the external parameters (Q_c and H_s). Comparison of L_b's in EXP1 (Q_c = 0.76 l/min) and EXP2 (Q_c = 2.46 l/min), and L_b's in EXP3 (H_s = 7 mm) and EXP4 (H_s = 2 mm) support this relation of grain size to substrate surface temperature. Also, diamond grain size increases with decreasing D_n (D_n = 1.067 mm in EXP1 and 2, D_n = 0.939 mm in EXP3, 4 and 5) as shown in Table 5.2. In the case of small nozzle size, well developed crystals (octahedral and cubo-octahedral structures) are produced through the entire film. Prediction of grain size and morphology is very important for proper application of diamond films.

Table 5.3 Summary of Experimental Results from Synthesized Diamond Films

Experiments	D_f (mm)	L_b (μm)	Morphology	Substrate Temp. (°C)	
				r = 0 (mm)	r = 4 (mm)
EXP1	12	~ 1.4	cauliflower, octahedral	781	766
EXP2	9.5	~ 1.2	ball-like, cauliflower, octahedral	744	718
EXP3	9.0	~ 10.0	octahedral, cubo-octahedral	938	899
EXP4	7.5	~ 4.0	octahedral	722	676
EXP5	10.0	~ 9.0	octahedral, cubo-octahedral	1059	1023

The resulting film diameters are different depending on the experimental conditions as shown in Table 5.3. D_f is related to the flame shape and substrate surface temperature. As discussed earlier, wide acetylene feather is desired to produce a diamond film with large D_f (however, the substrate surface temperature should be higher than 680 °C). The width of the acetylene feather increases with increasing internal parameters (D_n and Q_{O_2}) at the same value of R. Thus D_f increases with increasing D_n and Q_{O_2}. Comparisons of D_f's of EXP1 and 2 (D_n = 1.067 mm) to those of EXP3, 4 and 5 (D_n = 0.939 mm), and D_f of EXP3 (Q_{O_2} = 3.0 l/min) to that of EXP5 (Q_{O_2} = 3.13 l/min) support this relation of D_f to D_n and Q_{O_2} with the same value of R. The understanding of the resulting D_f's from different experimental conditions is essential in the development of the oxy-acetylene

combustion CVD method for large area coating by using a moving single-nozzle system or a multi-nozzle system.

The diamond growth rates for the five experiments presented in this study ranged from 10 to 20 μm/h. The Reynolds number based on the nozzle diameter ($Re = \rho V D_n/\mu$, where ρ and μ are density and absolute viscosity of the mixed gas at the room temperature, V is the gas velocity at the exit of the nozzle, and D_n is the nozzle diameter) for the five experiments ranged from about 7900 to 11200, which makes the combustion flame turbulent (Snail and Craigie, 1991; Snails et al., 1992). According to Snail and Craigie (1991) and Snails et al. (1992), diamond films grown in turbulent flames have growth rates lower than those in laminar flames. However, the quality of diamond films produced in a turbulent flame is better than those in a laminar flame. Their reported diamond growth rates in turbulent combustion flames were from 10 to 30 μm/hr which is in agreement with the growth rates observed in this study.

5.3 Prediction of Substrate Temperature Profile

Computer simulations were made with eight different conditions. They are referred to as SIM1 through SIM8. SIM1 and SIM2 were the simulations for a nozzle of 1.067 mm in diameter while the others were the simulations for a nozzle of 0.939 mm in diameter. To verify the reliability of the simulation results, four actual experiments of temperature measurements were conducted with constant oxygen and acetylene cylinder (gauge) pressures of 137.9 kPa and 68.9 kPa, respectively. The ratio of oxygen to acetylene flow rates, R, was fixed at 0.98 for all the experiments, but oxygen flow rate, Q_{O_2}, was different: 2.5 l/min for the large nozzle and 3.0 l/min for the small nozzle. The inner cone-substrate distance, L_S, was kept at 4 mm for all the experiments. The coolant flow rate, Q_C, varied from 0.76 to 2.46 l/min. The substrate-heat sink distance, H_S, was in the range of 0.7 to 7.0 mm. The specific conditions used for the four experiments and eight computer simulations are tabulated in Table 5.4. The input data for the eight

computer simulations are tabulated in Table 5.5. Heat transfer coefficients given in Table 5.5 were estimated using measured boundary temperatures and coolant temperatures (see Section D.1 of Appendix D for details). The coolant temperatures given in Table 5.5 are the average temperatures from the measured inlet and outlet coolant temperatures. The emissivity of the combustion flame (ε_f) depends on the substrate-heat sink distance (H_S). The estimation of ε_f is discussed in Section C.3 of Appendix C.

Table 5.4 Experimental and Simulation Conditions

Simulations	D_n (mm)	Q_{O_2} (l/min)	$Q_{C_2H_2}$ (l/min)	Q_C(l/min)	H_S(mm)	Experiments
SIM1	1.067	2.5	2.55	0.76	7.0	conducted
SIM2	1.067	2.5	2.55	2.46	7.0	conducted
SIM3	0.939	3.0	3.06	1.13	2.0	conducted
SIM4	0.939	3.0	3.06	1.13	7.0	conducted
SIM5	0.939	3.0	3.06	1.13	4.0	
SIM6	0.939	3.0	3.06	1.13	0.7	
SIM7	0.939	3.0	3.06	1.89	7.0	
SIM8	0.939	3.0	3.06	2.65	7.0	

Table 5.5 Input Data to Computer Simulations

	$\bar{h}\times10^3$ (W/mm^2-K)					
Simulations	Bottom of H.S. *	Cylindrical surface of H.S. *	Coolant	$\bar{h}_t$ at H.S. * (W/mm^2-K)	Coolant temp. (°C)	ε_f
SIM1	0.00924	0.00978	0.635	0.00015	44.4	0.007
SIM2	0.00764	0.00843	0.736	0.00015	30.6	0.007
SIM3	0.00904	0.00954	0.689	0.00013	39.9	0.011
SIM4	0.00911	0.00976	0.689	0.00013	39.7	0.007
SIM5	0.00904	0.00964	0.689	0.00013	39.5	0.0095
SIM6	0.00904	0.00954	0.689	0.00013	39.7	0.014
SIM7	0.00821	0.00876	0.725	0.00013	33.5	0.007
SIM8	0.00749	0.00825	0.742	0.00013	31.7	0.007

* H.S.: Heat Sink

The total heat transfer coefficients, h_t's at the substrate surface should be calculated before computer simulations for the prediction of temperature field of the system with change of external parameters such as Q_C and H_S. Then, the calculated h_t's at the substrate surface were used for computer simulations with a convective surface boundary at the substrate surface as discussed in the previous chapter. For the calculation of h_t's at the substrate surface, it was assumed that the substrate temperature profiles (shapes) at the surface and at 0.5 mm below the surface are similar to each other except in magnitude, as discussed in the previous chapter. With this assumption, substrate temperatures measured at 0.5 mm below the surface were used in the computer simulation as the substrate surface temperatures, and finally h_t's were calculated with the procedure discussed in the previous chapter.

If the assumption and the procedure used prior to the actual simulations are reasonable, the substrate temperatures at 0.5 mm below the surface calculated at the end of the third step (refer to Section 4.3 of Chapter IV) should be very close to those measured in the experiments. SIM1 and SIM3 were mainly for the calculation of h_t's at the substrate surface. The resulting h_t's were used for the actual computer simulations for the prediction of the temperature field including the substrate surface temperatures. The resulting substrate temperatures at the surface and 0.5 mm below the surface from these two simulations are shown in Figures 5.16 and 5.17. Also, the measured substrate temperatures at 0.5 mm below the surface are shown in these two figures. The simulated substrate temperatures at 0.5 mm below the surface are very close to the measured temperatures as shown in these figures. The deviations were very small: only 2 °C (0.25 %) deviation in SIM1 and 6 °C (0.81%) deviation in SIM3 at most. Thus, the assumption and the procedure used prior to the actual simulations were reasonable.

The resulting total heat transfer coefficients at the substrate surface from SIM1 and SIM3 are shown in Figure 5.18. The two resulting h_t profiles have different shapes at the center region ($r \leq 3.0$ mm). h_t decreases in the radial direction at the center region

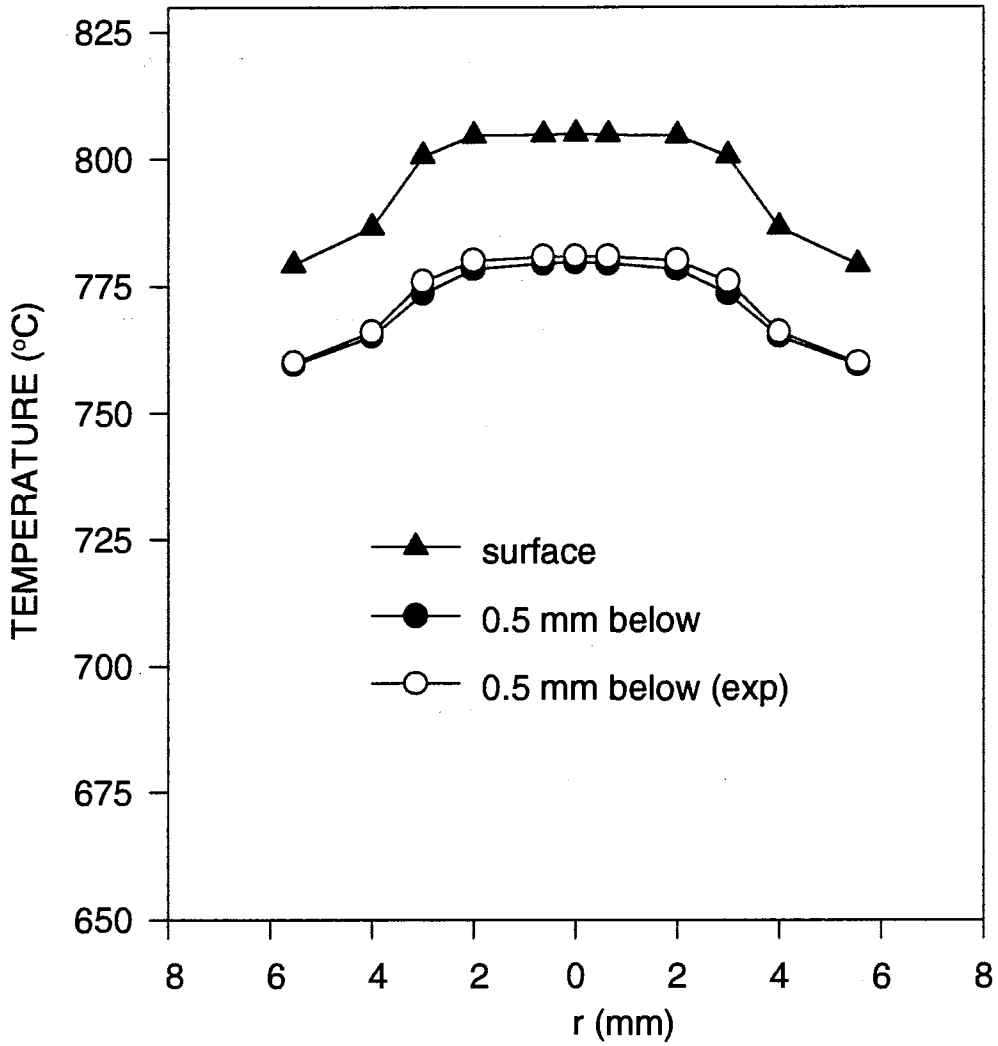

Figure 5.16 Substrate Temperatures from SIM1 and Experiment

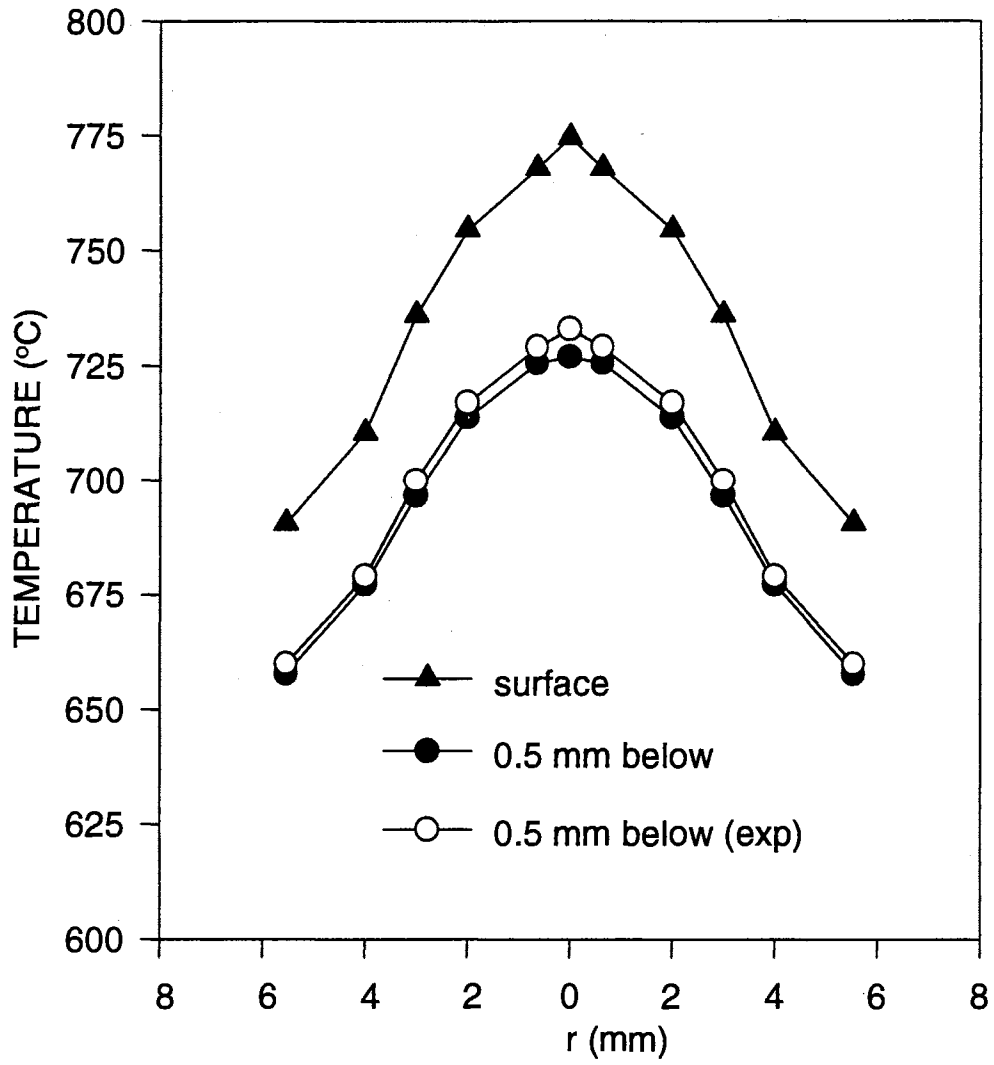

Figure 5.17 Substrate Temperatures from SIM3 and Experiment

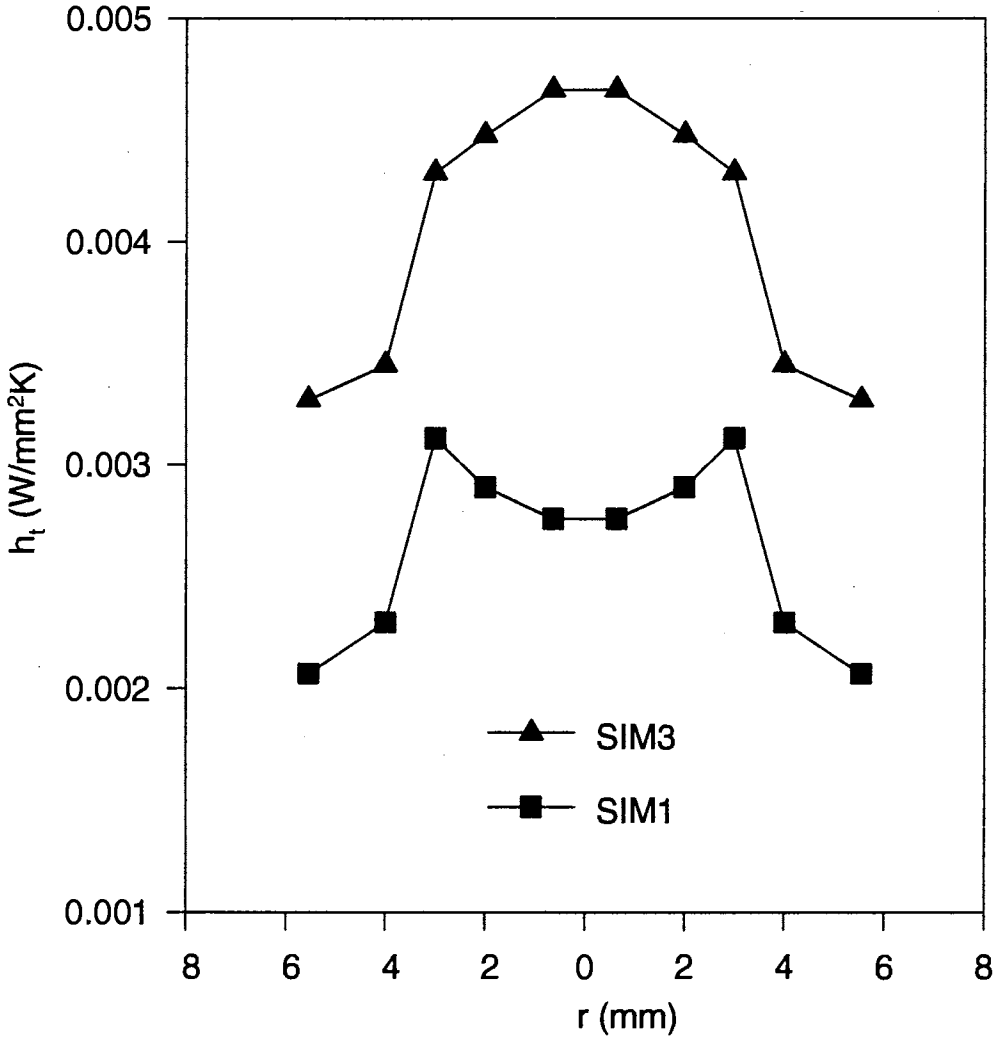

Figure 5.18 Distributions of Total Heat Transfer Coefficient at the Substrate Surface from SIM1 and SIM3

(8% drop from center to r = 3 mm) in the results from SIM3 whereas it increases in the same region (13% increase from center to r = 3 mm) in the results from SIM1, as shown in Figure 5.18. The main difference in simulation conditions between SIM1 and SIM3 is the nozzle size (see Table 5.4). The nozzle size in SIM1 was larger than that in SIM3. The nozzle size influences the combustion characteristics such as flame shape and concentration distributions of chemical species. As illustrated in Table 2.12, there exist a number of chemical species in the feather flame. The heat transferred to the substrate from the flame comes from the heat release in the flame due to chemical reactions (mainly oxidization) of the chemical species. The total heat transfer coefficient is associated with the heat release rate in the flame which varies in the axial and radial directions. Thus, the resulting profiles of the total heat transfer coefficient from different nozzle size should be different. However, the calculated h_t's from SIM1 were not expected. The increasing tendency of h_t in the radial direction at r $\leq$ 3 mm is hard to explain. To explain the resulting h_t's from SIM1, we need to consider the fact that diamond growth at the center region of the substrate surface is not active compared to other regions under a large nozzle size as shown in Figures 5.8 and 5.9. The nozzle size in SIM1 was identical to that used in the diamond synthesis experiments whose results are shown in Figures 5.8 and 5.9. When a diamond crystal is growing, a large amount of energy is required to combine additional carbons in the diamond structure. When the diamond crystal is growing inside a combustion flame, a considerable amount of energy is absorbed from the flame into the crystal surface where chemical reactions for the crystal growth occur. Some amount of the energy absorbed from the flame can flow to the substrate through the diamond crystals via conduction. Then, the total heat transfer coefficient at the region of substrate surface which is covered with diamond crystals must be larger than that at the other regions which are not covered with diamond crystals, similar to the case of SIM1.

The unexpected distribution of the total heat transfer coefficient from SIM1 may be explained by the combustion characteristics. To oxidize the acetylene supplied from

the fuel tank, oxygen diffuses from the ambient air into the combustion field in addition to the oxygen supplied from the oxygen tank. The amount of the oxygen diffused from the ambient air is slightly higher than 60% of the total oxygen required for the complete oxidization of the acetylene (see the chemical reaction equation , Equation (C.16) in Section C.3 of Appendix C), since acetylene (fuel) is slightly rich in the combustion field for the experimental conditions used in this study. A wide acetylene feather flame is observed when a large nozzle size is used. Thus, it is expected that the amount of oxygen arriving at the center region of the acetylene feather flame is not sufficient to oxidize the acetylene as completely as the other regions. Consequently, the heat release rate per unit volume at the center region of the feather flame is lower than that at the other regions similar to the distribution of h_t from SIM1 shown in Figure 5.18 since h_t is related to the heat release rate.

There is a possibility of experimental error in the temperature measurements of the substrate at 0.5 mm below the surface. If the measured substrate temperatures were in error, the distribution of h_t from SIM1 shown in Figure 5.18 may result since the measured temperatures were used to calculate h_t's in the computer simulations. Some computer simulations were conducted to verify this possibility by adjusting the substrate temperatures at 0.5 mm below the surface to lie within the error range of the measured temperatures. However, the resulting total heat transfer coefficients at the center region were still not higher than that at r =3 mm even though the difference between the center and r =3 mm was reduced.

The conditions of SIM2 were identical to SIM1, except that the coolant flow rate was increased from 0.76 l/min to 2.46 l/min. The heat transfer coefficient of coolant in SIM2 increased by 16% compared to SIM1 (see Table 5.5) due to the increased Q_C. The resulting substrate temperatures at the surface and 0.5 mm below are shown in Figure 5.19 with the experimental temperatures at 0.5 mm below the surface. Deviation of the predicted temperatures at 0.5 mm below the substrate surface from the measured

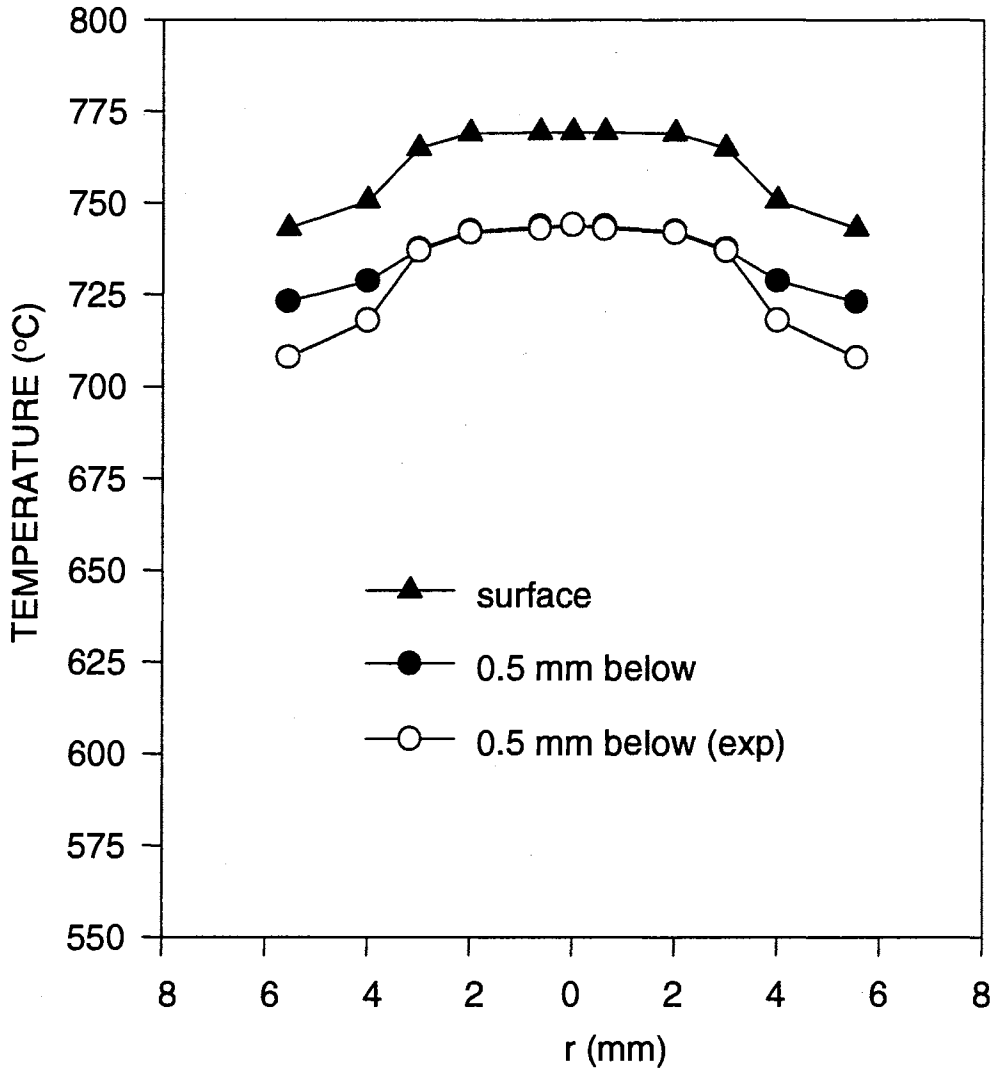

Figure 5.19 Substrate Temperatures from SIM2 and Experiment

temperatures was only 16 °C (2%) at most. The largest deviation (2%) was observed at the edge of the substrate whereas the predicted temperatures at the center region were almost identical to the measured temperatures. The actual heat transfer rate at the substrate edge from the combustion flame via radiation and conduction appeared to be slightly lower than that calculated by Equation (18) in the computational procedure. As a result, the predicted substrate temperatures were slightly higher than the measured temperatures (by 2%). This 2% deviation in the computer simulation is negligible. Thus, SIM2 was successful. Temperature distributions at the substrate surface from SIM1 and SIM2 are shown in Figure 5.20. As shown in this figure, increase of coolant flow from 0.76 to 2.46 l/min (224% increase) caused temperature drop at the substrate surface by about 36 °C (approximately 4% drop) due to the increase of heat dissipation rate into the coolant by approximately 3.4%. The temperature drop (36 °C or 4%) resulted from 224% increase of Q_c was apparently not remarkable. However, diamond films produced under the conditions of SIM1 and SIM2 were different in the film size (D_f): the film with the conditions of SIM2 was smaller than that with the conditions of SIM1 by 20% due to the low temperature especially at the edge of the substrate. Thus, the change of diamond film quality due to the substrate temperature change from the variation of Q_c is not negligible although the resulting substrate temperature change seems to be small.

The resulting heat flux distributions at the substrate surface from SIM1 and SIM2 are shown in Figure 5.21. As shown in this figure, the heat flux distributions from both cases are close to each other, and the shapes are similar to the h_t distribution shown in Figure 5.18. Temperature fields of substrate from SIM1 and SIM2 are shown in Figure 5.22. In both temperature fields, isothermal curves were plotted every 100 °C difference. Comparing these two temperature fields, it is clear that the substrate temperature fields over the heat sink (down to region I) are similar, but this similarity is broken below the heat sink (regions II and III) as shown in Figure 5.22. Region II in both temperature fields has different thicknesses, which means the temperature gradients in the axial direction are

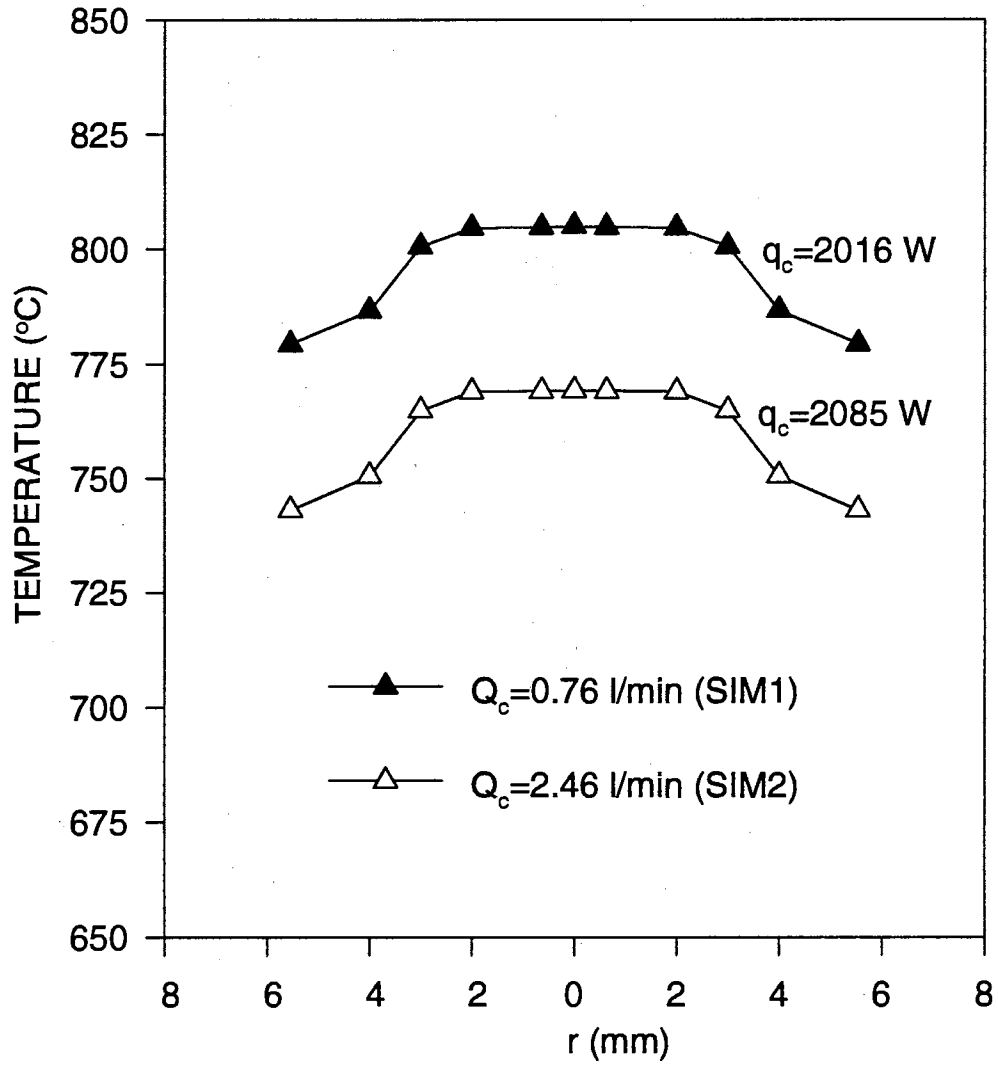

Figure 5.20 Comparison of Substrate Surface Temperatures with Different Coolant Flow Rates from SIM1 and SIM2

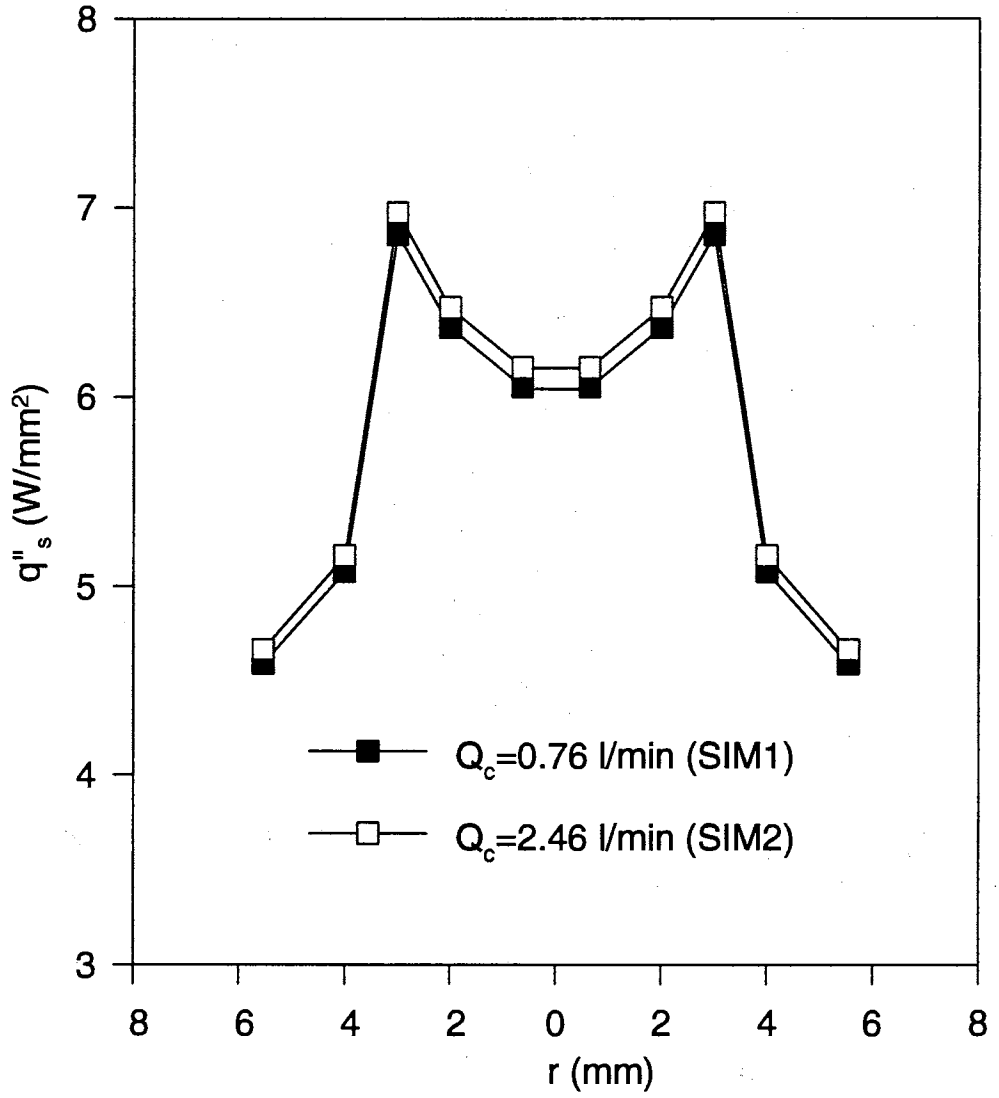

Figure 5.21 Distributions of Heat Flux at the Substrate Surface from SIM1 and SIM2

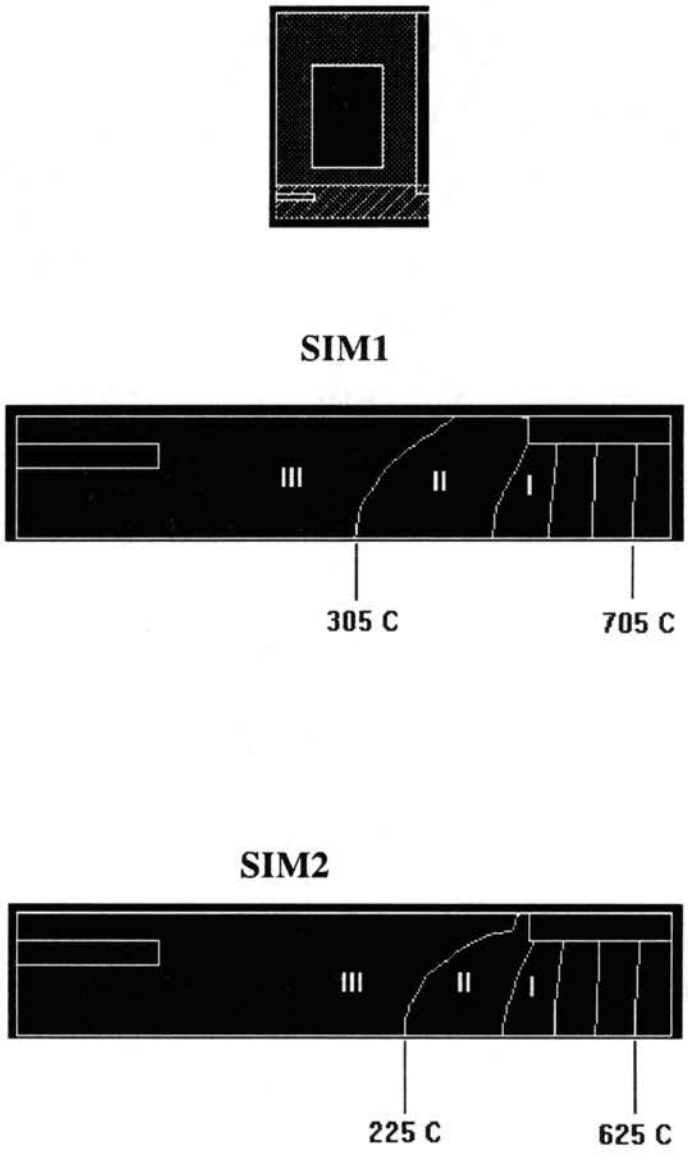

Figure 5.22 Substrate Temperature Fields from SIM1 and SIM2

different. The temperature gradient (in the axial direction) of SIM2 is larger than that of SIM1. At the interface of substrate and heat sink of region II in SIM2, the temperature gradient in the radial direction is seen to be larger than SIM1. Thus, heat flowing in the axial and radial directions through region II in SIM2 exceeds that in SIM1. This phenomena was caused by the increase of the coolant flow rate in SIM2.

SIM4 through SIM6 were for the predictions of the temperature field of the system with variation of substrate-heat sink distance, H_S. Total heat transfer coefficients at the substrate surface used in these three simulations were calculated in SIM3. The H_S values in SIM3 through SIM6 are listed in Table 5.4. The resulting substrate temperatures at the surface and 0.5 mm below the surface from SIM4 are shown in Figure 5.23. In this figure, the experimental substrate temperatures 0.5 mm below the surface are also shown. The predicted substrate temperatures 0.5 mm below the surface from SIM4 were higher than the experimental temperatures by 26.6 °C (2.8% deviation) at the center and 45.8 °C (5.0% deviation) at the edge. The main cause of the over-predicted temperature profile at the substrate is believed to be the thermal contact resistance at the interface between the substrate and heat sink. H_S in SIM3 was 2.0 mm, and in SIM4 was increased to 7.0 mm. Thus, SIM4 had a smaller contact area between the substrate and the heat sink compared to that of SIM3: the thermal contact resistance in SIM4 was less than that in SIM3. The thermal contact resistance blocks heat flow from the substrate to the heat sink. However, the computer code does not have the capability of accounting for the thermal contact resistance. As a result of the smaller contact resistance in SIM4, the predicted substrate temperatures were slightly higher than the actual temperatures by 2.8 to 5.0%.

To confirm the effect of thermal contact resistance on the predicted temperatures, two more simulations were conducted. First, the total heat transfer coefficients at the substrate surface were calculated using the measured substrate temperatures at 0.5 mm below the surface from the experiment corresponding to SIM4, where H_S was 7.0 mm. Then, the calculated h_t's at the substrate surface were used in the simulation for the case

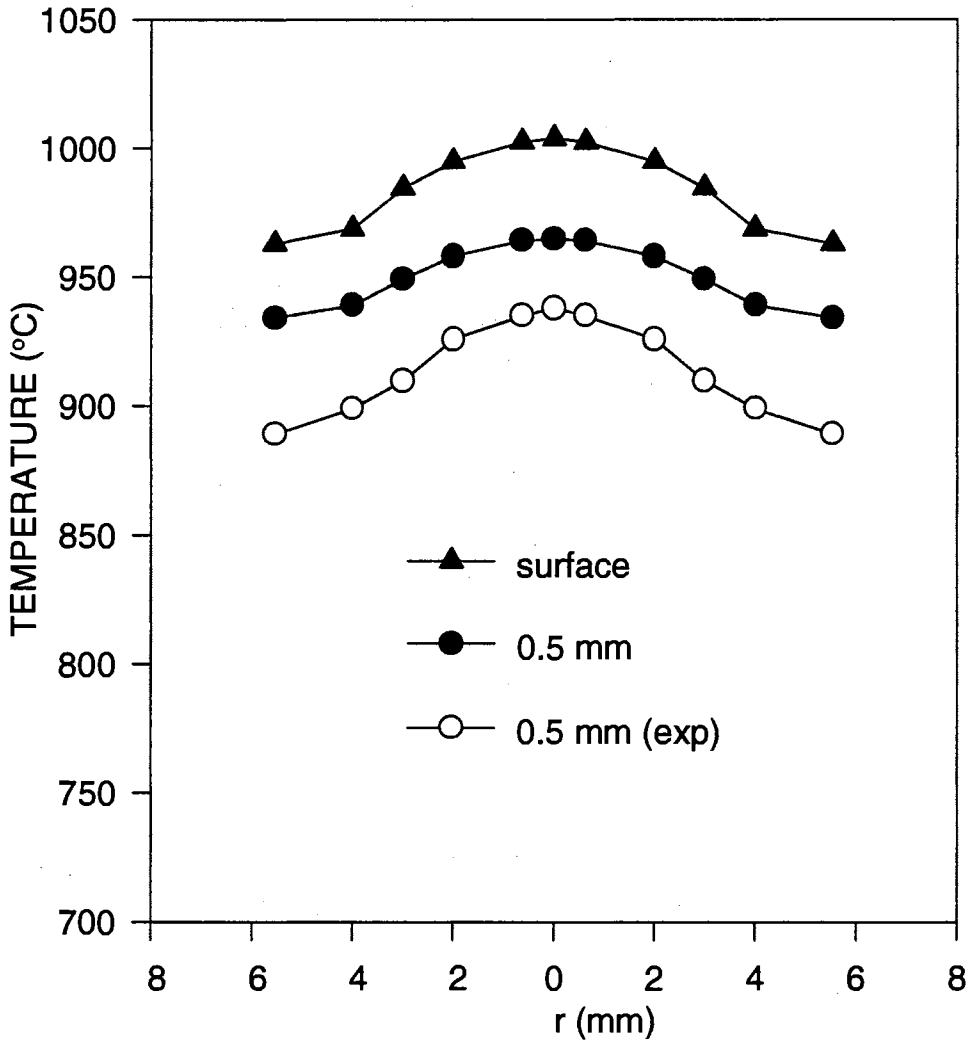

Figure 5.23 Substrate Temperatures from SIM4 and Experiment

where H_S = 2.0 mm, which is the condition of SIM3. Thus, the thermal contact resistance in the second simulation was larger than that in the first simulation. However, the computer simulation could not account for the larger thermal contact resistance in the second simulation. As a result, it was expected that the predicted substrate temperatures from the second simulation should be lower than the actual temperatures. The resulting substrate temperatures at 0.5 mm below the surface from the second simulation are shown in Figure 5.24 along with the measured temperatures. As shown in this figure, the predicted substrate temperatures at 0.5 mm below the surface were lower than the measured temperatures by 3.9% to 5.5%, which was expected.

Predicted temperatures at the substrate surface from SIM3 through SIM6 are shown in Figure 5.25. This figure shows the effect of H_S on the substrate surface temperature distribution. As shown in this figure, the substrate temperatures decrease and temperature gradient in the radial direction becomes larger as H_S decreases. Heat dissipation rate to the coolant in the system increases with decreasing H_S since temperature gradient in the radial direction at the substrate increases. The dependence of the temperature gradient in the radial direction at the substrate on H_S is shown in Figure 5.26. In this figure, the predicted substrate temperature fields from SIM4 (H_S=7.0 mm) and SIM6 (H_S=0.7 mm) are shown. The two substrate temperature fields presented in Figure 5.26 show isothermal curves plotted every 100 °C difference. Observing the isothermal curves, it is very clear that the temperature gradient in the radial direction at the substrate becomes severe when H_S is very small. The resulting distributions of heat flux at the substrate surface are shown in Figure 5.27. Compared to the distributions of the substrate surface temperatures shown in Figure 5.25, the heat flux distributions from SIM3 through SIM6 have the opposite tendency, that is heat flux decreases with increasing H_S.

The input data of the average heat transfer coefficients for SIM3 through SIM6 were close to each other, as shown in Table 5.5. The maximum difference was found in

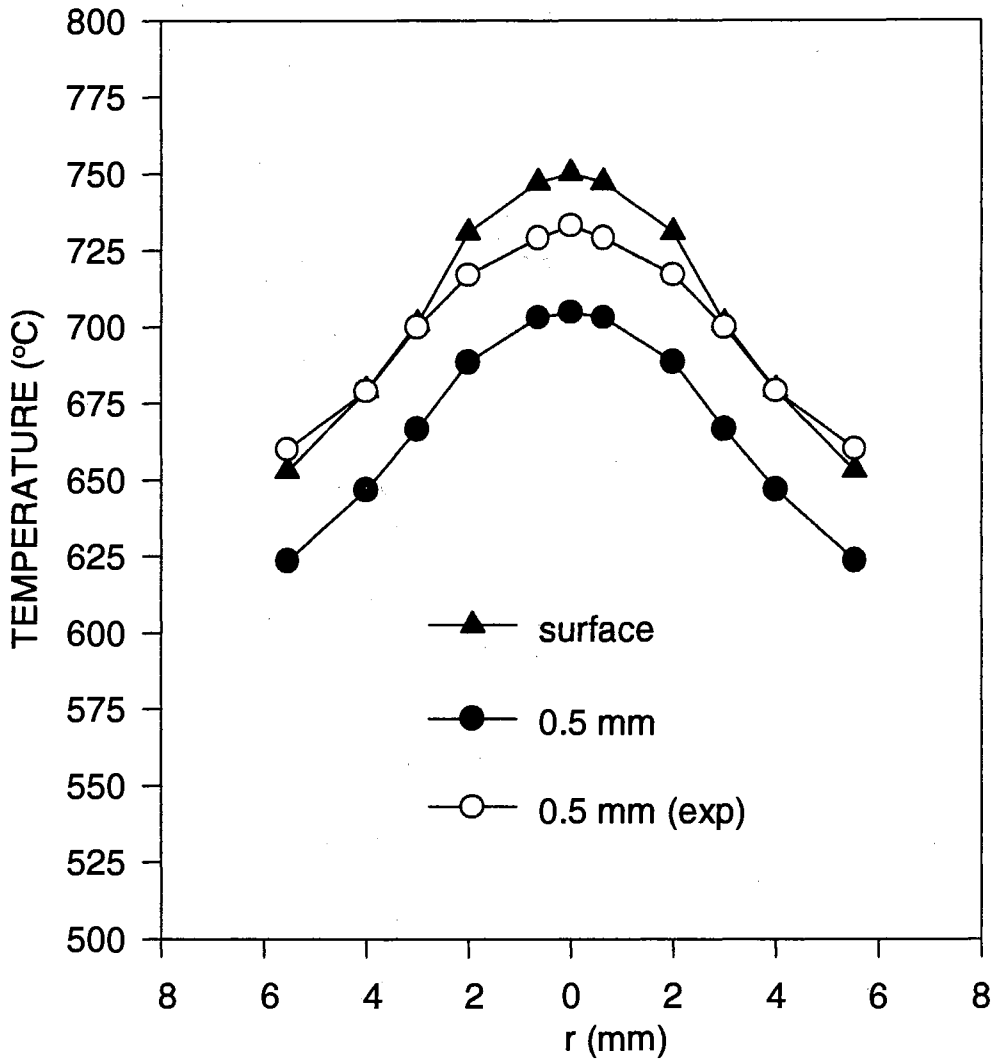

Figure 5.24 Substrate Temperatures Showing the Effect of Thermal Contact Resistance between SIM3 and SIM4

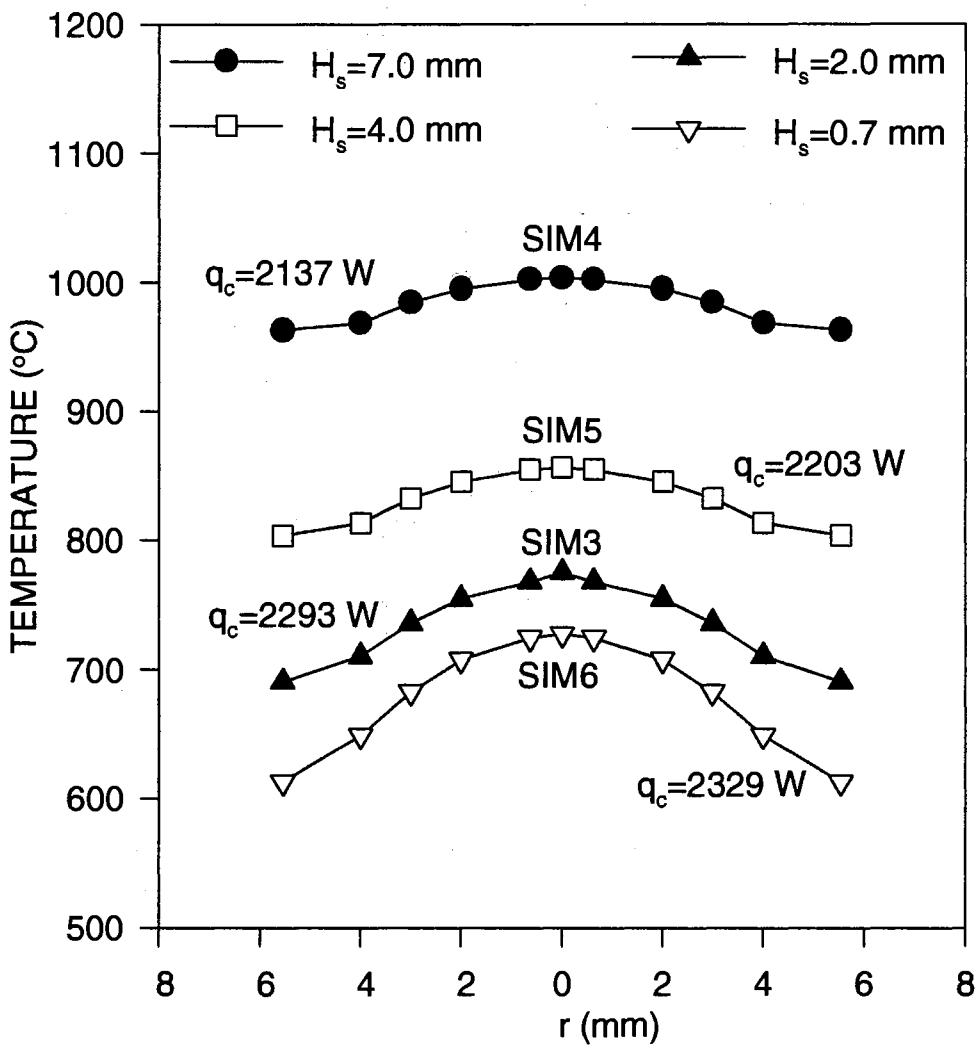

Figure 5.25 Comparison of Substrate Surface Temperatures with Different Substrate-Heat Sink Distances from SIM3 through SIM6

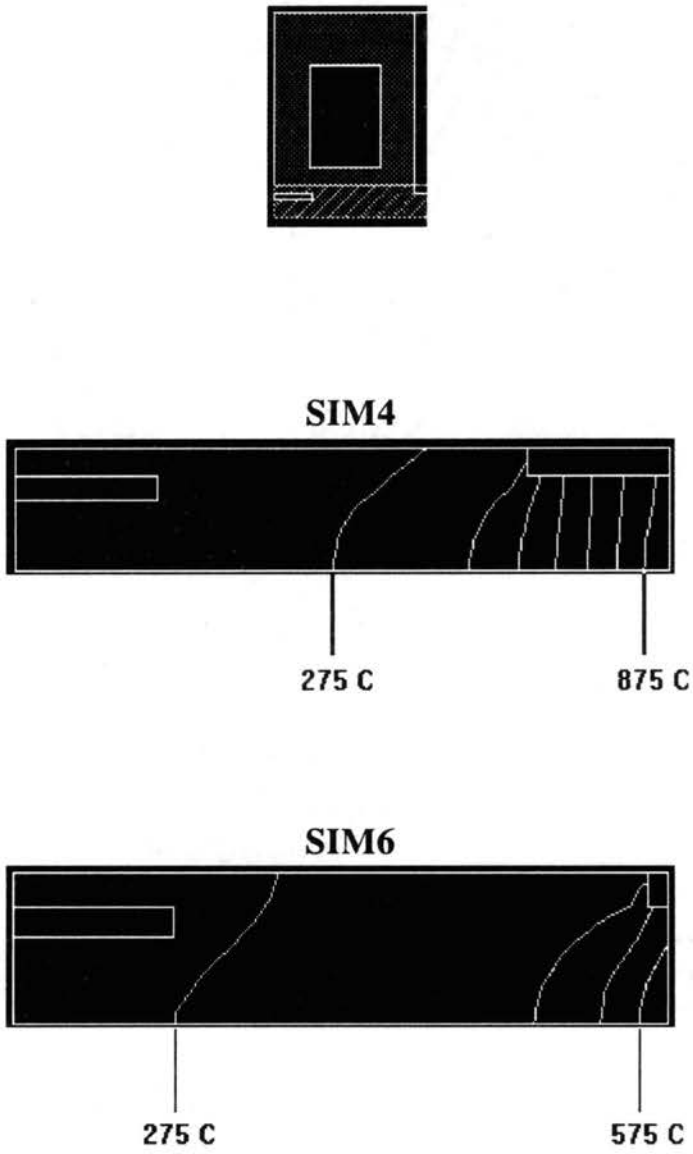

Figure 5.26 Substrate Temperature Fields from SIM4 and SIM6

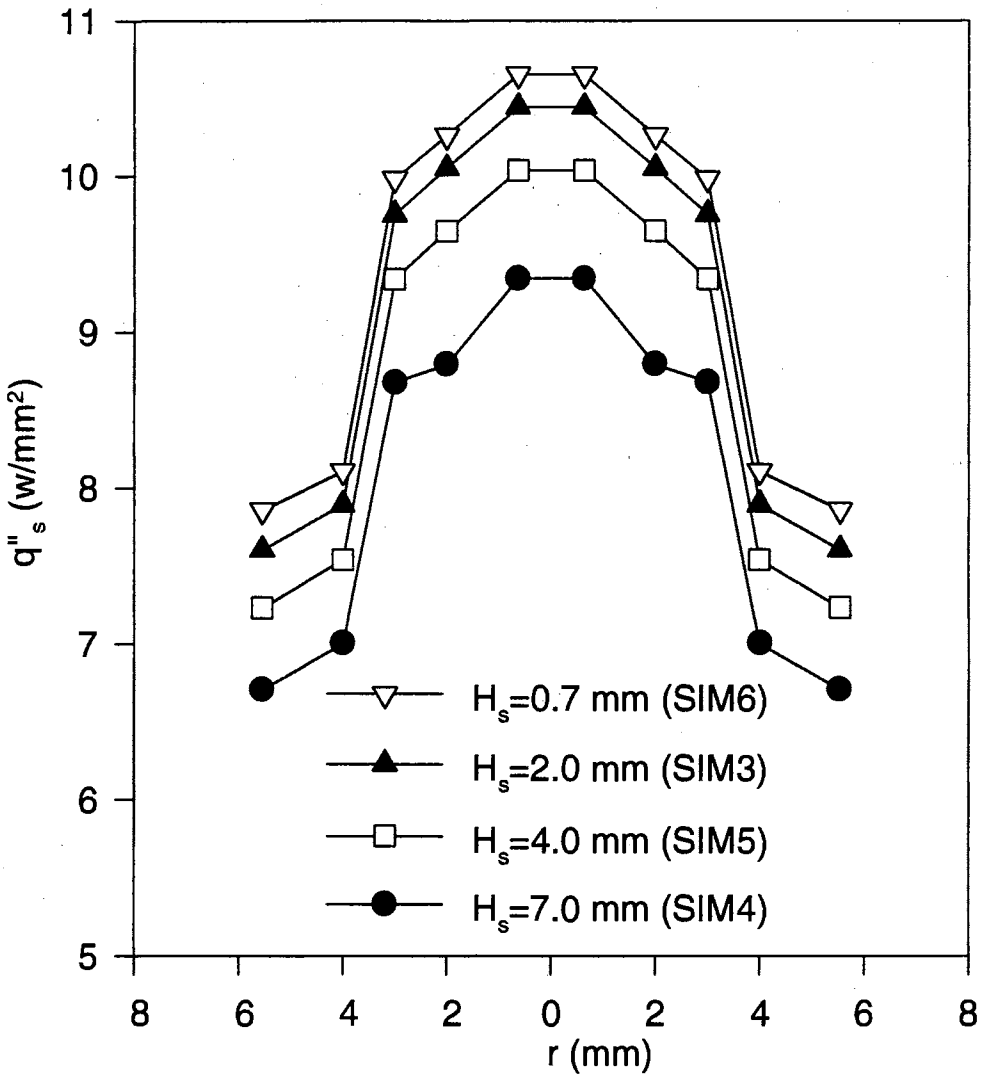

Figure 5.27 Distributions of Heat Flux at Substrate Surface from SIM3 through SIM6

the average heat transfer coefficients at the cylindrical surface of the heat sink between SIM3 and SIM4. However, the difference was only 2.3%. As presented in Section D.1 of Appendix D, the average heat transfer coefficients shown in Table 5.5 were estimated using the measured temperatures at the boundaries. The measured temperatures at the cylindrical surface of the heat sink for SIM3 through SIM6 were in the small temperature range of 78 to 83 °C whereas those at the bottom surface of the heat sink and for the coolant were in even a smaller range (79 ~ 81 °C). Thus, the dependency of the boundary and coolant temperatures in the system on the substrate-heat sink distance was negligible, which resulted in the closeness of the average heat transfer coefficients at the boundaries and coolant for SIM3 through SIM6. When the average heat transfer coefficients for SIM3 were applied to the cases of SIM4 through SIM6 in the computer simulations, the results were almost identical to those from the simulations with the estimated average heat transfer coefficients in each case, as shown in Table 5.5. The differences in the predicted substrate surface temperatures were within 1 °C. Therefore, it was not necessary to measure the boundary and coolant temperatures for the prediction of the temperature field of the system with variation of the substrate-heat sink distance.

SIM4, SIM7, and SIM8 were for the prediction of the temperature field of the system with variation of Q_C using the calculated h_t's at the substrate surface from SIM3. The effect of Q_C on the temperature field of the system was demonstrated by SIM1 and SIM2. The main difference between the two set of simulations (SIM1, SIM2, SIM4, SIM7, SIM8) was the nozzle size. The nozzle diameter in SIM1 and SIM2 was larger than that in SIM4, SIM7, and SIM8 (see Table 5.4). Comparing the results from SIM4, SIM7, and SIM8, they had the same tendency as illustrated in SIM1 and SIM2. The resulting temperatures at the substrate surface are compared in Figure 5.28. As shown in this figure, substrate temperatures decrease with increasing Q_C. However, the heat dissipation rate to the coolant, q_C, increased with increasing Q_C as demonstrated in Figure 5.20.

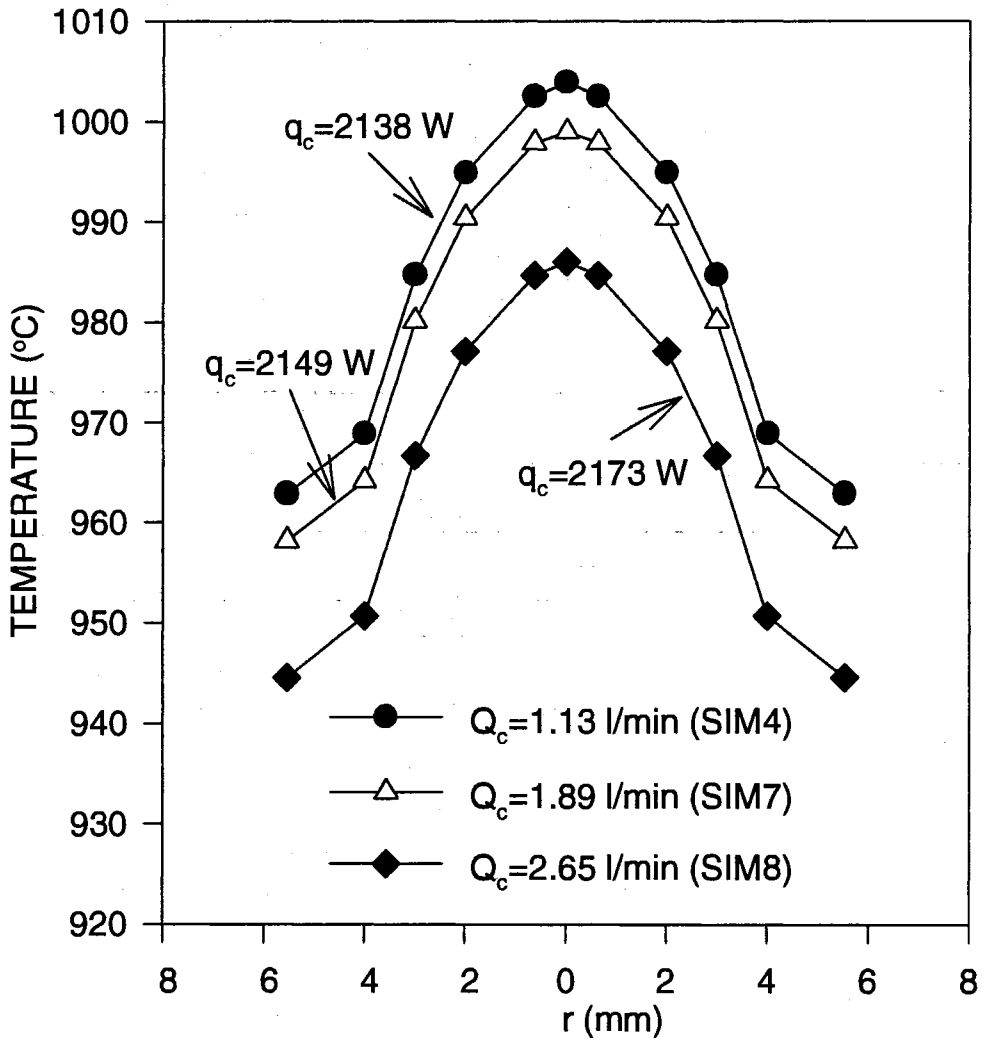

Figure 5.28 Comparison of Substrate Surface Temperatures with Different Coolant Flow Rates from SIM4, SIM7, and SIM8

The resulting temperature fields throughout the eight computer simulations showed that very high temperature gradients in the axial direction exist in the substrate above the heat sink compared to the other regions including the heat sink and the substrate below the heat sink. Figure 5.29 illustrates the temperature field in the substrate and heat sink. This figure is based on SIM4. The whole domain of the substrate and heat sink was divided into six regions labeled as I through VI based on the temperature levels in Figure 5.29, where temperature decreases with numerical order of the region. All divided regions are bounded by two isothermal curves of 150 °C difference except coolant flow region which has the lowest temperature. In Figure 5.29, the isothermal curve of 225 °C was straight from the coolant region to the substrate. There is a very thin silicon layer (gasket) of 0.15 mm thickness along the straight line of 225 °C. The thermal conductivity of the silicon is very small (0.001715 W/mm-K): only 0.44% of copper (heat sink). Thus, the silicon layer blocks the heat flow to the bottom of the heat sink. This fact explains why the isothermal curve is straight along the thin silicon layer.

The control-volume method was adopted as a numerical scheme in the computational simulations. Discretization equations for every control volume in the computational domain were derived from the concept of energy conservation over each control volume as discussed in the previous chapter. Then, all the discretized algebraic equations were solved for temperatures of all the control volumes in the computational domain. If all of the derived discretization equations were correctly transferred in the computer code and the calculation of the temperature field of the system was successful, the energy conservation over the entire computational domain should be satisfied from the concept of the control-volume method. To test the validity of the computer code and the resulting temperature field of the system, the status of energy conservation in the entire computational domain was checked in each computer simulation. If conservation of energy was satisfied, the total heat transfer rate to the system from the combustion flame via convection, radiation, and conduction should be same as that from the system to the

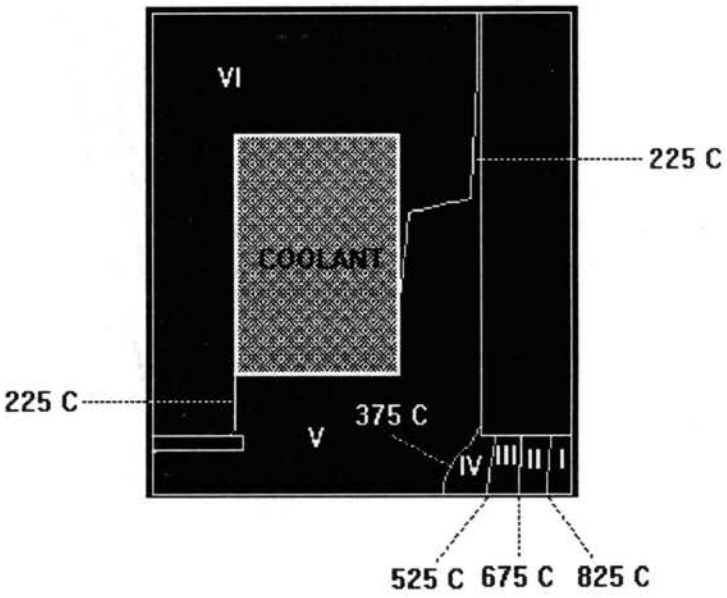

Figure 5.29 Temperature Field of System from SIM4

ambient air and coolant via convection. Tables 5.6 and 5.7 illustrate results of the heat balance checking in the system from SIM1 and SIM4, respectively. As shown in these two tables, the total heat transfer rate to the system was proved to be the same as that from the system (mainly to the coolant) for the two simulations. Thus, the energy conservation over the entire computational domain was satisfied in each simulation. All the simulations conducted in this study showed successful energy conservation over the entire computational domain.

Table 5.6 Heat Balance in the System (Substrate and Heat sink) from SIM1:
$D_n = 1.067$ mm; $Q_{O_2} = 2.5$ l/min; $Q_{C_2H_2} = 2.55$ l/min;
$Q_C = 0.76$ l/min; $H_S = 7.0$ mm

Heat Entering System		Heat Leaving System	
	Rate (W)		Rate (W)
to heat sink (conv. + rad.)	1345.1 (65.3%)	to coolant	2016.7 (98.0%)
to heat sink (cond. + rad.)	16.2 (0.8%)	from bottom surface	19.8 (0.9%)
to threaded area of substrate	35.0 (1.7%)	from cylindrical surface	22.3 (1.1%)
to substrate surface	662.6 (32.2%)		
TOTAL	2058.9	TOTAL	2058.8

Table 5.7 Heat Balance in the System (Substrate and Heat sink) from SIM4:
$D_n = 0.939$ mm; $Q_{O_2} = 3.0$ l/min; $Q_{C_2H_2} = 3.06$ l/min;
$Q_C = 1.13$ l/min; $H_S = 7.0$ mm

Heat Entering System		Heat Leaving System	
	Rate (W)		Rate (W)
to heat sink (conv. + rad.)	1177.1 (54.1%)	to coolant	2138.0 (98.2%)
to heat sink (cond. + rad.)	16.2 (0.7%)	from bottom surface	18.6 (0.8%)
to threaded area of substrate	48.8 (2.2%)	from cylindrical surface	21.2 (1.0%)
to substrate surface	935.8 (43.0%)		
TOTAL	2177.9	TOTAL	2177.8

From the experiments of temperature measurements, it was demonstrated that the temperature profile at the substrate surface is strongly related to the nozzle size. The

magnitude of the temperature profile at the substrate surface becomes larger as the nozzle size decreases with other process parameters fixed. The only source causing the substrate to be at a high temperature is undoubtedly the heat release in the combustion flame. Thus, it is important to know the flame behavior over the system. During diamond film producing experimentation, the feather flame was observed to disappear outside the substrate after impinging on the substrate surface. The outer flame impinges on the substrate and heat sink. However, it is not in contact with the substrate surface since the feather flame covers the substrate surface. Considering that the heat release rate per unit volume in the feather flame is much more than that in the outer flame, the magnitude of the temperature profile at the substrate surface is dominated by the feather flame rather than the outer flame. Therefore, it was hypothesized based on the experimental observations that the heat release rate per unit volume increases as the nozzle size decreases while holding other internal parameters (such as flow rates of oxygen and acetylene) influencing the combustion field constant. This hypothesis could not be proved due to the instrumentation limitation at the laboratory. However, computational simulations made it possible surprisingly. SIM1 and SIM4 were for different size nozzles (SIM1 for D_n=1.067 mm and SIM4 for D_n=0.939 mm). The flow rates of oxygen and acetylene in SIM4 were higher than those in SIM1 by 20 % (see Table 5.4). As illustrated in Tables 5.6 and 5.7, the resulting total heat transfer rates to the system from the combustion flame were 2058.9 W in SIM1 and 2177.9 W in SIM4: only 5.8% increase in the total heat transfer rate from the combustion flame due to 20% increase in the reactants (O_2 and C_2H_2) flow rates. The resulting heat transfer rate by convection, radiation, and conduction to the upper surface of the heat sink from the combustion flame (outer flame) decreased to 1187.3 W from 1361.3 W (12.8% decrease) with 20% increase in reactants flow rates. However, the heat transfer rate to the substrate surface and the threaded area from the combustion flame (mainly feather flame) increased to 984.6 W from 697.6 W (41.1% increase). These opposite changes of the heat transfer rates to the heat sink and

substrate with variation of the nozzle size (decreasing direction) support that the heat release rate per unit volume in the acetylene feather flame increases as the nozzle size decreases. As a result of nozzle size change, the ratio of heat entering the heat sink to that entering the substrate was changed (66.1%/33.9% in SIM1 and 54.8%/45.2% in SIM4). The lower ratios of the heat entering the heat sink to that entering the substrate were observed in other simulations for the smaller nozzle.

The results for the computer simulations have been presented in this section. The temperature fields of the system converged very rapidly (within five iterations) to a tolerance of 0.01°C for all simulations (SIM1 through SIM8). These profiles for SIM1 through SIM4 were then compared to the experimental temperature profiles at 0.5 mm below the substrate surface. The simulated profiles agree very well with the experimental profiles, showing deviations of less than 5%.

The computer simulations also indicate that nozzle size and substrate-heat sink distance are the dominant parameters influencing the shape and magnitude of the temperature profiles at the substrate surface. Increasing the nozzle size reduces both the magnitude and the temperature gradients of the temperature profile. Decreasing the nozzle size reverses both of these effects, giving the profiles larger magnitudes and temperate gradients.

The morphology and grain size of a film are directly related to the magnitude of the temperature profile at the substrate surface. Thus, by predicting the temperature profiles at the substrate surface under certain experimental conditions, we can predict the resulting morphology and grain size based on the results from the film analysis given in Section 5.2.

The experimental conditions used in this study can be applied as the input data to the computer simulations for the prediction of the temperature field of the system. However, the coolant flow rate and substrate-heat sink distance may be changed for the given flow rates of oxygen and acetylene, substrate-inner cone distance, and nozzle size, in

order to get the desired temperature profile at the substrate surface from the computer simulations.

5.4 Guidelines for Diamond Film Synthesis by Oxy-Acetylene Combustion Method

The results from the experiments and computer simulations conducted to meet the objectives of this study have been presented and discussed in Sections 5.1 through 5.3 of this chapter. Several parameters influencing the substrate temperature profile at the surface where a diamond film is deposited were identified in Section 5.1. These parameters were the oxygen and acetylene flow rates, the substrate-inner cone distance, the coolant flow rates, the substrate-heat sink distance, and nozzle size. The substrate temperature profiles at the surface were shown to be most sensitive to the substrate-heat sink distance and nozzle size. The morphology and quality (grain size, film diameter, and nucleation density) of a diamond film were shown to be strongly dependent on the substrate surface temperature and nozzle size in the results from the analysis of the produced diamond films presented in Section 5.2. Thus, it is very important to control the substrate surface temperature in the right range during the synthetic process in order to produce a desired type of diamond film. Considering that the substrate surface temperature profile is dependent on the parameters mentioned above, the operating conditions for diamond film synthesis should be properly set prior to the synthetic stage. There is no information available in the literature about the resulting substrate surface temperature profiles for all the possible combinations of the operating conditions. However, the computer codes, SUBTEMP (developed in this study) and CONDUCT by Patankar, can predict the resulting substrate surface temperature profiles from the restricted operating conditions used in this study, with the exception of the heat-sink distance and coolant flow rate which are changeable for the desired substrate surface temperature profile (see Table 3.2 and 5.4 in Chapters III and V for the detailed information of the process parameters used in this study). The input data to the computer

simulations for the prediction of the substrate surface temperature profiles are listed in Table 5.5 of this chapter. The substrate surface temperatures measured in this study (presented in Sections 5.1 and 5.2 of this chapter) were in the range of 500 ~ 1100 °C, and the corresponding experimental conditions (process parameters) except the substrate-heat sink distance and coolant flow rate, can be used as the basic operating conditions for controlling the proper substrate surface temperature profile when producing a desired type of diamond film. The substrate-heat sink distance and coolant flow rate can be changed for the desired substrate surface temperature. In changing these two parameters, computer simulations are needed to decide the proper values of these parameters for the desired substrate surface temperature profile. Therefore, after computer simulations to find the proper values of the substrate-heat sink distance and coolant flow rate, the required operating conditions for the desired type of a diamond film are set.

This study was unique in the sense that it was the first attempt to provide the information about the role of the substrate surface temperature and nozzle size on the morphology and quality of a diamond film. This information is essential to the industrialization of the oxy-acetylene combustion method in manufacturing diamond films along with the identification of several parameters influencing the substrate surface temperature. The computer simulations conducted in this study were also the first attempt to predict the substrate surface temperature profile based on the heat transfer modeling. Further computer simulations would help other investigators to further develop the oxy-acetylene combustion method.

The goal of this study was to facilitate the industrialization of the oxy-acetylene combustion method by developing guidelines for the production of diamond films having a particular morphology and quality. Since the required morphology and quality depend on the type of application, there can be no absolute rules for producing diamond films. However, based on the results of this study, the following suggestions can serve as guidelines for producing a film with a desired morphology and quality.

- Substrate surface temperatures should be between 700 and 1250 °C for successful diamond film synthesis. The resulting film size is determined by the area of the substrate that is in this temperature range, as well as by the nozzle size and the flow rates of oxygen and acetylene.
- Substrate surface temperatures should be less than 900 °C to produce octahedral morphology.
- Substrate surface temperatures should be greater than 1000 °C to produce cubo-octahedral and cubic morphologies.
- Use a nozzle diameter less than or equal to 0.939 mm to produce diamond films with grain sizes (L_b) greater than 4μm and up to 10μm.
- Use a nozzle diameter greater than or equal to 1.067 mm to produce diamond films with grain sizes (L_b) less than 4μm. Also notice that, for a fixed nozzle size, grain size increases with an increase in the substrate surface temperature.
- Use a small nozzle to produce diamond films with uniform morphology, nucleation density, and grain size. However, the substrate temperature should be controlled to be relatively uniform.
- Either use the computer code developed in this study or refer to the operating conditions used in this study to set the conditions for the desired temperature profile at the substrate surface. In this process, the proper values of the key parameters in the oxy-acetylene combustion method (such as the flow ratio of oxygen to acetylene, substrate surface temperature, and substrate position in the combustion flame) are determined.

CHAPTER VI

SUMMARY, CONCLUSIONS AND RECOMMENDATIONS

To develop the guidelines to the industrialization of the oxy-acetylene combustion method, a series of experimental and computational studies of the thermal effect in this method have been conducted. The results were presented in detail in Chapter V. In this chapter, the accomplishments of the present study will be summarized and the recommendations for the future work on the oxy-acetylene combustion method will be presented.

6.1 Summary and Conclusions

The general conclusions drawn from this study may be summarized as:

1. The experimental techniques used in this study for temperature measurements established the radial variation of the substrate surface temperature under a variety of operating conditions. The results clearly indicated that the shape and the magnitude of the measured temperature profiles were influenced by several parameters. These parameters were the oxygen and acetylene flow rates (Q_{O2} and Q_{C2H2}), the substrate-inner cone distance (L_S), the substrate-heat sink distance (H_S), the coolant flow rate (Q_C), and the nozzle size (D_n). All of these factors contributed to the uniformity or non-uniformity of the substrate temperature profile and the temperature levels at the substrate surface where a diamond film is deposited. The substrate temperature profiles were significantly sensitive to H_S and D_n among the parameters mentioned above. For a desired substrate temperature level and shape, it was found that a proper combination of

these parameters should be used. The results of this study are unique in the sense that it is the first attempt at reporting how and why certain parameters influence the substrate surface temperature distribution by oxy-acetylene combustion method.

2. Diamond films were synthesized during this study. The diamond films were analyzed with respect to morphology and some quality components such as the grain size, film size, and nucleation density. The morphology and quality of a diamond film was shown to have a strong relation with the substrate temperature profile and nozzle size. The cubo-octahedral structure was found to be produced at temperatures above 900 °C while the octahederal structure was dominant at temperatures below 900 °C. The grain size was seen to be a function of the nozzle size and the substrate surface temperature. Diamond films consisting of large grains resulted from small nozzles. When the nozzle size was fixed, larger grains were produced at higher substrate temperatures. The individual grains in a diamond film produced from a small nozzle (0.939 mm of diameter) were shown to be close-packed to form a continuous diamond film. However, the resulting diamond film from a large nozzle was observed to have spaces between the neighboring grains at the center region of the film. Moreover, the morphology at the center region was different from the other regions. Thus, a small nozzle size is recommended to produce a diamond film with high and uniform nucleation density and uniform morphology if the substrate surface temperature profile can be controlled to be relatively uniform. The results from analyzing diamond films can help in studying the optimal conditions for producing a good quality diamond film with a desired morphology. Considering that the desired morphology and quality of the diamond film depend on the type of application of the film, prediction of the resulting morphology and quality of a diamond film and controlling of the substrate temperature are essential to successful application of this method for diamond synthesis.

3. The lower temperature limit for diamond deposition (nucleation) was found to be about 700 °C through this study. When the substrate surface temperature dropped

below the lower limit, no film was produced. However, no diamond crystal appeared in the resulting deposition on the substrate at temperatures above 1250 °C. Thus, no matter how other parameters are controlled, diamond film synthesis by oxy-acetylene combustion method will fail if T_S distribution is not within 700 ~ 1250 °C. To make a successful diamond deposition on the entire substrate, it is necessary to control the substrate surface temperatures within 700 ~ 1250 °C. Even in the right range of T_S, the morphology of a diamond film is a strong function of T_S. Therefore, the prediction or measurement of T_S is essential to the study of optimal conditions for diamond synthesis by the oxy-acetylene combustion method as well as for the confirmation of diamond deposition on the substrate surface.

4. A computer code was developed for the prediction of the temperature field of the system (substrate and heat sink). The computer code was based on the mathematical modeling of the heat transfer in the system. The code employed the control-volume approach as a numerical scheme. The deviation of the predicted substrate surface temperatures from those measured experimentally were within 5%. Experimental substrate temperature measurements are time and labor intensive. Moreover, there are a number of different operating conditions that have similar temperature profiles, but result in different quality diamond films. Consequently, computer simulation would be a powerful and efficient tool for the prediction of the temperature profiles at the substrate surface. The quality and morphology of a diamond film are most sensitive to the substrate surface temperature. Thus, by using the computer code to predict the substrate surface temperature, we can predict the resulting morphology and quality of a diamond film under certain operating conditions. This computer simulation is also good for studying the effects of the process parameters (such as the coolant flow rate and the substrate-heat sink distance) on the substrate surface temperature profile, since the results from the predicted substrate surface temperatures agree very well with the results from experimental measurements.

6.2 Recommendations

Based on the observations and conclusions made during this study, the following recommendations are suggested:

1. The experimental setup of the oxy-acetylene combustion method should be further developed in the direction to have a uniform temperature at the substrate surface and constant concentrations of the chemical species related to the diamond growth (nucleation) just over the substrate surface. This desired condition in the oxy-acetylene combustion method can result in a diamond film with uniformities in the thickness, grain size, nucleation density, and morphology which is required in the industry. The computer code (SUBTEMP) can be used for developing the experimental setup which makes relatively uniform substrate surface temperature by changing the geometry of the system (heat sink and substrate).

2. A multi-nozzle system should be adopted in the oxy-acetylene combustion method instead of a single nozzle in order to improve the deposition area of the substrate. One of the main drawbacks in the oxy-acetylene combustion method is the relatively small area of diamond deposition. If this method is successfully further studied to increase the deposition area, this method will be industrialized easily because of its excellencies in the growth rate and quality of the diamond film.

3. The effect of substrate material on the morphology and quality of diamond films should be further investigated. The specific results presented in this study for molybdenum substrate are fairly dependent on the substrate material. Different substrate materials commonly used in oxy-acetylene combustion CVD diamond synthesis such as silicon or tungsten, will produce different specific results due to the differences in the thermophysical properties of the materials. That is, different substrate surface temperature distribution and substrate material would lead to different grain size and morphology distribution for the produced diamond films. However, the general behavior of the results of this study should be applicable to other substrates. The computer code developed in

this study can be used for the prediction of the substrate surface temperatures in the case of other substrate material rather than molybdenum by changing the thermophysical properties of the substrate, such as the thermal conductivity and emissivity.

BIBLIOGRAPHY

Aisenberg, S. and Chabot R. (1971), Ion Beam Deposition of Thin Films of DIamond-Like Carbon, J. Appl. Phys., v. 42, no. 7, pp. 2953-2958.

Angus, J. C., Will, H. A. and Stanko, W. S. (1968), Growth of Diamond Seed Crystals by Vapor Deposition, J. Appl. Phys., v. 39, pp. 2915-2922.

Angus, J. C., Gardner, N. C., Poferi, D. J., Chauhan, S. P., Byble, T. J. and Sung, P. (1971), The Growth of Semiconductive Diamonds at a Pressure Lower Than the Atmospheric, Sint. Almazy, v. 3, pp. 38-41.

Angus, J. C. and Hayman, C. C. (1988), Low-Pressure Metastable Growth of Diamond and Diamondlike Phases, Science, v. 241, 913-921.

ASTM Special Technical Publication 470 (1970), Manual on the Use of Thermocouples in Temperature Measurement, American Society for Testing and Materials.

Avigal, Y. (1992), The Effect of Silicon Surface Preparation on the Nucleation of Diamond by Chemical Vapor Deposition, Diamond and Related Materials, v. 1, pp. 216-219.

Baba, K., Aikawa, Y. and Shohata, N. (1991), Thermal Conductivity of Diamond Films, J. Appl. Phys., v. 69, part 10, pp. 7313-7315.

Bachmann, P. K., Drawl, W., Knight, D., Weimer, R., Messier, R. F. (1988), Badzian, A., Geis, M. and Johnson, G. (1988), Diamond and Diamond-Like Materials, Materials Research Society, Pittsburgh, Extended Abstract, v. EA-15, p. 99.

Bachmann, P. K., Leers, D. and Lydtin, H. (1991), Towards a general Concept of Diamond Chemical Vapour Deposition, Diamond and Related Materials, v. 1, pp. 1-12.

Bachmann, P. K., Messier, R. (1989), Emerging Technology of Diamond Thin Films, Chem. Engr. News, May 15, pp. 24-39.

Bachmann, P. K. and Enckevort W. V. (1992), Diamond Deposition Technologies, Diamond and Related Materials, v. 1, pp. 1021-1034.

Bang, K. (1992), Personal Observations from Analysis of Diamond Film Experimental Results.

Bang, K., Ghajar, A. J. and Komanduri, K. (1994), The Effect of Substarte Surface Temperature on Morphology and Quality of Diamond Films by Oxy-Acetylene Combustion Method, Thin Solid Films, v. 238, pp. 172-183.

Berman, R. and Martinez, M. (1976), Diamond Research 1976 (Suppl. to Ind. Diam. Rev.), pp. 7-13.

Boelter, L. M. K., Young, G. and Iversen, H. W. (1948), NACA TN 1451 (now NASA), Washington.

Bogli, U., Blatter, A., Pimenov, S. H., Smolin, A. A. and Konov, V. I. (1992), Smoothening of Diamond Films with an ArF Laser, Diamond and Related Materials, v. 1, pp 949-953.

Bovenkerk, H. P., Bundy, F. P., Hall, H. P., Strong, H. M. and Wentorf, R. H. (1959), Preparation of Diamond, Nature, v. 184, pp. 1094-1098.

Brown, A. (1991), Diamonds Are Technology's Best Friend, Aerospace America, Feb., pp. 26-30.

Buckley, I. M. and Collins, A. T. (1992), Active ELectronic Apllications for Diamond, Diamond and Related Materials, v. 1, pp. 1083-1101.

Cappelli M. A. and Paul, P. H. (1990), An Investigation of Diamond Film Deposition in a Premixed Oxyacetylene Flame, J. Appl. Phys., v. 67, part 5, pp. 2596-2603.

Carrington, W. A., Hanssen L. M., Snail K. A. Oakes, D. B. and Butler, J. E. (1989), Diamond Growth in O_2 + C_2H_4 and O_2 + C_2H_2 Flames, Metallurgical Transactions, v. 20A, pp. 1282-1284.

Chauhan, S. P., Angus, J. C. and Gardner, N. C. (1976), Kinetics of Carbon Deposition on Diamond Powder, J. Appl. Phys., v. 47, no. 11, pp. 4746-4754.

Choi, B. I., Flik, M. I. and Anderson A. C. (1992), Adaptively Calibrated Pyrometry for Film Deposition Processes, in Khanpara J. C. and Bishop, P. (eds.), Heat Transfer in Material Processing, American Society of Meachnical Engineers, New York, v. 224, pp 19-26.

Churchill, S. W. and Chu, H. H. S. (1975), Correlating Equations for Laminar and Turbulent Free Convection from a Vertical Plate, Int. J. Heat Mass Transfer, v. 18, 1323.

Clausing, R. E., Heatherly, L., Horton, L. L., Specht, E. D., Begun, G. M. and Wang, Z. L. (1992), Textures and Morphologies of Chemical Vapor Deposited (CVD) Diamond, Diamond and Related Materials, v. 1, pp. 411-415.

Crookes, W. (1897), Proc. R. Inst., v. 15, 477.

Decarli, P. S. and Jamieson, J. C. (1961), Formation of Diamond by Explosive Schock, Science, v. 133, 1821.

Deryagin, B. and Fedoseev, D. B. (1975), The Synthesis of Diamond at Low Pressure, Sci. Am., v. 233, no. 5, pp. 102-109.

Deryagin, B., Bouilov, L. L. and Spitsyn, B. V. (1986), Crystallization and Certain Properties of Diamond Films, Arch. Nauki. Mater., v. 7, no. 2, pp. 111-119.

Eversole, W. G. (1962), Synthesis of Diamond, U.S. Patent No. 3030188.

Field, J. E. (1979), The Properties of Diamond, Academic Press, London.

Geary, D. (1980), The Welder`s Bible, Tab Books Inc., 1980.

Geis, M. W., Rathman, D. D., Ehrlich, D. J., Murphy, R. H. and Lindley, W. T. (1987), High-Temperature Point Contact Transistors and Schottky Diodes Formed on Synthetic Boron-Doped Diamond, IEEE Electronic Device Letters, v. 8, no. 8, pp. 342-343.

Ghajar, A. J. and Bang, K. (1993a), Parametric Effects on the Substrate Temperature Profile in Oxy-Acetylene Flames, Heat Transfer Engineering, v. 14, no. 3, pp. 48-59.

Ghajar, A. J. and Bang, K. (1993b), Experimental and Analytical Studies of Different Methods for Producing Stratified Flows, Energy, v. 18, no. 4, pp 323-334.

Gildenblat, G. S., Grot, S. A., Hatfield, C. W., Wronski, C. R., Badzian, A. R., Badzian, T. and Messier, R. (1990), High Temperature Schottky Diodes with Boron-Doped Homoepitaxial Diamond Base, Mat. Res. Bull., v. 25, pp. 129-134.

Glesener, J. W., Morrish, A. A. and Snail, K. A. (1991), A Thin-Film Schottky Diode Fabricated from Flame-grown Diamond, J. Appl. Phys., v. 70, part 9, pp. 5144-5146.

Goldstein, R. J., Sparrow, E. M. and Jones, D. C. (1973), Natural Convection Mass Transfer Adjacent to Horizontal Plates, Int. J. Heat Mass Transfer, v. 16, 1025.

Golozar, M. A., McColl, I. R., Grant, D. M. and Wood, J. V. (1992), Combustion Flame Growth Diamond Films, Diamond and Related Materials, v. 1, pp. 262-266.

Hannay, J. B. (1880), Proc. Roy. Soc., v. 30, 188.

Hanssen, L. M., Carrington, W. A., Butler, J. E., and Snail, K.A. (1988), Diamond Synthesis Using an Oxygen-Acetylene Torch, Mater. Ltrs., v. 7, pp 289-296.

Hanssen, L. M., Snail, K. A., Carrington W. A., Butler, J. E., Kellogg, S. and Oakes, D. B. (1991), Diamond and Nondiamond Carbon Synthesis in an Oxygen-Acetylene Flame, Thin Solid Films, v. 196, pp. 271-281.

Hawtin, P., Lewis, J. B., Moul, N. and Phillips, R. H. (1966), Phil. Trans. R. Soc., v. A261, pp. 67-95.

Hershey, J. W. (1929), Trans. Kansas Acad. Sci., v. 32, 52.

Hirose, Y. and Kondoh, N. (1988), Extended Abstracts of 35th Spring Meeting of the Japanese Society os Applied Physics and Related Societies, Tokyo, March, Japan Society of Applied Physics, Tokyo, p. 343.

Hirose, Y. and Amanuma, S. (1990), The Synthesis of High-Quality Diamond in Combustion Flames, J. Appl. Phys., v. 68, part 12, pp. 6401-6405.

Hoff, H. A., Morrish, A. A., Butler, J. E. and Rath, B. B. (1990), Comparative Fractography of Chemical Vapor and Combustion Deposited Diamond Films, J. Mater. Res., v. 5, no. 11, pp. 2572-2588.

Hottel, H. C. (1954), Heat Transmission, McGraw-Hill Book Company, New York.

Huang, D., Frenklach, M. and Maroncelli, M. (1988), Energetics of Acetylene-Addition Mechanism of Diamond Growth, J. Physical Chemistry, v. 92, pp. 6379-6381.

Incropera F. P. and De Witt, D. P. (1990), Fundamentals of Heat and Mass Transfer, 2nd Edition, John Wiley & Sons, Inc., New York.

Janssen, G., Van Enckevort, W. J. P., Schaminee, J. J. D., Vollenberg, W., Giling, L. J. and Seal, M. (1990), Rapid Single Cryatalline Diamond Growth by Acetylene-Oxygen Flame Deposition, J. Crystal Growth, v. 104, pp. 752-757.

Jin, S., Graebner, J. E., Tiefel, T. H., Kammlott, G. W. and Zydzik, G. J. (1992), Polishing of CVD Diamond by Diffusional Reaction with Manganese Powder, Diamond and Related Materials, v. 1, pp. 949-953.

Joffreau, P. O., Haubner, R. and Lux, B. (1988a), J. Refractory and Hard Metals, v. 7, no. 2, pp. 92-97.

Joffreau, P. O., Haubner, R. and Lux, B. (1988b), J. Refractory and Hard Metals, v. 7, no. 4, pp. 186-194

Joffreau, P. O., Haubner, R. and Lux, B. (1988c), Low-Pressure Diamond Growth on Refractory Metals, Ext. Abs. Diamond and Diamond-Like Materials Synthesis, pp. 15-18.

Kamo, M., Sato, Y., Matsumoto, S. and Setaka, N. (1983), Diamond Synthesis from Gas Phase in Microwave Plasma, J. Crystal Growth, v. 62, pp. 642-644.

Kline, S. J. and McClintock, F. A. (1953), Describing Uncertainties in Single-Sample Experiments, Mechanical Engineering, v. 75, no. 1, pp. 3-9.

Kobashi, K., Nishimura, K., Kawate, Y. and Hiriuchi, T. (1988), Synthesis of Diamond by Use of Microwave Plasma Chemical Vapor Deposition: Morphology and Growth of Daimond Films, Phys. Rev. B., v. 38, pp. 4067-4084.

Komanduri, R., Snail, K. S. and Fehrenbacher, L. L. (1990), Growth of Diamond Crystals by Combustion Synthesis, Philosophical Magazine Lett., v. 62, no. 4, pp. 283-290.

Kondoh, E., Ohta, T., Mitomo, T., Ohtsuka, K. (1991), Determination of Activation Energies for Diamond Growth by an Advanced Hot Filament Chemical Vapor Deposition Method, Appl. Phys. Lett., v. 59, part 4, pp. 488-490.

Koshino, N., Kurihara, K., Kawarada, M. and Sasaki K. (1988), High-Rate Synthesis of Diamond Films by DC plasma jet CVD, Ext. Abs. Diamond and Diamond-Like Materials Synthesis, pp. 95-98.

Kosky, P. G. and McAtee, D. S. (1989), An Experimental and Theoretical Investigation of Flame-Formed Diamond, Material Letters, v. 8, no. 9, pp. 369-374.

Lander, J. J. and Morrison, J. (1966), Low Energy Electron Diffraction Study of the (111) Diamond Surface, Surface Science, v. 4, pp. 241-246.

Lee, Y. H., Bachmann, K. J., Glass, J. T., LeGrice, Y. M. and Nemanich, R. J. (1990), Vapor Deposition of Diamond Thin Films on Various Substrates, Appl. Phys. Lett., v. 57, part 18, pp. 1916-1918.

Liander, H. and Lundblad, E. (1960), Ark. Kemi., v. 16, p. 139.

Lux, B. and Haubner, R. (1989), Low Pressure Synthesis of Superhard Coatings, Int. J. Ref. and Hard Materials, pp. 158-174.

Lux, B. and Haubner, R. (1992), Diamond for Tooling and Abrasive, Diamond and Related Materials, v. 1, pp. 1035-1047.

Matsui, Y., Yuuki, A., Sahara, M. and Hirose, Y. (1989), Flame Structure and Diamond Growth Mechanism of Acetylene Torch, Jap. J. Appl. Phys., v. 28, no. 9, pp. 1718-1724.

Matsui, Y., Yabe, H. and Hirose, Y. (1990), The Growth Mechanism of Diamond Crystals in Acetylene Flames, Jap. J. Appl. Phys., v. 29, no. 8, pp. 1552-1560.

Matsui, Y., Yabe, H., Sugimoto, T. and Hirose, Y. (1991), The Structure of Acetylene Flames for Diamond Synthesis, Diamond and Related Materials, v. 1, pp. 19-24.

Matsumoto, Y. and Setaka, N. (1979), Thermal Desorption Spectra of Hydrogenated and Water Treated Diamond Powders, Carbon, v. 17, pp. 485-489.

Matsumoto, Y. and Setaka, N. (1981), Effect of the Preceding Heat Treatment on Hydrogen Chemisorption of Diamond Powders, Carbon, v. 19, pp. 232-234.

Matsumoto, S., Sato, Y., Kamo, M. and Setaka, N. (1982a), Vapor Deposition of Diamond Particles from Methane, Jap. J. Appl. Phys., v. 21, no. 4, pp. L183-L185.

Matsumoto, S., Sato, Y., Tsutsumi, M. and Setaka, N. (1982b), Growth of Diamond Particles from Methane-Hydrogen Gas, J. Metr. Sci., v. 17, pp. 3106-3112.

Matsumoto, S. and Matsui, Y. (1983), Electron Microscopic Observation of Diamond Particles Grown from the Vapor Phase, J. Mater. Sci., v. 18, pp. 1785-1793.

Matsumoto, S., Hino, M. and Kobayashi, T. (1987), Synthesis of Diamond Films in a RF Induction Thermal Plasma, Appl. Phys. Lett., v. 51, part 10, pp. 737-739.

McClure, M. T., Windheim, J. A., Glass, J. T. and Prater, J. P. (1994), Effect of Native SiO_2 Layer on the Nucleation of Diamond Using a Combustion Flame, Diamond and Related Materials, v. 3, pp. 239-244.

Mitsuda, Y., Yoshida, T., Akahi, K. (1989), Development of a New Microwave Plasma Torch and its Application to Diamond Synthesis, Rev. Sci. Instrum., v. 60, no. 2, pp. 249-252.

Moissan, H. (1894), Cr. Acad. Sci. Paris (France), v. 118, 320.

Murakawa, M., Takeuchi, S. and Hirose, Y. (1989), Diamond Coating of a Long Substrate by Use of a Combustion Flame, Surface and Coating Technology, v. 39/40, pp. 235-240.

Nandyal, S. (1991), Combustion Synthesis of Diamond Films, M. S. thesis, Oklahoma State University, Stillwater, Oklahoma.

Oakes, D. B., Butler, J. E., Snail, K. A., Carrington W. A. and Hanssen, L. M. (1991), Diamond Synthesis in Oxygen-Acetylene Flames: Inhomogeneities and the Effects of Hydrogen Addition, J. Appl. Phys., v. 69, part 4, pp. 2603-2610.

Ohtake N. and Yoshikawa, M. (1990), Diamond Film Preparation by Arc Discharge Plasma jet Chemical Deposition in the Methane Atmosphere, J. Electrochem. Soc., v. 137, no. 2, pp. 717-722.

OMEGA (1987), Complete Temperature Measurements Handbook and Encyclopedia, OMEGA Engineering Inc.

Parsons, C. A. (1920), Phil. Trans., A220, 67.

Patankar S. V. (1991), Computation of Conduction and Duct Flow Heat Transfer, Innovative Research Inc., Maple Grove, Minnesota.

Pate, B. B. (1985), The Diamond Surface: Atomic and Electronic Structure, Surface. Sci., v. 165, pp. 83-142.

Patterson, D. E., Bai, B. J., Chu, C. J., Hauge, R. H. and Margrave, J. L. (1991), in Messier, R. F., Glass, J. T., Butler, J. E. and Roy, R. (eds.), New Diamond Science and Technology, Meterial Society, Pittsburg, Pennsylvania, p. 433.

Peploski, J., Thompson, D. L. and Raff, L. M. (1992), Molecular Dynamics Studies of Elementary Surface Reactions of C_2H_2 and C_2H in Lower-Pressure Diamond-Film Formation, J. Physical Chemistry, v. 96, pp. 8538-8544.

Plumley, S. (1939), Oxy-Acetylene and Arc Welding, Minn. University Printing Company.

Poferl, D. J., Gardner, N. C. and Angus, J. C. (1973), Growth of Boron-Doped Diamond Seed Crystals by Vapor Deposition, J. Appl. Phys., v. 44, no. 4, pp. 1428-1434.

Polini, R., Gazzoli, D., Molinari, E., Terranova, M. L., Ascarelli, P. and Fontana, S. (1992), Diamond Crystallites Nucleation on Sintered Tungsten: Temperature ans Thermal Treatment Effects, Diamond and related Materials, v. 1, pp. 205-210.

Ravi, K. V. and Joshi, A. (1991), Evidence for Ledge Growth and Lateral Epitaxy of Diamond Single Crystals Synthesized by the Combustion Flame Technique, Appl. Phys. Lett., v. 58, part 3, pp. 246-248.

Ravi, K. V. and Koch, C. A. (1990), Nucleation Enhancement of Diamond Synthesis by Combustion Flame Techniques, Appl. Phys. Lett., v. 57, part 4, pp. 348-350.

Roder, H. M. and Weber, L. A. (1972), Thermophysical Properties, v. 1: ASRDI Oxygen Technology Survey, NASA SP-3071, Washington.

Sato, Y. and Kamo, M. (1989), Surf. Coat. Technol., v 39/40, pp. 183-198.

Snail, K. A. and Hanssen, L.M. (1991), High Temperature, High Rate Homoepitaxial Growth of Diamond in an Atmospheric Pressure Flame, J. Crystal Growth, v. 112, pp. 651-659.

Snail, K. A. and Craigie, C. J. (1991), Synthesis of High Quality Diamonf Films in a Turbulent Flame, Appl. Phys. Lett., v. 58, part 17, pp. 1875-1877.

Snail, K. A., Vold, C. L., Marks, C. M. and Freitas Jr, J. A. (1992), High-Temperature Epitaxy of Diamond in a Turbulent Flame, Diamond and Related Materials, v. 1, pp. 180-186.

Sparrow, W. M. and Gregg, J. L. (1956), Laminar Free Convection Heat Transfer from the Outer Surface of a Vertical Circular Cylinder, Trans. ASME, v. 78, 1823.

Spear, K. E. (1987), Earth Miner. Sci., v. 56, pp. 53-59.

Spencer, E. G., Schmidt, P. H., Joy, D. H., Sansalone, F. J. (1976), Applied Phys. Lett., v. 29, 118

Spitsyn, B. V. and Deryagin, B. V. (1956), USSR Inventors Cerificate (Patent Application).

Spitsyn, B. V., Bouilov, L. L. and Deryagin, B. V. (1981), Vapor Growth of Diamond on Diamond and Other Surfaces, J. Cryst. Growth, v. 52, pp. 219-226.

Spitsyn, B. V. and Bouilov, L. L. (1988), The Growth of Diamond-Like Films from a Gas Phase, 1988, Ext. Abs. Diamond and Diamond-Like Materials Synthesis, pp. 3-14.

Suzuki, K., Sawabe, A., Yasuda, H. and Inzuka, T. (1987), Growth of Diamond Thin Films by DC Plasma Chemical Vapor Deposition, Appl. Phys. Lett., v. 50, part 12, pp. 728-729.

Suzuki, K., Sawabe, A., Yasuda, H. and Inzuka, T. (1990), Growth of Diamond Thin Films by DC Plasma Chemical Vapor Deposition and Charateristics of the Plasma, Jap. J. Appl. Phys., v. 29, no. 1, pp. 153-157.

Tzeng, Y., Cutshaw, C., Phillips, R. and Srivinyunon, T. (1990), Growth of Diamond Films on Silicon from an Oxygen-Acetylene Flame, Appl. Phys. Lett., v. 56, part 2, pp. 134-136.

Tzeng, Y., Phillips, R., Cutshaw, C. and Srivinyunon, T. (1991), Multiple Flame Deposition of Diamond Films, Appl. Phys. Lett. , v. 58, part 23, pp. 2645-2647

Vardiman, R. G., Vold, C. L., Snail, K. A., Butler, J. E. and Pande, C. S. (1989), X-ray and Electron Channeling Characterization of CVD and Combustion Deposited Diamond, Material Letters, v. 8, no 11/12, pp. 468-471.

Vargaftik, N. B. (1975), Tables of Thermophysical Properties of Liquids and Gases, Hemisphere Publishing Corp., New York.

Wilbuswas, P. (1966), Laminar -Flow Heat-Transfer in Non-Circular Ducts, Ph.D. Thesis, London University, London.

Yarbrough, W. A., Stewart M. A. and Cooper, Jr. J. A. (1989), Combustion Synthesis of Diamond, Surf. Coat. Tech., v. 39/40, pp. 241-252.

Yashiki, K., Nakamura, T., Fujimori, N. and Nakai, T. (1991), 18th Int. Conf. on Metallurgical Coating and Thin Films, San Diego, California.

Yazu, S., Sato, S. and Fujimori, N. (1988), SPIE Proceedings, August 16-20, San Diego, California.

Zhu, W., Messier, R. and Badzian, A. R. (1989), Proceedings of the First International Symposium on Diamond and Diamond-Like Films, The Electrochemical Society, Pennington, New Jersey.

Zhu, W., Tan, B. H. and Tan, H. S. (1993), Diamond Thin Films Synthesized by a Multinozzle Oxy-Acetylene Chemical Vapour Deposition Method, Thin Solid FIms, v. 236, pp. 106-110.

APPENDIX A

PROPERTIES OF DIAMOND

APPENDIX A

PROPERTIES OF DIAMOND

Diamond is a fascinating material since its mechanical, thermal, and electrical properties are very unique compared to other materials. The various properties of diamond are briefly presented and compared with others in this Appendix. Comprehensive information on the properties of diamond can be found in the book by Field (1979).

A.1 Classification of Diamond

Natural diamond can be classified into four different types (Ia, Ib, IIa, and IIb) by the degree of defects they contain. The defects are associated mainly with nitrogen contained in diamond. The properties (especially, the thermal conductivity) of diamond depend on the degree of defects (impurity).

Type Ia: About 98% of the natural diamonds are of this type. The amount of nitrogen contained in the diamond of this type, as an impurity is substantial (~1%). Nitrogen appears to be segregated into aggregates or platelets. The nitrogen which is not paramagnetic, strongly absorbs ultra-violet and infra-red light. These diamonds are optically transparent at wavelengths greater than 320 nm. At room temperature, the thermal conductivity is ~1000 W/m-K.

Type Ib: Most of the diamonds synthesized by high-pressure and high-temperature

techniques are of this type. These diamonds contain dispersed single substitutional nitrogen atoms which are paramagnetic up to 0.2%. The thermal conductivity at room temperature is ~1000 W/m-K. Optical, thermal, and electrical properties are similar to type Ia diamond.

Type IIa: Diamonds of this type are very rare in nature. They are almost free of nitrogen and have enhanced optical and thermal properties. These are transparent to ultra-violet above 225 nm and their thermal conductivities at room temperature are about 2000 W/m-K which is the limit attainable with diamond of natural isotropic constitution.

Type IIb: Diamonds of this type are extremely rare in nature. The concentration of nitrogen contained in these diamonds is the lowest among the four types of diamonds. Thus, type IIb diamonds are very pure. Generally, these are blue in color due to the presence of boron. They have good semiconducting properties. The thermal conductivity of this type diamond is slightly less than that of type IIa by 0 ~ 5%.

A.2 Properties of Diamond

Specific values of mechanical, thermal, physical and electrical properties are listed in Tables A.1, A.2, and A.3, respectively. The hardness and thermal conductivity are not compatible with other materials on earth. The thermal conductivity of diamond is a strong function of temperature and impurity, as are other electrical properties. Figure A.1 shows the variation of thermal conductivity with temperature for two type IIa diamonds having slightly different impurities. The curves shown in this figure came from the Berman and Martinez's correlation of the natural diamond thermal conductivity. As shown in Figure A.1, the thermal conductivity becomes maximum at around 80 K and falls into two

Table A.1 Mechanical Properties of Diamond (Field, 1979)

Properties at 25 °C	Values
Hardness (kg/mm^2)	10000
Coefficient of Friction	~0.1 in air ~1 in vacuum
Elastic Modulii ($\times 10^{11}$ Pa)	
C_{11}	10.8
C_{12}	1.25
C_{44}	5.77
Young's Modulus (Pa)	10.5×10^{11}
Poisson's Ratio	0.104
Bulk Modulus (Pa)	4.42×10^{11}
Tensile Strength (MPa)	~750
Compressive Strength (MPa)	~750

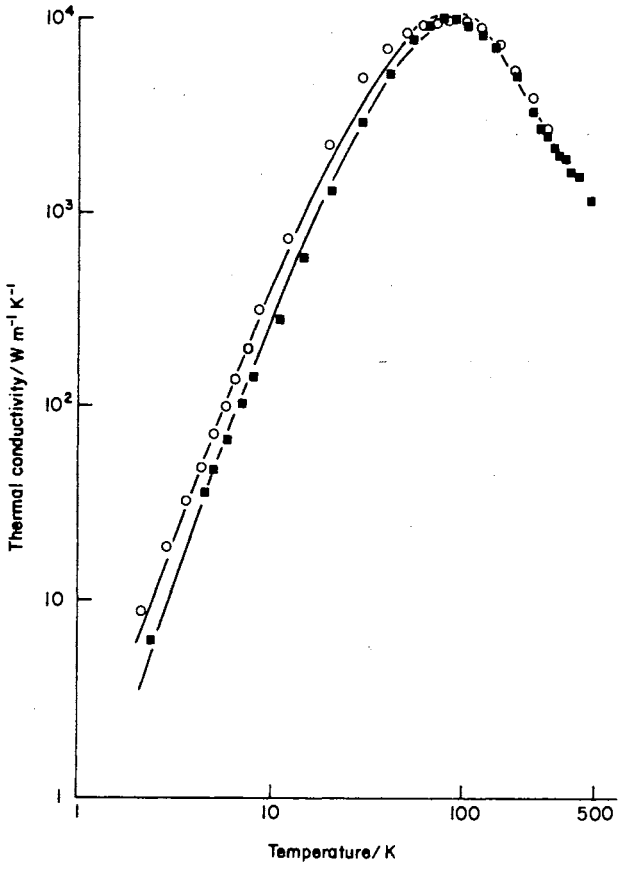

Figure A.1 The Thermal Conductivity of Two Type IIa Diamonds (Berman and Martinez, 1976)

regions, one on either side of the maximum. For a perfect diamond, the shape of thermal conductivity vs. temperature would be sharper at the maximum.

Table A.2 Thermal Properties of Diamond (Field, 1979)

Properties	Values
Thermal Conductivity (W/m-K) at 293 K	
Type Ia	600 - 1000
Type IIa	2000 - 2100
Thermal Expansion Coefficient ($\times 10^{-6}$ K^{-1})	
at 193 K	0.4
at 293 K	0.8
at 400 - 1200 K	1.5 - 4.8
Heat Capaity, c_p (J/mol-K)	
at 1800 K	24.7
at 3000 K	26.3

Table A.3 Electrical and Optical Properties of Diamond (Field, 1979; Buckley and Collins, 1992)

Properties at 25 °C	Value
Lattice Constant (nm)	0.3567
Density ($\times 10^3$ kg/m^3)	3.18
Band Gap (eV)	5.45
Saturated Electron Velocity ($\times 10^7$ cm/s)	2.7
Carrier Mobility (cm^2/V-s)	
Electron	2200
Hole	1600
Breakdown ($\times 10^5$ V/cm)	100
Dielectric Constant	5.5
Resistivity ($\times 10^{13}$ Ω cm)	2.42
Absortion Edge (μm)	0.2
Refractive Index	2.42
Johnson Figure of Merit ($\times 10^{23}$ WΩ/s^2)	73856
Keyes Figure of Merit ($\times 10^2$ W°C/cm-s)	444

Sometimes, absolute values of properties are not easy to understand physically. However, the comparison of properties with the materials used in the same applications may help one appreciate the properties of diamond. For this, Table A.4 summarizes the main mechanical, physical, and thermal properties compared with the major nitrides and carbides which are used in abrasive purposes. From Table A.4, it is clear that diamond outclasses the nitrides and the other carbides to a considerable extent. Overall, diamond represents a standard of performance against which other advanced ceramic materials can be judged.

The semiconducting properties of diamond were compared with other semiconductor materials such as beta silicon carbide, gallium arsenide, and silicon, in Table A.5. According to this table, diamond easily outclasses other advanced semiconductor materials from most perspectives. Table A.5 demonstrates the point: it is clear that the saturated electron velocity of diamond is higher than the competing materials; the carrier mobilities (especially of holes) far surpass those of other materials; the breakdown voltage is at least 60% higher than the nearest competitor; the dielectric constant is almost a factor of 2 lower than the nearest competitor; the thermal conductivity is a factor of 4 better than the nearest competitor.

Diamond is extremely inert chemically and is not affected by any acids or chemicals. Substances such as sodium nitrate are known to affect diamond in the molten state at temperatures as low as ~450 °C. When diamond is heated to high temperatures it transforms to graphite. Results of experiments on the heating of diamond in vacuum show that the onset of graphitization is detectable around 1500 °C and the rate of graphitization increases rapidly until around 2000 °C diamond completely transforms into graphite in a short time. Conversely, graphite can transform to diamond. The heat of transition from graphite to diamond at vacuum and 25 °C is 1872±75 J/mol (Hawton et al., 1966).

Table A.4 Comparison of the Representative Properties of Diamond, Ceramic Nitride, and Carbide Materials (Buckley and Collins, 1992)

	Hardness (kg/mm^2) at 25 °C	Young's Modulus ($\times 10^6$ Pa) at 100 °C	Tensile Strength ($\times 10^9$ Pa) at 25 °C	Compressive Strength ($\times 10^9$ Pa) at 25 °C	Melting Point (°C)	Thermal Conductivity (W/m-K) at 100 °C	Density ($\times 10^3 kg/m^3$)
(Nitrides)							
Si_3N_4-HPSN		280 - 310	320	689 - 2760	1871	22 - 32	3.18
Si_3N_4-RBSN	1700 - 2200	140 - 250	79 - 200	340 - 620	1871	4 - 10	3.18
Sialon	2500 - 3500	300	400	3500		20 - 25	3.2
Sl_2ON_2	1580	100 - 200			1550	6.5	3.1
AlN	1225	27 - 34		2070	2299	30	3.26
TiN	1800	599			2950	5 - 10	5.44
ZrN	1500	496			2980	11	13.94
BN(hex)	210 - 390	41 -103	50	103 -290	2704	30 - 40	2.28
Diamond	**10000**	**1000**	**~750**	**~750**	**4000**	**2000**	**3.5**
(Carbides)							
B_4C	2800	290 - 450	330	2752	2427	15 - 25	2.52
SiC-HPSC	2500	400 - 430	300	1380 - 3900		65	3.21
TiC	2700 - 3300	460	241	757 - 2958	3067	30	4.92
ZrC	2700 - 3300	370	103	826 - 2958	3420	23	6.56
HfC	2700 - 3300	290			3928	14	12.67
NbC	1900 - 2600	440	244	2374	3497	16	7.82
TaC	1600 - 2400	490	96 - 291		3879		14.60
Cr_2C_3	1350 - 2280	385		1039	1893		6.68
Mo_2C	1500 - 1800	227 - 533		901	2488		9.12
Wc	1700 - 2400	668	344	2683 - 2958	2777	86.0	15.8

Table A.5 Comparison of the Properties of Diamond and Semiconducting Materials (Field, 1979; Bukley and Collins, 1992)

Properties	Diamond	β-Silicon Carbide	GaAs	Silicon
Lattice Constant (A)	3.567	4.358	5.65	5.430
Thermal Expansion ($\times 10^{-6}$/°C)	1.1	4.7	5.9	2.6
Density (g/cm^3)	3.515	3.216		2.438
Melting Point (°C)	4000	2540	1238	1420
Bandgap (eV)	5.45	3.0	1.43	1.1
Saturated Electron Velocity ($\times 10^7$ cm/s)	2.7	2.5	1.0	1.0
Carrier Mobility (cm^2/V-s)				
Electron	2200	400	8500	1500
Hole	1600	50	400	600
Breakdown ($\times 10^5$ V/cm)	100	40	60	3
Dielectric Constant	5.5	9.7	12.5	11.8
Resistivity (Ω cm)	2.42×10^{13}	150	10^8	10^3
Thermal Conductivity (W/m-K)	2000	500	46	150
Absorption Egde (μm)	0.2	0.4		1.4
Refractive Index	2.42	2.65	3.4	3.5
Johnson Figure of Merit ($\times 10^{23}$ WΩ/s^2)	73856	10240	62.5	9.0
Keyes Figure of Merit ($\times 10^2$ W °C/cm-s)	444	90.3	6.3	13.8

APPENDIX B

INSTRUMENT SPECIFICATIONS

APPENDIX B

INSTRUMENT SPECIFICATIONS

Mass Flow Meters

Model: MKS 2259C

Full Scale Ranges: 10.0 l/min (acetylene) and 5.0 l/min sccm (oxygen)

Accuracy: ±0.8% of full scale at 760 torr/0 °C

Resolution: 0.1% of full scale

Settling Time: less than two seconds within 2% of set point

Maximum Inlet Pressure: 1034 kPa in gauge pressure

Mass Flow Programmer

Model: MKS 147B

Number of Built Channels: four

Measuring Rate: 250 msec/measurement

Output Rate: 4 measurements/sec

Input Voltage: 4 × 0-5 VDC (flow signal)

Output Voltage: 4 × 0-5 VDC (flow set points)

Dual Wavelength Infrared Pyrometer

Model: Williamson Tempmatic 8000 Series

Accuracy: 0.75% of full scale in the ideal working condition

Repeatability: 0.25% of full scale in the ideal working condition

Working Distance: 15 to 91 cm

Response Time: Adjustable 0.2 to 5 seconds

Range: 550-1100 °C

Target Area: minimum 0.635 cm of diameter at the working distance of 45.7 cm

Datalogger

Model: Electronic Controls Design Model 5100

Accuracy: 0.1 °C in T-type and 1.0 °C in B-type thermocouples, respectively

Resolution: 0.1 °C in T-type and 1.0 °C in B-type thermocouples, respectively

Response Time: approximately 0.1 sec

Number of Built-In Channels: forty

Data Acquisition: built-in RAM for temporary storage of temperature data, A software supplied by datalogger manufacturer can interface the datalogger with a personal computer through a shielded cable.

Control System: Functions such as type of thermocouple, log interval, unit, etc., can be adjusted by using the keyboard.

APPENDIX C

RADIATION HEAT TRANSFER AT SURFACES SURROUNDED BY FLAME

APPENDIX C

RADIATION HEAT TRANSFER AT SURFACES SURROUNDED BY FLAME

The substrate and heat sink are surrounded by a combustion flame as shown in Figure C.1. The combustion flame is at about 1500 °C, and observed to be thin and transparent optically. The air between the flame and system (substrate and heat sink) is assumed to have a stratified density profile. In a stratified fluid, the fluid motion is restricted due to buoyancy force (Ghajar and Bang, 1993b). Thus, the agitation of the air due to flame stretching can be negligible. This implies that heat exchange between the flame and system occurs by radiation and conduction. The main purpose of the computer simulations is to predict the temperature field of the system (especially substrate surface temperatures) by solving discretization equations derived from the heat conduction equation for all control volumes in the computational domain. Radiation and conduction between the flame and the system are treated as a source term in the discretization equations for heat conduction as discussed in Chapter IV. Therefore, it is necessary to build an appropriate source term formula for the radiation and conduction for the region of the system surrounded by the combustion flame. This Appendix presents derivations of net radiative heat transfer rate at a control surface and configuration factor between the control surfaces of the substrate and heat sink, and estimation of the combustion flame emissivity.

Nomenclature

English Letters

A	surface area
dA1	differential area in a finite area, A1
F_{ij}	configuration factor, the fraction of the radiative energy leaving i-surface that arrives at j-surface
G	irradiation absorbed at a control surface
L_e	mean beam length for radiation
P	pressure
q	net radiative heat transfer rate
$q_{i\to j\to k}$	irradiation absorbed at k-surface; originally emitted at i-surface, then reflected at j-surface, finally absorbed at k-surface
R1	radius of area 1 which is the radius of the substrate (see Figure C.2)
r	radial direction
T	temperature (K)

Greek Letters

α	absorptivity
β	angle of a finite area
ε	emissivity
$\Delta\varepsilon$	correction for spectral overlap in emissivity
φ	relative angle between two differential areas (see Figure C.2)
θ	angle from normal
ρ	reflectivity
σ	Stefan-Boltzmann constant (5.67×10^{-8} W/m^2-K^4)

Subscripts

f	flame
h	h-th control surface in i-direction (see Figure C.1)
i	control surfaces in i-direction (see Figure C.1)
j	control surfaces in j-direction (see Figure C.1)
k	k-th control surface in j-direction (see Figure C.1)
1, 2	at area 1 or 2

C.1 Radiation Heat transfer

The actual situation in heat exchange between the flame and system is very complicated. However, that can be simplified as long as the simplification does not change the actual situation significantly. Several assumptions are required to simplify the heat exchange between the flame and system. These are:

- Steady state
- Surfaces of the system exposed to the flame are diffuse, gray, and opaque.
- Air between the flame and system is transparent to radiation.
- Reflectivity of the flame is negligible.

Figure C.1 shows the schematic of the given situation. Selecting the k-th control surface on j surfaces (substrate) and using the negative sign for the energy leaving a surface, the net radiative transfer rate to the control surface (q_k) can be expressed in terms of the surface emissive power and the absorbed irradiation as

$$q_k = \sum G - A_k \varepsilon_k \sigma T_k^4 \qquad \text{(C.1)}$$

where G presents any kind of irradiation absorbed at the control surface. The irradiation absorbed at the control surface comes from the flame and the heat sink surface (i-surfaces) through the air surrounded by the i and j surfaces and the flame. The sources of the absorbed irradiation are the emissive powers from i and j surfaces and the flame. Thus,

the irradiation absorbed at the control surface can be estimated by tracing all of the emissive powers.

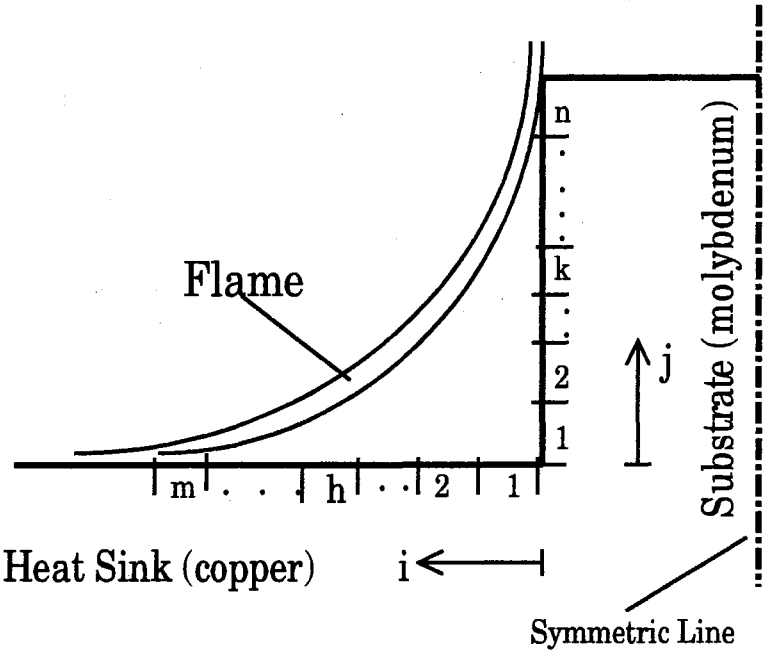

Figure C.1. Schematic Diagram of the Surfaces Surrounded by Flame

First, the surface emissive power from the flame is considered. From the surface emissive power of $A_f \varepsilon_f \sigma T_f^4$, the amount of energy absorbed directly at the control surface ($q_{f \to k}$) is

$$q_{f \to k} = A_f \varepsilon_f \sigma T_f^4 F_{fk} \alpha_k \qquad \text{(C.2)}$$

The rest of the surface emissive power is reflected at the control surface to the flame and i-surfaces. The amount of the irradiation reflected to the i-surfaces ($q_{f \to k \to i}$) is negligible since the absorptivity at the j-surfaces is high (α_k = 0.8) and F_{ki} is small. The energy reflected at the control surface to the flame ($q_{f \to k \to f}$) is not reflected again to the control surface since the reflectivity of the flame is negligible. The reflectivity of i-surfaces is not

negligible (α_i = 0.5). Thus, from the energy which comes to i-surfaces from the flame surface emissive power, the amount of energy reflected at the i-surfaces to the control surface ($q_{f\to i\to k}$) is not relatively negligible. $q_{f\to i\to k}$ is given by

$$q_{f\to i\to k} = A_f \varepsilon_f \sigma T_f^4 \sum_i (F_{fi}\rho_i F_{ik}\alpha_k) \tag{C.3}$$

Further consideration such as $q_{f\to i\to k\to i\to k}$ is negligible.

Next, the emissive powers from i-surfaces (heat sink) are considered. From the surface emissive powers of $\sum_i (A_i\varepsilon_i\sigma T_i^4)$, the amount of energy absorbed at the control surface ($q_{i\to k}$) is

$$q_{i\to k} = \sum_i (A_i\varepsilon_i\sigma T_i^4 F_{ik}\alpha_k) \tag{C.4}$$

and the rest of all the i-surface emissive powers arrived at the control surface is reflected to the flame ($q_{i\to k\to f}$) and i surfaces ($q_{i\to k\to i}$). $q_{i\to k\to f}$ is not reflected again at the flame to the control volume since the reflectivity of the flame is negligible. From the irradiation reflected to the i surfaces ($q_{i\to k\to i}$), the amount of energy to be reflected again to j-surfaces is negligible.

Finally, the emissive powers from j-surfaces, $\sum_j (A_j\varepsilon_j\sigma T_j^4)$, are considered. The consideration may be limited to $q_{j\to i\to k}$ only. It can be written as

$$q_{j\to i\to j} = \sum_j [A_j\varepsilon_j\sigma T_j^4 \sum_i (F_{ji}\rho_i F_{ik}\alpha_k)] \tag{C.5}$$

Therefore, summation of all kinds of irradiation absorbed at the control surface (k-th control surface on j-surfaces) can be expressed by

$$\sum G = q_{f\to k} + q_{f\to i\to k} + q_{i\to k} + q_{j\to i\to k} \tag{C.6}$$

Substituting into Equation (C.1) gives

$$q_k = q_{f\to k} + q_{f\to i\to k} + q_{i\to k} + q_{j\to i\to k} - A_k\varepsilon_k\sigma T_k^4 \tag{C.7}$$

Substituting Equations (C.2) through (C.5) into Equation (C.7),

$$q_k = \alpha_k \varepsilon_f \sigma T_f^4 [A_f F_{fk} + \sum_i (A_f F_{fi} \rho_i F_{ik})] + \alpha_k \sum_i (\varepsilon_i \sigma T_i^4 A_i F_{ik})$$

$$+ \sum_j [A_j \varepsilon_j \sigma T_j^4 \sum_i (F_{ji} \rho_i F_{ik} \alpha_k)] - A_k \varepsilon_k \sigma T_k^4$$

Applying $\alpha_k = \varepsilon_k$ and $\rho_i = 1 - \varepsilon_i$ since the substrate and heat sink are opaque,

$$q_k = \varepsilon_k \varepsilon_f \sigma T_f^4 [A_f F_{fk} + \sum_i A_f F_{fi} (1-\varepsilon_i) F_{ik}] + \varepsilon_k \sum_i (\varepsilon_i \sigma T_i^4 A_i F_{ik})$$

$$+ \sum_j [A_j \varepsilon_j \sigma T_j^4 \varepsilon_k \sum_i (1-\varepsilon_i) F_{ji} F_{ik}] - A_k \varepsilon_k \sigma T_k^4 \qquad \text{(C.8)}$$

From the reciprocity $A_f F_{fk} = A_k F_{kf}$, $A_f F_{fi} = A_i F_{if}$, $A_i F_{ik} = A_k F_{ki}$,

and $A_i F_{ij} = A_j F_{ji}$

From $\sum F = 1$, $F_{kf} = 1 - \sum_i F_{ki}$ and $F_{kf} = 1 - \sum_i F_{ki}$

Substituting these into Equation (C.8) and rearranging gives

$$q_k = \varepsilon_k \varepsilon_f \sigma T_f^4 [A_k F_{kf} + \sum_i (A_i - \sum_j A_j F_{ji})(1-\varepsilon_i) \frac{A_k}{A_i} F_{ki}] + \varepsilon_k \sum_i (\varepsilon_i \sigma T_i^4 A_k F_{ki})$$

$$+ \varepsilon_k \sum_j [A_j \varepsilon_j \sigma T_j^4 \sum_i (1-\varepsilon_i) \frac{A_k}{A_i} F_{ji} F_{ki}] - A_k \varepsilon_k \sigma T_k^4 \qquad \text{(C.9)}$$

The net radiative heat transfer rate at a control volume on i-surfaces can be expressed as similar to Equation (C.9) using the same procedure for deriving q_k above. Selecting the h-th control surface on i-surfaces (heat sink) and using the negative sign for the energy leaving a surface, the net radiative transfer rate at the control surface (q_l) would be

$$q_h = \varepsilon_h \varepsilon_f \sigma T_f^4 [A_h F_{lf} + \sum_j (A_j - \sum_i A_i F_{ij})(1-\varepsilon_j) \frac{A_h}{A_j} F_{hj}] + \varepsilon_h \sum_j (\varepsilon_j \sigma T_j^4 A_h F_{hj})$$

$$+ \varepsilon_h \sum_i [A_i \varepsilon_i \sigma T_i^4 \sum_j (1-\varepsilon_j) \frac{A_h}{A_j} F_{ij} F_{hj}] - A_h \varepsilon_h \sigma T_h^4 \qquad \text{(C.10)}$$

C.2 Configuration Factor Between the Control Surfaces of the Substrate and Heat Sink

Configuration factor between two control surfaces of the substrate and heat sink is required in calculation of the net radiative heat transfer rate at a control surface [see Equations (C.9) and (C.10)].

From Figure C.2a, $\cos\theta_1$, $\cos\theta_2$, and S are seen to be

$$\cos\theta_1 = \frac{c}{S}, \quad \cos\theta_2 = \frac{y}{S}, \text{ and } \quad S^2 = y^2 + b^2$$

Figure C.2b allows evaluation of b and c, where $\cos\varphi$ and h are seen to be

$$\cos\varphi = \frac{R1 + c}{r} \quad \text{and} \quad h = r\cos\varphi$$

Here, $\cos\varphi$ relation gives $c = r\cos\varphi - R1$

Substituting c and h into $b^2 = c^2 + h^2$ (see Figure C.2b),

$$b^2 = r^2 + R1^2 - 2rR1\cos\varphi$$

Substituting b^2 into S^2 equation,

$$S^2 = y^2 + r^2 + R1^2 - 2rR1\cos\varphi \qquad \text{(C.11)}$$

Using $c = r\cos\varphi - R1$, $\cos\theta_1$ can be expressed by

$$\cos\theta_1 = \frac{r\cos\varphi - R1}{S} \qquad \text{(C.12)}$$

Configuration factor, F_{dA1-A2} is expressed by the following equation.

$$F_{dA1-A2} = \int \frac{\cos\theta_1 \cos\theta_2}{\pi S^2} dA2$$

where $dA2 = r\,dr\,d\varphi$ and $0 \le \varphi \le \pi$

Substituting $\cos\theta_1 = \frac{c}{S}$, $\cos\theta_2 = \frac{y}{S}$, Equation (C.11) and (C.12) into the above equation,

$$F_{dA1-A2} = \frac{y\,r\,dr}{\pi} \int \frac{r\cos\varphi - R1}{y^2 + r^2 + R1^2 - 2rR1\cos\varphi} d\varphi \,, \; 0 \le \varphi \le \pi \qquad \text{(C.13)}$$

In Equation (C.13), the dependence of F_{dA1-A2} on dr was neglected. Equation (C.13) is for the configuration factor between a differential area ($dA1$) and a finite area ($A2$).

The configuration factor between two finite areas, F_{A1-A2} is expressed by

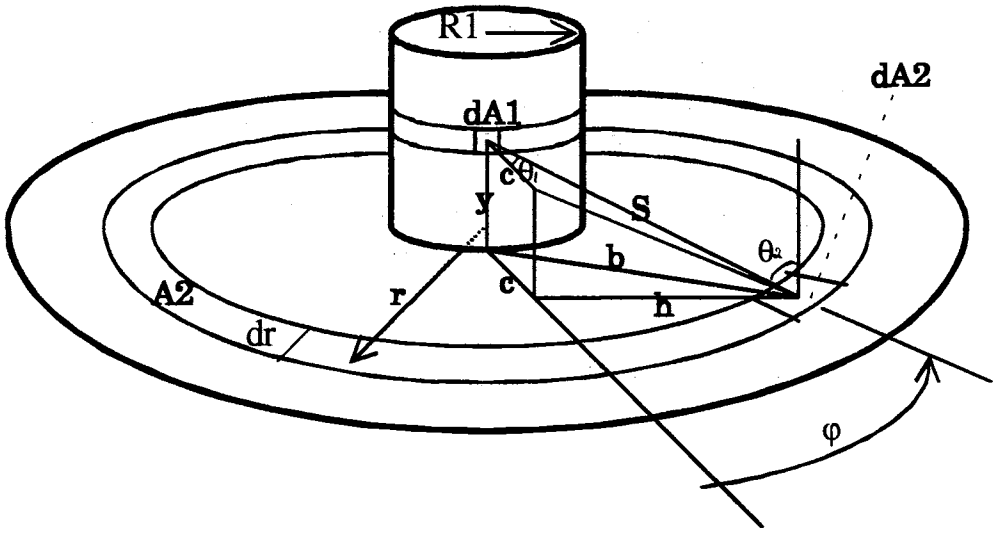

(a)

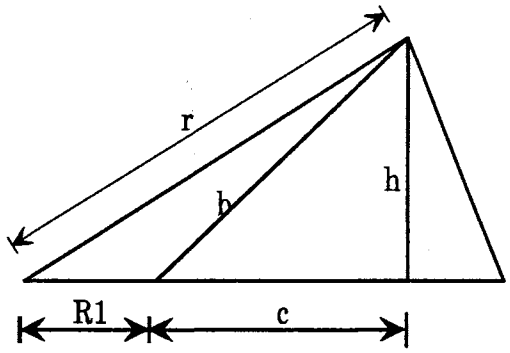

(b)

Figure C.2. Geometry for Radiative Exchange between Differential Areas of Substrate and Heat Sink: (a) Geometry of the System; (b) Auxiliary Construction for Determining b and c

$$F_{A1-A2} = \frac{1}{A1}\int F_{dA1-A2}\, dA1$$

where $dA1 = dy\, R1\, d\beta$ with $0 \le \beta \le 2\pi$. Neglecting the dependence of F_{dA1-A2} on dy gives

$$F_{A1-A2} = F_{dA1-A2}$$

Thus, the results of the left hand side of Equation (C.13) is the configuration factor between two finite areas of A1 and A2 (F_{A1-A2}). F_{A1-A2} means the fraction of the radiative energy leaving a finite surface, A1, of the substrate that arrives at a finite surface, A2, of the heat sink. Sometimes it is expressed as F_{A1A2}. Finally, F_{A1-A2} has the following expression after solving the integration part in the left hand side of Equation (C.13).

$$F_{A1-A2} = \frac{2y\,r\,dr}{\pi(K+2r\,R1)^2}\left[\frac{(K+2r\,R1)(r-R1)}{K-2r\,R1}+(r+R1)\right]\left[\frac{K+2r\,R1}{2K}+\sqrt{\frac{K+2r\,R1}{K-2r\,R1}}\tan^{-1}\sqrt{\frac{K+2r\,R1}{K-2r\,R1}}\right]$$

$$-\frac{4y\,r\,dr(r+R1)}{\pi(K+2rR1)^2}\sqrt{\frac{K+2rR1}{K-2rR1}}\tan^{-1}\sqrt{\frac{K+2rR1}{K-2rR1}} \qquad \text{(C.14)}$$

where $K = y^2 + R1^2 + r^2$

C.3 Estimation of Flame Emissivity

For the estimation of combustion flame emissivity (ε_f), several assumptions are needed. The proposed assumptions are:

- Flame is a hot gas consisting of CO_2, H_2O, and N_2.
- Flame temperature is constant (approximately 1773 K).
- Nitrogen in the flame does not emit or absorb radiative energy.
- Total pressure of the flame is 1 atm.

From the assumptions, only CO_2 and H_2O emit radiative energy. Then, the flame emissivity (ε_f) is given by

$$\varepsilon_f = \varepsilon_{CO2} + \varepsilon_{H2O} - \Delta\varepsilon \qquad \text{(C.15)}$$

where $\Delta\varepsilon$ is band gap correction. Emissivities of H_2O and CO_2 can be estimated using the Hottel's charts of ε_{CO2} and ε_{H2O} (Hottel, 1954). To use the Hottel's charts, partial

pressures of CO_2 and H_2O (P_{CO_2}, P_{H_2O}), and mean beam length (L_e) according to the geometry of the gas (flame) are needed.

Oxidization of one mole of C_2H_2 from the tank is expressed by the following reaction equation.

$$C_2H_2 + O_2 + 1\tfrac{1}{2}(O_2 + 4N_2) \rightarrow 2CO_2 + H_2O + 6N_2 \qquad \text{(C.16)}$$

where one mole of oxygen is supplied from the oxygen tank and one and half moles of oxygen is supplied from the ambient air. Thus, the partial pressures of CO_2 and H_2O in the flame are 2/9 and 1/9 atm, respectively.

The flame radiates to the entire surface surrounded by the flame (see i and j surfaces in Figure C.1). The mean beam length (L_e) in the given situation shown in Figure C.1, can be calculated by the following relation (Incropera and De Witt, 1990).

$$L_e = 3.6V/A$$

where V is volume of the flame and A is the area of the surface exposed to the flame. In the given situation, the volume of the flame and area of the surface exposed to the flame depend on the height of the substrate from the heat sink (substrate-heat sink distance, H_S). For H_S = 7.0 mm, the resulting mean beam length is about 7.36 mm. Then, from Hottel's charts for the case of H_S = 7.0 mm with P_{CO_2} of 2/9 atm, P_{H_2O} of 1/9 atm, and L_e of 7.36 mm, the resulting emissivities of CO_2 and H_2O, and the band gap correction are:

$\varepsilon_{CO_2} \approx 0.007$, $\varepsilon_{H_2O} \approx 0$, and $\Delta\varepsilon \approx 0$

Substituting these into Equation (C.15) gives $\varepsilon_f \approx 0.007$.

Using the same procedure as above, the resulting flame emissivities for different H_S's are tabulated in Table C.1

Table C.1. Oxy-Acetylene Flame Emissivities with Different Substrate-Heat Sink Distances

Substrate-Heat Sink Distance (mm)	Flame Emissivity
0.7	0.014
2.0	0.011
4.0	0.0095
7.0	0.007

APPENDIX D

ESTIMATION OF HEAT TRANSFER COEFFICIENTS AND UNCERTAINTY ANALYSIS

APPENDIX D

ESTIMATION OF HEAT TRANSFER COEFFICIENTS AND UNCERTAINTY ANALYSIS

The procedure for estimation of the heat transfer coefficients and uncertainty analysis are presented in this Appendix. Selected sample calculations for estimation of the heat transfer coefficients are also presented. In the calculations, the thermophysical properties of air and tap water were obtained from *Tables of Thermophysical Properties of Liquid and Gases* by Vargaftik (1975) and NASA SP-3071 by Roder and Weber (1972), respectively.

D.1 Estimation of Heat Transfer Coefficients

In the computer simulations for the prediction of the temperature field of the system including the substrate surface temperatures, average heat transfer coefficients of the ambient air and the coolant were required. Undoubtedly, proper values of these heat transfer coefficients were desired for the reliable results from the computer simulations. These heat transfer coefficients are dependent on the properties of air or coolant (tap water) which vary with temperature. Thus, some experiments for the temperature measurements were done in order to get relatively proper values of the average heat transfer coefficients. Among all the simulations, SIM1 was chosen as a sample case for the illustration of the procedure of the average heat transfer coefficients estimation. The simulation condition of SIM1 were: D_n = 1.067 mm; Q_{O2} = 2.5 l/min; Q_{C2H2} = 2.55

l/min; Q_C = 0.76 l/min; and H_S = 7.0 mm. The results of the temperature measurements for SIM1 are listed in Table D.1.

Table D.1 Results of Temperature Measurements for SIM1

	Ambient Air	Cylindrical Surface of Heat Sink	Bottom of Heat Sink	Coolant
Temperature (°C)	23.0	85.0	87.0	T_{in} = 25.4 T_{out}=63.4

As discussed in Chapter IV, the average heat transfer coefficient, $\bar{h}$, related to the free convection on the cylindrical surface of the heat sink can be calculated by the following nondimensional correlation (Churchill and Chu, 1975).

$$\overline{Nu_L} = 0.68 + \frac{0.67 Ra_L^{1/4}}{\left[1+(0.492/\mathrm{Pr})^{9/16}\right]^{4/9}} \qquad (0 < Ra_L < 10^9) \qquad (14)$$

where, $\overline{Nu_L}$ is the average Nusselt number based on the height of the cylinder (L), defined as $\overline{Nu_L} = \bar{h}L/k$ (k is the thermal conductivity of the ambient air). The height of the heat sink is 0.0254 m. The Rayleigh number shown in Equation (14) is defined as

$$Ra_L = \frac{g\beta(T_w - T_\infty)L^3}{\nu\alpha}$$

where, g is the gravitational acceleration; β is the volumetric thermal expansion coefficient of ambient fluid (air); T_W is the temperature of the surface exposed to free convection; T_∞ is the ambient fluid (air) temperature; ν is the kinematic viscosity of ambient fluid (air); and α is the thermal diffusivity of ambient fluid (air). All properties of air such as β, ν, α, and Pr used in calculating Ra_L and $\overline{Nu_L}$ were evaluated at the film temperature of $(T_W + T_\infty)/2$. The temperatures of the cylindrical surface of the heat sink and the ambient temperature in SIM1 were 85.0 and 23.0 °C , respectively as shown

in Table D.1. Thus, the film temperature of the ambient air over the cylindrical surface of the heat sink was 54 °C.

Table D.2 gives all the properties of the ambient air needed for the estimation of the average heat transfer coefficient of the air at the cylindrical surface of the heat sink. All properties shown in this table were estimated at the film temperature of 54 °C. Calculation of Ra_L with the properties shown in Table D.2, T_W = 85.0 °C, T_∞ = 23.0 °C, and L = 0.0254 m yields Ra_L = 63225 which is less than 10^9. Thus, Equation (14) can be applied for the calculation of the average Nusselt number. The calculated average Nusselt number is 8.824. Finally, the average heat transfer coefficient of the ambient air at the cylindrical surface of the heat sink in SIM1 is 9.78×10^{-6} W/mm^{2}K from $\overline{Nu_L} = \bar{h}L/k$ with k of 28.15×10^{-3} W/m·K as given in Table D.2.

Table D.2 Properties of the Ambient Air for Estimation of Average Heat Transfer Coefficient at the Cylindrical Surface of Heat Sink in SIM1

β (K^{-1})	ν (m^2/s)	Pr	k (W/m·K)
3.058×10^{-3}	18.4×10^{-6}	0.702	28.15×10^{-3}

The average heat transfer coefficient related to the free convection on the bottom surface of the heat sink can be calculated by the following nondimensional correlation (Goldstein et al., 1973) as discussed in Chapter IV.

$$\overline{Nu_{Lc}} = 0.54 Ra_{Lc}^{1/4} \qquad (10^4 < Ra_{Lc} < 10^7) \qquad (15)$$

The convection heat transfer characteristic length (L_C) in Equation (15) is defined as the ratio of plate surface area to the plate perimeter. The radius of the heat sink was 0.058 m. Then, the characteristic length, L_C, is calculated as

$$L_c = \frac{\pi(0.058)^2}{2\pi(0.058)} = 0.029\ m$$

Temperature at the bottom surface of the heat sink was 87 °C which is close to that at the cylindrical surface (85 °C) as shown in Table D.1. The resulting film temperature of the ambient air at the bottom surface of the heat sink is 55 °C which has only 1 °C difference compared to that at the cylindrical surface. The change of the properties of air due to 1 °C can be negligible. Thus, the estimated properties of the ambient air for the calculation of the average heat transfer coefficient at the cylindrical surface of the heat sink can be used for that at the bottom surface of the heat sink. In the calculation of the Rayleigh number, the characteristic length calculated above is applied. Using the properties of air given in Table D.2, the resulting Rayleigh number is 9683 which is in the restricted range of Rayleigh number for Equation (15). Calculation of the Nusselt number by Equation (15) gives $\overline{Nu_{Lc}} = 9.525$. Finally, the average heat transfer coefficient of the ambient air at the bottom surface of the heat sink in SIM1 is 9.78×10^{-6} W/mm^{2}K from $\overline{Nu_L} = \bar{h} L_C/k$ with k of 28.15×10^{-3} W/m·K as given in Table D.2 and L_C of 0.029 m.

Table D.3 Properties of Water at 44.4 °C

ν (m^2/s)	Pr	k (W/m·K)	ρ (kg/m^3)	c_p (W/kg K)
60.58×10^{-8}	3.95	0.633	990.2	4180

Some properties of the coolant in SIM1 are given in Table D.3. These properties were estimated at the average coolant temperature (44.4 °C) from the measured inlet and outlet coolant temperatures shown in Table D.1. The heat transfer mechanism in the heat dissipation into the coolant inside the heat sink is forced convection. The heat transfer coefficient in the forced convection inside a duct is strongly dependent on the flow regime (laminar, transition, or turbulent) and the configuration of the fluid flowing region. In most of the conducted experiments, the coolant flow inside the heat sink was laminar.

Obviously, the coolant flow was hydrodynamically and thermally developing. Moreover, the configuration of the coolant flowing region in the heat sink is a 360° bend as shown in Figure 3.2. There is no correlation or data for the average heat transfer coefficient of the coolant corresponding to the given conditions of the coolant flowing inside the heat sink. However, the combination of the results from Wilbuswas (1966) and Boelter et al. (1948) may give the appropriate average heat transfer coefficient of the coolant inside the heat sink.

Table D.4 Modified Results from Wilbuswas (1966) and Boelter et al. (1948)

x*	0.002	0.0025	0.00286	0.00333	0.00385	0.00455
Nu_m	17.4	15.4	14.75	14.05	13.45	12.75

x* is nondimensional length and Nu_m is mean Nusselt number.
x* = x/(D_hRePr) where x is the distance from the inlet; D_h is hydraulic diameter; and Re is Reynolds number.

The available data from Wilbuswas and Boelter et al. are shown in Table D.4. The hydraulic diameter shown in this table is defined by

$$D_h = 4A_c/P$$

where Ac is the cross-sectional area of the flow region and P is the wetted perimeter. The calculated hydraulic diameter of the system in this study was 0.017 m with $A_c = 3.2258\times 10^{-4}$ m^2 and $P = 0.017$ m. The Reynolds number is defined by

$$Re = VD_h/\nu$$

where V is the average velocity of the coolant inside the heat sink. The average velocity can be calculated from the coolant flow rate using $V = Q_c/A_c$. The average velocity of the coolant in SIM1 is 0.039 m/s with Q_c of 0.76 l/min and A_c of 3.2258×10^{-4} m^2. Then, the Reynolds number in the coolant flow of SIM1 turns out to be about 1100. In the heat sink, the ratio of the flowing length for the coolant between inlet and outlet to D_h is about 9.4. Then, the nondimensional length (x*) in the coolant flow can be calculated by its

definition given below Table D.4. The result is $x^* = 2.16\times10^{-3}$ which is in the range of x* given in Table D.4. Thus, the corresponding mean Nusselt number can be estimated by interpolation: $Nu_m \approx 17.077$. Finally, the average heat transfer coefficient ($\bar{h}$)of the coolant in SIM1 can be calculated using $\overline{Nu_m} = \bar{h}D_h/k$ (k is available from Table D.3). The calculated $\bar{h}$ is 635.0×10^{-3} W/mm^2-K.

However, the available data from Wilbuswas and Boelter et al. are limited for the use of this study. The calculated nondimensional lengths (x*'s) in the coolant flow for all cases in this study are in the range of 0.000607 to 0.00216. Thus, in most cases,the data given in Table D.4 can not be used directly to estimate the average heat transfer coefficients of the coolant. In order to make the estimation of $\bar{h}$ of coolant in all cases in this study, a correlation equation of $\bar{h}$ vs. x* was made by curve fitting the data given in Table D.4. Figure D.1 shows the results from the curve fitting with the data given in Table D.4. The deviations between the results from the curve fitting and Wilbuswas and Boelter et al. were within ±6.2% in the region where the data from Wilbuswas and Boelter et al. are available.

D.2 Uncertainty Analysis

The probable error in the experimental measurements of substrate temperature (T_S), inlet and outlet coolant temperatures (T_{in} and T_{out}), flow rate of coolant (Q_C), flow rates of oxygen and acetylene (Q_{O_2} and $Q_{C_2H_2}$), and heat dissipation rate into the coolant (q_C) can be expressed by their uncertainty intervals (δ's). Except for the heat dissipation rate into the coolant, the uncertainty interval can be estimated from the instrumentation errors as follow:

$\delta T_S = \pm(0.01T_S + 1.0)$ °C due to errors from B-type thermocouple and datalogger

$\delta T_{in} = \pm(0.5 + 0.1)$ °C due to errors from T-type thermocouple and datalogger

$\delta T_{out} = \delta T_{in} = \pm0.6$ °C

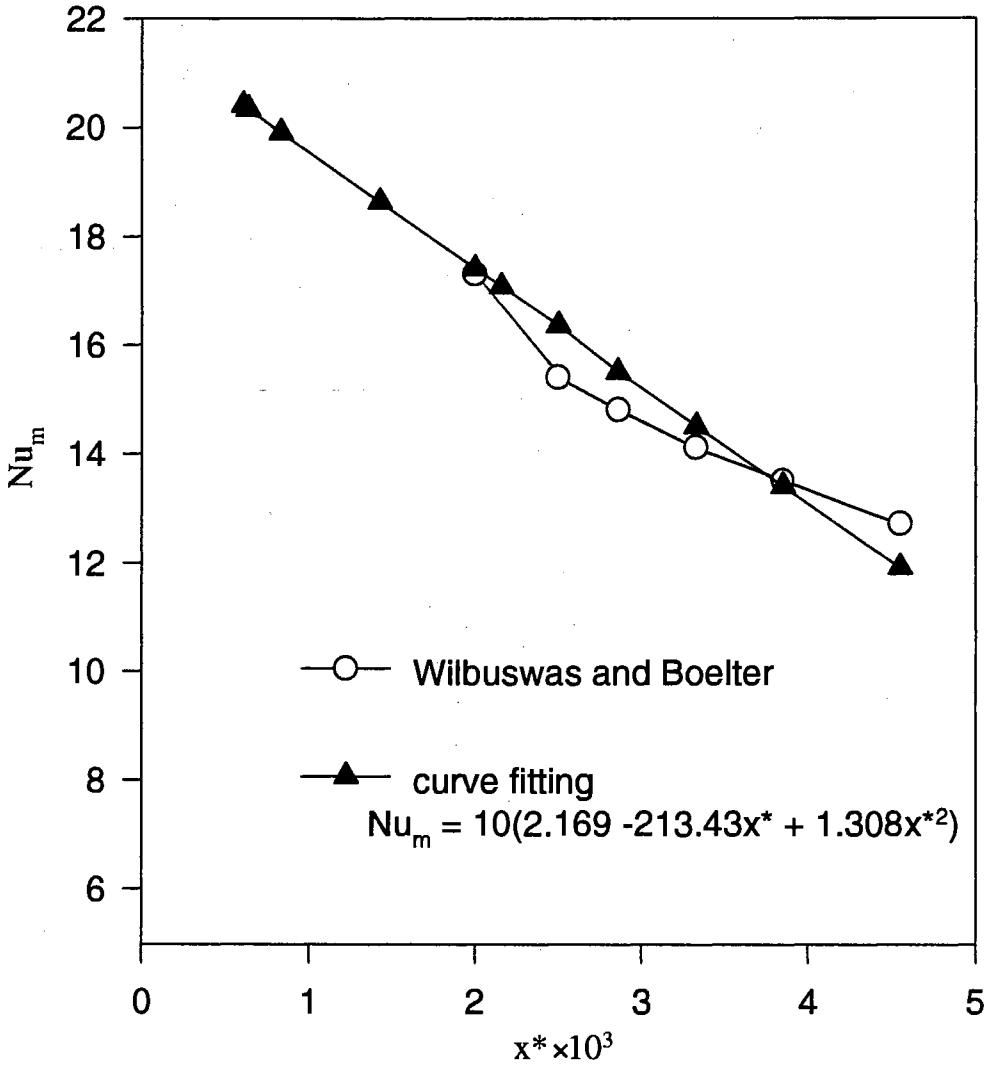

Figure D.1 Results of Curve Fitting Using the Modified Data from Wilbuswas (1966) and Boelter et al. (1948)

$\delta Q_C = \pm 0.02 Q_C$

$\delta Q_{O2} = \pm(0.008 \times 5.0 \text{ l/min}) = \pm 0.04 \text{ l/min}$

$\delta Q_{C2H2} = \pm(0.008 \times 10.0 \text{ l/min}) = \pm 0.08 \text{ l/min}$

Thus, uncertainty intervals in T_{in}, T_{out}, Q_{O2}, and Q_{C2H2} were constant through the experiments as ±0.6°C in T_{in} and T_{out}; ±0.04 l/min and ±0.08 l/min in Q_{O2} and Q_{C2H2}, respectively. The uncertainty interval in Q_C was 2%. However, the uncertainty interval in T_S (δT_S) depends on the measured temperature. The maximum δT_S in the conducted experiments was found in EXP5. These experiments were conducted in order to study the effect of substrate temperature on morphology and quality of diamond films, where the (highest) temperature at the center was 1059°C. The calculated uncertainty interval in the substrate temperature of 1059°C was 11.6°C or 1.1%.

The heat dissipation rate into the coolant is calculated by

$$q_c = Q_c \rho c_p (T_{out} - T_{in}) \tag{16}$$

Here, the density and specific heat of coolant are assumed to be accurately known. From Kline and McClintock (1953), the uncertainty in q_C may then be found as

$$\delta q_c = \pm\left[\left(\frac{\partial q_c}{\partial Q_c}\delta Q_c\right)^2 + \left(\frac{\partial q_c}{\partial \Delta T}\delta \Delta T\right)^2\right]^{1/2} \tag{D.1}$$

where $\Delta T = T_{out} - T_{in}$. The uncertainty in ΔT can be calculated by

$$\delta \Delta T = \pm\left[\left(\frac{\partial \Delta T}{\partial T_{out}}\delta T_{out}\right)^2 + \left(\frac{\partial \Delta T}{\partial T_{in}}\delta T_{in}\right)^2\right]^{1/2} \tag{D.2}$$

Substituting $\delta T_{out} = \delta T_{in} = 0.6°C$ and the partial derivatives of ΔT with respect to T_{out} and T_{in} into Equation (D.2),

$$\delta \Delta T = \pm\left[(0.6°C)^2 + (0.6°C)^2\right]^{1/2} = \pm 0.845°C$$

Then, the percentage uncertainty in the heat dissipation rate into the coolant (δq_C), which can be obtained with the substitution of δQ_C, $\delta \Delta T$, and the partial derivatives of Equation (16) with respect to Q_C and ΔT into Equation (D.1) and division of its result by Equation (16), can be written as

$$\frac{\delta q_c}{q_c}(\%) = \pm 100 \times \left[\left(\frac{\delta Q_c}{Q_c}\right)^2 + \left(\frac{\delta \Delta T}{\Delta T}\right)^2\right]^{1/2}$$

or $$\frac{\delta q_c}{q_c}(\%) = \pm 100 \times \left[(0.02)^2 + \left(\frac{0.845^\circ C}{\Delta T}\right)^2 \right]^{1/2} \quad \text{(D.3)}$$

As suggested in Equation (D.3), the worst percentage uncertainty interval in q_c is in the case of smallest coolant temperature change (ΔT) between inlet and outlet at the heat sink. The smallest ΔT was found in EXP2 in this study. ΔT and q_c in EXP2 were 9.1°C and 1552 W, respectively. Thus, the resulted percentage uncertainty in q_c in EXP2 was about 1% which was the highest in this study.

APPENDIX E

COMPUTER PROGRAMS AND SAMPLE OUTPUT

APPENDIX E

COMPUTER PROGRAMS AND SAMPLE OUTPUT

In this Appendix, a listing of the computer programs (SUBTEMP and CONDUCT), a file (called COMMON) providing the information about the variables used in SUBTEMP and CONDUCT, and a sample output from computer simulations are given.

E.1 Computer Program of SUBTEMP

As mentioned in Chapter IV, SUBTEMP was designed to control a problem specifications such as the geometry, grid system, material properties, desired output, and the treatments of boundary conditions and source terms. SUBTEMP should be linked with CONDUCT which was developed by Patankar to solve two-dimensional partial differential equations of heat conduction type. The executable file from SUBTEMP and CONDUCT was used for the computer simulations to predict the temperature field of the system including the substrate surface temperatures. The executable file was in an interactive mode. Thus, several input data were required during running. The input data for the computer simulations (H_s, $\bar{h}$, $\bar{h}_t$, coolant temperature, and ε_f) were shown in Tables 5.4 and 5.5 in Chapter V. The units used in the executable file are: mm in H_s, W/mm^2-K in heat transfer coefficients, and °C in temperatures. Some constants used in SUBTEMP were: temperatures of the flame above the substrate surface and above the heat sink which are 3000 and 1500 °C, respectively, and the ambient air temperature (23.3 °C). The text file of SUBTEMP follows.

```
CCCCCCCCCCCCCCCCCCCCCCCCCCCCCCCCCCCCCCCCCCCCCCCCCCCCCCCCCCCCCCCCCC
C     PROGRAM SUBTEMP                                                C
CCCCCCCCCCCCCCCCCCCCCCCCCCCCCCCCCCCCCCCCCCCCCCCCCCCCCCCCCCCCCCCCCCCC
      SUBROUTINE ADAPT
C-------------------------------------------------------------
C---- THIS PROGRAM IS FOR THE COMPUTER SIMULATIONS TO
C---- PREDICT THE TEMPERATURE FIELD OF THE SYSTEM
C---- (SUBSTRATE AND HEAT SINK) USED FOR DIAMOND SYNTHESIS
C----  BY OXY-ACETYLENE COMBUSTION METHOD
C----
C----    TYPE  : CONDUCTION IN A COMPLEX CYLINDRICAL
C----            GEOMETRY
C----            WITH COMPLEX BOUNDARY CONDITION:
C----            KNOWN HEAT TRANSFER COEFFICIENTS OR
C----            TEMPERATURES AT
C----            THE SUBSTRATE SURFACE
C----
C----
C---- THIS PROGRAM WAS DEVELOPED BY:
C----
C----                          KIYOUNG BANG (APRIL, 1994)
C----
C---- UNDER THE SUPERVISION OF:
C----
C----                          Dr. AFSHIN J. GHAJAR
C----                          SCHOOL OF MECHANICAL AND
C----                          AEROSPACE ENGINEERING
C----                          OKLAHOMA STATE UNIVERSITY
C----                          STILLWATER, OK 74078
C-------------------------------------------------------------
$INCLUDE:'COMMON'
C*************************************************************
      DIMENSION T(NI,NJ)
      EQUIVALENCE (F(1,1,1),T(1,1))
C*-*-*-*-*-*-*-*-*-*-*-*-*-*-*-*-*-*-*-*-*-*-*-*-*-*-*-*-*-*-*-*-*-
      ENTRY GRID
      HEADER='HEAT TRANSFER IN COMBUSTION CVD METHOD'
C****** INPUT DATA ******
      WRITE(*,*) ' NAME OF OUTPUT FILE ?'
      READ(*,*) PRINTF
      WRITE(*,*) ' NAME OF PLOT FILE ?'
      READ(*,*) PLOTF
      MODE=2
      R(1)=0.0
      FCR=25.4
      PI=3.141592654
      WRITE(*,*) 'WHAT IS Hs IN mm ?'
      READ(*,*) HS
C
CONSTRUCT CONTROL VOLUME FACES IN AXIAL DIRECTION
```

```
      XU(2)=0.0
      L1=23
      M1=22
      DX1=6.35/4.
      DX5=(HS-0.8)/3.
      XU(3)=2.0
      XU(4)=4.2
      XU(5)=6.2
      XU(6)=6.35
      DO 22 I=7,9
      XU(I)=XU(I-1)+DX2
 22   CONTINUE
      IF(HS .LE. 6.35) THEN
        DX2=12.7/8.
        DX3=6.35/4.
        DO 23 I=7,14
          XU(I)=XU(I-1)+DX2
 23   CONTINUE
        DO 24 I=15,18
          XU(I)=XU(I-1)+DX3
 24     CONTINUE
      ELSE
        DX2=(HS-6.35)/3.
        DX3=(12.7-(HS-6.35))/5.
        DX4=6.35/4.
        DO 25 I=7,9
          XU(I)=XU(I-1)+DX2
 25     CONTINUE
        DO 26 I=10,14
          XU(I)=XU(I-1)+DX3
 26     CONTINUE
        DO 27 I=15,18
          XU(I)=XU(I-1)+DX4
 27     CONTINUE
      END IF
C
      XU(L1)=25.4+HS
      XU(L1-1)=XU(L1)-0.2
      XU(L1-2)=XU(L1-1)-0.6
      XU(L1-3)=XU(L1-2)-DX5
      XU(L1-4)=XU(L1-3)-DX5
C
CONSTRUCT CONTROL VOLUME FACES IN RADIAL DIRECTION
      YV(2)=0.0
      DY2=6.35/5.
      DY3=25.4/6.
      DY4=12.7/4.
      YV(3)=1.27
      YV(4)=2.73
      YV(5)=3.27
```

```
      YV(6)=4.73
      YV(7)=6.35
      DO 31 J=8,12
      YV(J)=YV(J-1)+DY2
 31   CONTINUE
      DO 32 J=13,18
      YV(J)=YV(J-1)+DY3
 32   CONTINUE
      DO 33 J=19,M1
      YV(J)=YV(J-1)+DY4
 33   CONTINUE
C
      RETURN
C*-*-*-*-*-*-*-*-*-*-*-*-*-*-*-*-*-*-*-*-*-*-*-*-*-*-*-*-*-*-*-*-*-*-
      ENTRY BEGIN
      TITLE(1)='   TEMPERATURE '
      CALL INTA4(KSOLVE(1),1,KPRINT(1),1,KPLOT(1),1,LAST,10)
      CALL DATA7(COND1,0.12,COND2,0.39,COND3,0.001715,
     #  TFLAME0,3000.,TFLAME1,1500.,TFLAME2,1500.,TAIR,23.3)
      CALL DATA2(CAIRS,0.0000821,CAIRG,0.00003305)
      CALL DATA4(SBOLZ,5.67E-14,ECOP,0.5,EMOLY,0.8,
     #           EFLAME,0.007)
C** TFLAME0: FEATHER FLAME TEMPERATURE
C** TFLAME1: TEMP. OF FLAME NEAR THREADED AREA OF SUBSTRATE
C** TFLAME2: TEMP. OF OUTER FLAME OVER COPPER
C** TAIR: AMBIENT AIR TEMP.
C** TWAT: COOLANT TEMP.
C******** INPUT DATA *******
      WRITE(*,*) '   COOLANT TEMPERATURE ?'
      READ(*,*) TWAT
      WRITE(*,*) '   HEAT TRANSFER COEFFICIENT OF COOLANT ?'
      READ(*,*) HWAT
      WRITE(*,*) '   HEAT TRANSFER COEFFICIENT AT THE UPPER
     #               SURFACE OF HEAT SINK ?'
      READ(*,*) HFLAME2
      WRITE(*,*)'    HEAT TRANSFER COEFFICIENT AT THE BOTTOM
     #               OF COPPER HEAT SINK ?'
      READ(*,*) HAIRH
      WRITE(*,*)'    HEAT TRANSFER COEFFICIENT AT THE
     #               CYLINDRICAL SURFACE OF HEAT SINK ?'
      READ(*,*) HAIRV
      WRITE(*,*)'    EMISSIVITY OF THE COMBUSTION FLAME ?'
      READ(*,*) EFLAME
C ***INITIAL GUESS
      DO 100 J=1,M1
      DO 100 I=1,L1
      T(I,J)=100.
      IF(Y(J).LT.6.35) T(I,J)=250.
 100  CONTINUE
C
```

```
C****** PUT WATER TEMP. IN COOLANT PASSING REGION
      DO 110 J=12,17
      DO 110 I=6,13
      T(I,J)=TWAT
 110  CONTINUE
C
       DO 166 I=1,L1
       DO 166 J=1,M1
      IF((X(I) .GT. 25.4) .AND. (Y(J) .GT. 6.35)) THEN
        T(I,J)=TFLAME2
      END IF
 166   CONTINUE
C
C======== CALCULATION OF CONFIGURATION FACTORS, Fij
C========= i:CYLINDRICAL SUBSTRATE SURFACE
C========= J: UPPER SURFACE OF HEAT SINK, WHICH IS
C=========    SURROUNDED
C=========    BY FLAME AND SUBSTRATE
C
      PI=3.141592654
      R1=6.35
      X1=25.4
      DO 182 I=18,L2
      DO 183 J=7,20
      IF(R(J) .GT. (R1+HS)) GO TO 182
      JFLAME=J
      AF1=(X(I)-25.4)*R(J)*YCV(J)/PI
      AF2=(X(I)-25.4)**2+R1**2+R(J)**2
      AF3=AF2-2.0*R(J)*R1
      AF4=AF2+2.0*R(J)*R1
      AF5=1.0/(1.0+AF3/AF4)
     # +SQRT(AF4/AF3)*ATAN(SQRT(AF4/AF3))
       CONFF(I,J)=2.0*AF1/AF4**2*((R(J)-
     # R1)*AF4/AF3+(R(J)+R1))*AF5-
     # 4.0*AF1*(R(J)+R1)/AF4**2*SQRT(AF4/AF3)*
     # ATAN(SQRT(AF4/AF3))
 183  CONTINUE
 182  CONTINUE
      RETURN
C*-*-*-*-*-*-*-*-*-*-*-*-*-*-*-*-*-*-*-*-*-*-*-*-*-*-*-*-*-*-*-*-*-*-*-*-*-*
      ENTRY OUTPUT
      DO 200 IUNIT=IU1,IU2
      IF(ITER.EQ.0) WRITE(IUNIT,210)
  210    FORMAT(2X,'ITER',2X,'T(4,5)',4X,'T(6,10)',
     #   3X,'T(17,4)',3X,'T(15,20)')
      WRITE(IUNIT,220) ITER,T(4,5),T(6,10),T(17,4),T(15,20)
  220    FORMAT(3X,I2,1P4E10.2)
  200 CONTINUE
      IF(ITER.EQ.LAST) THEN
C************ HEAT BALANCE CHECKING
```

```
      SUM1=0.
      SUM2=0.
      SUM3=0.
      SUM4=0.
      SUM5=0.
      SUM6=0.
      SUM7=0.
      SUM8=0.
      SUM9=0.
      SUM10=0.
      PI=3.141592654
C\\\\\  HEAT DISSIPATION TO COOLANT
C\\\\\\\\\ RADIAL DIRECTION
      DO 231 I=6,13
        S1=(SC(I,11)+SP(I,11)*T(I,11))*YCVR(11)*XCV(I)
        S2=(SC(I,18)+SP(I,18)*T(I,18))*YCVR(18)*XCV(I)
C
C
        SUM1=SUM1+S1
        SUM2=SUM2+S2
 231     CONTINUE
      SUM1=SUM1*2.*PI
      SUM2=SUM2*2.*PI
C
C
C\\\\\\\\\ AXIAL DIRECTION
      DO 232 J=12,17
        S3=(SC(5,J)+SP(5,J)*T(5,J))*YCVR(J)*XCV(5)
        S4=(SC(14,J)+SP(14,J)*T(14,J))*YCVR(J)*XCV(14)
        SUM3=SUM3+S3
        SUM4=SUM4+S4
 232     CONTINUE
      SUM3=SUM3*2.*PI
      SUM4=SUM4*2.*PI
C
        DO 234 J=2,M2
          S8=FLUXI1(J,1)*ARX(J)
          SUM8=SUM8+S8
 234     CONTINUE
         SUM8=SUM8*2.*PI
C
C
C***** HEAT LOSS AT THE CYLINDRICAL SURFACE OF COPPER BLOCK
      DO 235 I=2,17
        S9=FLUXM1(I,1)*RV(M1)*XCV(I)
        SUM9=SUM9+S9
 235     CONTINUE
         SUM9=SUM9*2.*PI
C
C
```

```
C********* HEAT GAIN FROM FLAME
C***** TO SUBSTRATE
      DO 236 J=2,6
        S10=FLUXL1(J,1)*ARX(J)
        SUM10=SUM10+S10
 236     CONTINUE
         DO 623 J=1,6
      DO 621 IUNIT=IU1,IU2
        WRITE(IUNIT,*)'J= ', J,T(21,J),T(23,J)
 621  CONTINUE
 623     CONTINUE
      SUM10=SUM10*2.*PI
      GAIN3=SUM10
         GAIN1=GAIN1*2.*PI
         GAIN1N=GAIN1N*2.*PI
         GAIN2=GAIN2*2.*PI
C
C****** HEAT GAINS FROM FLAME TO COPPER AND THREADED AREA
C****** OF SUBSTRATE HAVE BEEN CALCULATED IN SUBROUTINE PHI
C*** TO COPPER BLOCK: GAIN1(FROM OUTER FLAME)
C***                  GAIN1N(VIA CONDUCTION + RADIATION)
C*** TO THREADED SURFACE OF SUBSTRATE: GAIN2 (VIA
C***                                 CONDUCTION + RADIATION)
C
       TGAIN=GAIN1+GAIN2+GAIN3+GAIN1N
       HLOSS1=SUM1+SUM2+SUM3+SUM4
       HLOSS2=SUM5+SUM6+SUM7
       HLOSS3=SUM8
       HLOSS4=SUM9
       TLOSS=COOL+HLOSS3+HLOSS4
       DO 240 IUNIT=IU1,IU2
         WRITE(IUNIT,250) HS,HFLAME2,
     #                    TAIR,HAIRV,
     #      HAIRH, HWAT,TWAT,TGAIN,GAIN1,GAIN1N,
     #      GAIN2,GAIN3,COOL,HLOSS3,HLOSS4,TLOSS
 250  FORMAT(///20('^'),' USED DATA ',20('^')//2X,
     #    'Hs = ',F4.1/
     #    2X,'h OF OUTER FLAME ZONE = ',F10.6/
     #    2X,'h AT CYLINDRICAL SURFACE OF COPPER = ',F10.7/
     #    2X,'h AT THE BOTTOM OF COPPER = ',F10.7/
     #    2X,'h OF COOLANT = ',F10.6/
     #    2X,'TEMP. OF COOLANT = ',F6.2/
     #    2x,'EMISSIVITY OF FLAME = ',F6.4//
     #    2X,'==== HEAT BALANCE CHECKING ===='/5X,
     #  'ALL UNITS ARE WATTS'//3X,
     #  'TOTAL HEAT GAIN FROM FLAME: ',
     #      F12.4/20('-')/10X,
     #    'TO COPPER(CONV. + RAD.): ',F12.4/10X,
     #      'TO COPPER(COND. + RAD.): ',F12.4/10X,
     #      'TO THREADED AREA OF SUBSTRATE: ',F12.4/10X,
```

```
     #      'TO TOP SURFACE OF SUBSTRATE: ',
     #     F12.4/20('-')/3X,
     #     'HEAT LOSS TO COOLANT: ',F12.4/3X,
     #     'HEAT LOSS AT BOTTOM OF COPPER BLOCK: ',F12.4/3X,
     #     'HEAT LOSS AT CYLINDRICAL SURFACE : ',F12.4/3X,
     #     'TOTAL HEAT LOSS FROM COPPER BLOCK: ',F12.4////)
         WRITE(IUNIT,*)  ' === HEAT FLUX FROM FLAME ===  '
 240   CONTINUE
       CALL PRINT
C
C------
COME HERE TO FILL IBLOCK(I,J) BEFORE CALLING PLOT
         DO 260 J=2,M2
         DO 260 I=2,L2
           IF((X(I) .GT. 6.35) .AND. (X(I) .LT. 19.05) .AND.
     #        (Y(J) .GT. 12.7) .AND. (Y(J) .LT. 38.1)) THEN
             IBLOCK(I,J)=1
           END IF
           IF((X(I) .GT. 25.4) .AND. (Y(J) .GT. 6.35)) THEN
             IBLOCK(I,J)=1
           END IF
 260     CONTINUE
C
         IF(HS .GT. 6.35) KK=8
         IF(HS .LE. 6.35) KK=5
           DO 280 I=2,KK
            IBLOCK(I,6)=1
 280     CONTINUE
         CALL PLOT
C------
      END IF
      RETURN
C*-*-*-*-*-*-*-*-*-*-*-*-*-*-*-*-*-*-*-*-*-*-*-*-*-*-*-*-*-
      ENTRY PHI
      DO 300 J=2,M2
      DO 300 I=2,L2
         GAM(I,J)=COND2
         IF(Y(J).LT.6.35) GAM(I,J)=COND1
         IF(X(I).GT.25.4.AND.Y(J).GT.6.35) GAM(I,J)=SMALL
         IF(X(I).GT.6.35.AND.X(I).LT.19.05.AND.
     #      Y(J).GT.12.7 .AND. Y(J).LT.38.1) GAM(I,J)=SMALL
 300  CONTINUE
      DO 302 J=7,11
       GAM(5,J)=COND3
 302  CONTINUE
      DO 305 J=18,M2
       GAM(5,J)=COND3
 305  CONTINUE
C
      IF(HS .GT. 6.35) DELTA1=HS
```

```
      IF(HS .LE. 6.35) DELTA1=6.35
      DO 301 I=2,L2
      IF(X(I) .LT. DELTA1) GAM(I,6)=CAIRG
 301  CONTINUE
C
C
C***********************************
C********** HEAT GAIN FROM FLAME
C
C***** TO COPPER(AXIAL DIRECTION)
      DO 323 J=7,M2
         ABYV=1./XCV(17)
         IF(Y(J) .GT. (6.35+HS)) THEN
         RES=1./HFLAME2+0.5*XCV(17)/GAM(17,J)
      CONS=ABYV/RES
         SC(17,J)=SC(17,J)+CONS*TFLAME2
         SP(17,J)=SP(17,J)-CONS
         ELSE
C** DUMMY VARIABLES
         SUMA1=0.0
         SUMA3=0.0
         DO 324 I=18,L2
         SUMA1=SUMA1+RV(7)*XCV(I)/ARX(J)*CONFF(I,J)
         SUMA3=SUMA3+RV(7)*XCV(I)/ARX(J)*CONFF(I,J)*T(I,6)
 324     CONTINUE
         A1=ECOP*SBOLZ*((1.0-EMOLY)*ECOP*SUMA1-1.0)
         A2=EFLAME*SBOLZ*(TFLAME1+273.15)**4
         A2=A2*(ECOP+(1.0-EMOLY)*ECOP*SUMA1)
         A3=EMOLY*SBOLZ*ECOP*SUMA3
         SL=(6.35+HS)-Y(J)
         DUM1=-3.0*A1*(T(17,J)+273.15)**4+A2+A3+
     #   TFLAME1*CAIRS/SL
         DUM2=4.0*A1*(T(17,J)+273.15)**3 - CAIRS/SL
         SC(17,J)=SC(17,J)+ABYV*DUM1
         SP(17,J)=SP(17,J)+ABYV*DUM2
         END IF
 323  CONTINUE
C
C***** TO THREADED AREA OF SUBSTRATE(RADIAL DIRECTION)
         DO 325 I=18,L2
C** DUMMY VARIABLES
         SUMB1=0.
         SUMB3=0.
         DO 326 J=7,JFLAME
         SUMB1=SUMB1+CONFF(I,J)
         SUMB3=SUMB3+CONFF(I,J)*(T(17,J)+273.15)**4
 326     CONTINUE
         B1=EMOLY*SBOLZ*((1.0-ECOP)*EMOLY*SUMB1-1.0)
         B2=EFLAME*SBOLZ*(TFLAME1+293.15)**4
         B2=B2*(EMOLY+(1.0-ECOP)*EMOLY*SUMB1)
```

```
            B3=ECOP*SBOLZ*EMOLY*SUMB3
            ABYV=RV(7)/YCVR(6)
            RL=(25.4+HS)-X(I)
            DUM1=-3.0*B1*(T(I,6)+273.15)**4+B2+B3+
     #           TFLAME1*CAIRS/RL
            DUM2=4.0*B1*(T(1,6)+273.15)**3-CAIRS/RL
            SC(I,6)=SC(I,6)+DUM1*ABYV
            SP(I,6)=SP(I,6)+DUM2*ABYV
 325  CONTINUE
C
C
C*************************************************************
C
C********** HEAT DISSIPATION TO COOLANT
C*****RADIAL DIRECTION
      DO 330 I=6,13
         ABYV=RV(12)/YCVR(11)
         RES=1./HWAT+0.5*YCV(11)/GAM(I,11)
         CONS=ABYV/RES
         SC(I,11)=SC(I,11)+CONS*TWAT
         SP(I,11)=SP(I,11)-CONS
         ABYV=RV(18)/YCVR(18)
         RES=1./HWAT+0.5*YCV(18)/GAM(I,18)
         CONS=ABYV/RES
         SC(I,18)=SC(I,18)+CONS*TWAT
         SP(I,18)=SP(I,18)-CONS
 330  CONTINUE
C
C*****AXIAL DIRECTION
      DO 340 J=12,17
         ABYV=1./XCV(5)
         RES=1./HWAT+0.5*XCV(5)/GAM(5,J)
         CONS=ABYV/RES
         SC(5,J)=SC(5,J)+CONS*TWAT
         SP(5,J)=SP(5,J)-CONS
         ABYV=1./XCV(14)
         RES=1./HWAT+0.5*XCV(14)/GAM(14,J)
         CONS=ABYV/RES
         SC(14,J)=SC(14,J)+CONS*TWAT
         SP(14,J)=SP(14,J)-CONS
  340 CONTINUE
C
C************ HEAT BALANCE CHECKING
         SUM1=0.
         SUM2=0.
         SUM3=0.
         SUM4=0.
         SUM5=0.
         SUM6=0.
         SUM7=0.
```

```
          PI=3.141592654
C\\\\\  HEAT DISSIPATION TO COOLANT
C\\\\\\\\\ RADIAL DIRECTION
          DO 801 I=6,13
            S1=(SC(I,11)+SP(I,11)*T(I,11))*YCVR(11)*XCV(I)
            S2=(SC(I,18)+SP(I,18)*T(I,18))*YCVR(18)*XCV(I)
C
C
            SUM1=SUM1+S1
            SUM2=SUM2+S2
 801      CONTINUE
          SUM1=SUM1*2.*PI
          SUM2=SUM2*2.*PI
C
C
C\\\\\\\\\ AXIAL DIRECTION
          DO 802 J=12,17
            S3=(SC(5,J)+SP(5,J)*T(5,J))*YCVR(J)*XCV(5)
            S4=(SC(14,J)+SP(14,J)*T(14,J))*YCVR(J)*XCV(14)
            SUM3=SUM3+S3
            SUM4=SUM4+S4
 802      CONTINUE
          SUM3=SUM3*2.*PI
          SUM4=SUM4*2.*PI
          COOL=SUM1+SUM2+SUM3+SUM4
C
C******* CALCUALTION OF HEAT GAIN FROM FLAME **********
          SUM8=0.
          SUM9=0.
          SUM11=0.
C***** TO COPPER
          DO 356 J=7,M2
            IF(Y(J) .GT. (6.35+HS)) THEN
            S8=(SC(17,J)+SP(17,J)*T(17,J))*YCVR(J)*XCV(17)
            SUM8=SUM8+S8
            ELSE
            SUM11=SUM11+(SC(17,J)+SP(17,J)*T(17,J))*
     #            YCVR(J)*XCV(17)
            END IF
 356      CONTINUE
C
C***** TO THREADED AREA OF SUBSTRATE
       DO 357 I=18,L2
          S9=(SC(I,6)+SP(I,6)*T(I,6))*YCVR(6)*XCV(I)
          SUM9=SUM9+S9
 357      CONTINUE
          GAIN1=SUM8
          GAIN1N=SUM11
          GAIN2=SUM9
C
```

```
C-----------------------------------------------------------
C-----------------------------------------------------------
C
C BONDARY CONDITIONS ***********
C                    ***********
C***** AT THE BOTTOM BOUNDARY (AXISYMMETRIC)
C      AND AT THE TOP BOUNDARY (CYLINDRICAL SURFACE OF THE
C      HEAT SINK)
      DO 360 I=2,L2
      KBCJ1(I)=2
      KBCM1(I)=2
         FLXCM1(I)=HAIRV*TAIR
         FLXPM1(I)=-HAIRV
 360  CONTINUE
      DO 361 I=18,L2
      FLXCM1(I)=0.0
      FLXPM1(I)=0.
 361  CONTINUE
C
C***** AT THE LEFT BOUNDARY (BOTTOM OF THE HEAT SINK)
      DO 370 J=2,M2
      KBCI1(J)=2
         FLXCI1(J)=HAIRH*TAIR
         FLXPI1(J)=-HAIRH
 370  CONTINUE
C
C***** AT THE RIGHT BOUNDARY (SUBSTRATE SURFACE)
      DO 371 J=2,6
      KBCL1(J)=2
 371  CONTINUE
       TFLAME0=3000.
       FLXCL1(2)=0.004679*TFLAME0
       FLXPL1(2)=-0.004679
       FLXCL1(3)=0.004477*TFLAME0
       FLXPL1(3)=-0.004477
       FLXCL1(4)=0.004309*TFLAME0
       FLXPL1(4)=-0.004309
       FLXCL1(5)=0.003449*TFLAME0
       FLXPL1(5)=-0.003449
       FLXCL1(6)=0.003293*TFLAME0
       FLXPL1(6)=-0.003293
C
      RETURN
      END
CCCCCCCCCCCCCCCCCCCCCCCCCCCCCCCCCCCCCCCCCCCCCCCCCCCCCCCCCCCCCCCCCCC
CCCCCCCCCCCCCCCCCCCCCCCCCCCCCCCCCCCCCCCCCCCCCCCCCCCCCCCCCCCCCCCCCCC
```

E.2 Computer Program of CONDUCT

To solve the general discretization heat conduction equation, Equation (22) in Chapter IV, CONDUCT was used in the computer simulations of this study. CONDUCT was developed by Patankar (1991) for the solution of two-dimensional partial differential equations of heat conduction type such as Equation (11) in Chapter IV. CONDUCT was designed to employ three coordinate systems: Cartesian, axisymmetric and polar coordinates. It provides the general calculation scheme using the control-volume approach. The text file of CONDUCT follows.

```
CCCCCCCCCCCCCCCCCCCCCCCCCCCCCCCCCCCCCCCCCCCCCCCCCCCCCCCCCCCCCCCCCCCC
C       PROGRAM CONDUCT                                               C
COMPUTER PROGRAM 'CONDUCT' BY DR. SUHAS V. PATANKAR                   C
COPYRIGHT (C) 1991 INNOVATIVE RESEARCH, INC.                          C
C*************************************************************
$INCLUDE:'COMMON'
C*************************************************************
CALCULATIONS IN THE GETTING-READY PHASE
      CALL DEFLT
      CALL GRID
      CALL READY
      CALL BEGIN
   10 CONTINUE
COME HERE TO START THE ITERATION OR TIME-STEP LOOP
      CALL OUTPUT
      IF(KSTOP.NE.0) STOP
      CALL HEART
      GO TO 10
      END
CCCCCCCCCCCCCCCCCCCCCCCCCCCCCCCCCCCCCCCCCCCCCCCCCCCCCCCCCCCCCCCCCCCC
      SUBROUTINE DEFRD
C*************************************************************
$INCLUDE:'COMMON'
C*************************************************************
C
      ENTRY DEFLT
C
COME HERE TO SET THE DEFAULT VALUES
C
      HEADER='USE THE CHARACTER VARIABLE HEADER TO SPECIFY A
     * PROBLEM TITLE'
      PRINTF='PRINT1'
      PLOTF='PLOT1'
```

```
      CALL INTA7(KSTOP,0,LAST,5,ITER,0,KORD,2,MODE,1,
     *           KPGR,1,KOUT,3)
      CALL DATA5(SMALL,1.E-20,BIG,1.E+20,TIME,0.,DT,1.E+20,
     *           R(1),0.)
      CALL DATA2(POWERX,1.,POWERY,1.)
      DO 10 NZ=1,NZMAX
      POWRX(NZ)=1.
   10 POWRY(NZ)=1.
      DO 20 N=1,NFMAX
      CRIT(N)=1.E-5
      KSOLVE(N)=0
      NTIMES(N)=10
      KBLOC(N)=1
      RELAX(N)=1.
      TITLE(N)='                                        '
      KPRINT(N)=0
      KPLOT(N)=0
      DO 30 I=2,NI
      FLUXJ1(I,N)=0.
   30 FLUXM1(I,N)=0.
      DO 40 J=2,NJ
      FLUXI1(J,N)=0.
   40 FLUXL1(J,N)=0.
   20 CONTINUE
      DO 50 J=1,NJ
      DO 50 I=1,NI
      CON(I,J)=0.
      AP(I,J)=0.
      ALAM(I,J)=1.
      GAM(I,J)=1.
      IBLOCK(I,J)=0
      DO 60 N=1,NFMAX
   60 F(I,J,N)=0.
   50 CONTINUE
      DO 70 I=2,NI
      KBCJ1(I)=1
      KBCM1(I)=1
      FLXCJ1(I)=0.
      FLXCM1(I)=0.
      FLXPJ1(I)=0.
      FLXPM1(I)=0.
   70 CONTINUE
      DO 80 J=2,NJ
      KBCI1(J)=1
      KBCL1(J)=1
      FLXCI1(J)=0.
      FLXCL1(J)=0.
      FLXPI1(J)=0.
      FLXPL1(J)=0.
   80 CONTINUE
```

```
C
      RETURN
C*-*-*-*-*-*-*-*-*-*-*-*-*-*-*-*-*-*-*-*-*-*-*-*-*-*-*-*-*-*-*-*-*-*-*-*-*-*
      ENTRY READY
C
      IF(KOUT.NE.1) OPEN(UNIT=7,FILE=PRINTF)
      IU1=6
      IF(KOUT.EQ.2) IU1=7
      IU2=7
      IF(KOUT.EQ.1) IU2=6
CREATE INITIAL OUTPUT
      DO 100 IUNIT=IU1,IU2
C
      IF(MODE.EQ.1) WRITE(IUNIT,1)
    1 FORMAT(1X,'RESULTS OF CONDUCT FOR CARTESIAN COORDINATE
    * SYSTEM'/1X,50(1H*)//)
      IF(MODE.EQ.2) WRITE(IUNIT,2)
    2 FORMAT(1X,'RESULTS OF CONDUCT FOR AXISYMMETRIC
    * COORDINATE SYSTEM'/1X,53(1H*)//)
      IF(MODE.EQ.3) WRITE(IUNIT,3)
    3 FORMAT(1X,'RESULTS OF CONDUCT FOR POLAR COORDINATE
    * SYSTEM'/1X,46(1H*)//)
      WRITE(IUNIT,5) HEADER
    5 FORMAT(1X,64('-')/1X,A64/1X,64('-')//)
      IF(L1.GT.NI.OR.M1.GT.NJ.OR.L1.LT.4.OR.M1.LT.4) THEN
      WRITE(IUNIT,6)
    6 FORMAT(1X,'EXECUTION TERMINATED DUE TO ONE(OR MORE) OF
    * THE FOLLOWI1NG REASON(S)'/2X,1') L1 GREATER THAN
    * NI'/2X,'2) M1 GREATER THAN NJ
    * '/2X,'3) L1 LESS THAN 4'/2X,'4) M1 LESS THAN 4'/)
      KSTOP=1
      ENDIF
  100 CONTINUE
      IF(KSTOP.NE.0) STOP
CALCULATE GEOMETRICAL QUANTITIES
      L2=L1-1
      L3=L2-1
      M2=M1-1
      M3=M2-1
      X(1)=XU(2)
      DO 110 I=2,L2
  110 X(I)=0.5*(XU(I+1)+XU(I))
      X(L1)=XU(L1)
      Y(1)=YV(2)
      DO 120 J=2,M2
  120 Y(J)=0.5*(YV(J+1)+YV(J))
      Y(M1)=YV(M1)
      DO 130 I=2,L2
  130 XCV(I)=XU(I+1)-XU(I)
      DO 140 J=2,M2
```

```
  140 YCV(J)=YV(J+1)-YV(J)
      IF(MODE.EQ.1) THEN
      DO 150 J=1,M1
      RV(J)=1
  150 R(J)=1
      ELSE
      RY1=R(1)-Y(1)
      DO 160 J=2,M1
  160 R(J)=Y(J)+RY1
      RV(2)=R(1)
      DO 170 J=3,M2
  170 RV(J)=RV(J-1)+YCV(J-1)
      RV(M1)=R(M1)
      ENDIF
      IF(MODE.EQ.3) THEN
      DO 180 J=1,M1
  180 SX(J)=R(J)
      ELSE
      DO 190 J=1,M1
      SX(J)=1.
  190 CONTINUE
      ENDIF
      DO 200 J=2,M2
      YCVR(J)=R(J)*YCV(J)
      IF(MODE.EQ.3) THEN
      ARX(J)=YCV(J)
      ELSE
      ARX(J)=YCVR(J)
      ENDIF
  200 CONTINUE
C
      RETURN
      END
CCCCCCCCCCCCCCCCCCCCCCCCCCCCCCCCCCCCCCCCCCCCCCCCCCCCCCCCCCCCCCCCCCCCCCC
      SUBROUTINE HEART
C*************************************************************
$INCLUDE:'COMMON'
C*************************************************************
CONSTRUCT LOOP FOR ALL EQUATIONS
      DO 999 N=1,NFMAX
      NF=N
      IF(KSOLVE(NF).EQ.0) GO TO 999
C
      CALL PHI
C
CALCULATE COEFFICIENTS IN THE DISCRETIZATION EQUATION
C
      BETA=4./3.
      IF(KORD.EQ.1) BETA=1.
      RLX=(1.-RELAX(NF))/RELAX(NF)
```

```
CONSIDER VOLUMETRIC TERMS
      DO 10 J=2,M2
      DO 10 I=2,L2
      VOL=YCVR(J)*XCV(I)
      APT=ALAM(I,J)/DT
      CON(I,J)=(CON(I,J)+APT*F(I,J,NF))*VOL
      AP(I,J)=(APT-AP(I,J))*VOL
   10 CONTINUE
COEFFICIENTS FOR X-DIRECTION DIFFUSION
      DO 20 J=2,M2
      DO 20 I=2,L3
      DIFF=ARX(J)*2.*GAM(I,J)*GAM(I+1,J)/((XCV(I)*
     * GAM(I+1,J)+ XCV(I+1)*GAM(I,J)+SMALL)*SX(J))
      AIP(I,J)=DIFF+SMALL
      AIM(I+1,J)=AIP(I,J)
   20 CONTINUE
      DO 30 J=2,M2
CONSIDER I=1 BOUNDARY
      DIFF=GAM(2,J)/(0.5*XCV(2)*SX(J))+SMALL
      AIM(2,J)=BETA*DIFF
      AIP(1,J)=AIM(2,J)
      AIM(2,J)=AIM(2,J)*ARX(J)
      AIM(1,J)=(BETA-1.)*AIP(2,J)/ARX(J)
      AIP(2,J)=AIP(2,J)+AIM(1,J)*ARX(J)
      IF(KBCI1(J).EQ.1) THEN
      CON(2,J)=CON(2,J)+AIM(2,J)*F(1,J,NF)
      ELSE
      AP(1,J)=AIP(1,J)-FLXPI1(J)
      CON(1,J)=FLXCI1(J)
      TEMP=AIM(2,J)/AP(1,J)
      AP(2,J)=AP(2,J)-AIP(1,J)*TEMP
      AIP(2,J)=AIP(2,J)-AIM(1,J)*TEMP
      CON(2,J)=CON(2,J)+CON(1,J)*TEMP
      ENDIF
      AP(2,J)=AP(2,J)+AIM(2,J)
      AIM(2,J)=0.
CONSIDER I=L1 BOUNDARY
      DIFF=GAM(L2,J)/(0.5*XCV(L2)*SX(J))+SMALL
      AIP(L2,J)=BETA*DIFF
      AIM(L1,J)=AIP(L2,J)
      AIP(L2,J)=AIP(L2,J)*ARX(J)
      AIP(L1,J)=(BETA-1.)*AIM(L2,J)/ARX(J)
      AIM(L2,J)=AIM(L2,J)+AIP(L1,J)*ARX(J)
      IF(KBCL1(J).EQ.1) THEN
      CON(L2,J)=CON(L2,J)+AIP(L2,J)*F(L1,J,NF)
      ELSE
      AP(L1,J)=AIM(L1,J)-FLXPL1(J)
      CON(L1,J)=FLXCL1(J)
      TEMP=AIP(L2,J)/AP(L1,J)
      AP(L2,J)=AP(L2,J)-AIM(L1,J)*TEMP
```

```
      AIM(L2,J)=AIM(L2,J)-AIP(L1,J)*TEMP
      CON(L2,J)=CON(L2,J)+CON(L1,J)*TEMP
      ENDIF
      AP(L2,J)=AP(L2,J)+AIP(L2,J)
      AIP(L2,J)=0.
   30 CONTINUE
COEFFICIENTS FOR Y-DIRECTION DIFFUSION
      DO 40 J=2,M3
      DO 40 I=2,L2
      AREA=RV(J+1)*XCV(I)
      DIFF=AREA*2.*GAM(I,J)*GAM(I,J+1)/(YCV(J)*GAM(I,J+1)+
     * YCV(J+1)*GAM(I,J)+SMALL)
      AJP(I,J)=DIFF+SMALL
      AJM(I,J+1)=AJP(I,J)
   40 CONTINUE
      DO 50 I=2,L2
CONSIDER J=1 BOUNDARY
      AREA=RV(2)*XCV(I)
      DIFF=GAM(I,2)/(0.5*YCV(2))+SMALL
      AJM(I,2)=BETA*DIFF
      AJP(I,1)=AJM(I,2)
      AJM(I,2)=AJM(I,2)*AREA
      AJM(I,1)=(BETA-1.)*AJP(I,2)/(RV(3)*XCV(I))
      AJP(I,2)=AJP(I,2)+AJM(I,1)*AREA
      IF(KBCJ1(I).EQ.1) THEN
      CON(I,2)=CON(I,2)+AJM(I,2)*F(I,1,NF)
      ELSE
      AP(I,1)=AJP(I,1)-FLXPJ1(I)
      CON(I,1)=FLXCJ1(I)
      TEMP=AJM(I,2)/AP(I,1)
      AP(I,2)=AP(I,2)-AJP(I,1)*TEMP
      AJP(I,2)=AJP(I,2)-AJM(I,1)*TEMP
      CON(I,2)=CON(I,2)+CON(I,1)*TEMP
      ENDIF
      AP(I,2)=AP(I,2)+AJM(I,2)
      AJM(I,2)=0.
CONSIDER J=M1 BOUNDARY
      AREA=RV(M1)*XCV(I)
      DIFF=GAM(I,M2)/(0.5*YCV(M2))+SMALL
      AJP(I,M2)=BETA*DIFF
      AJM(I,M1)=AJP(I,M2)
      AJP(I,M2)=AJP(I,M2)*AREA
      AJP(I,M1)=(BETA-1.)*AJM(I,M2)/(RV(M2)*XCV(I))
      AJM(I,M2)=AJM(I,M2)+AJP(I,M1)*AREA
      IF(KBCM1(I).EQ.1) THEN
      CON(I,M2)=CON(I,M2)+AJP(I,M2)*F(I,M1,NF)
      ELSE
      AP(I,M1)=AJM(I,M1)-FLXPM1(I)
      CON(I,M1)=FLXCM1(I)
      TEMP=AJP(I,M2)/AP(I,M1)
```

```
      AP(I,M2)=AP(I,M2)-AJM(I,M1)*TEMP
      AJM(I,M2)=AJM(I,M2)-AJP(I,M1)*TEMP
      CON(I,M2)=CON(I,M2)+CON(I,M1)*TEMP
      ENDIF
      AP(I,M2)=AP(I,M2)+AJP(I,M2)
      AJP(I,M2)=0.
   50 CONTINUE
COME HERE TO INTRODUCE UNDERRELAXATION
CONSTRUCT AP(I,J) AND CON(I,J) IN THEIR FINAL FORM
      DO 60 J=2,M2
      DO 60 I=2,L2
      ANB=AIP(I,J)+AIM(I,J)+AJP(I,J)+AJM(I,J)
      AINR=ANB*RLX
      AP(I,J)=AP(I,J)+ANB+AINR
      CON(I,J)=CON(I,J)+AINR*F(I,J,NF)
   60 CONTINUE
C
CALL THE SOLVE ROUTINE TO OBTAIN THE SOLUTION OF THE
C                              DISCRETIZATION EQUATIONS
C
      CALL SOLVE
  999 CONTINUE
C
      TIME=TIME+DT
      ITER=ITER+1
      IF(ITER.GE.LAST) KSTOP=1
      RETURN
      END
C
CCCCCCCCCCCCCCCCCCCCCCCCCCCCCCCCCCCCCCCCCCCCCCCCCCCCCCCCCCCCCCCCCCCC
      SUBROUTINE SOLVE
C*************************************************************
$INCLUDE:'COMMON'
      DIMENSION RT(6)
C*************************************************************
      BIG1=1.E+10
      SMALL1=1.0E-5
      LL2=2*L2
      LL=LL2-2
      MM2=2*M2
      MM=MM2-2
      N=NF
      NTM=NTIMES(N)
      DO 999 NT=1,NTM
      NTT=NT
      ICON=1
COME HERE TO PERFORM THE I-DIRECTION BLOCK CORRECTION
C-------------------------------------------------------------
      PTX(1)=0.
      QTX(1)=0.
```

```
      DO 10 I=2,L2
      BL=SMALL
      BLP=0.
      BLM=0.
      BLC=0.
      DO  20 J=2,M2
      IF(AP(I,J).LT.BIG1) THEN
      BL=BL+AP(I,J)
      IF(AP(I,J+1).LT.BIG1) BL=BL-AJP(I,J)
      IF(AP(I,J-1).LT.BIG1) BL=BL-AJM(I,J)
      IF(AP(I+1,J).LT.BIG1) BLP=BLP+AIP(I,J)
      IF(AP(I-1,J).LT.BIG1) BLM=BLM+AIM(I,J)
CONVERGENCE CRITERION FOR THE SOLUTION ROUTINE
      RT(1)=AIP(I,J)*F(I+1,J,N)
      RT(2)=AIM(I,J)*F(I-1,J,N)
      RT(3)=AJP(I,J)*F(I,J+1,N)
      RT(4)=AJM(I,J)*F(I,J-1,N)
      RT(5)=-AP(I,J)*F(I,J,N)
      RT(6)=CON(I,J)
      RES=0
      TERM=1.0E-8
      DO 30 IRT=1,6
      RES=RES+RT(IRT)
   30 TERM=MAX(TERM,ABS(RT(IRT)))
      IF(ABS(RES/TERM).GT.CRIT(N))ICON=0
      BLC=BLC+RES
      ENDIF
   20 CONTINUE
      DENOM=BL-PTX(I-1)*BLM
      IF(ABS(DENOM/BL).LT.SMALL1) DENOM=BIG
      PTX(I)=BLP/DENOM
      QTX(I)=(BLC+BLM*QTX(I-1))/DENOM
   10 CONTINUE
      IF(NTT.NE.1.AND.ICON.EQ.1) GO TO 990
      IF(KBLOC(NF).EQ.0) GO TO 80
      BL=0.
      DO 40 I=L2,2,-1
      BL=BL*PTX(I)+QTX(I)
      DO 40 J=2,M2
      IF(AP(I,J).LT.BIG1) F(I,J,N)=F(I,J,N)+BL
   40 CONTINUE
COME HERE TO PERFORM THE J-DIRECTION BLOCK CORRECTION
C-------------------------------------------------------------
      PTY(1)=0.
      QTY(1)=0.
      DO 50 J=2,M2
      BL=SMALL
      BLP=0.
      BLM=0.
      BLC=0.
```

```
      DO 60  I=2,L2
      IF(AP(I,J).LT.BIG1) THEN
      BL=BL+AP(I,J)
      IF(AP(I+1,J).LT.BIG1) BL=BL-AIP(I,J)
      IF(AP(I-1,J).LT.BIG1) BL=BL-AIM(I,J)
      IF(AP(I,J+1).LT.BIG1) BLP=BLP+AJP(I,J)
      IF(AP(I,J-1).LT.BIG1) BLM=BLM+AJM(I,J)
      BLC=BLC+CON(I,J)+AIP(I,J)*F(I+1,J,N)+AIM(I,J)*
     *     F(I-1,J,N)+AJP(I,J)*F(I,J+1,N)+AJM(I,J)*
     *     F(I,J-1,N)-AP(I,J)*F(I,J,N)
      ENDIF
   60 CONTINUE
      DENOM=BL-PTY(J-1)*BLM
      IF(ABS(DENOM/BL).LT.SMALL1) DENOM=BIG
      PTY(J)=BLP/DENOM
      QTY(J)=(BLC+BLM*QTY(J-1))/DENOM
   50 CONTINUE
      BL=0.
      DO 70 J=M2,2,-1
      BL=BL*PTY(J)+QTY(J)
      DO 70 I=2,L2
      IF(AP(I,J).LT.BIG1) F(I,J,N)=F(I,J,N)+BL
   70 CONTINUE
   80 CONTINUE
CARRY OUT THE I-DIRECTION TDMA
C-----------------------------------------------------------
      DO 90 JJ=2,MM
      J=MIN(JJ,MM2-JJ)
      PTX(1)=0.
      QTX(1)=0
      DO 100 I=2,L2
      DENOM=AP(I,J)-PTX(I-1)*AIM(I,J)
      PTX(I)=AIP(I,J)/DENOM
      TEMP=CON(I,J)+AJP(I,J)*F(I,J+1,N)+AJM(I,J)*F(I,J-1,N)
      QTX(I)=(TEMP+AIM(I,J)*QTX(I-1))/DENOM
  100 CONTINUE
      DO 110 I=L2,2,-1
  110 F(I,J,N)=F(I+1,J,N)*PTX(I)+QTX(I)
   90 CONTINUE
CARRY OUT THE J-DIRECTION TDMA
C-----------------------------------------------------------
      DO 120 II=2,LL
      I=MIN(II,LL2-II)
      PTY(1)=0.
      QTY(1)=0
      DO 130 J=2,M2
      DENOM=AP(I,J)-PTY(J-1)*AJM(I,J)
      PTY(J)=AJP(I,J)/DENOM
      TEMP=CON(I,J)+AIP(I,J)*F(I+1,J,N)+AIM(I,J)*F(I-1,J,N)
      QTY(J)=(TEMP+AJM(I,J)*QTY(J-1))/DENOM
```

```
  130 CONTINUE
      DO 140 J=M2,2,-1
  140 F(I,J,N)=F(I,J+1,N)*PTY(J)+QTY(J)
  120 CONTINUE
C-------------------------------------------------------------
  999 CONTINUE
      NTC(N)=NTT
      GO TO 991
  990 NTC(N)=NTT-1
  991 CONTINUE
CALCULATE THE UNKNOWN BOUNDARY VALUES AND FLUXES
C-------------------------------------------------------------
      DO 160 I=2,L2
      TEMP=AJM(I,1)*(F(I,3,N)-F(I,2,N))
      IF(KBCJ1(I).EQ.2)
     1 F(I,1,N)=(AJP(I,1)*F(I,2,N)-TEMP+CON(I,1))/AP(I,1)
      FLUXJ1(I,N)=AJP(I,1)*(F(I,1,N)-F(I,2,N))+TEMP
      TEMP=AJP(I,M1)*(F(I,M3,N)-F(I,M2,N))
      IF(KBCM1(I).EQ.2)
     1 F(I,M1,N)=(AJM(I,M1)*F(I,M2,N)-
     *           TEMP+CON(I,M1))/AP(I,M1)
  160 FLUXM1(I,N)=AJM(I,M1)*(F(I,M1,N)-F(I,M2,N))+TEMP
      DO 170 J=2,M2
      TEMP=AIM(1,J)*(F(3,J,N)-F(2,J,N))
      IF(KBCI1(J).EQ.2)
     1 F(1,J,N)=(AIP(1,J)*F(2,J,N)-TEMP+CON(1,J))/AP(1,J)
      FLUXI1(J,N)=AIP(1,J)*(F(1,J,N)-F(2,J,N))+TEMP
      TEMP=AIP(L1,J)*(F(L3,J,N)-F(L2,J,N))
      IF(KBCL1(J).EQ.2)
     1 F(L1,J,N)=(AIM(L1,J)*F(L2,J,N)-
     *           TEMP+CON(L1,J))/AP(L1,J)
  170 FLUXL1(J,N)=AIM(L1,J)*(F(L1,J,N)-F(L2,J,N))+TEMP
C
COME HERE TO RESET CON,AP,KBC,FLXC, AND FLXP
C-------------------------------------------------------------
      DO 180 J=2,M2
      KBCI1(J)=1
      KBCL1(J)=1
      FLXCI1(J)=0.
      FLXCL1(J)=0.
      FLXPI1(J)=0.
      FLXPL1(J)=0.
      DO 180 I=2,L2
      CON(I,J)=0.
      AP(I,J)=0.
  180 CONTINUE
      DO 190 I=2,L2
      KBCJ1(I)=1
      KBCM1(I)=1
      FLXCJ1(I)=0.
```

```
      FLXCM1(I)=0.
      FLXPJ1(I)=0.
      FLXPM1(I)=0.
  190 CONTINUE
      RETURN
      END
CCCCCCCCCCCCCCCCCCCCCCCCCCCCCCCCCCCCCCCCCCCCCCCCCCCCCCCCCCCC
      SUBROUTINE TOOLS
C***********************************************************
$INCLUDE:'COMMON'
C***********************************************************
      ENTRY EZGRID
C
CONSTRUCT THE X-DIRECTION GRID
      L1=NCVLX+2
      XU(2)=0.
      XU(L1)=XL
      L2=L1-1
      FCVLX=FLOAT(NCVLX)
      DO 20 I=3,L2
      DD=FLOAT(I-2)/FCVLX
      IF(POWERX.GT.0.) THEN
      XU(I)=XL*DD**POWERX
      ELSE
      XU(I)=XL*(1.-(1.-DD)**(-POWERX))
      ENDIF
   20 CONTINUE
CONSTRUCT THE Y-DIRECTION GRID
      M1=NCVLY+2
      YV(2)=0.
      YV(M1)=YL
      M2=M1-1
      FCVLY=FLOAT(NCVLY)
      DO 30 J=3,M2
      DD=FLOAT(J-2)/FCVLY
      IF(POWERY.GT.0.) THEN
      YV(J)=YL*DD**POWERY
      ELSE
      YV(J)=YL*(1.-(1.-DD)**(-POWERY))
      ENDIF
   30 CONTINUE
      RETURN
C*_*_*_*_*_*_*_*_*_*_*_*_*_*_*_*_*_*_*_*_*_*_*_*_*_*_*_*_*_
*_*_*_*_*_*_*
      ENTRY ZGRID
CONSTRUCT THE GRID ZONE-BY-ZONE
C
CONSIDER THE X DIRECTION
      XU(2)=0.
      I2=2
```

```
      DO 100 NZ=1,NZX
      FCVLX=FLOAT(NCVX(NZ))
      ILAST=I2
      I1=ILAST+1
      I2=ILAST+NCVX(NZ)
      DO 100 I=I1,I2
      DD=FLOAT(I-ILAST)/FCVLX
      IF(POWRX(NZ).GT.0.) THEN
      XU(I)=XU(ILAST)+XZONE(NZ)*DD**POWRX(NZ)
      ELSE
      XU(I)=XU(ILAST)+XZONE(NZ)*(1.-(1.-DD)**(-POWRX(NZ)))
      ENDIF
  100 CONTINUE
      L1=I2
C
CONSIDER THE Y DIRECTION
      YV(2)=0.
      J2=2
      DO 110 NZ=1,NZY
      FCVLY=FLOAT(NCVY(NZ))
      JLAST=J2
      J1=JLAST+1
      J2=JLAST+NCVY(NZ)
      DO 110 J=J1,J2
      DD=FLOAT(J-JLAST)/FCVLY
      IF(POWRY(NZ).GT.0.) THEN
      YV(J)=YV(JLAST)+YZONE(NZ)*DD**POWRY(NZ)
      ELSE
      YV(J)=YV(JLAST)+YZONE(NZ)*(1.-(1.-DD)**(-POWRY(NZ)))
      ENDIF
  110 CONTINUE
      M1=J2
      RETURN
C*-*-*-*-*-*-*-*-*-*-*-*-*-*-*-*-*-*-*-*-*-*-*-*-*-*-*-*-*-*-*-*-*-*-*-*-*
      ENTRY PRINT
C
      DO 999 IUNIT=IU1,IU2
C
COME HERE TO ARRANGE THE PRINTOUT OF TWO-DIMENSIONAL FIELDS
      IF(KPGR.NE.0) THEN
C
CREATE PRINTOUT FOR GRID
C
      WRITE(IUNIT,1)
    1 FORMAT(' ')
      IBEG=1
      IEND=L1
      IREP=(IEND-IBEG+7)/7
      DO 200 K=1,IREP
      INCR=MIN(6,IEND-IBEG)
```

```
      ISTOP=IBEG+INCR
      WRITE(IUNIT,2) (I,I=IBEG,ISTOP)
    2 FORMAT(/2X,'I =',2X,7(I4,5X))
      IF(MODE.EQ.3) THEN
      WRITE(IUNIT,3) (X(I),I=IBEG,ISTOP)
    3 FORMAT(1X,'TH =',1P7E9.2)
      ELSE
      WRITE(IUNIT,4) (X(I),I=IBEG,ISTOP)
    4 FORMAT(2X,'X =',1P7E9.2)
      ENDIF
      IBEG=ISTOP+1
  200 CONTINUE
C
      WRITE(IUNIT,1)
      JBEG=1
      JEND=M1
      JREP=(JEND-JBEG+7)/7
      DO 210 K=1,JREP
      INCR=MIN(6,JEND-JBEG)
      JSTOP=JBEG+INCR
      WRITE(IUNIT,5) (J,J=JBEG,JSTOP)
    5 FORMAT(/2X,'J =',2X,7(I4,5X))
      WRITE(IUNIT,6) (Y(J),J=JBEG,JSTOP)
    6 FORMAT(2X,'Y =',1P7E9.2)
      JBEG=JSTOP+1
  210 CONTINUE
      ENDIF
CREATE PRINTOUT FOR THE VALUES OF DEPENDENT VARIABLES
      DO 220 N=1,NFMAX
      IF(KPRINT(N).NE.0) THEN
      WRITE(IUNIT,7) TITLE(N)
    7 FORMAT(/1X,6(1H*),3X,A18,3X,6(1H*)/9X,20(1H-))
      IBEG=1
      JBEG=1
      IEND=L1
      JEND=M1
      IREP=(IEND-IBEG+7)/7
      DO 230 K=1,IREP
      INCR=MIN(6,IEND-IBEG)
      ISTOP=IBEG+INCR
      WRITE(IUNIT,8) (I,I=IBEG,ISTOP)
    8 FORMAT(/'  I =',I6,6I9)
      WRITE(IUNIT, 9)
    9 FORMAT('  J')
      DO 240 J=JEND,JBEG,-1
      WRITE(IUNIT,10) J,(F(I,J,N),I=IBEG,ISTOP)
   10 FORMAT(1X,I2,3X,1P7E9.2)
  240 CONTINUE
      IBEG=ISTOP+1
  230 CONTINUE
```

```
      ENDIF
  220 CONTINUE
  999 CONTINUE
      RETURN
C*-*-*-*-*-*-*-*-*-*-*-*-*-*-*-*-*-*-*-*-*-*-*-*-*-*-*-*-*-*-*-*-*-*-*-*-*-*
      ENTRY PLOT
      OPEN(UNIT=8,FILE=PLOTF)
COME HERE TO CREATE DATA FOR PLOTTING
C
      KFLOW=2
      WRITE(8,300) HEADER
  300 FORMAT(A64)
      WRITE(8,310) KFLOW,L1,M1,NFMAX,MODE,
     *             (KPLOT(I),I=1,NFMAX)
  310 FORMAT(18I5)
      IBLOK=0
      DO 320 J=2,M2
      DO 320 I=2,L2
         IF(IBLOCK(I,J).EQ.1) THEN
            IBLOK=1
            GO TO 330
         ENDIF
  320 CONTINUE
  330 CONTINUE
      WRITE(8,310) IBLOK
      WRITE(8,340) (TITLE(N),N=1,NFMAX)
  340 FORMAT(4A18)
      WRITE(8,350) (X(I),I=1,L1),(Y(J),J=1,M1),
     *      (XU(I),I=2,L1),(YV(J),J=2,M1),(R(J),J=1,M1)
  350 FORMAT(5E12.6)
      DO 360 N=1,NFMAX
      IF(KPLOT(N).NE.0) WRITE(8,350) ((F(I,J,N),I=1,L1),
     *    J=1,M1)
  360 CONTINUE
      IF(IBLOK.EQ.1) THEN
         WRITE(8,310) ((IBLOCK(I,J),I=1,L1),J=1,M1)
      ENDIF
      CLOSE(8)
      RETURN
      END
CCCCCCCCCCCCCCCCCCCCCCCCCCCCCCCCCCCCCCCCCCCCCCCCCCCCCCCCCCCCCCCCCCCCCCCCCCC
      SUBROUTINE VALUES
C*************************************************************
C
CREATE A FACILITY TO ASSIGN VALUES TO REAL VARIABLES
C
      ENTRY DATA9(A1,C1,A2,C2,A3,C3,A4,C4,A5,C5,A6,C6,
     *            A7,C7,A8,C8,A9,C9)
      A9=C9
      ENTRY DATA8(A1,C1,A2,C2,A3,C3,A4,C4,A5,C5,A6,C6,
```

```
     *              A7,C7,A8,C8)
       A8=C8
       ENTRY DATA7(A1,C1,A2,C2,A3,C3,A4,C4,A5,C5,A6,C6,A7,C7)
       A7=C7
       ENTRY DATA6(A1,C1,A2,C2,A3,C3,A4,C4,A5,C5,A6,C6)
       A6=C6
       ENTRY DATA5(A1,C1,A2,C2,A3,C3,A4,C4,A5,C5)
       A5=C5
       ENTRY DATA4(A1,C1,A2,C2,A3,C3,A4,C4)
       A4=C4
       ENTRY DATA3(A1,C1,A2,C2,A3,C3)
       A3=C3
       ENTRY DATA2(A1,C1,A2,C2)
       A2=C2
       ENTRY DATA1(A1,C1)
       A1=C1
       RETURN
C*-*-*-*-*-*-*-*-*-*-*-*-*-*-*-*-*-*-*-*-*-*-*-*-*-*-*-*-*-*-*-*-*-*-*-*-*-*
CREATE A FACILITY TO ASSIGN VALUES TO INTEGER VARIABLES
C
       ENTRY INTA9(I1,J1,I2,J2,I3,J3,I4,J4,I5,J5,I6,J6,
     *             I7,J7,I8,J8,I9,J9)
       I9=J9
       ENTRY INTA8(I1,J1,I2,J2,I3,J3,I4,J4,I5,J5,I6,J6,
     *             I7,J7,I8,J8)
       I8=J8
       ENTRY INTA7(I1,J1,I2,J2,I3,J3,I4,J4,I5,J5,I6,J6,I7,J7)
       I7=J7
       ENTRY INTA6(I1,J1,I2,J2,I3,J3,I4,J4,I5,J5,I6,J6)
       I6=J6
       ENTRY INTA5(I1,J1,I2,J2,I3,J3,I4,J4,I5,J5)
       I5=J5
       ENTRY INTA4(I1,J1,I2,J2,I3,J3,I4,J4)
       I4=J4
       ENTRY INTA3(I1,J1,I2,J2,I3,J3)
       I3=J3
       ENTRY INTA2(I1,J1,I2,J2)
       I2=J2
       ENTRY INTA1(I1,J1)
       I1=J1
       RETURN
       END
CCCCCCCCCCCCCCCCCCCCCCCCCCCCCCCCCCCCCCCCCCCCCCCCCCCCCCCCCCCCCCCCCCCCCCCCCCC
CCCCCCCCCCCCCCCCCCCCCCCCCCCCCCCCCCCCCCCCCCCCCCCCCCCCCCCCCCCCCCCCCCCCCCCCCCC
```

E.3 File of COMMON

The file called COMMON provides all the declaration statements needed in SUBTEMP and CONDUCT. Using the COMMON file, all the variables are shared in all the subroutines in SUBTEMP and CONDUCT. The text file of COMMON follows.

```
CCCCCCCCCCCCCCCCCCCCCCCCCCCCCCCCCCCCCCCCCCCCCCCCCCCCCCCCCCCCCCCCCC
C          FILE OF COMMON                                          C
CCCCCCCCCCCCCCCCCCCCCCCCCCCCCCCCCCCCCCCCCCCCCCCCCCCCCCCCCCCCCCCCCC
      PARAMETER(NI=52,NJ=52,NFMAX=5,NZMAX=10)
      CHARACTER*18 TITLE
      CHARACTER*64 HEADER,PRINTF,PLOTF
      COMMON F(NI,NJ,NFMAX),ALAM(NI,NJ),GAM(NI,NJ),
             CON(NI,NJ),AIP(NI,NJ),AIM(NI,NJ),AJP(NI,NJ),
             AJM(NI,NJ),AP(NI,NJ),IBLOCK(NI,NJ),X(NI),
             XU(NI),XCV(NI),ARX(NJ),Y(NJ),YV(NJ),YCV(NJ),
             YCVR(NJ),R(NJ),RV(NJ),SX(NJ),PTX(NI),QTX(NI),
             PTY(NJ),QTY(NJ),FLUXI1(NJ,NFMAX),
             FLUXL1(NJ,NFMAX),FLUXJ1(NI,NFMAX),
             FLUXM1(NI,NFMAX),KBCI1(NJ),KBCL1(NJ),
             KBCJ1(NI),KBCM1(NI),FLXCI1(NJ),FLXCL1(NJ),
             FLXCJ1(NI),FLXCM1(NI),FLXPI1(NJ),FLXPL1(NJ),
             FLXPJ1(NI),FLXPM1(NI),CONFF(NI,NJ)
      COMMON/GENL/NF,L1,L2,L3,M1,M2,M3,ITER,SMALL,BIG,
     1        LAST,TIME,DT,MODE,KORD,KOUT,IU1,IU2,KPGR,KSTOP
      COMMON/NFF/RELAX(NFMAX),KPRINT(NFMAX),KSOLVE(NFMAX),
     1        KBLOC(NFMAX),KPLOT(NFMAX),NTIMES(NFMAX),
     2        NTC(NFMAX),CRIT(NFMAX)
      COMMON/TTL/TITLE(NFMAX),HEADER,PRINTF,PLOTF
      COMMON/EZG/NCVLX,NCVLY,XL,YL,POWERX,POWERY
      COMMON/ZG/NZX,NZY,NCVX(NZMAX),NCVY(NZMAX),
     1        XZONE(NZMAX),YZONE(NZMAX),POWRX(NZMAX),
     2        POWRY(NZMAX)
      DIMENSION SC(NI,NJ),SP(NI,NJ)
      EQUIVALENCE (CON,SC),(AP,SP)
CCCCCCCCCCCCCCCCCCCCCCCCCCCCCCCCCCCCCCCCCCCCCCCCCCCCCCCCCCCCCCCCCC
CCCCCCCCCCCCCCCCCCCCCCCCCCCCCCCCCCCCCCCCCCCCCCCCCCCCCCCCCCCCCCCCCC
```

E.4 Sample Output from Computer Simulations

The output file for SIM4 from the computer simulation follows, where the used units are: mm for H_S, W/mm^2-K for heat transfer coefficients, °C for temperatures, and W (Watts) for heat transfer rates.

```
RESULTS OF CONDUCT FOR AXISYMMETRIC COORDINATE SYSTEM
 ****************************************************


 ---------------------------------------------------------------
 HEAT TRANSFER IN COMBUSTION CVD METHOD
 ---------------------------------------------------------------


  ITER  T(4,5)    T(6,10)   T(17,4)   T(15,20)
    0  2.50E+02  1.00E+02  2.50E+02  1.00E+02
    1  3.25E+02  3.16E+02  4.88E+02  2.96E+02
    2  3.29E+02  3.22E+02  5.01E+02  2.99E+02
    3  3.30E+02  3.23E+02  5.02E+02  2.99E+02
    4  3.31E+02  3.23E+02  5.03E+02  2.99E+02
    5  3.31E+02  3.23E+02  5.03E+02  2.99E+02
    6  3.31E+02  3.23E+02  5.03E+02  2.99E+02
    7  3.31E+02  3.23E+02  5.03E+02  2.99E+02
    8  3.31E+02  3.23E+02  5.03E+02  2.99E+02
    9  3.31E+02  3.23E+02  5.03E+02  2.99E+02
   10  3.31E+02  3.23E+02  5.03E+02  2.99E+02


^^^^^^^^^^^^^^^^^^^^ USED DATA ^^^^^^^^^^^^^^^^^^^^

  Hs =  7.0
  h AT THE UPPER SURFACE OF HEAT SINK =     .000130
  h AT THE CYLINDRICAL SURFACE OF HEAT SINK =    .0000098
  h AT THE BOTTOM OF HEAT SINK =    .0000091
  h OF COOLANT =     .000689
  TEMP. OF COOLANT =  39.70
  EMISSIVITY OF FLAME =  0.007

  ==== HEAT BALANCE CHECKING ====
     ALL UNITS ARE WATTS

   TOTAL HEAT GAIN FROM FLAME:    2177.9170
--------------------
          TO COPPER(CONV. + RAD.):    1177.0950
          TO COPPER(COND. + RAD.):      16.1559
          TO THREADED AREA OF SUBSTRATE:      48.8412
          TO TOP SURFACE OF SUBSTRATE:     935.8255
--------------------
   HEAT LOSS TO COOLANT:   -2137.9590
   HEAT LOSS AT BOTTOM OF COPPER BLOCK:     -18.5950
   HEAT LOSS AT CYLINDRICAL SURFACE :     -21.2221
   TOTAL HEAT LOSS FROM COPPER BLOCK:   -2177.7760


******     GRID SYSTEM     ******

  I =     1        2        3        4        5        6        7
  X = 0.00E+00 1.00E+00 3.10E+00 5.20E+00 6.27E+00 6.46E+00 6.68E+00

  I =     8        9       10       11       12       13       14
  X = 6.89E+00 8.20E+00 1.06E+01 1.30E+01 1.54E+01 1.78E+01 1.98E+01

  I =    15       16       17       18       19       20       21
  X = 2.14E+01 2.30E+01 2.46E+01 2.64E+01 2.85E+01 3.06E+01 3.19E+01
```

```
 I =    22       23
 X = 3.23E+01 3.24E+01


 J =     1        2        3        4        5        6        7
 Y = 0.00E+00 6.35E-01 2.00E+00 3.00E+00 4.00E+00 5.54E+00 6.98E+00

 J =     8        9       10       11       12       13       14
 Y = 8.25E+00 9.52E+00 1.08E+01 1.21E+01 1.48E+01 1.91E+01 2.33E+01

 J =    15       16       17       18       19       20       21
 Y = 2.75E+01 3.18E+01 3.60E+01 3.97E+01 4.29E+01 4.60E+01 4.92E+01

 J =    22
 Y = 5.08E+01

******       TEMPERATURE        ******
        --------------------

 I =     1        2        3        4        5        6        7
 J
22    1.00E+02 2.80E+02 2.80E+02 2.80E+02 2.84E+02 2.92E+02 2.92E+02
21    2.79E+02 2.79E+02 2.80E+02 2.80E+02 2.86E+02 2.92E+02 2.92E+02
20    2.79E+02 2.79E+02 2.79E+02 2.80E+02 2.86E+02 2.91E+02 2.91E+02
19    2.78E+02 2.78E+02 2.78E+02 2.79E+02 2.85E+02 2.91E+02 2.91E+02
18    2.76E+02 2.76E+02 2.76E+02 2.77E+02 2.83E+02 2.90E+02 2.90E+02
17    2.74E+02 2.74E+02 2.74E+02 2.73E+02 2.73E+02 2.71E+02 2.62E+02
16    2.71E+02 2.71E+02 2.71E+02 2.71E+02 2.70E+02 2.67E+02 2.46E+02
15    2.70E+02 2.70E+02 2.70E+02 2.69E+02 2.69E+02 2.65E+02 2.41E+02
14    2.69E+02 2.69E+02 2.69E+02 2.69E+02 2.68E+02 2.64E+02 2.40E+02
13    2.70E+02 2.70E+02 2.70E+02 2.69E+02 2.69E+02 2.66E+02 2.44E+02
12    2.72E+02 2.72E+02 2.72E+02 2.72E+02 2.71E+02 2.70E+02 2.63E+02
11    2.74E+02 2.74E+02 2.74E+02 2.75E+02 2.99E+02 3.22E+02 3.23E+02
10    2.75E+02 2.75E+02 2.75E+02 2.77E+02 3.00E+02 3.23E+02 3.23E+02
 9    2.75E+02 2.75E+02 2.76E+02 2.78E+02 3.01E+02 3.24E+02 3.24E+02
 8    2.76E+02 2.76E+02 2.77E+02 2.78E+02 3.02E+02 3.24E+02 3.24E+02
 7    2.76E+02 2.76E+02 2.77E+02 2.79E+02 3.02E+02 3.25E+02 3.25E+02
 6    2.37E+02 2.83E+02 2.98E+02 3.04E+02 3.19E+02 3.22E+02 3.25E+02
 5    3.31E+02 3.31E+02 3.31E+02 3.31E+02 3.31E+02 3.31E+02 3.31E+02
 4    3.31E+02 3.31E+02 3.31E+02 3.31E+02 3.31E+02 3.31E+02 3.31E+02
 3    3.31E+02 3.31E+02 3.31E+02 3.31E+02 3.31E+02 3.31E+02 3.31E+02
 2    3.31E+02 3.31E+02 3.31E+02 3.31E+02 3.31E+02 3.31E+02 3.31E+02
 1    2.50E+02 3.31E+02 3.31E+02 3.31E+02 3.31E+02 3.31E+02 3.31E+02

 I =     8        9       10       11       12       13       14
 J
22    2.92E+02 2.92E+02 2.93E+02 2.94E+02 2.95E+02 2.97E+02 2.98E+02
21    2.92E+02 2.92E+02 2.93E+02 2.94E+02 2.95E+02 2.97E+02 2.98E+02
20    2.91E+02 2.92E+02 2.93E+02 2.94E+02 2.95E+02 2.97E+02 2.98E+02
19    2.91E+02 2.91E+02 2.92E+02 2.94E+02 2.95E+02 2.97E+02 2.98E+02
18    2.90E+02 2.90E+02 2.91E+02 2.93E+02 2.95E+02 2.97E+02 2.99E+02
17    2.53E+02 2.30E+02 2.09E+02 2.08E+02 2.29E+02 2.76E+02 3.02E+02
16    2.25E+02 1.73E+02 1.27E+02 1.23E+02 1.65E+02 2.57E+02 3.07E+02
15    2.17E+02 1.58E+02 1.06E+02 1.02E+02 1.50E+02 2.54E+02 3.11E+02
14    2.16E+02 1.57E+02 1.05E+02 1.02E+02 1.51E+02 2.59E+02 3.17E+02
13    2.23E+02 1.71E+02 1.25E+02 1.23E+02 1.69E+02 2.69E+02 3.24E+02
12    2.55E+02 2.34E+02 2.13E+02 2.14E+02 2.42E+02 3.01E+02 3.33E+02
11    3.23E+02 3.25E+02 3.28E+02 3.32E+02 3.36E+02 3.40E+02 3.41E+02
10    3.24E+02 3.25E+02 3.29E+02 3.33E+02 3.37E+02 3.41E+02 3.44E+02
 9    3.24E+02 3.26E+02 3.30E+02 3.34E+02 3.38E+02 3.43E+02 3.47E+02
```

8	3.25E+02	3.27E+02	3.30E+02	3.34E+02	3.39E+02	3.45E+02	3.51E+02
7	3.25E+02	3.27E+02	3.31E+02	3.35E+02	3.40E+02	3.47E+02	3.55E+02
6	3.27E+02	3.29E+02	3.32E+02	3.36E+02	3.43E+02	3.51E+02	3.63E+02
5	3.31E+02	3.30E+02	3.33E+02	3.38E+02	3.46E+02	3.58E+02	3.75E+02
4	3.31E+02	3.31E+02	3.34E+02	3.39E+02	3.47E+02	3.61E+02	3.81E+02
3	3.31E+02	3.32E+02	3.35E+02	3.40E+02	3.49E+02	3.64E+02	3.86E+02
2	3.31E+02	3.32E+02	3.35E+02	3.41E+02	3.50E+02	3.66E+02	3.89E+02
1	3.31E+02	3.32E+02	3.35E+02	3.41E+02	3.50E+02	3.66E+02	3.90E+02

I =	15	16	17	18	19	20	21
J							
22	2.99E+02	2.99E+02	3.00E+02	5.19E+02	9.82E+02	1.29E+03	1.43E+03
21	2.99E+02	2.99E+02	3.00E+02	5.19E+02	9.82E+02	1.29E+03	1.43E+03
20	2.99E+02	3.00E+02	3.00E+02	5.19E+02	9.82E+02	1.29E+03	1.43E+03
19	2.99E+02	3.00E+02	3.01E+02	5.20E+02	9.82E+02	1.29E+03	1.43E+03
18	3.00E+02	3.01E+02	3.02E+02	5.21E+02	9.82E+02	1.29E+03	1.43E+03
17	3.03E+02	3.04E+02	3.05E+02	5.23E+02	9.83E+02	1.29E+03	1.43E+03
16	3.07E+02	3.08E+02	3.09E+02	5.26E+02	9.85E+02	1.29E+03	1.43E+03
15	3.12E+02	3.13E+02	3.13E+02	5.30E+02	9.86E+02	1.29E+03	1.43E+03
14	3.18E+02	3.18E+02	3.19E+02	5.34E+02	9.88E+02	1.29E+03	1.43E+03
13	3.25E+02	3.26E+02	3.26E+02	5.40E+02	9.89E+02	1.29E+03	1.43E+03
12	3.34E+02	3.35E+02	3.36E+02	5.46E+02	9.86E+02	1.28E+03	1.43E+03
11	3.42E+02	3.44E+02	3.45E+02	5.49E+02	9.60E+02	1.25E+03	1.41E+03
10	3.46E+02	3.49E+02	3.50E+02	5.47E+02	9.36E+02	1.23E+03	1.40E+03
9	3.51E+02	3.55E+02	3.57E+02	5.41E+02	8.99E+02	1.18E+03	1.38E+03
8	3.56E+02	3.62E+02	3.67E+02	5.37E+02	8.41E+02	1.10E+03	1.34E+03
7	3.62E+02	3.72E+02	3.82E+02	5.50E+02	7.61E+02	9.53E+02	1.20E+03
6	3.77E+02	3.99E+02	4.45E+02	5.84E+02	7.23E+02	8.55E+02	9.34E+02
5	3.96E+02	4.30E+02	4.88E+02	5.95E+02	7.26E+02	8.57E+02	9.39E+02
4	4.05E+02	4.43E+02	5.03E+02	6.02E+02	7.29E+02	8.61E+02	9.49E+02
3	4.13E+02	4.54E+02	5.14E+02	6.08E+02	7.32E+02	8.65E+02	9.58E+02
2	4.18E+02	4.60E+02	5.20E+02	6.12E+02	7.34E+02	8.68E+02	9.64E+02
1	4.18E+02	4.61E+02	5.21E+02	6.12E+02	7.35E+02	8.68E+02	9.65E+02

I =	22	23
J		
22	1.49E+03	1.50E+03
21	1.49E+03	1.50E+03
20	1.49E+03	1.50E+03
19	1.49E+03	1.50E+03
18	1.49E+03	1.50E+03
17	1.49E+03	1.50E+03
16	1.49E+03	1.50E+03
15	1.49E+03	1.50E+03
14	1.49E+03	1.50E+03
13	1.49E+03	1.50E+03
12	1.49E+03	1.50E+03
11	1.49E+03	1.50E+03
10	1.49E+03	1.50E+03
9	1.49E+03	1.50E+03
8	1.48E+03	1.50E+03
7	1.46E+03	1.50E+03
6	9.57E+02	9.63E+02
5	9.63E+02	9.69E+02
4	9.77E+02	9.85E+02
3	9.87E+02	9.95E+02
2	9.95E+02	1.00E+03
1	9.95E+02	2.50E+02

VITA 2

Kiyoung Bang

Candidate for the Degree of

Doctor of Philosophy

Thesis: EXPERIMENTAL AND COMPUTATIONAL INVESTIGATION OF THE THERMAL EFFECTS ON CVD DIAMOND FILMS BY OXY-ACETYLENE COMBUSTION METHOD

Major Field: Mechanical Engineering

Biographical:

Personal Data: Born in Seoul, Korea, On February 20, 1960, the son of Suk Hong and Eui Yul Bang.

Education: Graduated from Youngdeung Po High School, Seoul, Korea, in February, 1979; received the Bachelor of Science degree in Mechanical Engineering from Sung Kyun Kwan University in February, 1986; received the Master of Science degree in Mechanical Engineering from Oklahoma State University in December, 1989; completed the requirements for the Doctor of Philosophy degree at Oklahoma State University in May, 1994.

Professional Experience: Graduate Research Assistant and Teaching Assistant, School of Mechanical and Aerospace Engineering, Oklahoma State University, 1986 to present.